UNIVERSITÀ
DEGLI STUDI
DI PADOVA

Sede Amministrativa: Universitá degli Studi di Padova
DIPARTIMENTO DI FISICA E ASTRONOMIA

SCUOLA DI DOTTORATO DI RICERCA IN: ASTRONOMIA
INDIRIZZO: EXTRAGALATTICO
CICLO: XXIV

INFRARED SUPERNOVA SEARCH IN STARBURST GALAXIES

Direttore della scuola: Ch.mo Prof. Giampaolo Piotto
Supervisore: Dr. Enrico Cappellaro

Dottorando: Matteo Miluzio

Abstract

The high FIR luminosity of starburst (SB) galaxies is a direct measure of their SFR and implies an high SN rate. This seems in contradiction with the fact that very few SNe have been discovered in SB. Likely, this is related to the presence of dust that introduce a bias due to extinction . A search in the IR, because of the reduced extinction, is deemed to detected the hidden SN population. Early attempts of NIR searches (e.g Mannucci et al 2003, Mattila et al 2007) show no evidence of enhanced SN rate in starbursts, but statistics is still very low. For this reason we started a new complementary search to measure the SN rate using an excellent instrument as HAWK-I@VLT in a sample of 30 nearby starburst galaxies. We obtained about 270 visits during 3 different runs, during which we found 6 SNe: 4 with spectroscopic confirmation and 2 without spectroscopic confirmation, due to their faintness. Through 500 MonteCarlo simulations we extimated, from SFRs based on FIR luminosity, the expected number of events in our search and, with the adopted parameters (IMF, extinction distribution, SF distribution...) and the measured search detection efficiency, we predict, on average, the discovery of 5.4±2.3 SNe. The expected number agrees very well with the observed number. Indeed we found that the expected number of SNe is $\leq$ to 6 in 55% of the experiments. Even if we consider only the SNe with spectroscopic classification (4) their occurrence is significant (22%). We also discussed the effects of different assumptions and choices of the model parameters. The main conclusion is that the number of expected SNe is *consistent* with the observations, so *not* confirming the claim of previous infrared SN search that estimated a number of expected SNe higher than observed.
In another part of the PhD project we used LBC@LBT to estimate the SN rate at high redshift, in order to have an independent check of the claim of a decline of the Ia SNe rates at $z > 0.8$ (Dahlen et al., 2004, 2008). If confirmed, this may have important consequences for the use of Ia SNe as cosmological probes. We obtained only 2 of the 6 epochs planned. However, a sample of 14 candidates have been found, a number consisent with expectations (18). Unfortunately, although this is a very interesting and promising work, the chances of success were limited by bad weather and scheduling problems.

The first chapter introduce the phenomenon of supernovae, with thier classification and thier use as cosmological probes. In the second chapter is described the star formation history, with the main indicators of star formation. Is shown also the sueprnova rate problem introduce in the work of Horiuchi et a. (2011). The third chapter addresses the fundamental relation between star formation rate and supernova rate, with the different implications of the CC SN rate and type Ia rate. Then i show the measurements of the SN rate during the years at different redshift. In this context, a description of our work with LBT is shown. To introduce the next chpater, i describe the importance to analyze the SN rate in starburst galaxies, showing at the same time previous results of optical and IR SN searches in starburst galaxies. Th fourth chapter is a detailed description of our search strategy and data reduction. In the second part of the chapter is shown the SN sample, with description and light curves of all SN discovered. The fifth chapter is focused on the estimation of the expected SN rate with the MonteCarlo simulation. A detailed description of the simulation tool qith the main input parameter is given. In the second part i describe the results of simulation, comparing to the observed number. In the last chapter i summarized the entire work, with the scientific conclusion and the future perspective of the IR searches and the SN searches in starburst galaxies.

Sommario

L'elevata luminositá nel lontano infrarosso delle galassie starburst (SB) é una misura diretta del loro tasso di formazione stellare che a sua volta implica un'elevata frequenza di supernovae. Questo tuttavia sembra in contraddizione con il fatto che sono state scoperte poche supernovae in queste galassie. Molto probabilmente questo é legato alla presenza di grandi quantitá di polvere che introducono un bias dovuto al fenomeno dell'estinzione. Quindi, una ricerca di supernovae condotta alle lunghezze d'onda infrarosse, per via della ridotta estinzione, é piú indicata per rilevare la poplazione di supernovae oscurata dalla polvere. I primi tentativi di osservare queste seprnovae nel vicino infrarosso (Mannucci et al., 2003; Mattila et al., 2007) non hanno tuttavia mostrato un aumento evidente della frequenza di supernovae in galassie starburst, anche se fino ad ora la statistica rimane piuttosto bassa. Per questa ragione abbiamo iniziato un nuovo e complementare progetto che consiste nella ricerca di supernovae in un campione di 30 galassie starburst con lo scopo di misurare la frequenza di supernovae, utilizzando un eccellente strumento quale HAWK-I@VLT. Abbiamo ottenuto un totale di 270 epoche durante 3 differenti periodi di osservazioni, durante i quali abbiamo trovato 6 supernovae: 4 con conferma spettroscopica, 2 senza a causa della loro luminositá troppo debole. attraverso 500 esperimenti MonteCarlo abbiamo stimato, partendo dal tasso di formazione stellare basato sulla luminositá nel lontano infrarosso, il numero atteso di supernovae nella nostra campagna osservativa, e, con i parametri adottati (concernenti la funzione iniziale di massa, l'estinzioni, la distribuzione della formazione stellare...) e la misura della magnitudine limite di tutte le epoche, ci aspettiamo, in media, la scoperta di 5.4 ± 2.3 supernovae. Il numero atteso é quindi in ottimo accordo con quello delle supernovae osservate. Infatti il numero di supernovae attese é $\leq$ a 6 nel 55% degli esperimenti. Anche se consideriamo solo il numero di supernovae confermate spettroscopicamente (4), il loro verificarsi é comunque significativo (22%). Abbiamo inoltre discusso gli effetti delle differenti assunzioni e scelte dei parametri della simulazione. La principale conclusione é che il numero di supernovae é *consistente* con le osservazioni, *non* confermando in tal modo i risultati dei precedenti lavori di ricerca di supernovae nell'infrarosso, ovvero che la frequenza di supernovae aspettata risultava essere piú alta di quello osservata.

In un'altra parte del progetto di dottorato abbiamo utilizzato LBC@LBT per stimare la frequenza di supernovae ad alti redshift, con lo scopo di verificare il declino della frequenza di supernovae di tipo Ia a redshift >0.8 (Dahlen et al., 2004, 2008). Se confermato, questo potrebbe avere importanti conseguenze sull'utilizzo delle supernovae Ia in ambito cosmologico. Abbiamo ottenuto solo 2 epoche delle 6 previste, riuscendo comunque a scoprire 14 robusti candidati (un numero consistente con le attese, 18). Sfortunatamente, sebbene questo fosse un progetto molto interessante e promettente, le chances di successo sono state severamente limitate dal cattivo tempo e dai numerosi problemi sofferti dallo strumento.

Il primo capitolo introduce il fenomeno delle supernovae, con la relativa classificazione e la loro importanza in ambito cosmologico. Il secondo capitolo è dedicato all'importanza dello studio della formazione stellare in cosmologia, con la descrizione dei relativi indicatori. Viene anche illustrato il problema relativo alla frequenza di supernovae così come descritto in Horiuchi et al. (2011). Il terzo capitolo è dedicato alla fondamentale relazione tra tasso di formazione stellare e frequanza di supernovae. Vengono quindi illustrate le diverse misure della frequenza di supernovae negli anni a differenti redshift. viene poi descritto brevemente il nostro lavoro sulla frequenza di supernovae ad alti redshift con l'utilizzo del telescopio LBT. In seguito, vengono introdotti i concetti base per i futuri capitoli: cosa sono e perchè sono importanti le galassie starburst e i precedenti lavori di ricerca di supernovae nell'ottico e nell'infrarosso. Nel quarto capitolo viene descritta la strategia osservativa ed il procedimento di riduzione dei dati. La seconda parte è dedicata alla desfrizione del campione di supernovae trovate. Il quinto capitolo introduce i dettagli della simulazione MonteCarlo per stimare il numero di supernovae aspettate, e confronta questo numero con quello osservato. Il quinto capitolo è dedicato al riassunto del lavoro con relativo conclusioni scientifiche e prospettive future della ricerca infrarossa di supernovae e della ricerca in generale in galassie starburst.

Contents

List of Figures

List of Tables

Aims of the work

The rate of Supernovae is a crucial quantity in astrophysics. Measurements of the core collapse SN rates give information on the range of initial masses of their progenitors, as well as on the slope of the initial mass function at the high mass end. The SN Ia rate in galaxies undergoing strong SF can instead help to asses the relative importance of the prompt component, which is strongly debated. But one of the main problems for measuring SN rate is related to the presence of dust that introduce a bias due to extinction. This is true in particular in star forming systems, as SB galaxies, where dust obscuration is usually larger than in normal galaxies. At the same time, the role of SN rate is especially important in SB, where their high FIR luminosity is a direct measure of their high SFR, that implies an high SN rate. In particular, a large fraction of the massive star formation took place in LIRGs and ULIRGs: this implies that most SNe in starburst galaxies are expected to be core collapse events, with an expected rate at least one or two orders of magnitude larger than in normal galaxies. This seems in contradiction with the fact that very few SN have been discovered in SB galaxies.
The immediately explanation is that most of the SNe are so embedded into the dust that their luminosity is vastly reduced even at near-IR wavelengths (likely $A_V > 30$ mag). In this case, a NIR search for SN can detect only a fraction of the total SN rate, and a survey at longer wavelenght should also be planned (e.g. radio searches).
Another possibility is that if 100% of the FIR flux comes from the central arcsec, then the majority of the SNe are in the nuclear regions, where the presence of the residuals after subtraction, the problem of the spatial resolution of the instruments and the higher extinction in these regions make the discovery of the SNe very difficult.
Another possibility is the presence of AGNs dominating the FIR flux of most of the galaxies: in this case the FIR flux would not be related to the SN rate.
The possibility that the relation between SFR and FIR (and than the relation between SFR-SNR) is incorrect could have fundamental implication on the study of the galaxy evolution. However, this is not a likely possibility as there is a robust concordance among several different methods and this relation has been stable through the years.
At the present day, unfortunately, the statistics is still very low to say with

certainty where the problem lies. For this reason we follow an alternative complementary approach, which makes use of an excellent instrument as HAWK-I at the ESO Very Large Telescope. Through a series of MonteCarlo simulations we will compute the expected SN rate and we will compare this value with the observed rate, in order to verify whether the observed SN rates in SB galaxies is consistent with their star formation rate, the latter as deduced from the FIR luminosity.

Chapter 1

An introduction to supernovae

Since antiquity, observers of the sky were affected by the sudden appearance of new stars in the sky and, for at least 2000 years, these phenomena have noted in their records and archives. Only with the work of F. Zwicky and W. Baade in 1930 they began to understand the difference between what were then classified as ordinary novae and objects much more brilliant, for which was coined the term *supernova*. Since then, thousands of supernovae have been discovered, either randomly or through specific research and today we observe several hundred events per year.
Probably the brightest supernova among those documented in the past was that which shone in 1006. One of the most famous supernovae is instead that appeared in 1054, she also extraordinarily bright enough to be visible in broad daylight. The last supernova observed in our galaxy is the SN 1604. In more recent times, the most studied supernova ever in all bands is the SN1987A in the LMC, the first visible to the naked eye in the last 400 years.
Generally speaking, a supernova originates from the thermonuclear explosion of a white dwarf or from the core collapse of a massive star. The subseqent explosion makes a lamp with brightness billions of times that of our Sun. In astrophysical significance, the explosion either marks the end of a massive (>8 $M_\odot$) star and the birt of a neutron star, or means the complete destruction of a cooling white dwarf forced into explosive carbon burning. Supernovae are linked to some of the most important astrophysical themes, such as stellar evolution, stellar mass loss, collapse and explosion physics, radiative hydrodynamics, shock physics, galactic structure and chemical evolution, and cosmology. Supernovae produce a major fraction of the heavy elements which are widely observed in interstellar medium. Because of their huge brightness, supernovae can be used as standard candle in measuring large scale of distances.

1.1 Classification

SNe are classified into two types according to the explosion mechanism. These types are thermonuclear (Ia) and core-collapse (II, Ib/c) SNe.
The type Ia SNe are believed to arise from binary star systems consisting of a degenerate carbon-oxygen white dwarf (WD) with a red giant or red supergiant companion (e.g. Woosley & Weaver 1986). A white dwarf is the endpoint for stars of up to about 8 times that of the Sun. When it get to the white dwarf stage the star has a mass less than 1.4 times the mass of the Sun, and is about the size of the Earth. In a binary star system, the white dwarf's companion star is often a red giant. The stars may be close enough to each other and the red giant large enough, that material may flow from the red giant onto the white dwarf. The WD accretes material from its companion until reaching the Chandrasekhar limiting mass ($\sim$1.4 $M_\odot$). At this point, the electrons degenerate pressure is no longer able to balance the gravitational pressure. As the radius of the WD decreases the density and temperature increase. This results in a thermonuclear detonation of the entire star. Nothing is left behind, except whatever elements were left over from the white dwarf or forged in the supernova blast. Among the new elements is radioactive nickel, which liberates huge amounts of energy that power the light curve. The type Ia SN luminosity and lightcurve are believed to be powered by the radioactive decay (^{56}Ni$\rightarrow^{56}$Co$\rightarrow^{56}$Fe) of the ^{56}Ni formed in the thermonuclear fusion reaction.
While the progenitors of type Ia SNe are old ($\sim$0.5-3 Gyr, Yoshii et al. 1996), low mass stars, core-collapse SN progenitors are massive stars with initial masses above $\sim$8 $M_\odot$ (Kennicutt, 1984) and lifetimes less than a few tens of Myrs. At the end of the lifetime of a massive star, an iron core is formed with its mass approaching the Chandrasekhar limiting mass. Then the core yields to gravity and begins shrinking (gravitational collapse). As it shrinks, it grows hotter and denser. A new series of nuclear reactions occur, temporarily halting the collapse of the core. When fusion in the core ceases, the star begins the final phase of gravitational collapse. The core temperature rises to over 100 billion degrees as the iron atoms are crushed together. The repulsive force between the nuclei is overcome by the force of gravity. So the core compresses but then recoils. The energy of the recoil is transferred to the envelope of the star, which then explodes and produces a shock wave. As the shock encounters material in the star's outer layers, the material is heated, fusing to form new elements and radioactive isotopes. The shock then propels that matter out into space. The total kinetic energy released in the expanding envelope of the star is $\sim 10^{51}$ ergs which is only $\sim$1% of the total energy emitted in the form of the neutrinos. As the envelope expands, $\sim 10^{49}$ ergs of energy is radiated, resulting in the SN reaching a peak luminosity of $\sim 10^9$ $L_\odot$. The CCSN luminosity and its evolution are believed to be powered mainly by the SN shock and the radioactive decay (^{56}Ni$\rightarrow^{56}$Co$\rightarrow^{56}$Fe)

of the (^{56}Ni formed in the explosion (e.g. Eastman 1994).

1.2 Observational classification of supernovae

SNe were originally separated into just two types, I and II, according to the observed presence of hydrogen in their spectra (Minkowski 1941). These two types were later divided into subtypes according to other spectral characteristics and light curve shapes. In Fig. 1.1, a diagram from Turatto (2003), demonstrates the optical classification of SNe. The classification of SNe is generally performed on the optical spectra but, to some extent, also on their light curves. Since SNe are brighter near their maximum light, for obvious reasons the classification is based on the early spectra, which consist of a thermal continuum and P-Cygni profiles of lines formed by resonant scattering. This means that the SN types are assigned on the basis of the chemical and physical properties of the outermost layers of the exploding stars. The first two main classes of SNe were identified on the basis of the presence or absence of hydrogen lines in their spectra: SNe of type I (SNI) did not show H lines, while those with the obvious presence of H lines were called type II (SNII). In the mid-1980s, evidence began to accumulate that the peculiar SNI formed a class physically distinct from the others. The objects of the new class, characterized by the presence of HeI , were called type Ib (SNIb), and "classical" SNI were renamed as type Ia (SNIa). The new class further branched into another variety, SNIc, based on the absence of He I lines. Whether these are physically distinct types of objects has been long debated. In several contexts they are referred to as SNIb/c.

1.2.1 Type Ia (thermonuclear) supernovae

Ignition of nuclear fuel under higly degenerate conditions leads to a thermonuclear runaway, because the gas does not expand in response to the local energy generation. The local temperature then increases, further promoting nuclear burning, which may lead to explosion. Type Ia SNe are believed to arise from this kind of explosion, as stellar evolution naturally provides ideal candidates for these events, i.e. WDs which manage to reach ignition conditions because their mass grows due to accretion from a companion. The most relevant observational facts which support this model are:

- H lines are not detected in the SNIa spectra, excluding progenitors which retain their H rich envelope until explosion, i.e. Red Supergiants, Blue Supergiants and AGB stars.

- SNIa occur in all galaxy types, including Ellipticals, and are not exclusively associated to young stellar populations. This implies that the delay time of their progenitor varies within a wide range. WDs are the

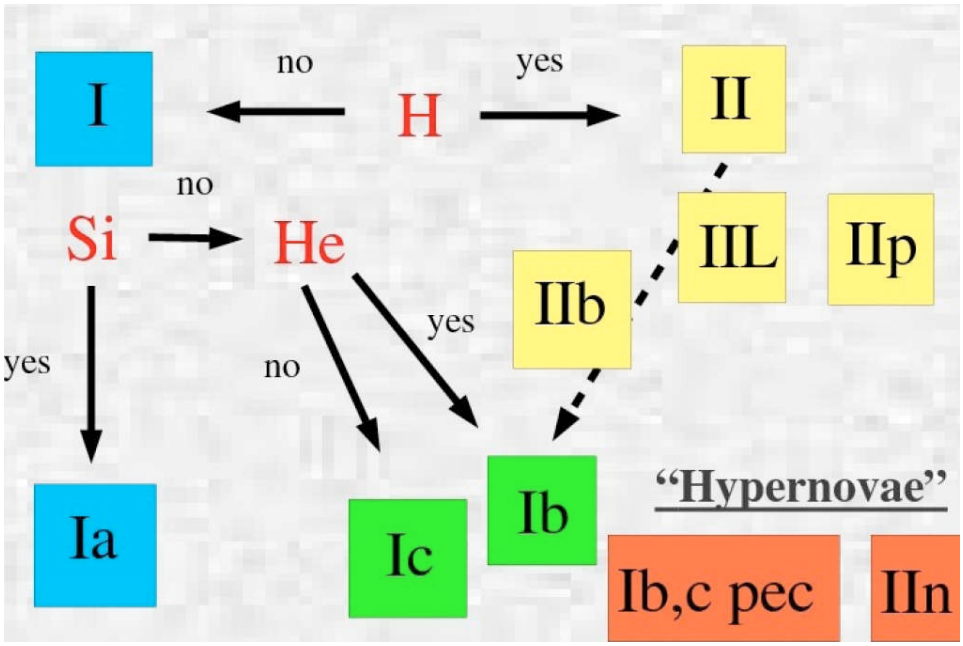

Figure 1.1: Supernova taxonomy according to spectra and light curves (from Cappellaro & Turatto (2001)).

evolutionary end point of stars with $M \leq 8M_{\odot}$, whose evolutionary lifetimes range from ~ 40 Myr up to a Hubble time.

- Light curves and spectra of SNIa are remarkably similar, especially compared to other SN kinds. WDs have a characteristic structure which easily accounts for the uniformity of SNIa events.

- The light curve of SNIa is well explained as powered by the radioactive decay of ^{56}Ni to ^{56}Co and then of ^{56}Co to ^{56}Fe. Ignition of He or of carbon under highly degenerate conditions leads to the production of 56Ni in high quantity, when the nucleosynthesis proceeds to full incineration and Fe group elements are the ultimate burning ashes.

The accepted paradigm for SNIa precursors consists in CO WDs (with $M \leq 8M_{\odot}$) which manage to explode. The explosion of a Chandra CO WD accounts very well for the light curves, nucleosynthetic yield, and spectra of the bulk of SNIa events, and it is considered the most successful model.
The spectra are characterized by lines of intermediate mass elements such as calcium, oxygen, silicon and sulfur during the peak phase and by the absence of H at any time. With age the contribution of the Fe lines increases and several months past maximum the spectra are dominated by [Fe II] and [Fe III] lines.

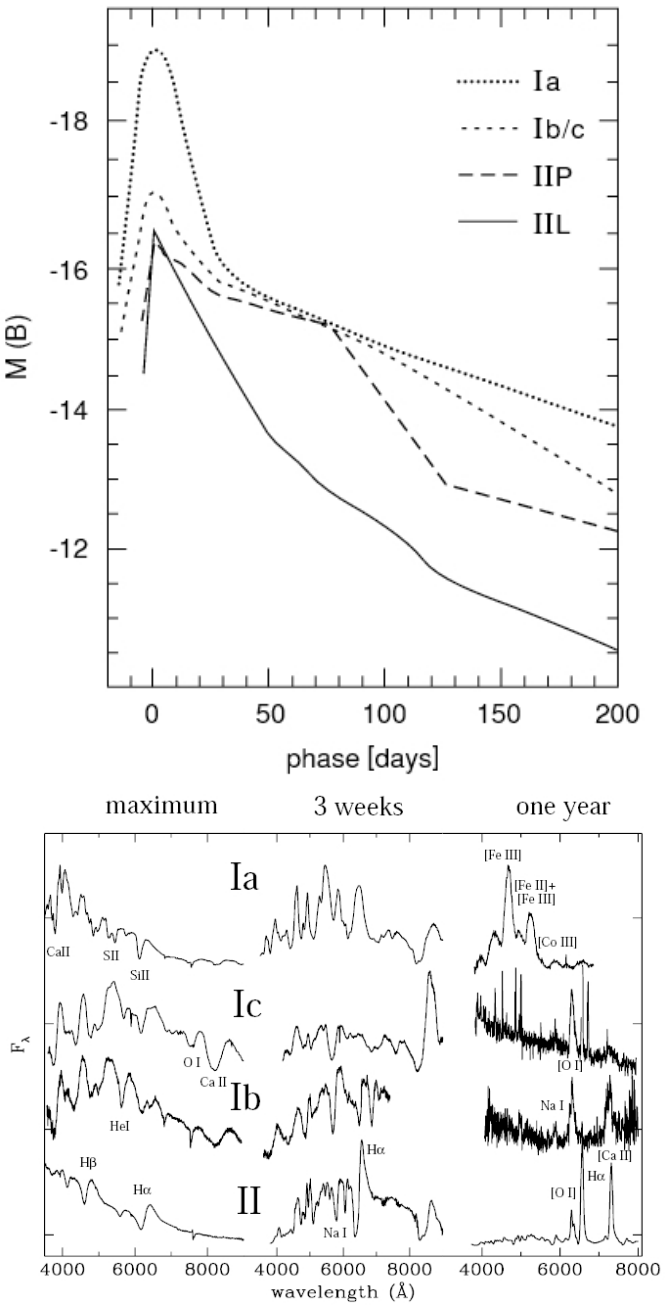

Figure 1.2: *Top*: Light curves of the main SN types. *Bottom*: The spectra of the main SN types at maximum, three weeks, and one year after maximum (from Cappellaro & Turatto (2001), Turatto (2003)).

The analysis of homogeneous sets of optical data led to the discovery of a correlation between the peak luminosity and the shape of the early light curve with brighter objects having a slower rate of decline than dimmer ones. This correlation has been employed to calibrate SNIa as useful distance indicators up to cosmological distances (see later). It is known that the peak luminosity of SNIa is directly linked to the amount of radioactive ^{56}Ni produced in the explosion. Hence SNIa, having different magnitudes at maximum, are probably the result of the synthesis of different amounts of radioactive ^{56}Ni. Moreover, there are indications of large variances (up to a factor 2) in the total mass of the ejecta.
Observations at other wavelengths have provided very useful information. In particular, infrared and I-band light curves have shown that the light curves of SNIa are characterized by a secondary peak 20-30 days after the B maximum.
The light curves of faint objects are steeper than those of other SNIa, probably because of a progressive transparency to positrons from radioactive decay. Faint SNIa also show slower expansion velocity of the emitting gas both at early and late epochs.
The calibration of the absolute magnitudes of a number of type Ia SNe by Cepheids range from M_V = -19.34 to M_V = -19.64 with small dispersions.

1.2.2 Core Collpase Supernovae

Core Collapse SNe exhibit a large variety of light curves and spectra. This class includes Type Ib and Ic (no hydrogen lines in the early spectra) and Type II Sne, which are distinguished in four classes (SNIIP, SNIIL, SNIIn and SNIIb), according to the shape of the light curve and spectral characteristics. There's no doubt that (most) CC SNe correspond to the death of massive stars which evolve all the way up to the formation of a massive iron core. The final collapse of the core and its bounce at the neutron star formation are responsible for initiating the explosion of the outer layers, which include a nuclearly processed mantle and any H rich envelope surviving the preceeding evolution. The successful ejection of these layers is secured by the absorption of a tiny fraction (~ 0.01) of the energy flux of the neutrinoes being released by the collapsed core. Other explosion mechanisms (e.g. electron capture in a collapsing ONeMg core, or pair instability SNe in very massive objects) may be resposible for a few events, respectively at the lower and upper mass range of SNII progenitors. A CC SN leaves a compact remnant, which may be a neutron star or a black hole depending on whether the remnant mass is lower or higher than about 2 $M_\odot$.

Type Ib and Ic Supernovae

Type Ia events which do not show the silicon feature are assigned subclasses Ib and Ic. Other characterizing features are the absence of H lines and the presence of He I. The excited levels of He producing such lines are thought

to be populated by fast electrons accelerated by γ-rays from the decay of ^{56}Ni and ^{56}Co. SNe Ib show lines of neutral helium near the maximum light whereas SNe Ic show only weak evidence for helium. Type Ib and Ic appear only in spiral type galaxies and are believed to be produced by the same mechanism as type II events i.e. core-collapse. The progenitors of SNe Ib and Ic are believed to have lost, respectively, their hydrogen, or even helium envelope via stellar mass-loss or mass transfer to a companion star (e.g. Filippenko 2001), before the explosion.
In order to investigate the physical differences between these two classes, the signatures of He were searched carefully. SNIc differ from SNIb by the He abundance rather than by the amount of mixing of ^{56}Ni in the helium envelope. Modest differences in the He I line optical depths might transform type Ib into type Ic objects. In addition to the different strengths of He lines, it has been suggested that permitted oxygen lines are relatively stronger in type Ic than in Ib and the nebular emission lines broader. In general, type Ib appear more homogeneous than type Ic.

Type II supernovae

Type II SNe are characterized by the obvious presence of H in their spectra. They avoid early type galaxies, are strongly associated with regions of recent star formation and are commonly associated with the core collapse of massive stars.
Type II events are divided into four sub-types: IIP, IIL, IIn, and IIb. The two most common ones IIP (plateau) and IIL (linear) are distinguished by the different shapes of their light curves. Type IIP SNe show a plateau in their optical light curves from about 20 days to about 100 days post maximum light. Due to the plateau phase the light from these events declines only by about 1-2 magnitudes during the first $\sim$100 days whereas the linearly declining (type IIL) SN light curve fades by about 4 magnitudes over the same period (Patat et al. 1994). The different light curve behaviour of the type IIP and IIL classes is believed to be due to the different masses of hydrogen in the SN ejecta. The hydrogen mass in SN IIP ejecta ranges around 5-10 $M_\odot$ whereas the SNe showing type IIL light curves have only $\sim$1-2 $M_\odot$ hydrogen in their ejecta (Cappellaro & Turatto 2001). During the plateau phase the radius of the SN photosphere and the effective temperature remain relatively constant due to the recombination and opacity effects in the massive hydrogen envelope (Eastman et al. 1994). After $\sim$100 days from the peak the luminosity of both types of SNe declines exponentially, being powered by the radioactive decay from ^{56}Co to ^{56}Fe.

1.2.3 Type IIb supernovae

A Type IIb supernova has a weak hydrogen line in its initial spectrum, which is why it is classified as a Type II. However, later on the H emission becomes undetectable, and the spectrum more closely resembles a Type Ib supernova.

The progenitor could have been a giant star which lost most of its hydrogen envelope due to interactions with a companion in a binary system, leaving behind the core that consisted almost entirely of helium. As the ejecta of a Type IIb expands, the hydrogen layer quickly becomes more transparent and reveals the deeper layers. The classic example of a Type IIb supernova is Supernova 1993J. The IIb class was first introduced (as a theoretical concept) by Ensman & Woosley 1987.

Type IIn supernovae

Type IIn SNe show narrow emission lines on top of broad emission components. They show only weak P-Cygni line profiles. The early time continua are very blue, He I emission is often present and, in some cases, narrow Balmer and Na I absorptions are visible.
The observed properties of type IIn SNe are believed to be due to the interaction of the SN ejecta with a dense circumstelalr medium (CSM). The interaction of the fast ejecta with the slowly expanding CSM generates a forward shock in the CSM and a reverse shock in the ejecta. The shocked material emits energetic radiation whose characteristics strongly depend on the density of both the CSM and the ejecta, and on the properties of the shock. Thus the great diversity of observed SNIIn can provide clues to the different history of the mass-loss in the late evolution of progenitors. High mass loss rates of up to $\sim 10^{-3} M_{\odot} yr^{-1}$ have been inferred for the progenitor stars of type IIn events resulting in high CSM densities of up to $\sim 10^{7}$ cm^{-3} (Chugai 1997).

1.3 Cosmology from Type Ia Supernovae

SNe Ia appear to be photometrically quite homogeneous, generally following standard light-curve shapes to within 0.1 mag and having an absolute magnitude scatter of no more than 0.25 mag. With an absolute-magnitude scatter of no more than 0.25 mag, SNe Ia were expected to play an increasingly important role in cosmology. This luminosity homogeneity, together with the extremely high luminosity of SNe Ia (approaching $10^{010} L_{\odot}$) that makes them detectable across the universe, plus the fact that unlike galaxies, supernovae are observed as point sources which facilitates accurate photometry, make SNe Ia extremely attractive as distance indicators for cosmology. With advances in observation and modeling, SNe Ia are certain to become increasingly valuable as extragalactic distance indicators. Relatively nearby SNe Ia ($z \leq 0.1$) have been used to probe departures from pure Hubble flow and to measure the value of the Hubble constant. More remote SNe Ia ($z \leq 1$) have been used to test the reality of the universal expansion and measure the deceleration parameter.
In the standard model, an obvious possible reason for the homogeneity of

SNe Ia is that each progenitor white dwarf must approach the fixed Chandrasekhar mass before it can explode. Possible reasons for the mild diversity that exists even among normal SNe Ia are that the range in the initial masses and compositions (especially the carbon to oxygen ratio) of the white dwarfs, and differences in the time history of their mass accretion rates, could lead to pre-explosion structural differences that cause a spread in the ejected masses of ^{56}Ni.
Phillips and Hamuy of the CTIO (Chile) have shown that it is possible to calibrate a relationship between the shape of the curve of light and magnitude of the maximum, which has made possible the measurement of the distance with an accuracy of about 7%. In this way the type Ia SNe have recovered their role as distance indicators.
In the nineties was born some research groups (*The High-Z Sn Search (HZSNS)* or *The supernova Cosmology Project (SCP)* with the express purpose of measuring the cosmological parameters of the universe through the observation of supernovae Ia at high redshift. At the end of the nineties both groups realized something unexpected: the results were in favor of an accelerated expansion and a non-zero cosmological constant.It appears that the universe is permeated with some form of dark energy that acts against gravity.
The error ellipses associated with the measures taken by the study of supernovae and those obtained from the study of the cmb, determined individually a wide range of allowed values. Due to their different orientation in the plane of Figure 1.3, their intersection defines a relatively narrow zone for the pairs $(\Omega_\Lambda, \Omega_M)$ of possible values. In particular, the best fits give a cosmologically flat Universe with $\Omega_\Lambda \simeq 0.7$ and $\Omega_M \simeq 3$.

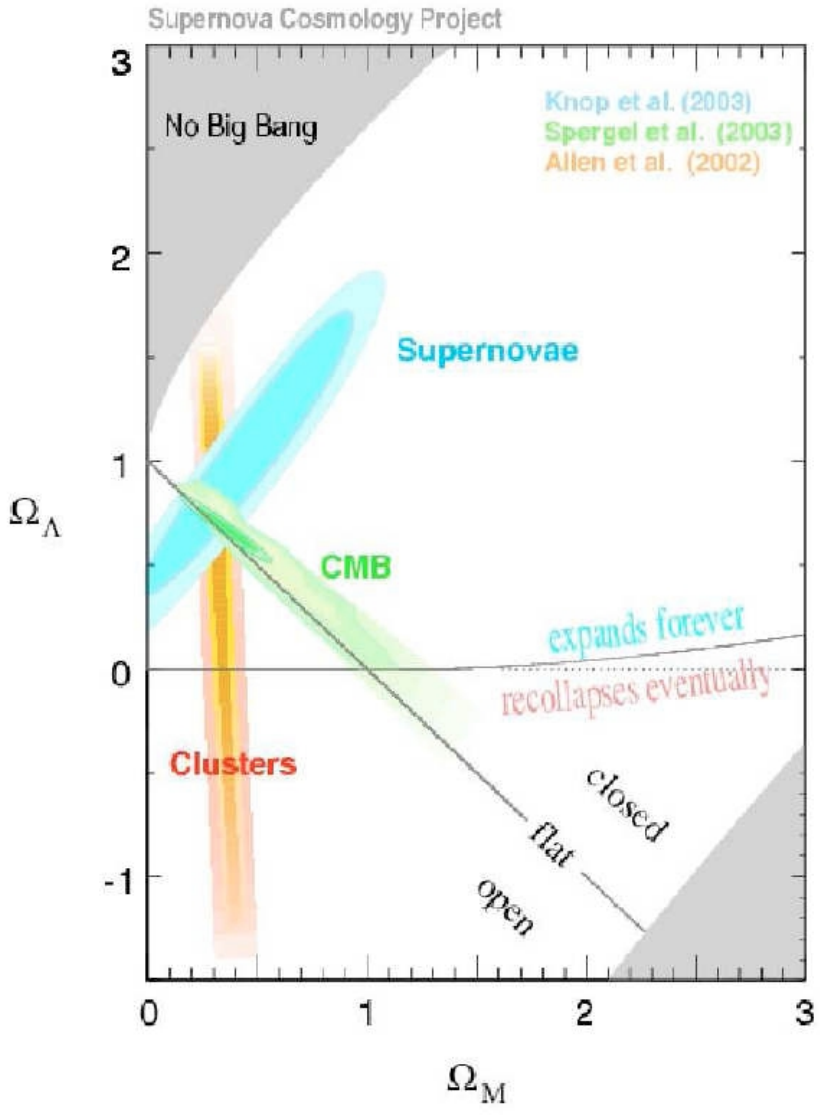

Figure 1.3: Diagram Ω_M, Ω_Λ. Are shown he error ellipses associated with the measures taken by the study of supernovae and those obtained from the study of the cmb (with the BOOMERanG experiment. From the intersection of the different results is clear that the Universe is flat, dominated by the Dark Energy.

Chapter 2

Star Formation

The determination of the star formation history (the temporal evolution of the star formation) of the Universe is a key goal of modern cosmology, as it is crucial to our understanding of how structure in the Universe forms and evolves. The process of galaxy formation is one of the many open questions in astronomy. Existing theories are grouped into two categories:

- *Monolithic*: Olin Eggen, Donald Lynden-Bell, and Allan Sandage in 1962 (Eggen et al., 1962), proposed a theory that disk galaxies form through a monolithic collapse of a large gas cloud. As the cloud collapses the gas settles into a rapidly rotating disk. This scenario is known as a top-down formation scenario;
- *Hierarchical*: observations of the early universe strongly suggest that objects grow from bottom-up, i.e. smaller galaxies build up larger ones by merger events (Cole et al., 1994)

Obviously, different galaxy formation models imply different star formation histories (hereafter, SFH):

- *Monolithic*: in this case a burst is followed by a declining rate of the star formation, driven by the gas supplied by evolved stars. Clearly, there are different SFH slope for different morphological types of galaxies;
- *Hierarchical*: in this case the star formation is not continuous: the burst is triggered by a tidal interactions. The different morphological types are created by the magnitude of the mergers.

The study of the SFH can help to discriminate the actual scenario.

2.1 Star Formation Indicators

Star formation is traced by a number of observables, often complementary to each other. IR-UV continuum emission and optical line emission can be

used to determine the specific SFR in galaxies, and an extinction corrected SF rate density, SFR, can be estimated.

Ultraviolet continuum

The ultraviolet (UV)(1250-2500Å) is where the bulk of the energy from young, massive stars is emitted. The main advantages of use UV continuum are that it is directly tied to the photospheric emission of the young stellar population and it can be applied to star-forming galaxies over a wide range of redshifts. As a result, it is the most powerful probe of the cosmological evolution in the SFR. The main drawback of the method is its sensitivity to extinction.
The other main limitation, which is shared by all of the direct methods, is the dependence of the derived SFRs on the assumed form of the IMF. The integrated spectrum in the 1500 to 2500 Å range is dominated by stars with masses above $\sim$5 $M_\odot$, so the SFR determination involves a large extrapolation to lower stellar masses.

Recombination lines

Young stars emit UV radiation that ionizes atoms (mostly H) in nearby gas clouds. Free electrons in the ionized gas then recombine with the atoms, then they jump down the energy level "ladder" to less excited states. In most applications the SFR has been derived from measurements of the H_α line, but other recombination lines, including Hβ, Pα, Pβ, Brα, and Brγ, have been used as well. The primary advantages of this method are its high sensitivity and the direct coupling between the nebular emission and the massive SFR. The star formation in nearby galaxies can be mapped at high resolution even with small telescopes, and the Hα line can be detected in the redshifted spectra of starburst galaxies to z$\gg$2.
Extinction is probably the most important source of systematic error in Hα derived SFRs. Much higher extinction is encountered in localized regions, especially in the the dense HII regions in circumnuclear starbursts, and there the near-IR Paschen or Brackett recombination lines are required to reliably measure the SFR.
The ionizing flux is produced almost exclusively by stars with $M > 10M_\odot$, so SFRs derived from this method are especially sensitive to the form of the IMF. Fortunately, both the Hα equivalent widths and broadband colors of galaxies are very sensitive to the slope of the IMF over the mass range 1-30 $M_\odot$, and these can be used to constrain the IMF slope.

Far Infrared

A significant fraction of the bolometric luminosity of a galaxy is absorbed by interstellar dust and re-emitted in the thermal IR($\sim 10 - 300\mu m$). The absorption cross section of the dust is strongly peaked in the ultraviolet, so in principle the FIR emission can be a sensitive tracer of the young stellar population and SFR.The efficacy of the FIR luminosity as an SFR tracer depends on the contribution of young stars to heating of the dust and on the optical depth of the dust in the star forming regions.The simplest physical situation is one in which young stars dominate the radiation field throughout the UV-visible and the dust opacity is high everywhere, in which case the FIR luminosity measures the bolometric luminosity of the starburst. In such a limiting case the FIR luminosity is the ultimate SFR tracer, providing what is essentially a calorimetric measure of the SFR. Such conditions roughly hold in the dense circumnuclear starbursts that power many IR-luminous galaxies. Therefore the FIR emission is an excellent measure of the SFR in dusty circumnuclear starbursts.

Radio continuum

The non-thermal radio emission is a tracer of the supernova activity (supernova remnants) in a galaxy and is correlated with far-infrared luminosity. For this tracers there isn't the problem of dust extinction but it suffers from uncertain calibration.
In recent years, all wavelength regions have been exploited to track down star formation at all redshifts, and trace the star formation history of the Universe. At high redshift the Lyman-break galaxies (Steidel et al., 1999, 1996) provide the bulk of the UV light from star formation, while SCUBA has been used to detect the brightest FIR sources in the range $1 \lesssim z \lesssim 3-4$ (e.g., Barger et al. 1999,2000; Smail et al. 2000; Chapman et al. 2003). The Lyman-break galaxies are, by selection, actively star-forming systems, resembling in many aspects local starburst galaxies (Pettini et al. 1998; Meurer et al. 1997; Meurer, Heckman & Calzetti 1999) , and possibly covering a large range in metal and dust contents (Pettini et al. 1999; Steidel et al. 1999; Calzetti 1997). The SCUBA sources occupy the high-end of the FIR luminosity function of galaxies (Blain et al. 1999), and are dust-rich objects. The relationship between the UV-selected and FIR-selected luminous systems is not yet clear.

2.2 Where is Star Formation?

There are two very different regions of star formation inside galaxies (with different regimes):one in the extended disks of spiral and irregular galaxies; the other in compact, dense gas disks in the centers of galaxies.

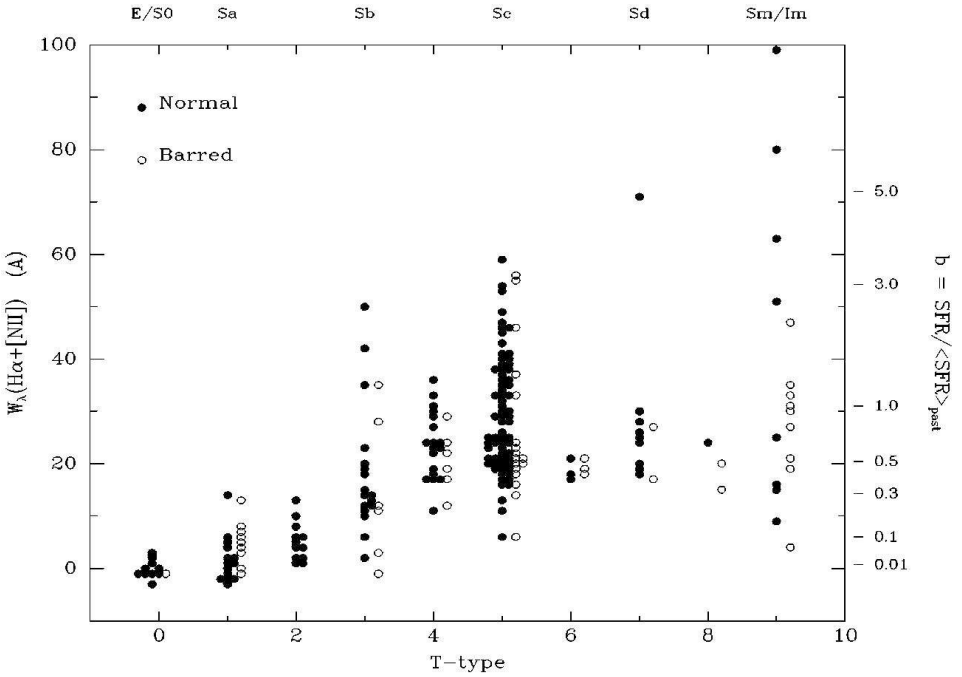

Figure 2.1: e
mission-line equivalent widths for a large sample of nearby spiral galaxies]Distribution of integrated Hα+[NII] emission-line equivalent widths for a large sample of nearby spiral galaxies, subdivided by Hubble type and bar morphology. The right axis scale shows corresponding values of the stellar birthrate parameter b, which is the ratio of the present SFR to that averaged over the past (Kennicut et al.1998)

Disks

The absolute SFRs in galaxies, expressed in terms of the total mass of stars formed per year, show an enormous range, from virtually zero in gas-poor elliptical, S0, and dwarf galaxies to $\sim 20 M_{\odot} yr^{-1}$ in gas-rich spirals. Much larger global SFRs, up to $\sim 100 M_{\odot} yr^{-1}$, can be found in optically selected starburst galaxies, and SFRs as high as $\sim 1000 M_{\odot} yr^{-1}$ may be reached in the most luminous IR starburst galaxies. The highest SFRs are associated almost uniquely with strong tidal interactions and mergers.

Figure 2.1 shows a range of more than two orders of magnitude in the SFR per unit luminosity

The strong trends in disk SFRs that characterize the Hubble sequence presumably arise from more fundamental relationships between the global SFR and other physical properties of galaxies, such as their gas contents or dynamical structure. Figure 2.2 shows the relationship between the disk-averaged

SFR surface density Σ_{SFR} and the average total (atomic plus molecular) gas density, for a sample of 61 normal spiral galaxies with H_α, HI, and CO observations (Kennicutt 1998). The figure shows that disks show large ranges in both the mean gas density (factor of 20-30) and mean SFR surface density (factor of 100). The data points are coded by galaxy type, and they show that both the gas and SFR densities are correlated with Hubble type on average, but with large variations among galaxies of a given type. In addition, there is an underlying correlation between SFR and gas density that is largely independent of galaxy type. This shows that much of the scatter in SFRs among galaxies of the same type can be attributed to an underlying dispersion in gas contents (Kennicutt 1989, 1998).
What other global properties of a galaxy influence its SFR? It is plausible to expect the mass, bar structure, spiral arm structure, or environment to be important.

2.2.1 Circumnuclear regions

The star formation that takes place in the circumnuclear regions of galaxies also follows quite different patterns along the Hubble sequence, relative to the more extended star formation in disks. These distinctions are especially important in early-type galaxies, where the nuclear regions often dominate the global star formation in their parent galaxies. It has been known from the early photographic work of Morgan (1958) and Sersic&Pastoriza (1967) that the circumnuclear regions of many spiral galaxies harbor luminous star-forming regions. The opening of the mid-IR and FIR regions fully revealed the distinctive nature of the nuclear star formation.The IRAS survey led to the discovery of large numbers of ultraluminous star-forming galaxies (Soifer et al 1987). The nuclear SFRs in most galaxies are quite modest, e.g on average $\sim 0.1 - 0.2 M_\odot yr^{-1}$. The IR observations also reveal a population of more luminous regions, with LFIR $\sim 10^{10} - 10^{13} L_\odot$, and corresponding SFRs on the order of $1 - 1000 M_\odot yr^{-1}$. Such high SFRs are not seen in optically selected samples, mainly because the luminous starbursts are uniquely associated with dense molecular gas disks.
The physical conditions in the circumnuclear star-forming disks are distinct in many respects from the more extended star-forming disks of spiral galaxies. The circumnuclear star formation is especially distinctive in terms of the absolute range in SFRs, the much higher spatial concentrations of gas and stars, its burst-like nature (in luminous systems), and its systematic variation with galaxy type.
The different range of physical conditions in the nuclear starbursts is clearly seen in Figure 2.3, which plots the average SFR surface densities and mean molecular surface densities for the circumnuclear disks of 36 IR-selected starbursts (Kennicutt 1998). The comparison is identical to the SFR-density plot for spiral disks in Figure 2.2. Figure 2.3 shows that the surface densities of

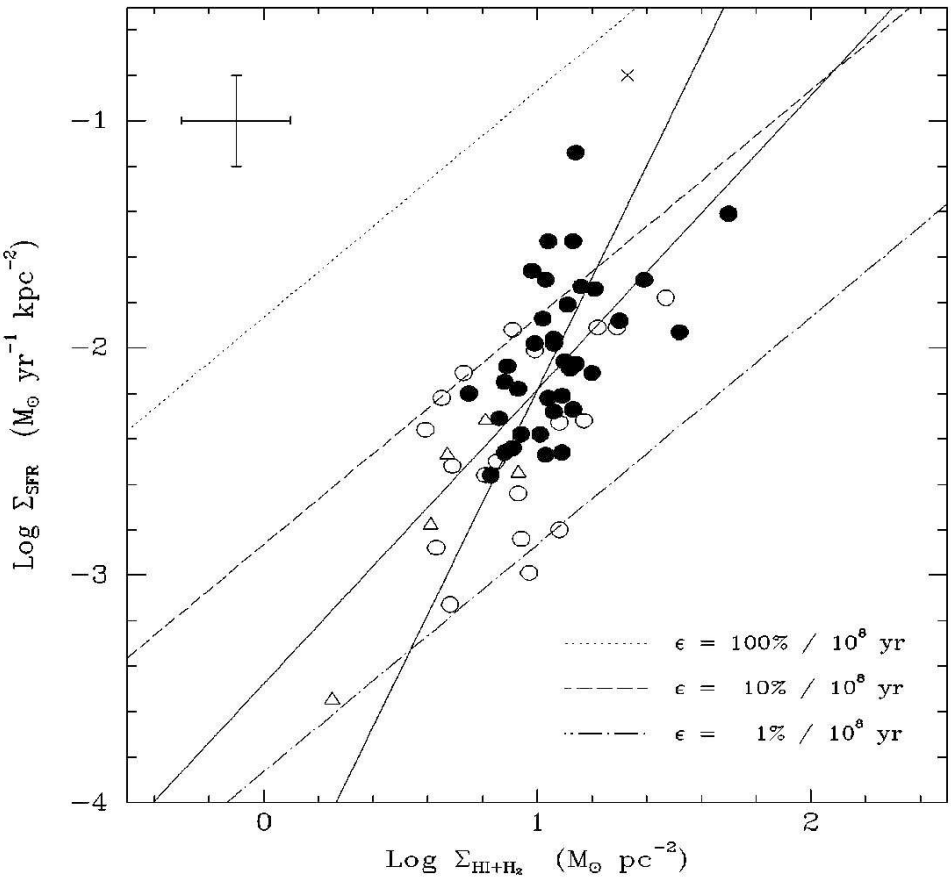

Figure 2.2: Correlation between disk-averaged SFR per unit area and average gas surface density, for 61 normal disk galaxies. Symbols are coded by Hubble type: Sa-Sab (open triangles); Sb-Sbc (open circles); Sc-Sd (solid points); Irr (cross). The dashed and dotted lines show lines of constant global star formation efficiency. The error bars indicate the typical uncertainties for a given galaxy, including systematic errors. (Kennicut et al.1998)

gas and star formation in the nuclear starbursts are 1-4 orders of magnitude higher than in spiral disks overall. Figure 2.3 also shows that the characteristic star formation efficiencies and time scales are quite different in the starbursts. The mean conversion efficiency is 30% per 10^8 years, six times larger than in the spiral disks. Likewise, the gas consumption time scale is six times shorter, about 0.3 Gyr on average. Finally, the IR starburst galaxies represent systems in which a mass of gas comparable to the entire ISM of a galaxy has been driven into a region on the order of 1 kpc in size, and this entire ISM is being formed into stars, with almost 100% efficiency, over a time scale on the order of 10^8 years. Such a catastrophic transfer of mass can only take place in a violent interaction or merger, or perhaps during the initial collapse phase of protogalaxies. The connection between starburst galaxies, star formation and far infrared emission will be analyzed later.

2.3 Cosmic Star Formation History

The increase by an order of magnitude in the global comoving space density of star formation rate (SFR) from $z = 0$ to $z \simeq 1$ has been well established by numerous measurements (e.g., Wilson et al. 2002; Haarsma et al. 2000; Flores et al. 1999; Cowie et al. 1999; Hogg et al. 1998; Hammer et al. 1997; Lilly et al. 1996; Madau et al. 1996). A large body of data has now been collected to measure this evolution and the shape of the star formation (SF) history redshifts. The recent results from the Sloan Digital Sky Survey (SDSS), the Galaxy Evolution Explorer (GALEX), the Classifying Objects byMedium-Band Observations in 17 Filters survey (COMBO17), and the Spitzer Space Telescope at far-infrared (FIR) wavelengths now allow this cosmic star formation history (SFH) to be quite tightly constrained (to within $\simeq 30\% - 50\%$) up to redshifts of $z \simeq 1$. Combined with measurements of the SFH at higher redshifts from the FIR, submillimeter, Balmer line, and UV emission, the SFH is reasonably well determined (within a factor of ~ 3 at $z \gtrsim 1$) up to $z \simeq 6$ (e.g., Hopkins 2004).
An exploration of quantities predicted from the SFH, namely the stellar and metal mass density evolution, and supernova (SN) rate evolution, provides further insight into the allowable normalization of the SFH (Strigari et al. 2005). This series of interconnected physical properties of galaxies and SNe provides an opportunity for determining the SFH normalization.. Constraining the normalization of the SFH will support a range of quantitative analyses of galaxy evolution, including the mass dependence of the SFH (e.g., Papovich et al. 2006; Juneau et al. 2005; Heavens et al. 2004) and the reasons underlying the decline in the SFH to low redshifts (e.g., Bell et al. 2005). Additional results from the Super-Kamiokande (SK) particle detector provide a strong limit on the electron antineutrino ($\overline{\nu}_e$) flux. originating from supernova Type II events associated with the SFH. This limit on the diffuse

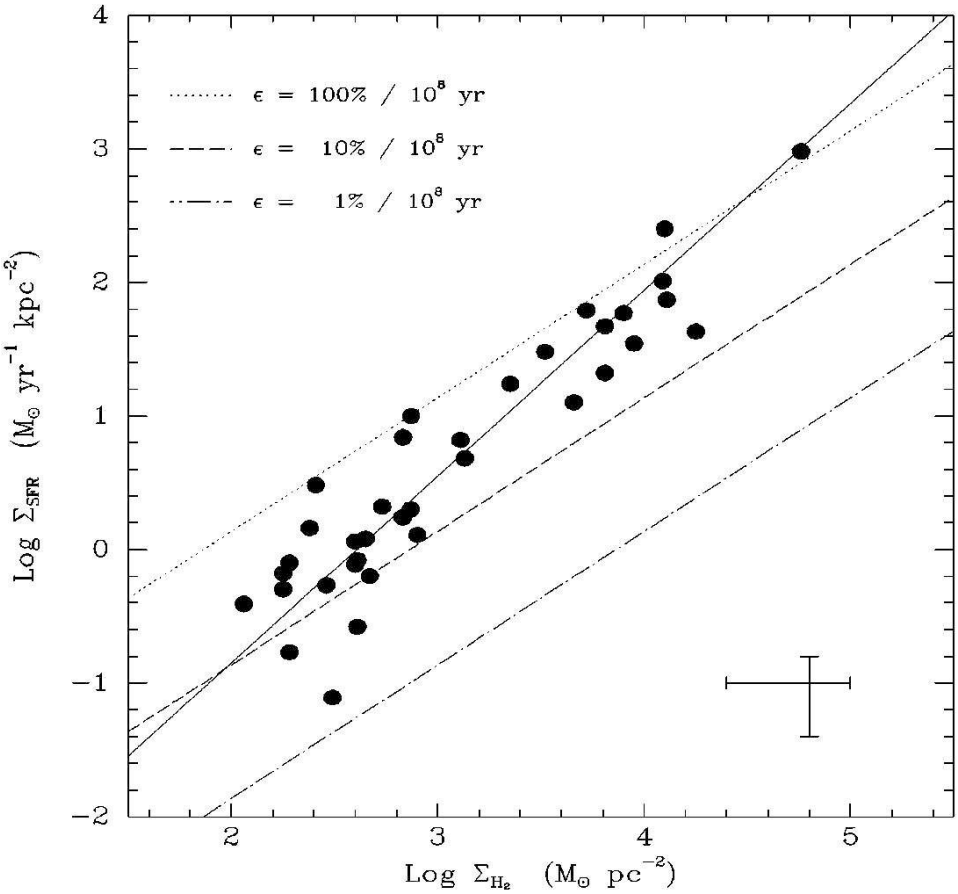

Figure 2.3: Correlation between disk-averaged SFR per unit area and average gas surface density, for 36 IR-selected circumnuclear starbursts. See Figure 2.2 for a similar comparison for normal spiral disks. The dashed and dotted lines show lines of constant star formation conversion efficiency, with the same notation as in Figure 5. The error bars indicate the typical uncertainties for a given galaxy, including systematic errors.(Kennicut et al.1998)

supernova neutrino background (DSNB) acts to constrain the normalization of the SFH and is consistent with the direct measurements of the SFR.

2.3.1 The *Madau Plot*

One of the first discussions of the issues described above has been provided by Madau et al. 1998 (e.g Madau et al. (1998)). In their paper they develop a method which focuses on the emission properties of the galaxy population as a whole. It traces the cosmic evolution with redshift of the galaxy luminosity density, as determined from several deep spectroscopic samples and the HDF imaging survey, and offers the prospect of an empirical determination of the global star formation history of the universe and initial mass function of stars. The technique relies on two basic properties of stellar populations: (1) the UV-continuum emission in all but the oldest galaxies is dominated by short lived massive stars and is therefore a direct measure, for a given IMF and dust content, of the instantaneous star formation rate (SFR); and (2) the rest-frame near-IR light is dominated by near-solar mass stars that make up the bulk of a galaxy's stellar mass and can then be used as a tracer of the total stellar mass density.
The main limitation of this approach is that they study the emission properties of "normal", optically selected field galaxies which are only moderately affected by dust. Moreover although in their calculations the IMF extends from 0.1 to 125 $M_{\odot}$ by modeling the rest-frame galaxy luminosity density from 0.15 to 2μm we will only be sensitive to stars within the mass range from $\sim$0.8 to about $20M_{\odot}$. This introduces non negligible uncertainties in their estimate of the total amount of stars and metals produced.
They trace the evolution with cosmic time of the luminosity density

$$\rho_{\nu}(z) = \int_{0}^{\infty} L_{\nu}\phi(L_{\nu}, z)dL_{\nu} \tag{2.1}$$

where $\phi(L_{\nu}, z)$ is the luminosity function in each redshift bin. The comoving luminosity density,$\rho_{\nu}(z)$, from the present epoch to z=4 is given in figure 2.4 in five broad passbands centered around 0.15, 0.28, 0.44, 1.0, and 2.2 μm (from UV to near IR) for a Salpeter IMF. For simplicity, the metallicity was fixed to solar values and the IMF truncated at 0.1 and 125 $M_{\odot}$. The model is able to account for the entire background light recorded in the galaxy counts down to the very faint magnitude levels probed by the HDF, and produces visible mass-to-light ratios at the present epoch which are consistent with the values observed in nearby galaxies of various morphological types. It result that the bulk ($\gtrsim$60 per cent by mass) of the stars present today formed relatively recently ($z \lesssim 1.5$).
One of the main uncertainties in our understanding of the evolution of luminous matter in the Universe is represented by the poorly constrained amount

of starlight that was absorbed by dust and reradiated in the far-IR at early epochs. Fig. 2.4 shows the model predictions for a monolithic collapse scenario, in which half of the present-day stars were formed at z $>$ 2.5 and were enshrouded by dust. Consistency with the HDF 'dropout' analysis has been obtained assuming a dust extinction which increases rapidly with redshift, $E(B-V) = 0.011(1+z)^{2.2}$. This results in a correction to the rate of star formation by a factor of $\simeq$2, 5, and 15 at z=2, 3 and 4, respectively. The model is still consistent with the global history of light, but overpredicts the metal mass density at high redshifts as sampled by QSO absorbers.

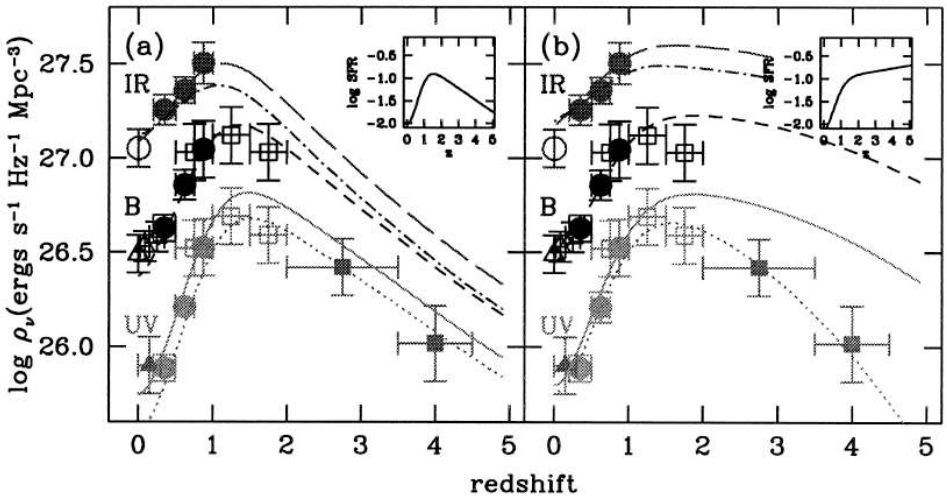

Figure 2.4: Evolution of the luminosity density at rest-frame wavelengths of 0.15 (dotted line), 0.28 (solid line), 0.44 (short-dashed line), 1.0 (long-dashed line), and 2.2 (dot-dashed line) μm. Data points with error bars are taken from Lilly et al. (1996) (filled dots at 0.28, 0.44, and 1.0 μm), Connolly et al. (1997) (empty squares at 0.28 and 0.44 μm),Madau et al. (1996) and Madau (1997a) (filled squares at 0.15 μm), Ellis et al. (1996) (empty triangles at 0.44 km), andGardner et al. (1997) (empty dot at 2.2 μm). Inset in the upper right-hand corner of the plot shows the SFR density ($M_\odot yr^{-1}Mpc^{-3}$) vs. redshift which was used as input to the population synthesis code. 8a) The model assumes a Salpeter IMF, SMC-type dust in a foreground screen, and a universal $E(B-V) = 0.1$.. (b) Test case with a much larger star formation density at high redshift than indicated by the HDF dropout analisys. The model, assigned to mimick a 'monolithic collapse scenario', assumes a Salpeter IMF and a dust opacity which increases rapidly with redshift, $E(B-V) = 0.011(1+z)^{2.2}$.

2.3.2 The *Madau plot* from recent observations

A large body of data has now been collected to measure this evolution and the shape of the star formation (SF) history at higher redshifts (now approaching $z \simeq 6$).
Hopkins et al. (2006), in their fundamental work analyze this large, heterogeneous data set, which appear to be highly consistent over the entire redshift range $0 < z \lesssim 6$ and constrains the SFR density to within a factor of about 3 at most redshifts.
They start their analysis focusing on the observed luminosity density measurements, with three different crucial assumptions:

- Dust corrections (where necessary), SFR calibrations, and standard IMF assumptions are SFH measurements;
- From the SFH, assumptions about the high-mass IMF fraction that produces SNe II lead to predictions for the SN II rate density;
- Assumptions about the neutrino emission of SNe II then give a prediction of the DSNB for comparison with the SK limit.

While uncertainties in SFR calibration act to increase the scatter in the SFH, and uncertainties in dust obscuration can raise it to greater or lesser degrees, Hopkins et al. 2006 argued that the choice of IMF is the only assumption that can systematically decrease the SFH normalization. While most authors over the past decade have assumed the traditional Salpeter (1955) IMF, observations within recent years have strongly ruled it out as a model for a universal IMF (e.g Baldri 2003). In their work, Hopkins et al. 2006 compare the fit of the SFH obtained with the use of a traditional Salpeter IMF (SalA IMF with a slope of -1.35) and with the IMF of Baldry and Glazebrook (SalB IMF, with a slope of -1.15).
The evolution of the SFR density with redshift is shown in figure 2.5. For the fitting of the SFH the authors choose to use the parametric form of Cole et al. 2001:

$$\rho_* = (a + bz)h/[1 + (z/c)^d] \tag{2.2}$$

where $h = 0.7$. For $z < 1$, the SFH now appears to be very tightly constrained by the combination of UV data from SDSS (Baldry et al. 2005), COMBO17 (Wolf et al. 2003), and GALEX (Arnouts et al. 2005), corrected for obscuration using the Spitzer FIR measurements of Le Floc'h et al. (2005). For $z > 1$, use all the data available in the compilation. Figure 2.6 shows the evolution of the stellar mass density, $\rho(z)$, along with the predictions from the best-fitting SFH for the two IMF assumptions. Both plots show the measurements lying systematically below the predictions from the SFH, although the difference becomes more significant at higher redshift ($z \gtrsim 1.5$). Causes for the apparent inconsistency at high redshift have been discussed by other

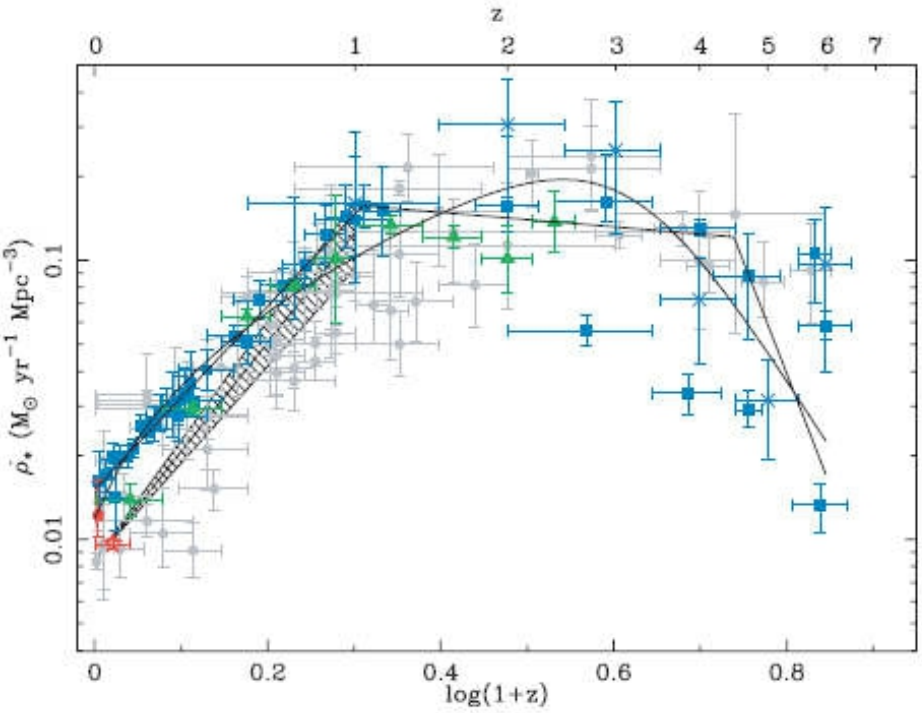

Figure 2.5: Evolution of SFR density with redshift. Data shown here have been scaled, assuming the SalA IMF. The gray points are from the compilation of Hopkins (2004). The hatched region is the FIR (24 1mum) SFH from Le Floc'h et al. (2005). The green triangles are FIR (24μ m) data from Perez-Gonzalez et al. (2005). The open red star at z =0.05 is based on radio (1.4 GHz) data from Mauch (2005). The filled red circle at z =0.01 is the H estimate from Hanish et al. (2006). The blue squares are UV data from Baldry et al. (2005),Wolf et al. (2003), Arnouts et al. (2005), Bouwens et al. (2003a, 2003b, 2005a), Bunker et al. (2004), and Ouchi et al. (2004). The blue crosses are the UDF estimates from Thompson et al. (2006). Note that these have been scaled to the SalA IMF, assuming they were originally estimated using a uniform Salpeter (1955) IMF. The solid lines are the best-fitting parametric forms (see text for details of which data are used in the fitting). Although the FIR SFH of Le Floc'h et al. (2005) is not used directly in the fitting, it has been used to effectively obscuration-correct the UV data to the values shown, which are used in the fitting. Note that the top logarithmic scale is labeled with redshift values, not $(1 + z)$.

authors (e.g., Nagamine et al. 2004; Hopkins et al. 2005), who suggest that, in this regime, the observations might be missing up to half the stellar mass density. At low redshift, the discrepancy between the measurements of $\rho_*(z)$ and the SFH prediction is more of a concern. A first attempt at resolving this might be to suggest that the measured SFH is too high at z=0, and the technique used (combining ρ_* from FIR and UV estimates) is not accurate. This cannot be the whole solution, as it does not address the problem at $z \simeq 1$, where the SFH is dominated by the FIR contribution, and the $\rho_*(z)$ values inferred fromthe SFH are similarly higher than the measurements. A partial solution might be found through the underlying measurement techniques used for the different quantities. It is possible that the discrepancy seen in Figure 2.6 may be reflecting limitations in our understanding of the relative shapes of the low- and highmass ends of our assumed IMFs.

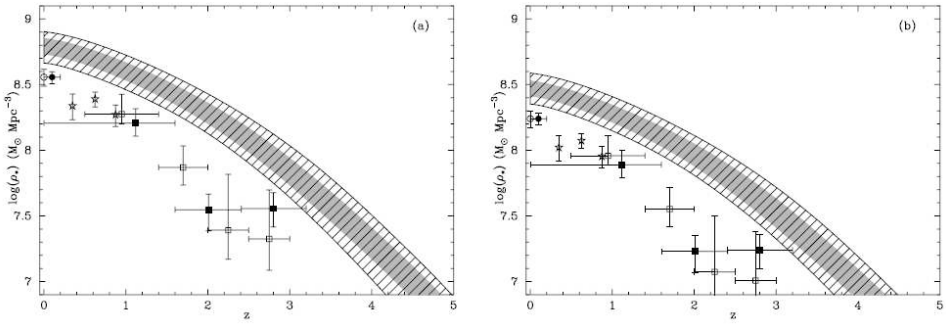

Figure 2.6: Evolution of stellar mass density buildup inferred from the SFH, assuming (a) SalA IMF and (b) BG IMF. The gray shaded and hatched regions come from, respectively, the 1 and 3 σ confidence regions. The open circle is the local stellar density from Cole et al. (2001); the filled circle and filled squares represent the SDSS and FIRES data, respectively, from Rudnick et al. (2003), scaled such that the SDSS measurement is consistent with that from Cole et al. (2001); the open stars are from Brinchmann and Ellis (2000), and the open squares are from Dickinson et al. (2003).

2.3.3 Evolution of the SN rate with redshift: the SN rate problem

The evolution of the SN rate with redshift contains unique information in particular on the star formation history of the universe and of the IMF of stars.

Because of their short-lived progenitors, core-collapse supernovae (CC SNe) trace directly the current star formation rate (SFR). On the other hand, type Ia SNe trace the whole history of star formation, due to wide range of delay times of their progenitors.

Early attempts to compare the evolution and normalization of the cosmic SFR and cosmic SNR were inconclusive due to their large uncertainties. In recent years, measurements of the cosmic SFR and cosmic SNR have rapidly improved.Based on the latest data, it has become clear that the measured cosmic SFR and the measured cosmic SNR both increase by approximately an order of magnitude between redshift 0 and 1, confirming our expectation that the progenitors of CC SNe are short-lived massive stars.
As Horiuchi et al. (2011) illustrate in Figure 2.7, the SNR predicted from the cosmic SFR is a factor of ∼2 larger than the cosmic SNR measured by SN surveys. The comparison of the predicted and measured cosmic SNR, and the relative sizes of the uncertainties, demonstrate two key points: they evolve similarly in redshift, and there is a systematic normalization mismatch. The lines are fits to the SFR and SNR data, respectively. The discrepancy persists over all redshiftswhere SNR measurements are available. So, becomes crucial to understand whether the cosmic SNR predicted from the cosmic SFR is too large, or whether the measurements underestimate the true cosmic SNR, or a combination of both.

The cosmic SNR is calculated from the cosmic SFR using knowledge of the efficiency of forming CC SNe. The most recent SFR is traced by the most massive stars that have the shortest lifetimes. However, since the total SFR is dominated by stars with smaller masses, the SFR derived from massive stars must be scaled upward according to the initial mass function (IMF).
The comoving volumetric SNR is determined by multiplying ρ_* by the efficiency of forming CC SNe. This is the number of stars that eventually explode as CC SNe per unit stellar mass formed in a burst of star formation. It is governed by the mass range for CC SNe, from M_{min} to M_{max}, resulting in an SNR of

$$R_{SN} = \rho_*(z)\frac{\int_{M_{min}}^{M_{max}} \psi(M)dM}{\int_{0.1}^{100} M\psi(M)dM} \tag{2.3}$$

where $\psi(M)$ is the IMF defined over the mass range 0.1-100$M_\odot$. Due to the steeply falling nature of the IMF, the lower mass limit M_{min} is the most important parameter. They assumed canonical parameters for optically luminous CC SNe, $M_{min} = 8M_\odot$ and $M_{max} = 40M_\odot$.

Possible explanations

Is the cosmic SFR too high? The uncertainties associated with SFR measurements are generally at the tens of percent level and does not allow the cosmic SFR to be decreased enough to explain the supernova rate problem.
Does the local SFR differ from the cosmic SFR? The local ($\sim$ 100 Mpc) SFR sets the birth rate of stars nearby and has important implications for our study of the local SNR. In Figure 2.8, is shown SFR measurements in

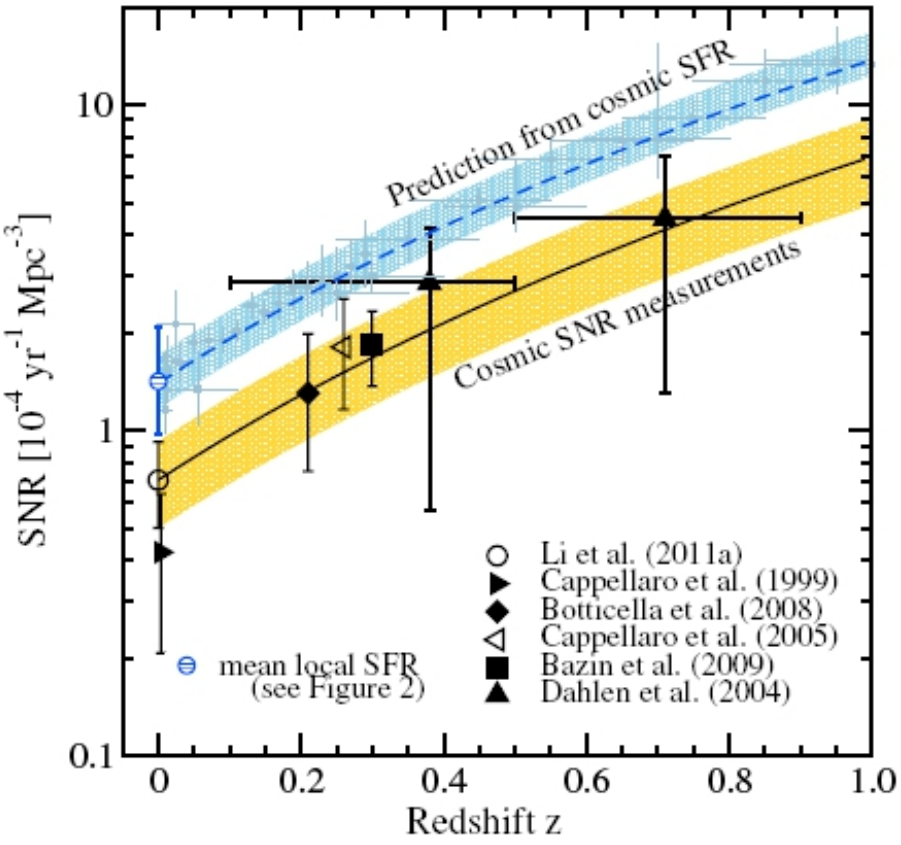

Figure 2.7: Comoving SNR (all types of luminous core collapses including Type II and Type Ibc) as a function of redshift. The SNR predicted from the cosmic SFR fit and its supporting data (Hopkins and Beacom 2006), as well as that predicted from the mean of the local SFR measurements, are plotted and labeled. The fit to the measured cosmic SNR, with a fixed slope of $(1+z)^{3.4}$ taken from the cosmic SFR, is shown with the uncertainty band from the LOSS measurement. The predicted and measured cosmic SNRs are consistently discrepant by a factor of ~ 2: the supernova rate problem.

the local volume. SFR measurements in the local volume are in agreement within uncertainties with the better-measured cosmic SFR, except for the volume within $\lesssim$ 10Mpc which has a factor of 2 enhancement.

Is the Fraction of Stars Resulting in CC SNe Too High? The pre-

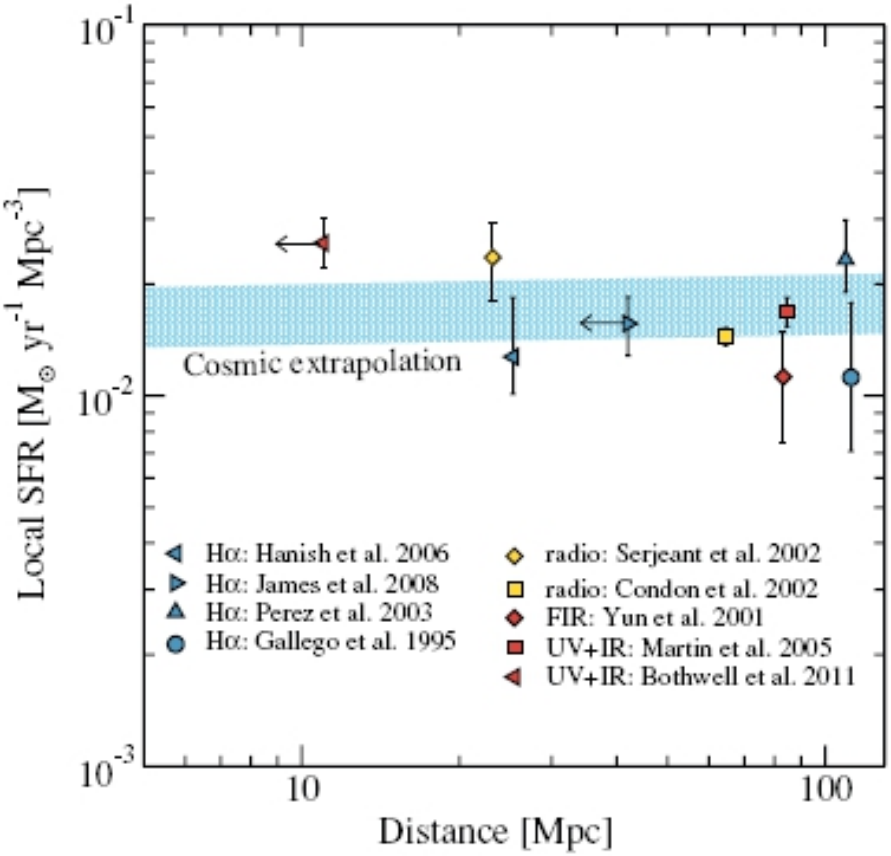

Figure 2.8: Local SFR density as a function of distance. Measurements are shown at the mean distances of their respective galaxy samples, except for 11HUGS (Bothwell et al. 2011) and HαGS (James et al. 2008) which are measurements within fixed distances and are shown at their distance limits (horizontal arrows). The SFR within 11 Mpc is enhanced with respect to the cosmic SFR (shaded band) due to cosmic variance. Beyond 20 Mpc, the measurements and their mean are compatible with the cosmic SFR, and show no significant cosmic variance in this distance range. Shown for a Salpeter A IMF.

dicted SNR depends on the number of stars that become CC SNe per unit stellar mass formed. There is observational evidence that a wide range of massive stars yield optically luminous CC SNe. Conceptually, the mass range

is controlled by two parameters, the lower mass limit that is the boundary between the formation of a white dwarf and a neutron star, and the upper mass limit that is less well defined but could be the boundary between forming a neutron star and a stellar mass black hole.
The lower mass limit is newly supported by direct observations of CC SNe progenitors. Different approaches seem to be converging to $M_{min} \simeq 8 \pm 1 M_{\odot}$ (e.g. Smartt et al. 2009). On the other hand, the upper mass limit is less certain. Fortunately, as long as the upper limit is large, it does not strongly affect the predicted SNR. The upper mass limit is $M_{max} \simeq 40 M\odot$.
adopt the nominal mass range for optically luminous CC SNe of 8-40$M_{\odot}$, based on stellar and supernova simulations; the maximum mass range 8-100$M_{\odot}$, and the conservative minimum mass range the combination of 8.5-16.5$M_{\odot}$ and 25-40$M_{\odot}$. Compared to the nominal 8-40$M_{\odot}$, the max- imum and minimum mass ranges affect the predicted cosmic SNR by +10% and -30%, which are insufficient to explain the supernova rate problem.
Are Measurements Missing Luminous CC SNe? Luminous CC SNe that fall within the sensitivity of SN surveys can still be missed. Based on current data on dwarf galaxies, the effect may be a $20\% - 50\%$ increase in the SNR measurements. The importance of small galaxies remains to be investigated further with more data.
Are CC SNe Dust Corrections Insufficient? Host dust extinction makes CC SNe appear dimmer and correcting for missing obscured CC SNe is often the most uncertain ingredient in SNR measurements. The dust correction applied to SNR measurements ranges from a few tens of percent at low redshifts to a factor of ∼2 at high redshifts. As pointed out in Mannucci et al. (2007), at high redshift there is additional extinction due to starburst galaxies and highly star-forming galaxies (luminous and Ultraluminous IR Galaxies). Identified by their strong FIR emission and high SFR, ULIRG should house many more CC SNe per galaxy, but we only detect a small fraction of CC SNe because of the higher dust obscuration.
Because the importance of ULIRG increases with redshift, the fraction of CC SNe that are expected to be missing increases from $\sim 5\%$ at $z \simeq 0$ to $20\% - 40\%$ at $z \simeq 1$ (Mannucci et al. 2007). Correction for host galaxy obscuration remains uncertain. Extreme corrections that would explain the supernova rate problem are not prohibited, in particular at high redshifts where the excess extinction due to starburst galaxies is considered.
Is the Contribution from Dim CC SNe Significant?Type IIP SNe are the most common type of CC SNe and also the most varied in terms of luminosity. The luminosity of a typical Type IIP SN remains nearly constant for a relatively long duration of ∼100 days (the plateau phase), after which it drops sharply.
The faintest confirmed type II SN is SN1999br ($M_R \simeq 13.5$, Pastorello et al. 2004).
The limiting absolute magnitudes of SN surveys are typically M≃-15 to -16.

Although SN surveys can discover dimmer CC SNe, the rapidly falling detection efficiency and the smaller volume from which dim CC SNe (they define CC SNe that are dimmer than M = -15 mag as "dim" CC SNe) may be confidently discovered makes collecting dim CC SNe challenging. To correct for missing dim CC SNe, a SN luminosity function that is complete to dimmer CC SNe must be adopted. To study dim (or faint) CC SNe Horiuchi et al. (2011) make use of SN discoveries recorded in SN catalogs and discuss the local (within $\sim 100Mpc$) volume for a qualitative analisys and then focus on the very local volume (within $\sim 10Mpc$).
In Figure 2.9, a catalog of SNR (binned in distance) is compared to the cosmic SNR predicted from the SFR and directly measured. The luminous catalog SNR is generally decreasing with distance but it is flat out to ∼25Mpc, suggesting reasonable completeness to that distance[1]. The total catalog SNR should be compared to the predicted cosmic SNR. The total catalog SNR is flat out to ∼25 Mpc and shows a normalization that is only slightly lower than expectations from the cosmic SFR. This supports their earlier claims that the true cosmic SNR is as large as expected. Finally, the dim catalog SNR falls with distance at all distances, a sign of incompleteness. At the smallest-distance bin, where dim CC SNe are least likely to be missed, the dim catalog SNR is, surprisingly, just as large as the luminous SNR measured by LOSS. This normalization is large enough to help solve the supernova rate problem, at least at $z \simeq 0$.

Due to incompletness of the faint CC SNe, Horiuchi et al. (2011) choose to quantify the importance of these type of CC SNe in the very local (within $\sim 10Mpc$) volume, which yields sufficient statistics. The very local volume has an enhanced absolute SFR. Therefore, we conservatively use the fraction of dim CC SNe, $f_{dim} = N_{dim}/(N_{dim} + N_{luminous})$, the ratio of definitely dim CC SNe over the sum of definitely dim and definitely luminous CC SNe.
Figure 2.10 show the plot of the probability density function of the dim CC SNe (f_{dim}) given the observed number of total and dim CC SNe, for different distance cuts. On the top panel is plotted a magnitude cut of -16 mag for illustration. Due to the broad distribution of f_{dim}, is not possible to derive a precise value for f_{dim} with the present data: the fractions are $f_{>-15} \sim 30\% - 50\%(f_{>-16} \sim 60\% - 80\%)$, but lower and higher values are not improbable. However, the estimates of Horiuchi et al.(2011) are clearly larger than previous studies based on more systematic samples at higher distances which were not as sensitive to the dim end of the CC SNe luminosity function ($f_{>-15} \sim 3\% - 20\%$). Their estimates decrease to $f_{>-15} \sim 20\% - 40\%(f_{>-16} \sim 50\% - 70\%)$ if possible SN impostors are ex-

[1] If the SN discoveries are sufficiently complete, the catalog SNR should be flat with distance. This is because they are number densities, and because the local SFR did not reveal significant cosmic variance. So, any significant decrease of the catalog SNR at any distance signifies an incompleteness of the SN discoveries at that distance.

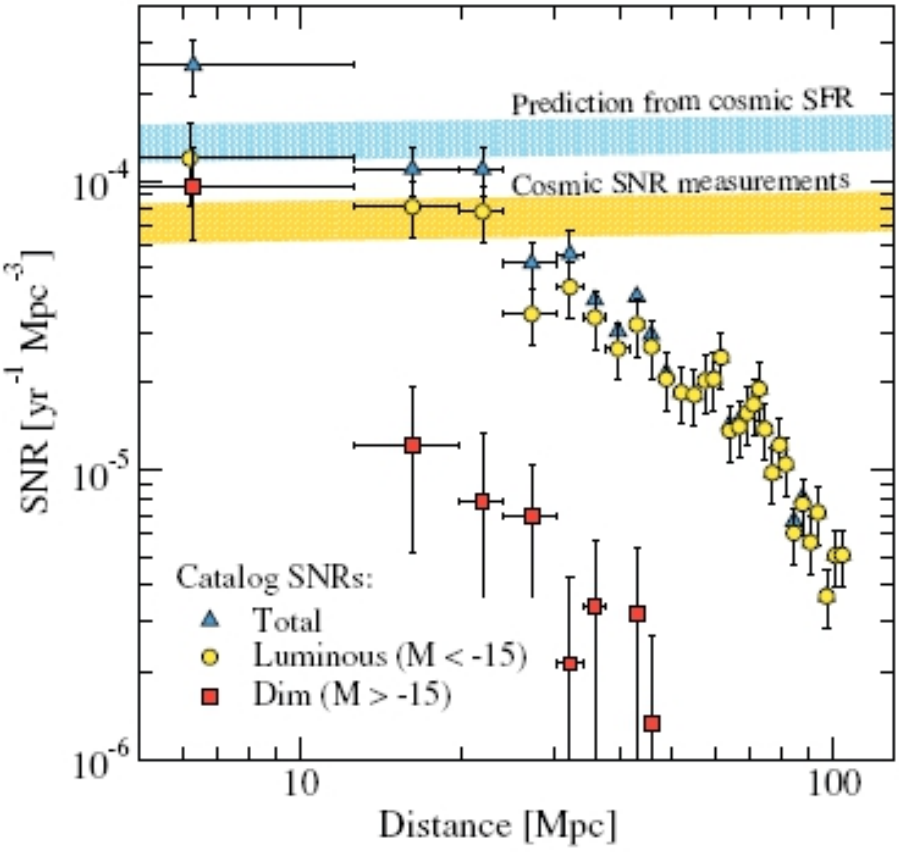

Figure 2.9: Differential catalog SNR density as a function of distance. The total, luminous, and dim catalog SNR are shown by points (lowest distance bin has been shifted slightly in distance for clarity). The total catalog SNR is larger than the sum of the luminous and dim catalog SNR. Vertical error bars are statistical only. The SNR predicted from the cosmic SFR and directly measured are shown and labeled. The total catalog SNR is comparable to the upper band out to ∼25 Mpc. The luminous catalog SNR is comparable to the lower band out to ∼25 Mpc. The dim catalog SNR is large out to ∼10 Mpc, indicating a significant fraction of dim CC SNe, independent of the absolute SFR enhancement within ∼10 Mpc.

cluded from their list of CC SN. This is still larger than previous studies.
Summarizing the analisys of Horiuchi et al. (2011), they find that the list

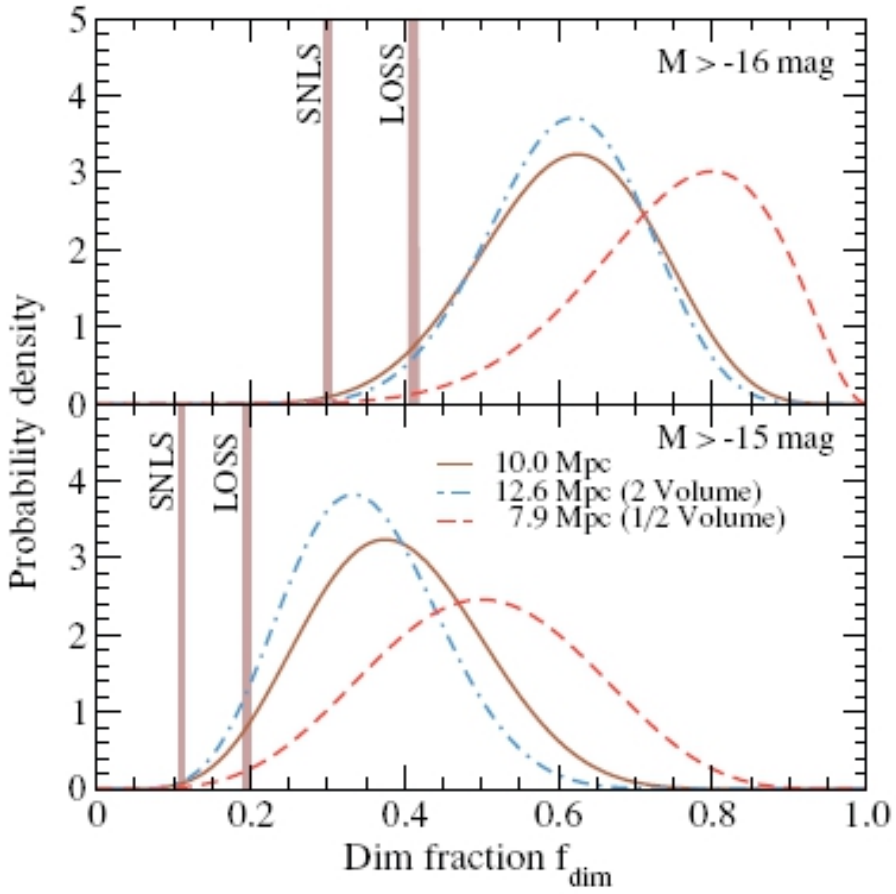

Figure 2.10: Probability density distribution for the dim fraction (f_{dim}), given the observed number of total and dim CC SNe, for three volume cuts. The dim fraction is significantly higher than previous estimates from larger distances (vertical bands). Top: for CC SNe dimmer than -16 mag. Bottom: for those dimmer than -15 mag (horiuchi et al. 2011)

of dim CC SNe in the local (within $\sim 100Mpc$) volume are very incomplete, while they are very numerous in the very local (within $\sim 10Mpc$) volume. The dim fraction could be as high as $f_{>-15} \sim 50\%$. This is significantly higher than previous estimates, which range between $f_{>-15} \sim 3\% - 20\%$. Thus the SNR measurements are scaled up by (1 - 0.2)/(1 - 0.5) = 1.6 (a factor of 1.9 if the original dim fraction is 5%), largely solving the supernova rate problem.

In Figure 2.11 is shown the supernova rate problem at $z \simeq 0$. The bands reflect the nominal uncertainties on each quantity: for the predicted SNR it is the 1σ uncertainty in the cosmic SFR fit by Hopkins & Beacom (2006), while for the measured SNR it is the combined statistical and systematic uncertainties of the fit to SNR measurements. Although the supernova rate problem remains over the entire redshift range where SNR measurements are available, the plot focus on the $z \simeq 0$ range where there is most data. Horiuchi et al. (2011) explore, first, whether the predicted SNR is too large. they investigate the intrinsic uncertainties in the SFR measurements (IMF, obscuration, and conversion factor) and the additional factors when the SFR is converted to a SNR (IMF and CC SN mass range). The results are shown in Figure 2.11 by dashed arrows.

- *IMF*:small effect on the predicted SNR;
- *Obscuration*: Extinction uncertainties are unlikely to reduce the SNR prediction normalization by a full factor of two;
- *CC SNe mass range*: The nominal mass range is 8-40$M_{\odot}$. they adopt the maximum mass range of 8-100$M_{\odot}$.

Therefore, the uncertainties affecting the predicted SNR are generally smaller than the normalization discrepancy.
Second, to investigate whether the measured SNR is too small, Horiuchi et al. (2011) explore the contribution from missing CC SNe (incomplete galaxy sample and dim CC SNe). This is shown by solid arrows in Figure 2.11.

- *Incomplete galaxy sample*: This aspect is no able to explain the SN rate problem;
- *Dim CC SNe*: There is an observational bias against the discovery and correction of dim CC SNe. In the very local ($\sim$10 Mpc) volume, where dim CC SNe are least likely to be missed, the fraction of dim CC SNe is higher than in SN surveys targeting larger distances.

Therefore, if possible SN impostors are true CC SNe, the fraction of dim CC SNe can be sufficiently high that dim CC SNe largely explain the supernova rate problem. If possible SN impostors are not true CC SNe, f_{dim} is smaller, and dim CC SNe do not fully bridge the normalization discrepancy. The nature of possible SN impostors remains, however, debated. In Figure 2.11 is shown how the different effects compare. The supernova rate problem is likely explained by a combination of the effects shown.

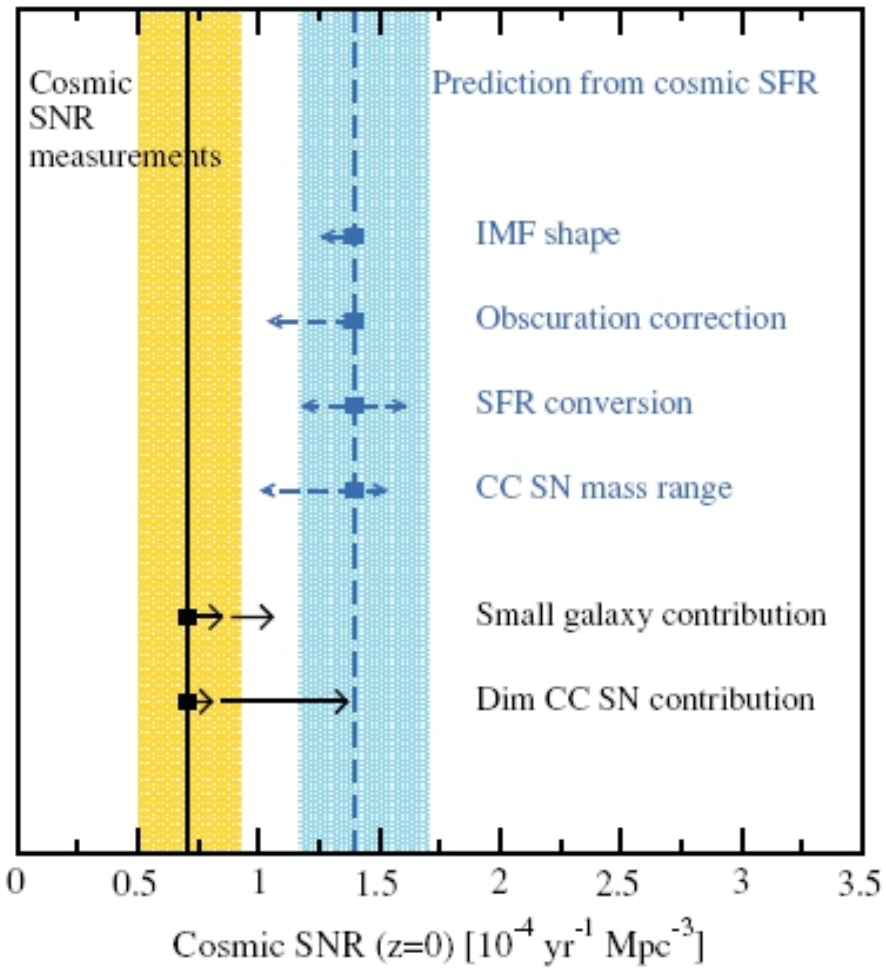

Figure 2.11: Measured and predicted SNR at $z \simeq 0$. Shaded bands reflect uncertainties: statistical and systematic combined for the measured SNR, and the 1σ uncertainty in the SFR for the predicted SNR. The results of varying the inputs for the predicted SNR are shown by dashed arrows, while the possible effects of missing CC SNe are shown for the measured SNR by solid arrows. Stacked arrows reflect different assumptions (see the text). The contribution from dim CC SNe can potentially increase the measured SNR to bridge the normalization discrepancy, although other effects can also be important

Chapter 3

SFR-SNR relation and SN searches in StarBurst Galaxies

3.1 The FIR-SFR relation

The relation between star formation, gas and dust is of indispensable importance in any attempt to understand the evolution of galaxies. Thus, a reliable method to determine the SFR has been among the main goals of research the last years.
As seen in the previous chapter, Kennicutt et al. (1998) introduce a plethora of diagnostics to address the problem of deriving an estimate for the SFR of a given galaxy.
One of the main problems of most methods is the attenuation from dust that obscures the measured quantities in the UV and optical bands. The best estimator for SFR will be based on a combination of tracers which together capture the full energetics of the system. Recent work by Calzetti et al. (2007) and Kennicutt et al. (2009) shows that a good estimator for the SFR emerges from the linear combination of a galaxy's near-UV or visible-wavelength emission (either UV continuum or line fluxes, attenuated by dust) and its emission in the infrared (e.g., 8, 24, or total IR λ 8-1000 and also radio).
In particular, a promising way to overcome the problem of attenuation of traditional SFR diagnostics is the use of dust emission itself as a SFR diagnostic. This is straightforward in starburst galaxies where dust opacity is high and most of the dust heating originates from the young stellar population. In this case, the FIR luminosity can be used as a direct measure of the SFR.
The SFR vs L_{FIR} conversion is derived using several synthesis models.
In this thesis is used the same relation between SFR and FIR of the work of Mannucci et al. (2003), derived form the paper of Dale et al. (2001). The far-infrared flux, defined as the flux between 42 and 122 μm, is considered

the favorite infrared diagnostic. Helou et al. (1988) provide a useful way of deriving the far-infrared flux from IRAS measurements:

$$FIR = 1.26 \times 10^{-14} \left[2.58\, f_\nu(60\mu m) + f_\nu(100\mu m)\right] \tag{3.1}$$

where FIR is in W m^{-2} ($= 10^3\ erg\, cm^{-2}\, s^{-1}$) and $f\nu$ are in Jansky. The total far infrared flux, TIR, results from:

$$\log \frac{TIR}{FIR} = a_0 + a_1 x + a_2 x^2 + a_3 x^3 + a_4 x^4$$

where $x = \log \frac{f_\nu(60\mu m)}{f_\nu(100\mu m)}$ and $[a(z=0)] \simeq [0.2378, -0.0282, 0.7281, 0.6208, 0.9118]$. Applying the models of Leitherer & Heckman (1995) for continuous bursts of age 10-100 Myr Kennicutt et al. (1998) yields the following relation between SFR and the total L_{TIR}:

$$SFR(M_\odot y^{-1}) = 2.2x10^{-43} L_{TIR}(ergs \quad s^{-1}) = 5.8x10^{-9} L_\odot^{-1} \tag{3.2}$$

where L_{TIR} refers to the IR luminosity integrated over the full-, mid-, and far- IR spectrum (8-1000μm).

3.2 SNR-SFR relation

The instantaneous SFR in a galaxy is directly traced by the number of currently existing massive stars since these stars have short life times. Usually the total SFR in a galaxy is obtained by extrapolating the massive star SFR to lower stellar masses given an initial mass function (IMF) describing the relative probability of stars of different masses forming. The luminosity of a galaxy is a direct and sensitive tracer of its stellar population so it is possible to directly connect a luminosity to the instantaneous SFR when the observed emission comes from stars which are short lived or from short lived phases of stellar evolution. The instantaneous SFR can be calculated from the observed luminosity in a wavelength band F which satisfies the above requirement from the relation:

$$L_F = \frac{\int_{m_l}^{m_u} t_F(m) l_F(m) \phi(m) \mathrm{d}m}{\int_{m_l}^{m_u} m \phi(m) \mathrm{d}m} \Psi \tag{3.3}$$

where L_F is the total galaxy luminosity, Ψ is the SFR, $l_F(m)$ is the luminosity of a single star of mass m, t_F is the characteristic timescale over which a star of mass m emits radiation in the wavelength band F and ϕ(m) the IMF. The limits of integration extend over the range of masses of the stars which are expected to emit radiation in the band F. The IMF generally is parametrized as a power law:

$$\mathrm{d}N = \phi(m)\mathrm{d}m \propto m^\gamma \mathrm{d}m \tag{3.4}$$

where dN is the number of single stars in the mass range m, $m + \mathrm{d}m$. We adopted a Salpeter IMF defined in the mass range 0.1-100$M_{\odot}$ with γ =-2.35 (Salpeter, 1955).
The constant of proportionality between SFR and luminosity can be derived by assuming an IMF and a stellar evolution model which provides lifetimes of stars as a function of their masses (see previous chapter, and Kennicutt (1998)).The emission from longer lived stars that encodes part or all of the past galaxy SFH dominates in many wavelength bands and only the UV stellar continuum, the emission of optical nebular recombination and forbidden lines and far infrared (FIR) emission can be used as probes of the young massive star population. Observations made at these wavelengths sample different aspects of the SF activity and are sensitive to different times scales over which SFR is averaged, i. e. the time interval over which radiation is emitted by a massive star in the wavelength band of interest (Botticella et al., 2012; Kennicutt, 1998). Most of the optical-UV energy emitted by the massive stars in the nuclear starburst regions is absorbed and reradiated by dust in the FIR. Therefore one can expect that the nuclear SN rate will correlate with the FIR luminosity.
Rates are generally normalized to the luminosity of the parent galaxy, either the B luminosity or L_{FIR} . The former normalization is applied when using the SN unit (SNu), i.e., the number of SNe per century per $10^{10}L$ of B luminosity. This luminosity has an ambiguous physical meaning: in starburst galaxies it is roughly proportional to the SFR, in quiescent galaxies it is related to the total mass in stars, and in dusty starbursts it is very sensitive to the dust content and distribution.
For galaxies with a significant SFR it is more useful, for many applications and especially when the core-collapse SNe are considered, to normalize the observed number of SNe to the FIR luminosity, known to be proportional to the SFR (Kennicutt, 1998). This is the reason for which the SN rates are express in terms of the galaxy FIR luminosity. Blanc & Greggio (2008) show an alternative and complementary approach to trace the SFR, based on the direct observation of the numbers of CC SNe occurring in a sample of galaxies or in a given volume. The general SN rate ($\mathcal{R}_{SN}$) as a function of time can be modeled as the convolution of the SFH (Ψ) with the distribution function (f_{SN}) of the delay times (τ):

$$\mathcal{R}_{SN}(t) = \int_{\tau_{min}}^{min(t,\tau_{max})} k_T(t-\tau) \cdot \Psi(t-\tau) f_{SN}(\tau) A_{SN}(t-\tau) \mathrm{d}\tau \qquad (3.5)$$

where t is the time elapsed since the beginning of star formation in the system under analysis; k is the number of stars per unit mass of the stellar generation with age τ; τ_{min} and τ_{max} bracket the range of possible delay times; A_{SN} is the number fraction of stars from the stellar generation born

at epoch $(t-\tau)$ that end up as SN. The factor k is given by:

$$k(\tau) = \frac{\int_{m_l}^{m_u} \phi(m,\tau)\mathrm{d}m}{\int_{m_l}^{m_u} m\phi(m,\tau)\mathrm{d}m} \tag{3.6}$$

where $\phi(m,\tau)$ is the IMF and $m_l - m_u$ is the mass range of the IMF. This factor can change if the IMF evolves with time.
The factor A_{SN} can be expressed by:

$$A_{SN}(\tau) = P_{SN}(\tau)\frac{\int_{m_l^{SN}}^{m_u^{SN}} \phi(m,\tau)\mathrm{d}m}{\int_{m_l}^{m_u} \phi(m,\tau)\mathrm{d}m} \tag{3.7}$$

where P_{SN} is the probability that a star with suitable mass (i.e., in the range $m_u^{SN} - m_l^{SN}$) to become a SN actually does it. This probability depends on SN progenitor models and on stellar evolution assumptions. The factor A_{SN} can vary with galaxy evolution, for example due to the effects of higher metallicities and/or the possible evolution of IMF. For core-collapse events, the progenitor life-time is very short, ($\tau < 0.05$ Gyr), then k and A_{CC} do not vary with time and the SFR has remained constant over this timescale obtaining a direct relation between CC SN rate and SFR, so that Eq. 3.5 can be approximated as:

$$\mathcal{R}_{CC}(t) = K_{CC} \cdot \Psi(t) \tag{3.8}$$

where the scaling factor between CC SN rate and SFR is given by the number fraction of stars per unit mass that produce CC SNe (Botticella et al., 2012):

$$K_{CC}(\tau) = \frac{\int_{m_l^{CC}}^{m_u^{CC}} \phi(m)\mathrm{d}m}{\int_{m_l^{CC}}^{m_u^{CC}} m\phi(m)\mathrm{d}m}. \tag{3.9}$$

This implies that the productivity of CC SNe, depends not only on the IMF slope, but also on the mass range of progenitors. More important is the dependence on the lower cut off mass, the productivity decreasing by a facor of $\simeq 0.7$ (Greggio & Renzini, 2011) if m_l^{CC} goes from 8 to 10 $M_\odot$ for a salpeter diet IMF.

3.2.1 The role of type Ia SN

Because o the long delay time, with τ_{min} of a few tens of Myr, and τ_{max} of the order or one Hubble time, or more, the expected number of SN Ia strongly depends on the SFR history of the stellar population (and on the adopted SN progenitor scenarios). (Blanc & Greggio, 2008) introduce a little simplification to Eq. 3.5 by assuming that the number of SNIa from 1 $M_\odot$ stellar generation does not depend on time and write:

$$\mathcal{R}_{Ia}(t) = k_T A_{Ia} \cdot \int_{\tau_{min}}^{\tau_{max}} \Psi(t-\tau) f_{Ia}(\tau)\mathrm{d}\tau. \tag{3.10}$$

which shows that the SN Ia rate evolution depends both on the SFH and on the distribution of delay times. Both A_{Ia} and A_{Ia} can be evaluated from stellar evolution, including a choice for the IMF. However, these theoretical values depend on assumption on the mass range of the progenitors. In addition, A_{Ia} depends on the distribution of binary separations and mass ratios, the outcome of the mass exchange phases, and of the final accretion on top of the WD.
The total number of SNe from star formed in one stellar generation is $k_{Ia} = 2.5 \times 10^{-3} M_{\odot}^{-1}$ (Greggio & Renzini, 2011), that is, 2.5 SN Ia every 1000 $M_{\odot}$ of stars. This means that from one stellar generation CC SNe outnumber SN Ia by a factor ~ 4.

3.3 Supernova Rate measurements

The rates of supernovae (SNe) at different redshifts provide important information about the evolution of a number of physical processes over cosmic times. Since core-collapse SNe (i.e., Type II and Ibc supernovae) originate from massive short-lived stars, the rate of these events should reflect ongoing star formation and therefore offers an independent way to determine the cosmic star formation rate (SFR). Furthermore, the SN rate directly probes the metal production at different cosmological epochs.
Poor statistics is a major limiting factor for using the CC SN rate as a tracer of the SFR. At low redshift the difficulty is in sampling large enough volumes of the local Universe to ensure significant statistics (e.g. Kennicutt (1984)). While at high redshift the difficulty lies in detecting and typing complete samples of intrinsically faint SNe (Botticella et al., 2008; Li et al., 2001). Moreover some fraction of CC SNe are missed by optical searches, since they are embedded in dusty spiral arms or galaxy nuclei. This fraction may change with redshift, if the amount of dust in galaxies evolves with time. Progress in using CC SN rates as SFR tracers requires accurate measurements of rates at various cosmic epochs and in different environments. The CC SN rate is also a powerful tool to investigate the nature of SN progenitor stars and to test stellar evolutionary models. Finally, it is possible to constrain the mass range of stars that produce CC SNe by comparing the CC SN rate expected for a given SFR and the observed one in the same galaxy sample or in the same volume. First high-redshift measurements of the CCSN rate have been published by two teams almost simultaneously, the STRESS survey (Cappellaro et al., 2005) and the GOODS survey (Dahlen et al., 2004). The result from STRESS survey by Botticella et al. (2008) supersedes the one of Cappellaro et al. (2005). One of the main source of uncertainty, as just said, may come from the extinction within the host, since CCSN are known to occur shortly after their birth in highly dusty star formation regions of galaxies. Measurements by Cappellaro et al. (1999) are not corrected for extinction. Dahlen

et al. (2004) attempted to make such a correction by simulating the host dust distribution according to the disk inclination, following the prescription by Hatano et al. (1998). Their corrected rates (as used in this paper) are a factor of ~ 2 higher than the uncorrected.
Type Ia SNe do not directly follow the SFR since there is a delay between the formation of the progenitor star and the explosion of the SN. Constraining this delay time is important for a better understanding of the processes leading to the Type Ia explosions and therefore essential for the usefulness of Type Ia SNe as cosmological distance indicators. With accurate measurements of the SN Ia rate, it should be possible to set constraints on this poorly known delay time.
Together with the first high-redshift supernova searches, the 1990's have seen the first type Ia rate measurement beyond the local universe (Pain et al., 1996) at z$\sim$ 0.4, using for the first time a homogeneous sample of CCD discovered SNe. Local and nearby SN Ia rates then have been measured in the field by numerous surveys, e.g., at redshifts $\langle z \rangle \sim 0.01$ (Cappellaro et al. 1999), $\langle z \rangle = 0.1$ (Hardin et al. 2000), $\langle z \rangle = 0.11$ (Strolger 2003), and $\langle z \rangle = 0.114$ (Reiss 2000). Similarly, at larger distances, rates have been measured at $\langle z \rangle = 0.38$ (Pain et al. 1996), $\langle z \rangle = 0.46$ (Tonry et al. 2003), $\langle z \rangle = 0.55$ (Pain et al. 2002), $\langle z \rangle = 0.21$(Botticella et al., 2008), .$\langle z \rangle \sim 1.0$ (Kuznetsova et al., 2008), z from 0.0 to 2.0 (Poznanski et al., 2007), $\langle z \rangle = 0.47$ (Neill et al., 2006). CC SNe are typically $\sim$2 mag fainter and searches are affected by severe selection biases; thus is easier to determine CC rate in the local Universe.

With this thesis we want to contribute to the study of the SN rate in different redshift ranges in two different ways. We proposed a SN search at high redshift with LBC@LBT to obtain new insight on the SFH and on the progenitor system of type Ia SN. The second and the main part of this work is focused to estimate the SN rate in nearby galaxies with high star formation and dust extinction. For this reason we perform an IR SN search in starburst galaxies.

3.4 The SN rate at high redshift and the SN search with LBC

SNe are the main producer of heavy elements and, as such, dominate the chemical evolution of the Universe. The kinetic energy released by their explosion can produce strong galactic winds, with implications on the dynamics of interstellar and intergalactic matter. In particular, SNe might be of fundamental importance for the feedback processes that shape galaxies.
The rate of SNe, as a function of redshift, provide a direct observational link to these processes. Specifically, the rates of CC SNe, because of their short-

lived progenitors, probes the initial mass function (IMF) of stars, traces the star formation history of the Universe and can be used to test the different scenarios for galaxy formation. On the other hand, the rate of type Ia SNe, which are believed to result from the thermonuclear disruption of a white dwarf in a bynary system, can be used to trace the long term star formation history and to shed light on the still unknown nature of their progenitors.
Several groups have devoted large efforts to measuring the SN rate (Cappellaro et al., 1999; Dahlen et al., 2004, 2008; Neill et al., 2006; Barris & Tonry, 2006; Botticella et al., 2008; Poznanski et al., 2007). These works have provided the evidence for strong increase of the SN rate with redshift up to z=1 for type Ia, and up to z=0.5 for CC. In contrast, at z>1 the observational results are still sparse. The only existing surveys probing the SN rate at z > 1 are those of HST/GOODS (Dahlen et al., 2004; Kuznetsova et al., 2008) and the SDF SN survey (Poznanski et al., 2007). The GOODS SN search has obtained 20 SNe at z>1. The SDF SN survey has used the prime-focus camera of the 8-m Subaru telescope to search for SNe in a ssingle 0.25 sq.deg. field. They detected ∼30 SNe above z=1 down to a similar limiting magnitudes, but their field lacks the unique ancillary information of the COSMOS field (morphology, accurate photometric redshifts, AGN identification by X-Rays...).
During of the first part of the PhD project we proposed to use LBC to search

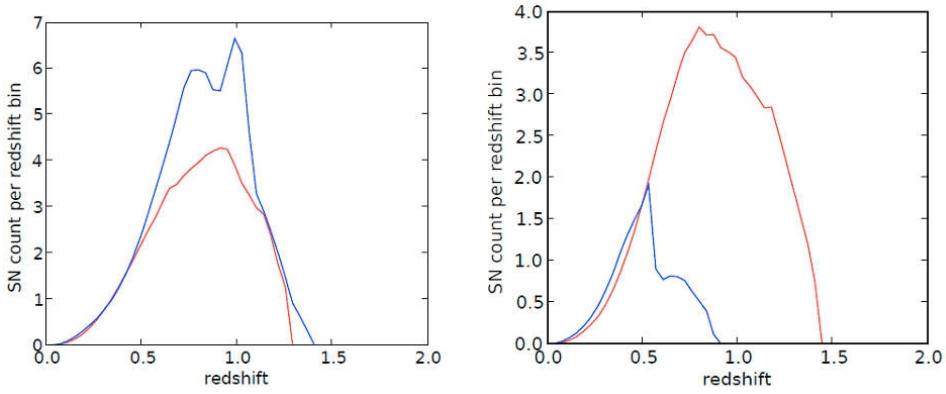

Figure 3.1: Number of expected SNe in the proposed search in the R-(left) and Z-band (right). The red lines show the espected number of SNe Ia in each redshift bin (z=0.1) detected in a 5-epoch search. The blue lines correspond to the CC SNe.

for high redshift SNe in the central part of COSMOS field. The COSMOS field is particularly well suited for a SN search because of the presence of a broad range of ancillary data (from HST, Galex, XMM, Subaru, CFHT, VLA) to derive the properties of the parent galaxy population, including

redshift, SFR, stellar age and stellar mass. We plan to measure the SN rate at high redshift, using R (sloan) and Z observations of one single pointing (about 500 sq.arcmin) in the COSMOS field. For each epoch, 3 hours of observing time are requested. LBC-red observe in the Z filter, reaching AB limiting magnitude of Z=25.4. As type Ia SNe have the peak of their brightness at about 4000 Å(rest-frame), obtaining deep image in the Z band is critical to detect SNe at z>1. In parallel, LBC-blue observe in the R-band, reaching a 5-sigma limiting magnitude of R 27.2 (AB). We asked, in total, for 6 epochs of observations in the R and Z filters. The spectroscopic classification of SNe at z>1 is not possible because of their faintness. For this reason the R-Z color and the SN light curve in both bands would be used to classify the SN. The images should allow to detect 120-180 SNe, including 60-100 of which SNe Ia at $z > 1$ (Fig. 3.1). Obviously, the expected number of SNe will be reduced in proportion of the number of lost epoch. The Z filter should provide the detection of the most of the type Ia SNe at z>1, while R should most sensitive to the CC SNe. About 2/3 of the SNe could be detected in both filters, providing a direct measurements of the color. The upper or lower limits on the R-Z colors for the other SNe should provide a strong constraint on the SN nature, once the redshifts of the host galaxies are available. The combined images will be added to other existing data and used to obtain an "ultra-deep" field to improve the study of galaxy population, in particular of the LBGs.
With this work we can have an independent chack of the claim of a decline of the Ia SNe rates at $z > 0.8$ (Dahlen et al., 2004, 2008). If confirmed, this may have important consequences for the use of Ia SNe as cosmological probes. Such a rapide decline would imply the existence of very long delays between the formation of progenitor system and its explosion as type Ia SN, a scenario in strong disagreement with the SN rates measured in the local universe (Mannucci et al., 2005) and with most models of SN explosion, predicting a constant rate at $z > 1$ (Matteucci & Recchi, 2001; Greggio, 2005). During the observations, bad weather and problems with telescope have limited the amount of collected data. We obtained only 2 epochs of the 6 planned: during 2008 only one epoch was obtained and its depth is hampered by the seeing, while the epoch obtained in 2009 reaches the required depth. All these images have been fully reduced and analyzed as follows:

- stacking images with SWarp, a program that resamples and coÂadds togheter FITS images
- take difference of images with PSF match using ISIS and DANDIA
- identify and characterize the possible candidates, considering parameters such as ellipticity, magnitude, elongation of the residuals.

A sample of 14 candidates have been found (fig. 4.12), a number consisent with expectations (18). This confirm that, despite the limited amount of time

requested (3 hours per epoch) the large LBT field of view allows for a large number of expected events. Unfortunately, although this is a very interesting and promising work, the chances of success were limited by bad weather and scheduling problems.

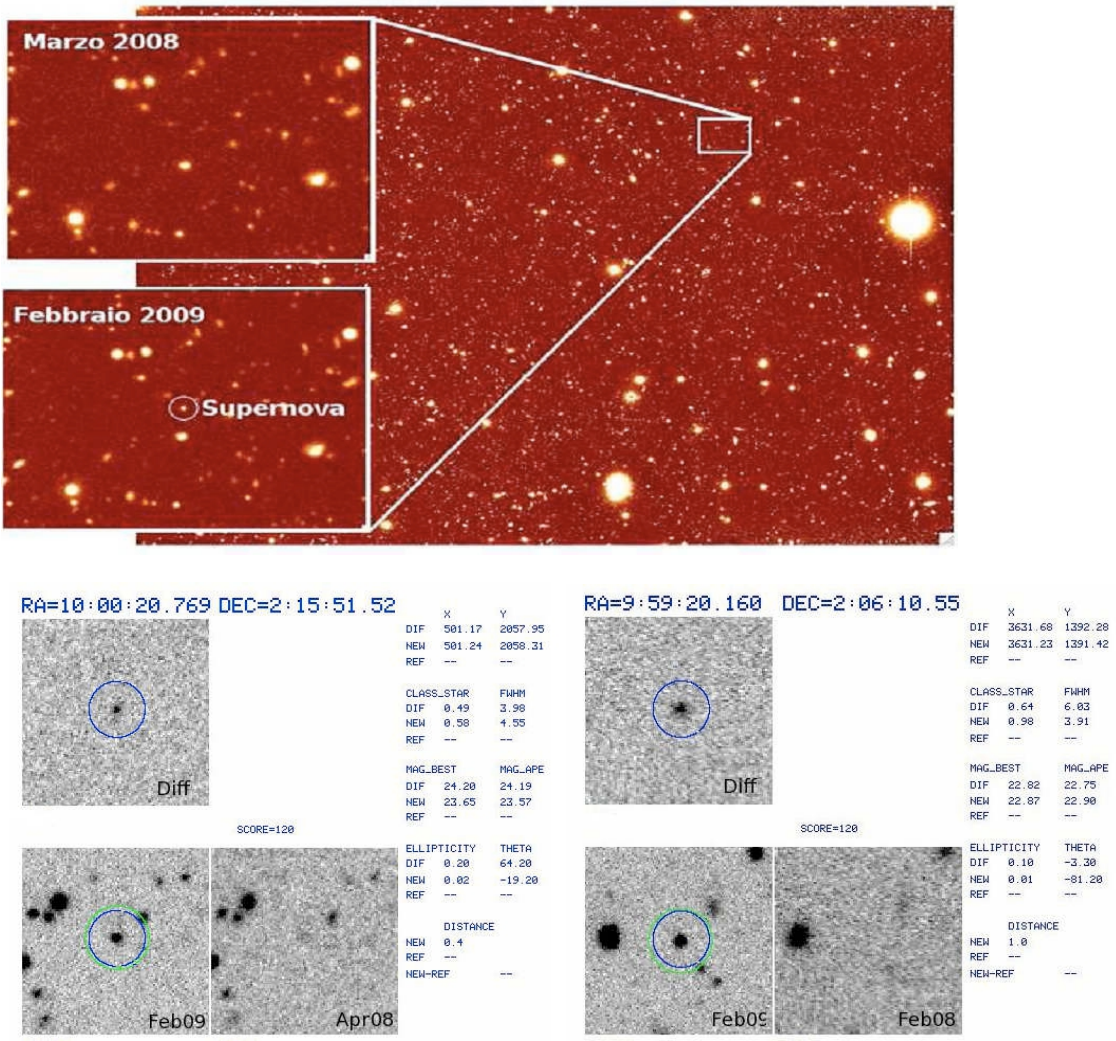

Figure 3.2: *Top:* Example of SN detected in the first two epoch of observations. The magnitude and colors of this event show that this is a type Ia SN at $z \sim 0.6$. *Bottom:* Example of two possible SNe, with different parameters useful for their characterization (e.g, ellipticity or magnitude).

3.5 Starburst galaxies

One of the main problem for measuring SN rate is related to the presence of dust. The effects of extinction can be expected to be especially severe in actively star forming galaxies. Richmond et al. (1998) was one of the first work that carried-out an optical CCD search for SNe. They analysed a sample of 142 nearby active star-forming galaxies. This yielded five SNe, all of which were outside the host galaxies' extinguished nuclear regions. The deduced SN rates were similar to those measured in normal galaxies. Therefore, it is of great importance to carry out a systematic survey for CC SNe in the nuclear regions of starburst galaxies at NIR wavelenghts which are much less affected by the extinction.
Starburst galaxies have long been known to be copious emitters of infrared luminosity. From early observations of nearby starburst systems such as M82 and NGC 253, it has been clear that the bulk of the energy of these systems emerges in the thermal infrared. Analysis of the IRAS Bright Galaxy Sample showed that 30% of the energy output in the local universe emerges in the mid- and far-infrared (5-200μm), and the bulk of this luminosity is due to star formation in these galaxies.
Infrared-luminous starbursts in the local universe afford us the best opportunity to study the processes by which such systems form and evolve.
These luminous infrare galaxies (LIRGs) become the dominant extragalctic population at IR luminosities above $10^{11}L_{\odot}$. At the most luminous end of the IRAS galaxy population lie the ultraluminous infrared galaxies (ULIRGs), those with $L_{IR} > 10^{12}L_{\odot}$. However the nature of the power source behind the IR emission of ULIRGs has remained controversial. Most ULIRGs ($\sim 80\%$) are powered mainly by starbursts but a great number of local ULIRGs show evidence for both starburst and AGN activity. Tran et al. (2001) showed that, at IR luminosities below $10^{12.4}L_{\odot}$, most ULIRGs were starburst dominated, while at IR luminosities above that value the AGN contribution was much higher. Starburst dominated systems were found up to luminosities around $10^{12.65}L_{\odot}$.
Because dust responds through its thermal emission instantaneously to the radiation field in which it is embedded, thermal radiation by dust is the ideal way to trace the current location of the dominant luminosity sources, i.e., the most luminous stars, in starbursts. In very dusty systems, such as those known from IRAS observations to be luminous starbursts, high spatial resolution imaging in the thermal infrared can address the location and extent of the current star formation in these galaxies unimpeded by foreground extinction. This is, as illustrated in the next chapters, one of the main goals of this thesis.
How the thermal dust emission is related to the other tracers of star formation is important for using these tracers in more distant galaxies.

3.6 SN searches in starburst galaxies: from optical to infrared

In star forming regions (as in SB galaxies) the dust reprocesses the UV-optical radiation emitted from young, massive stars into far infrared (FIR) radiation, which then becomes a very good tracer of the SFR. But if the rate of star formation in a galaxy increase greatly and the process does not discriminate against massive stars, then the rate at wich CC SNe occur must also rise. Since CC SNe comprise a significant fraction of all SNe, the overall SN rate of such a galaxy must likewise increase far above its normal value.
To shed light on the study of the SN rate in starburst galaxies, several searches, in particular in the last years, were conducted both in the optical and infrared wavelenght.

3.6.1 Optical searches

A number of efforts to measure the frequency of supernovae (SNe) have been made that include systematic recording of observation times and sensitivities and a relatively well defined sample of galaxies. It's important to remember the Asiago search with the discovery of 31 SNe (mostly by L. Rosino), the Crimea search (Tsvetkov 1983) or the search conducted by Evans et al (1989). In recent years there have been many attempts to measure the SN rate both in the local Universe (Cappellaro et al. 1999, Mannucci et al. 2005) and its evolution with redshift (Botticella et al. 2008 and reference therein), but unfortunately we are still facing major uncertainty and inconsistency.
These works have all used optical observations, usually in B. Such observations cannot detect SNe behind significant amounts of dust, such as those occurring in dusty star formation regions, because the dust causes up to tens of magnitudes of extinction in the optical bands. It is difficult to correct optical rate measurements for this effect, since some estimates suggest that SNe in these regions could dominate the total rate. For this reason, SN rate measurements from optical observations can only be lower limits to the true rate. Although SN searches in normal galaxies require many years or large samples to construct a statistically significant set of events, one might expect to discover a reasonable number of SNe in only 2-3 years of observation of a modest sample of starburst galaxies.
The main optical search for supernovae in starbursts was carried out in a sample of 142 nearby star-forming galaxies in 1988-1991 by Richmond, Filippenko & Galisky (1998). The observations were carried out with a 500×500 pixel charge-coupled device (CCD) camera (0.58 ascsec pixel^{-1}) on a 1-m telescope at the Lick Observatory. Two search procedures were used. In the first method, the search images were compared by eye. This yielded five supernovae, all of which were outside the estinguished nuclear regions of the host galaxies. The deduced SN rates were similar to those measured in nor-

mal galaxies. In the second method, differential photometry was carried out on the nuclei of the galaxies. However, they did not discover any brightening attributable to nuclear supernovae. From this, they deduced upper limits for the unobscured SN rates within the nuclear regions. This work confirmed that, given the likely high obscuration in nuclear starbursts, for a search for supernovae in such regions to be successful it would have to be carried out at infrared wavelenghts.
Attempts to correct for the bias induced by dust extinction include the model by Riello & Patat (2005), based on simplified assumptions for the distribution of the SNe and of the dust in galaxies, as well as on an adopted extinction law. However, this model is not able to account for the highly obscured star forming regions of SB galaxies. The problem is that when the FIR luminosity of these galaxies is used to estimate their current SFR, the expected SN rate is at least one order of magnitude higher than what measured from optical searches (Mannucci et al. 2006).
Then the conclusion is that optical measurements of the SN rate could be missing a significant fraction of SNe, particularly in the nuclei of starburst galaxies The missing SNe, while heavily obscured in the optical, are expected to show up at longer wavelength.

3.6.2 Infrared searches

The presence of dust extinction can seriously reduce the measured SN rate in most of the galaxies, especially in starburst systems where dust obscuration is usually larger than in normal galaxies. This explains the puzzling result by Richmond et al. (1998) who found starburst and quiescent galaxies to have the same SN rate. The effects of dust extinction can be vastly reduced by observing in the NIR: at 2 μm the extinction is about a factor of ten lower than in the optical V band, allowing for a much deeper penetration into the dusty star-forming regions. This strategy was originally proposed by van Buren & Norman (1989). They considered the use of mid-infrared narrow-nband ($10.52\mu m$) imaging. They estimated theat supernovae would be observable in the mid-Ir with ground-based 4-10 m telescopes at a distance of 15-40Mpc in one night's integration. Grossan et al. (1999) have studied, indeed, the supernova detection in K band. They emphasized the need for high spatial resolution to allow successfull image subtraction in the nuclear regions of galaxies.
The first monitoring campaign was conducted by Van Buren et al. (1994) a decade ago and produced the detection of one event, SN 1994bu. They use the Infrared Telescope Facility (Hawaii) for about two years. A more recent (1992-1994) NIR search for SNe in 177 nearby IRAS galaxies has been carried out in the K band by Grossan et al. (1999). The observations were performed with the 2.3 m Wyoming IT Observatory telescope. They did not discover any supernovae during the period. They conclude that this negative

result was likely due to the poor resolution spatial resolution (about 3"). Bregman et al. (2000) used ISO/ISOCAM to look for mid-infrared spectral signatures of recent SNe in the nuclei of 10 nearby galaxies. However they failed to detect any emission from SNe, such as the [NiII] emission line at 6.63 μm which is very bright in SN 1987A (e.g., Arnett et al. 1989). This is probably due to the fact that the number of events expected from the far-IR flux is lower than 0.5. Lorionov et al. (2002) reported the detection, while monitoring another event, of SN 2002cv, a bright type Ia SN showing a high extinction (Meikle & Mattila 2002). A possible SN was also discovered by Mattila et al. (2002) in an archive UKIRT K-band image.
But the first report by Maiolino et al. (2002) on a sample of SNe detected in the near-infrared (NIR) has opened a new window for the search of these events. This search is based on observations obtained at the ESO-NTT in La Silla, at the ESO-VLT in Paranal and at the Italian Telescopio Nazionale Galileo (TNG). SN 2001db, extinguished by $A_V \sim 5.5$ mag, is the first supernova discovered in the infrared that has received the spectroscopic confirmation. This result highlights the power of infrared monitoring in detecting obscured SNe and indicates that optical surveys probably miss a significant fraction of SNe, especially in obscured systems such as starburst galaxies. More recently,Mattila et al. (2005a,b) discovered two SNe during their monitoring in Ks band with the William Herschel Telescope. Di Paola et al. (2002) reported the near-IR serendipitous discovery of SN2002cv, a highly extincted ($A_V \sim$8) type Ia SN. In late 1999 Mannucci et al. (2003) started a K-band monitoring campaign of a sample of 46 Luminous Infrared Galaxies (LIRGs, $L_{FIR} > 10^{11} L_{\odot}$), aimed at detecting obscured SNe in the most powerful starbursting galaxies. During the monitoring 4 SNe were detected, two of which were discovered by our group: SN1999gw (Cresci et al. 2002) and SN2001db, the first SN detected in the near-IR which has received a spectroscopic confirmation (Maiolino et al. 2002), as said above.
Recently few groups have attempted to address this issue using the most advanced imaging systems. Cresci et al. (2007) use the near-infrared camera NICMOS of the HST, with an excellent angular resolution (0.2") and stable PSF. Their analysis found only a possible SN in Arp220 without spectroscopic confirmation. Then also in this work there is no evidence of enhanced SN rate, despite the great resolution of the HST camera. Other recent works describe the use of telescopes with adaptive optics and Laser Guide Stars. Mattila et al. (2007) report the discovery of one confirmed supernova with the NAOS CONICA adaptive optics system on the ESO Very Large Telescope. This SN (2004ip) is located near the nucleus of the host galaxies (1.4") and suffer form a host galaxy extinction of up to about 40 mag in the V band. This is the first supernova to be discovered making use of AO correction.Kankare et al. (2008) report the discovery of one confirmed supernova (SN2008cs) and a supernova candidate in near-infrared images from the ALTAIR/NIRI adaptive optics system on the Gemini-North Telescope.

However, these are very expensive programs in term of telescope time which, while certainly valuable, they cannot be performed systematically.
In conclusion, from all this work reveal firstly that NIR searches for SN in starburst galaxies are, as expected, more efficient than similar searches at optical wavelengths since at least some of the SNe occurs in dusty environments. Another conclusion is that with IR search can be detect more SNe than expected from the B luminosity, both considering or neglecting the contribution from type Ia SNe. This high value for the observed SN rate reflects the higher extinction affecting the B light of the galaxies, and the higher SN detection efficiency of the NIR observations with respect to the optical. A third crucial conclusion is that all this works yields the discovery of a few very obscured SNe. The number of detected events remaines short of a factor 3-10 with respect to expectations (Mannucci et al. 2003, Mattila et al. 2004).

Chapter 4

HAWK-I SN SEARCH

HAWK-I is a near-infrared (0.85-2.5 μm) wide-field imager installed at the Nasmyth A focus of UT4 of the ESO Very Large Telescopeat Cerro Paranal. It has been offered for the first time in ESO Period 81. The instrument is cryogenic (120 K, detectors at 80 K) and has a full reflective design. The light passes four mirrors and two filter wheels before hitting a mosaic of four Hawaii 2RG 2048 * 2048 pixels detectors. The final F-ratio is F/4.36 (1 arcsec on the sky corresponds to 169 μm on the detector). The Field of View of HAWK-I on the sky is 7.5 arcmin * 7.5 arcmin, covered by the mosaic of the four Hawaii-2RG chips. The four detectors are separated by a cross-shaped gap of 15 arcsec (figure 4.1). The four quadrants are very well aligned with respect to each other. Yet, small misalignments exist. They are sketched below in figure 4.2. Quadrants 2,3,4 are tilted with respect to quadrant 1 by 0.13, 0.04, 0.03 degrees, respectively. Accordingly, the size of the gaps changes along the quadrant edges. The default orientation (PA=0 deg) is North along the +Y axis, East along the -X axis, for quadrant number 1. The pixel scale is 0.1064 arcsec/pix with negligible distortions ($<$ 0.3 %) across the field of view. The image quality is seeing limited down to at least 0.4 arcsec seeing (i.e., 0.3 arcsec measured in K). In figure 4.3 is shown the quantum efficiency for the 4 detectors HAWK-I is equipped with 10 filters: 4 broad band filters, and 6 narrow band filters. The broad-band filters are the classical NIR filters: Y,J,H,Ks. The particularity of HAWK-I is that the broad band filter set has been ordered together with the ones of VISTA. There are thus identical which allows easy cross-calibrations and comparisons. The narrow band filters include 3 cosmological filters (for Ly_α at z of 7.7 (1.06μm) and 8.7 (1.19μm), and Hα at z = 2.2, i.e. 2.09μm) as well as 3 stellar filters (CH_4, H_2, Brγ). HAWK-I hosts large (105mm^2, i.e. expensive) filters, and was designed to have an easy access to the filter wheel (see tab. 4.4 and figure 4.5). Limiting magnitudes are of course very much dependent on the observing conditions. The exposure time calculator (ETC) is reasonably well calibrated. In order to have a rough idea of the performance to be expected, are list in table 4.6 the limiting magnitudes (S/N=5 for a

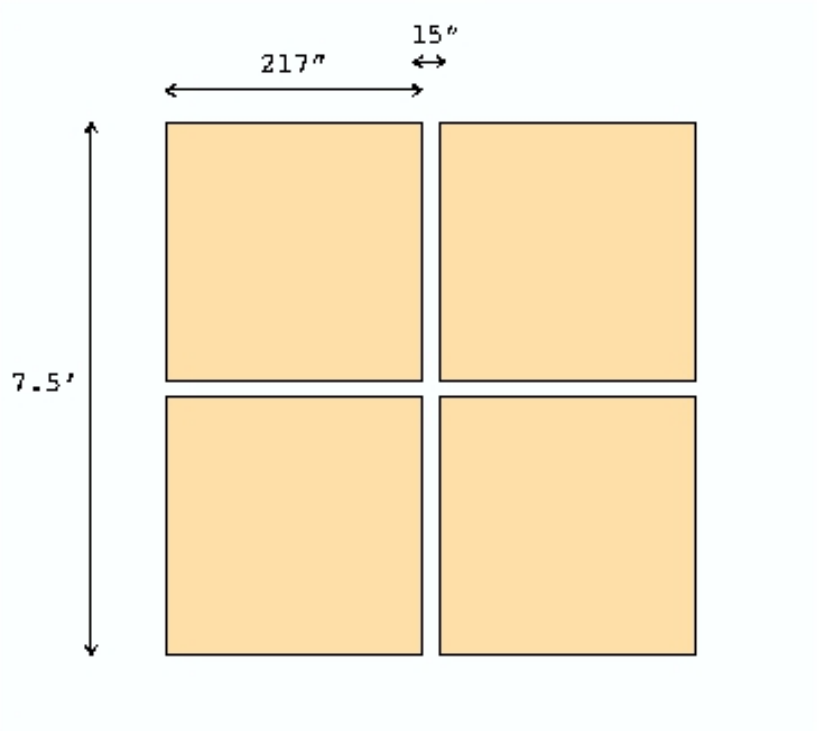

Figure 4.1: HAWK-I field of view.

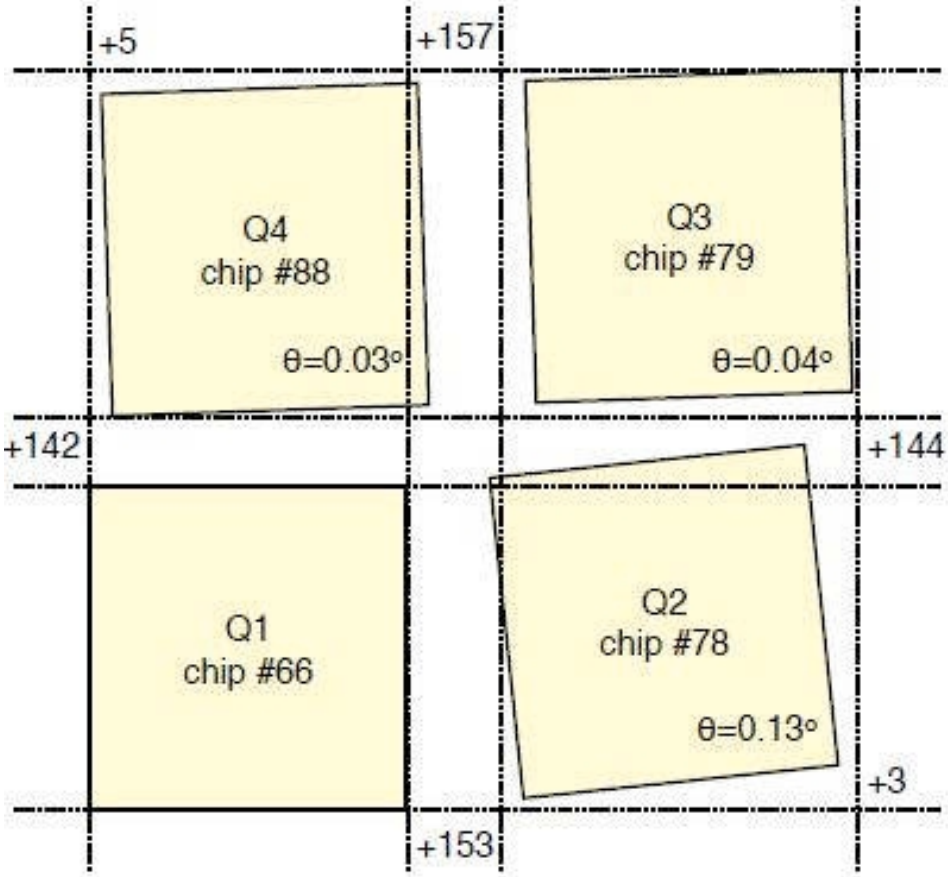

Figure 4.2: Alignment of the four chips.

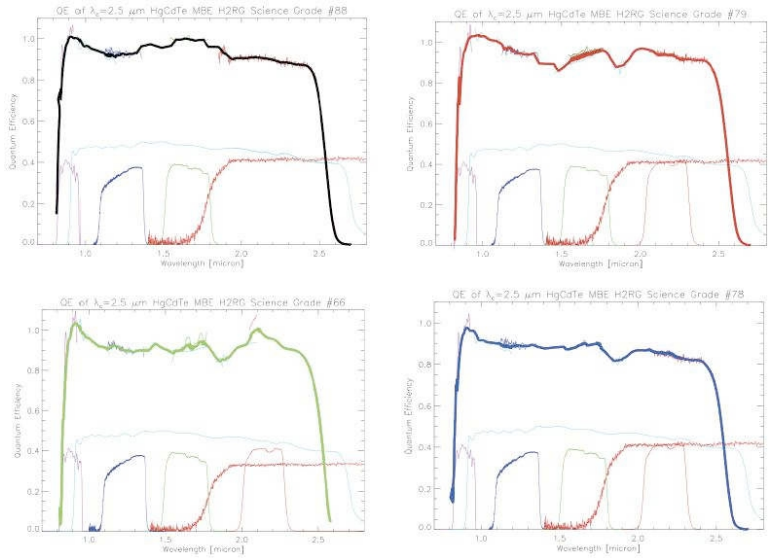

Figure 4.3: Quantum efficiency of the HAWK-I detectors.

Filter name	central wavelength [nm]	cut-on (50%) [nm]	cut-off (50%) [nm]	width [nm]	tansmission [%]	comments
Y	1021	970	1071	101	92%	LEAKS! 0.015% at 2300–2500 nm
J	1258	1181	1335	154	88%	
H	1620	1476	1765	289	95%	
K_s	2146	1984	2308	324	82%	
CH_4	1575	1519	1631	112	90%	
Brγ	2165	2150	2181	30	77%	
H_2	2124	2109	2139	30	80%	
NB1060	1061	1057	1066	9	70%	
NB1190	1186	1180	1192	12	75%	
NB2090	2095	2085	2105	20	81%	

Figure 4.4: HAWK-I filter summary.

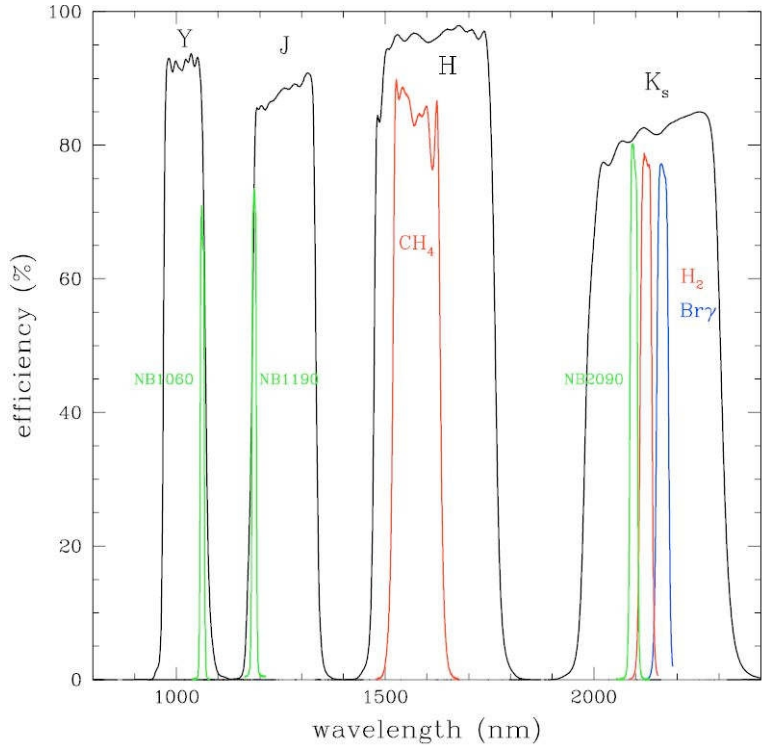

Figure 4.5: HAWK-I Filters. Black: broad-band filters Y, J, H, Ks, Green: cosmological filters NB1060, NB1190, NB2090; Red: CH4, H2; Blue: Brγ.

point source in 3600s integration on source) under average conditions (0.8" seeing, 1.2 airmass).
Due to persistence effect of the detector, in service mode, no observation will be accepted for fields containing objects brighter than Ks=8.1 , H=9.1 & J=8.8 ; i.e. ∼5 times the saturation level. This is really a generous lower limit, brighter objects will produce persistence, now more easily because of the larger minimum DIT (1.6762 secs). So far HAWK-I has been successfully

Filter	Limiting mag [Vega]	Limiting mag [AB]	Saturation limit (in 2 sec)*
J	23.9	24.8	10.0
H	22.5	23.9	10.3
K_s	22.3	24.2	9.2

*: assumed 0.8" seeing.

Figure 4.6: The limiting magnitudes (S/N=5 for a point source in 3600s integration on source) under average conditions (0.8" seeing, 1.2 airmass).

used to study the properties of medium redshift galaxy clusters (see e.g. Lidman et al. 2008, A&A 489,981), outer solar system bodies (Snodgrass et al. 2010, A&A 511, 72), the very high redshift universe (Castellano et al. 2010, A&A 511, 20), and exo-planets (Gillone et al. 2009, A&A 506, 359).

4.1 Survey strategy

The HAWK-I SN search is performed in K band, where the extinction is strongly reduced compared to optical band ($A_B = 10$ mag corresponds to $A_K = 0.8$ mag only), in a sample of 30 nearby starburst galaxies.
Given that the SN infrared light curves evolve relatively slowly (they remains within 1 mag from maximum for 1-2 months) there is no need for frequent visits: an average temporal separation of about 1 month between visits is well suited for the search purpose. Also, since is important the statistical information there are no constraints in the total number of visits per indivifual galaxy as soon as the visits for each target are separeted by > 15 days. So, assuming at least 3 visits per galaxy, per semester are planned 100 visits per observing period.
Most SNe have K absolute magnitudes in the range -16 and -18, which translates to apparent magnitudes 17-19 given the typical distances of the galaxies of our sample, or 1 mag fainter if we account for the possible presence of up to AB = 10 mag absorption. This is in the reach oh HAWK-I even in case of poor seeing and with modest investment of observing time.

Using the ETC (version 3.2.9) and assuming poor seeing conditions (2 arcsec) was estimated that with an exposure time of 13 min we can reach S/N=8 for a K=20 magnitude field star. Accounting for 10 min overheads (6 min telescope preset and 5 instrument overheads), we need 25 min per visit that imply a total request of 42h per period.
Our search is well suited as a filler for the gaps in the scheduling of service observing for non-optimal sky conditions, poor seeing or non-photometric conditions.
Spectroscopic confirmation of SN candidates has been obtained with ISAAC@VLT (P83) and X-Shooter@VLT (P85/87) in ToO/GTO mode.
ISAAC is an IR (1 - 5 μm) imager and spectrograph that lies at the Nasmyth A focus of UT3. It has two arms, one equipped with a 1024 x 1024 Hawaii Rockwell array, and the other with a 1024 x 1024 InSb Aladdin array from Santa Barbara Research Center. The Hawaii arm is used at short wavelengths (1 - 2.5 μm). Prior to ESO Period70, the Aladdin arm was used exclusively at long wavelengths (3- 5 μm). From Period70 onwards this arm is also offered for JHK imaging. We selected HAWK-I for the imaging instead of ISAAC, because of the larger field of view, in order to have a better control on the PSF of the images.
X-shooter is instead a single target spectrograph for the Cassegrain focus of one of the VLT UTs covering in a single exposure the spectral range from the UV to the K band. The spectral format is fixed. The instrument is designed to maximize the sensitivity in the spectral range through the splitting in three arms with optimized optics, coatings, dispersive elements and detectors. It operates at intermediate resolutions (R=4000-14000, depending on wavelength and slit width) sufficient to address quantitatively a vast number of astrophysical applications while working in a background-limited S/N regime in the regions of the spectrum free from strong atmospheric emission and absorption lines. X-shooter was built by a Consortium involving institutes from Denmark, Italy, The Netherlands, France and ESO.

4.2 Galaxy sample and Observations

From the IRAS Revised Bright Galaxy Sample (Kim & Sanders, 1998; Sanders et al., 1995; Soifer et al., 1987) we selected a sample of 30 SB galaxies with $z < 0.07$, FIR luminosity $\log(L_{FIR}) < 10.8$ and visible at ESO from April to October (see Table 4.1). The histogram in the top of the Fig. 4.7 represent the distribution in redshift of the galaxy sample. The mean value is $z \sim 0.029$, which corresponds to about 120 Mpc, while the most distant galaxy is IRAS14378-3651 at $\sim$ 280 Mpc ($z \sim 0.07$). The lower histogram represent, instead, the total infrared luminosity distribution of the sample, derived form equation 3.1. The galaxies of the sample are largely (90%)Luminous Infrared Galaxy (LIRGs, with $\log(L_{FIR} \geq 10^{11} L\odot)$, while the 3%

galaxy	R.A. (J2000)	DEC.	z	Log($L_{FIR}/L_{\odot}$)	L_B	Hubble type	SFR	SN rate
						($M_{\odot}\,yr^{-1}$)	(SN yr^{-1})	
CGCG011-076	11 21 13.3	-02 59 08	0.025	11.27	10.35	2.9	32.14	0.38
CGCG043-099	13 01 49.9	04 20 01	0.037	11.58	10.50	3.4	65.43	0.77
ESO148-IG002	23 15 46.6	-59 03 14	0.045	11.94	10.82	7.9	148.79	1.75
ESO239-IG002	22 49 39.6	-48 51 01	0.043	11.75	10.88	-0.1	95.70	1.13
ESO244-G012	01 18 08.6	-44 27 40	0.023	11.32	10.20	5.3	35.71	0.42
ESO264-G036	10 43 07.0	-46 12 43	0.023	11.24	10.70	1.5	29.14	0.34
ESO286-IG019	20 58 27.4	-42 38 57	0.043	11.95	11.13	10.0	151.59	1.78
ESO440-IG058	12 06 53.0	-31 57 08	0.023	11.33	10.17	99.0	36.33	0.43
ESO507-G070	13 02 51.3	-23 55 10	0.021	11.44	10.67	6.8	46.58	0.55
IC1623A/B	01 07 46.3	-17 30 32	0.020	11.63	10.42	6.0	72.68	0.86
IC2545	10 06 04.2	-33 53 04	0.034	11.66	10.58	-0.1	77.74	0.92
IC2810	11 25 47.3	14 40 23	0.034	11.60	10.61	1.5	67.98	0.80
IC4687/6	18 13 38.6	-57 43 36	0.017	11.45	10.43	2.9	47.29	0.56
IRAS12224-0624	12 25 02.8	-06 40 44	0.026	11.30	9.83	2.9	34.02	0.40
IRAS14378-3651	14 40 57.8	-37 04 25	0.068	12.13	10.40	5.1	233.02	2.74
IRAS16399-0937	16 42 39.2	-09 43 11	0.027	11.55	10.39	10.0	60.25	0.71
IRAS17207-0014	17 23 21.4	-00 17 00	0.043	12.42	10.32	-50.	447.48	5.27
IRAS18090+0130	18 11 37.3	01 31 40	0.029	11.63	10.54	2.0	71.76	0.84
MCG-02-01-051/2	00 18 51.4	-10 22 33	0.027	11.41	10.59	3.1	44.43	0.52
MCG-03-04-014	01 10 08.5	-16 51 14	0.035	11.59	10.53	-5.0	66.14	0.78
NGC0034	00 11 06.6	-12 06 27	0.020	11.43	10.34	-1.0	45.65	0.54
NGC0232	00 42 46.5	-23 33 31	0.020	11.51	10.71	1.1	55.70	0.66
NGC3110	10 04 02.7	-06 28 35	0.017	11.29	10.94	3.3	33.02	0.39
NGC5010	13 12 25.4	-15 47 45	0.021	10.84	9.79	-1.0	11.79	0.14
NGC5331	13 52 16.6	02 06 08	0.033	11.60	10.92	3.0	67.14	0.79
NGC6240	16 52 58.6	02 24 03	0.024	11.81	10.89	-0.3	108.42	1.28
NGC6926	20 33 04.8	-02 01 39	0.020	11.25	11.38	5.6	30.39	0.36
NGC7130	21 48 19.6	-34 57 05	0.016	11.34	10.75	1.2	37.15	0.44
NGC7592	23 18 22.2	-04 24 56	0.024	11.36	10.51	-1.0	38.42	0.45
NGC7674	23 27 56.9	08 46 46	0.029	11.37	10.92	1.1	39.99	0.47

Table 4.1: The galaxy sample, with the name of the galaxies,the redshift z, the Log($L_{FIR}/L_{\odot}$) (defined in the text), and the coordinates (RA and DEC) for each galaxy.

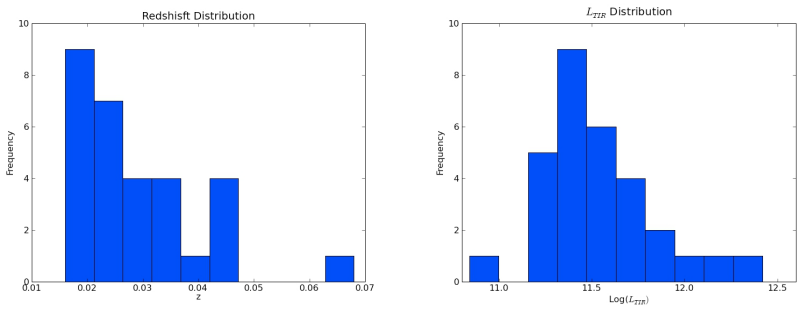

Figure 4.7: Redshift (*left*) and L_{TIR} (*right*) distribution of the galaxy sample.

(the most distant galaxies) belongs to ULIRGs (with $\log(L_{FIR} \geq 10^{12} L\odot)$.

Most of the galaxies of the sample are single galaxies (about 60-70%), and the remaining are double/interacting galaxies or contain double nucleus, sign of a recent merger. In figure 4.8 are shown the images of some galaxies of the sample analyzed in this work (the full set of images of all galaxies is in the Appendix A).
These different kind of galaxies (and galaxies interactions) reflects the different processes that induce the star formation. Some "local" mechanisms are, for example, the Supernova explosions with the shock waves into molecular cloud, the AGN activities or massive stars' winds. All these mechanisms can be enanched in the presence of galaxies interaction. For example, a merger promote an increase in SFR and a more rapid depletion of gas, "harassment" can disturb, or even radically change, the morphologies of the galaxies involved, often inducing new bursts of star formation. Several galaxies of the sample observed in the HAWK-I search are asymmetrical, disturbed, or contain warps, bars and tidal tails. All these structure are important site of star formation within a galaxy and can all be produced through galaxy harassment. Another "external" mechanism depending on the environment are, for example, strangulation, when galaxies fall into a cluster for the first time. In this case the gravitational potential of the cluster create tidal effects that enable the gas contained within the galaxies to escape and in this case the amount of gas acailable to produce stars inside the galaxy gradually falls, and eventually, SF within the galaxy will cease. Instead, as galaxies move within ICM, they experience this gas as a wind. the mechanism known as "Ram pressure stripping" occurs if this wind is strong enough to overcome the gravitational potential of the galaxy to remove the gas contained within it. Finally, some galaxies are barred or spirals, and the bar structures or the spiral arms can be an important site of star formation.
The program has been allocated in three periods, 83, 85 and 87(between April 2008 and October 2011) with completness respectively of 100% (P83)

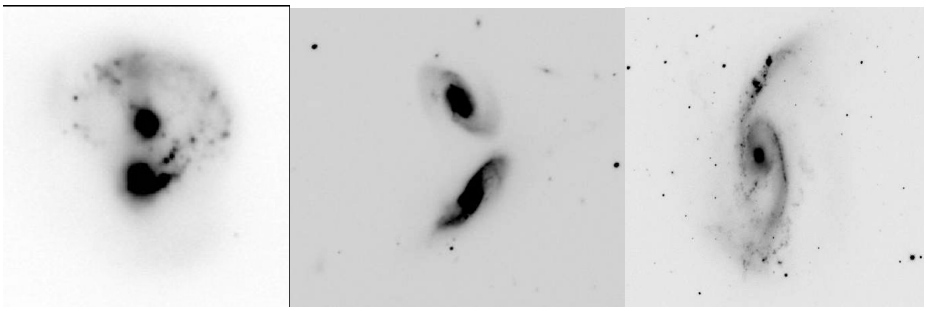

(a) IRAS16399-0937 (b) NGC5331 (c) NGC6926

Figure 4.8: HAWK-I images of 3 galaxies as an example of interacting/double nucleus galaxy (IRAS16399-0937), pair of galaxies (NGC5331) and single spiral galaxy (NGC6926).

and 70% (P85 and 87) (Table 4.2). The figure 4.9 represent the seeing dis-

Period	**Visits**			
	Nmax	Nmin	Total	Visits per galaxy
83	5	2	100	3.3
85	6	0	70	2.3
87	4	0	70	2.3

Table 4.2: The number of visits for each observing period

tribution of all the observations. Despite the lack of restriction due to the fact that our program is a filler, $\sim$ 87 % of visits have seeing $< 1.0''$, with an average value of about $0.6''$.

4.3 Data reduction and SN sample

Data reduction of HAWK-I images is a very complex process due to the fact that the field is a mosaic. A crucial point is, in fact, the build of the image from the four chips.
After downloading images from the HAWK-I archive, data analysis is performed integrating *Gasgano* and *EsoRex*(the ESO Recipe Execution Tool) with custom programs, consisting of:

- Pre-reduction and reduction
- Build mosaic images and set astrometry
- Image difference with PSF match (ISIS, Alard & Lupton (1998); Alard (2000)).

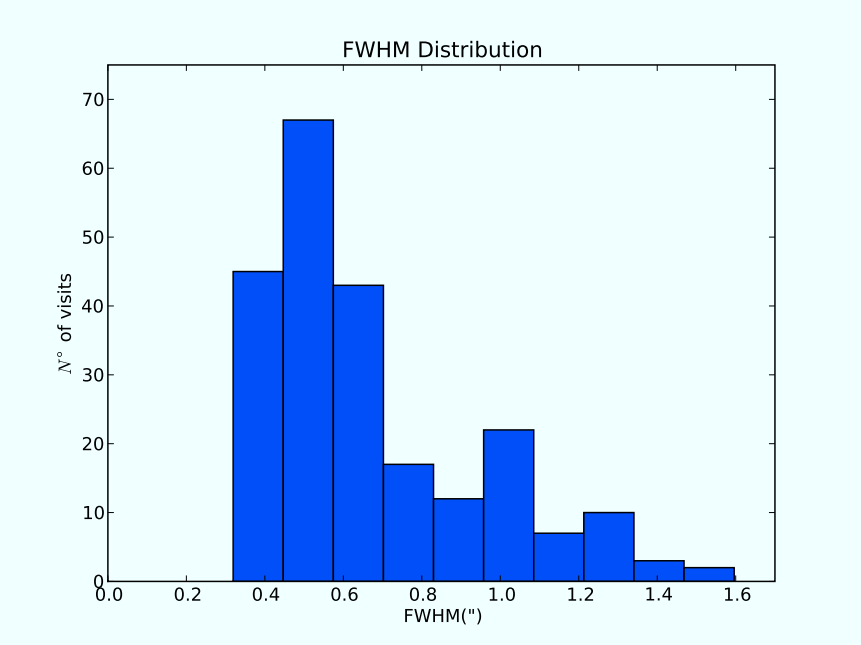

Figure 4.9: Seeing distribution of our sample.

Images of the first run were reduced using*Gasgano*, a data management tool, offering automatic data classification and making the data association easier. *Gasgano* determines the classification of a file by applying an instrument specific rule and allows the user to execute directly the pipeline recipes on a set of selected files.
EsoRex was used to reduce images of the second and third period. *EsoRex* is a command line utility for running pipeline recipes. It has the advantagemay be embedded by users into data reduction scripts for the automation of processing tasks. On the other side, *EsoRex* doesn't offer all the facilities available with *Gasgano*, and the user must classify and associate the data using the information contained in the FITS header keywords.
Images were reduced on short notice to allow for the possible activation of spectroscopic follow up.

4.3.1 Pre-reduction

However, the data reduction is strongly connected with the observation strategy which in turn depends on the nature of the observed object and the science goals of the observations. The most used observation technique is the jittering. Small shifts are applied between successive frames. This way, with a set of a sufficient number of frames, it is possible to make a precise estimation of the sky for all the pixels of the detector, the sky estimation being the most important and difficult part usually in IR.

The first step is the reduction of the calibration files, namely darks and flats.
The darks are reduced with `hawki_cal_dark` recipe. The recipe produces one master dark by computing the average with rejection of the highest value of the input images. The final master dark is divided by the exposure time to get a master dark in ADU/s units. The hot pixels map is created from the master dark with a simple 10-sigma threshold.
The flat field is created with `hawki_cal_flat` recipe, using twilight flats. The flats are derived by imaging the zenith with the tracking turned off. More than 30 exposures with constant DIT and NDIT are taken for each filter and a robust linear fit between the flux in each pixel and the median flux of all pixels is used to produce the flat field. In addition to frames classified as FLAT, there is in input the master dark. The frames are first classified by the recipe by different filters and different DITs, each group is then reduced separately. A 4-extension master flat is produced for each subset of frames with the same filter. In addition is produced a bad pixel map.

The recipe `hawki_step_basic_calib` apply the basic calibrations to science images: dark subtraction, flat fielding (the master flat is divided to all images) and bad pixel mask (the recipe replace bad pixels by an average of their valid neughbors). Most of these features are additive, so they are removed at the sky subtraction stage.
Background removal is crucial in HAWK-I. The firs step to do is to compute the background level. For HAWK-I images, the background is computed with a running median using the nearby frames. There are two possibilities:

(a) If the number of object images is lower than parameter `nmin_comb` (the minimum number of object frames to compute a running median) a simple median of the object images is computed and associated to all the input object images;

(b) The following steps are performed:

1. If an object mask has been provided in the frameset, the mask is first inverse-corrected from distortion (if distortion frames are provided).
2. If an object mask is provided to the recipe, the mask is shifted for each individual image taking into account the offsets. The offsets are retrieved from a frameset if provided or from the object header otherwise.
3. For a given target image and a given pixel, a running buffer is computed with the neighboring images, the number of which is given by parameter (`half_window`).

4. Once we have a given set of background values after mask rejection, the parameters `rejlow`, `rejhigh` are used to reject extreme values (basically a minmax algorithm). After that the median is taken from the remaining values. In the case that no values are left, the pixel is added to the bad pixel mask of the background.

The background computed in this way is then subtracted from all the input object images. This can be made with the recipe `hawki_step_subtract_bkg` or using a pyraf program created specifically for the subtraction. The steps taken by the esorex recipe are:

- If there is only one background image provided, this image is subtracted to all the input object images.
- If there are several background images provided, its number must match those of input object images. A one to one match is done to correct each object image by its corresponding background image.

The pyraf program give, instead, the possibility to compute the background in a different way. If there are 8 HAWK-I images of a given target, the program can compute the background for the firs 4 images, than for the second 4 images. In this way, there are 2 backrgound images (one for each group of 4 images). These two background images are the combined in order to have the final background to be subtracted from science frames. The program offers the possibility to choice a different images association (not only 1-4,5-8 showed in this example) to compute the backround. After several experiments, subtraction was better using the pyraf program.

Before to combine the images, it's necessary to apply the distorsion correction to the input frames. The recipe `hawki_step_apply_dist` includes the follow steps:

- The distortion table contains for several points in the image which are the distortions to apply. With this information a distortion map for each image pixel is created, using a linear interpolation with four nearest points in the table.
- For each input image the distortion correction is performed warping the original image (see 9.1.2). Note that the final image will show correlations between data values of different pixels.
- The WCS solution of the original images is retained, although now is only an approximate solution, since it does not take into account the correction of the distortion.

After refining offsets, the images are ready to be combined. This is done with the recipe `hawki_step_combine`. This recipe combines jittered images into

one single image taking into account the offsets. The algorithm to combine the images comprises the following actions:

- The offsets are read from the refined offsets frame if provided or the header telescope nominal offsets otherwise. Note that in the first case there could be different offsets for each detector and the final combined image may have different dimensions in each detector.
- Registering the images is done by resampling them with sub-pixel shifts to align them all to a common reference (usually the first frame).
- Stacking the resulting images is done by averaging them with a rejection of the outliers.
- There are two pair of keywords that inform about the offsets of this combined image. The raw images have nominal offsets in a given telescope reference system.
  The pair of keywords `QC COMBINED CUMOFFSET[X,Y]` report the position of the lower left corner of the combined image in that system. Additionally, the lower left corner of the first raw image would be placed at position `QC COMBINEDPOS[X,Y]` in the combined image.
- The WCS of the combined image is derived from the first image WCS applying the relative offset.

The final step is the creation of a single image out of the four HAWK-I chips. With the recipe `hawki_step stitch` the 4 combined images are used to reconstruct the whole field. If the jitter shift are big enough, the gaps are reconstructed. The images are not rotated or resampled, only the nominal gaps between the detectors are used. That means that the stitched image is meant only for visualization purposes and it is not recommended for scientific exploitation (specially when astrometry is important).

4.4 Sn detection method

Detection and photometry of variable source can be done by subtracting images taken at different epochs from each other and analysing the subtracted frames, a techinque known as *difference imaging*. The most complicated problem in the difference imaging process is the image mismatch due to the spatial and temporal variability of the point spread functions of the images. The difference imaging techinique used in this work is based on the Optimal Image Subtraction (OIS) code first presented in Alard & Lupton(1998), later improved upon in Alard (2000) and available in the ISIS 2.2 package.
Difference imaging, and OIS in particular, has been used to detect SNe in

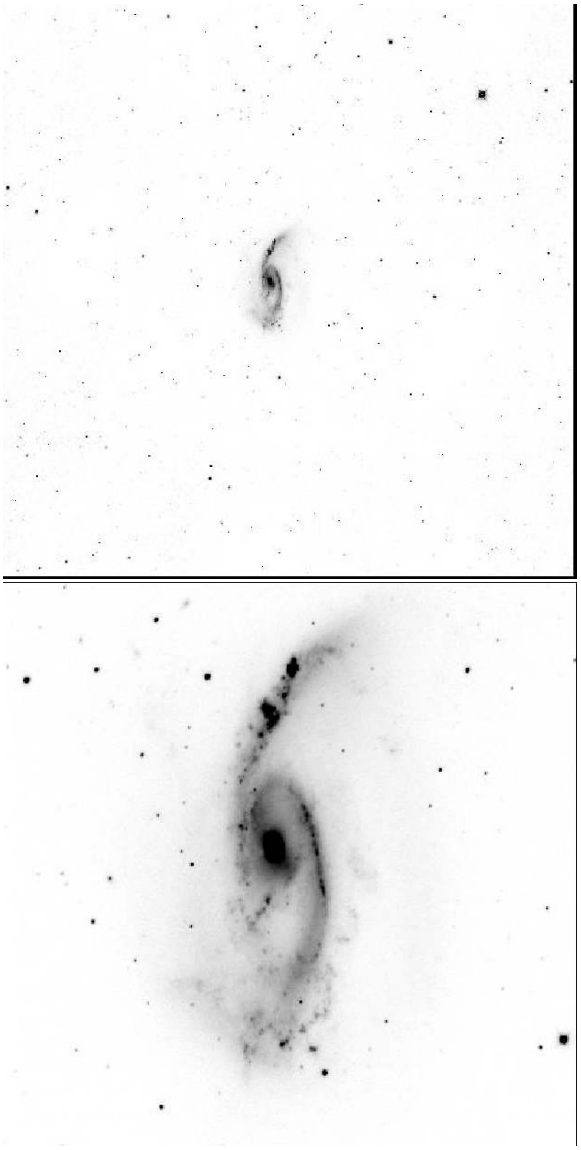

Figure 4.10: HAWK-I image of the galaxy NGC6926 after the reduction procedure. The upper panel show the entire HAWK-I field of view, the lower panel show a zoom on the galaxy.

many projects. Image subtraction using the OIS algorithm followed by detection of SN candidates in the subtracted frames is a technique that has been used by the ESSENCE survey (the observations and data analysis are described in Miknaitis et al. 2007), the Supernova Legacy Survey (Astier et al. 2006) and Poznanski et al. (2007). Cappellaro et al. (2005) and Botticella et al. (2008) used the same technique in their SN surveys aiming to determine the core collapse SN rate at intermediate redshift. Difference imaging has also successfully been used in near-infrared SN searches (e.g. Mattila & Meikle 2001; Maiolino et al. 2002) concentrating on individual starburst galaxies.
For studies of individual SNe difference imaging has been used to obtain accurate photometry of supernovae with a complicated background. This is particularly important at late times when the SN has become too faint compared to the background host galaxy in the unsubtracted image for PSF photometry to give reliable results.
The programs consits of:

- trimming of the images around the galaxies;
- accurate image alignment;
- convolving the PSF of the reference image with an appropriate kernel;
- subtracting the images;
- detection sources in the subtracted frames.

4.4.1 Registering images

The subtraction method is quite sensitive of how well the images are registered. Since the field of the HAWK-I images is large, the subtraction process may take a long time. In first approximation, is possible to trim the images around the galaxies. After the tirmming, the input image (the so-called "new epoch") is aligned to all the previous epoch. The image with the best PSF is identified and used as reference for the fture subtraction. The alignment is done by using IRAF tasks `geomap/gregister`. A number of bright sources visible in both the frames are used as input coordinate lists for these tasks.

4.4.2 Image Subtraction

The images just aligned are ready to be subtracted. The input of the program consists of the new-epoch image and the reference image. The reference image is subtracted from the new epoch image and objects with varying brightness are detected in the subtracted image. The search is repeated also for others previous epoch with the worst seeing, only as a test.
Image subtraction is a method by which one image is matched against another by using a convolution kernel, so that they can be differenced to detect

and measure variable objects. The method developed with ISIS (Alard 2000) correct the effects of the variable PSF convolving the reference image with an appropriate spatial-varying kernel determined by a least square fit.
The atmospheric conditions will affect the width and shape of the PSFs of the images. The combination of the atmospheric effects with the optics, focusing and camera setup results in variations of the PSF of the images both in spatial coordinates and over time (i.e. different epochs can have different PSFs, and also different spatial variation). A successful image subtraction technique must be able to match the PSF of the reference image to the PSF of the later epoch images also allowing the convolution kernel to vary spatially. The OIS technique presented in Alard (2000) allows this. The principal difficulty with image subtraction is to find a convolution kernel (K) that can transform the PSF of a reference image (R) to the PSF of an arbitrary image (I). The best-fit kernel can be found by minimising the sum over all pixels:

$$\sum_i ([R \otimes K](x_i, y_i) - I(x_i, y_i) + bg(x_i, y_i))^2, \tag{4.1}$$

where $bg(x_i, y_i)$ is a spatially varying background term. The kernel can be written as a sum of basis functions:

$$K(u, v) = \sum_n a_n(x, y) K_n(u.v), \tag{4.2}$$

where a_n contain the spatial variations of the kernel, which are polynomial functions of a given degree. K_n are the basis functions for the kernel and u and v denote the PSF kernel coordinates. The basis functions are Gaussian functions of the type

$$K_n(u, v) = \exp^{-(u^2+v^2)/2\sigma_k^2} u^i v^j \tag{4.3}$$

with the generalised index $n = (i, j, k)$. The basis functions can have different widths (the k index) and different orders (the i and j indices). To deal with a spatially varying background a polynomial background term is present in Eq. 4.1 and is also included in the solution which is found by solving the resulting linear system. The reference image is convolved with the kernel and subtracted from the search image. The parameters used for image subtraction are listed in Table 4.3. Parameters about images are simply the PSFs of the new and reference epochs and their zero point.
There are a number of important parameters for image subtraction. The most straightforward parameters are the kernel size (`half_mesh_size`) and the size of the stamp (`half_stamp_size`). The stamp size is the of the area taken by the program around each object. One can select the number of these stamps by using the keywords `nstamps_x` and `nstamps_y`. There is also the possibility to sub-divide the frames and process them pieces by pieces. One can control this sub-dividing through the keywords `nstamps_x` (number

IMAGES		
fw_new	7.0	seing for new image (FWHM in pixels)
fw_ref	6.8	seing for ref image (FWHM in pixels)
zero_new	27.7	photometric zero point for new image
zero_ref	27.67	photometric zero point for ref image
INSTRUMENT		
gain	5.	CCD gain
saturation	60000.	saturation limit
ISIS		
nstamps_x	9	Number of stamps along X axis
nstamps_y	9	Number of stamps along Y axis
sub_x	1	Number of sub_division of the image along X axis
sub_y	1	Number of sub_division of the image along Y axis
deg_bg	1	degree to fit differential bakground variations
pix_min	1	Minimum vaue of the pixels to fit
min_stamp_center	20	Minimum value for object to enter kernel fit
deg_spatial	1	Degree fit of the spatial variations of the Kernel
half_mesh_size	15	Half kernel size 2*FWHM
half_stamp_size	25	Half stamp size 3*FWHM
sigma_gauss1	0.7	Sigma of 1st Gaussian sigma_gauss2 /3
sigma_gauss2	2.	Sigma of 2nd Gaussian sigma_gauss3 /2
sigma_gauss3	4.0	Sigma of 3rd Gaussian FWHM/2.35.
magsel_min	10	Min mag for stamps selection (used by mydiff)
magsel_max	20	Max mag for stamps selection (used by mydiff)

Table 4.3: Example of subtraction parameters used in this work. *Column 1*:Parameter's name; *Column 2*:Parameter's value; *Column 3*: Parameter's description.

of sub-divisions along the X axis) and `nstamps_y`. The last fundamental parameter is the degree of spatial variations (`deg_spatial`) one will choose in order to fit the variations of the kernel coefficients as a function of the position in the image (see Alard 1999 for more details). If it's necessary to change the kernel size and stamp size is also useful to change the gaussian sigma of the (3 Gaussians)*(2d polynomial) kernel expansion. The relevant parameters are the 3 sigma_gauss.
The choice of the kernel is very important. A very small kernel size (smaller than the FWHM of the image) will likely cause the subtraction to fail. In ISIS a number of sources present in both reference and search image are used as the data that goes into the kernel solving procedure. A number of high S/N-sources are selected from the image and a small subimage (the stamp) is obtained for each of them. The selected sources do not have to be point sources, but they have to be non-saturated and well below the non-linear response regime of the detector. Since in the HAWK-I images the bright sources are not numerous, among the bright objects is possible to include the innermost region of the galactic nucleus to find the kernel in order to obtain a satisfactory result for the nuclear regions. Unfortunately, this makes the detection of supernovae falling on those innemrost pixels impossible (in particular, within the size of the nuclear region involved in the kernel solution). In the case of galaxies with double nucleus, ther is the possibility to include in the computation of the kernel one nucleus at a time; so it's possible to obtain a very good subtraction in each nuclei, allowing the identification of potential supernovae also close to the nucleus.
The residuals were usually concentrated at the position of the galactic nuclei, where the emission has a strong radial gradient. Non circular structures such as the diffraction spikes on the spider arms are not reproduced by the ISIS kernel. The presence of these residuals makes the detection of nuclear SNe much more diffcult, as seen in figure 4.11 (see also section 4.5). In figure 4.12 is instead shown an example of very good subtraction between images of different epochs. The case in figure is the discovery image of the supernova 2010hp (CBET2446).

4.5 Detection Efficiency

To measure the SN rate it is crucial to obtain an accurate estimate of the detection efficiency of the search. The magnitude limit of the SN detection in difference image has been estimated through artificial star experiments. It depends on the quality of the subtracted images (mainly seeing) together with the detailed technique (e.g. convolution) used to extract the signal (SNe candidates) from the background (cosmic rays, bad subtractions, etc). In addition, there is a slight dependence on the host galaxy magnitude. After

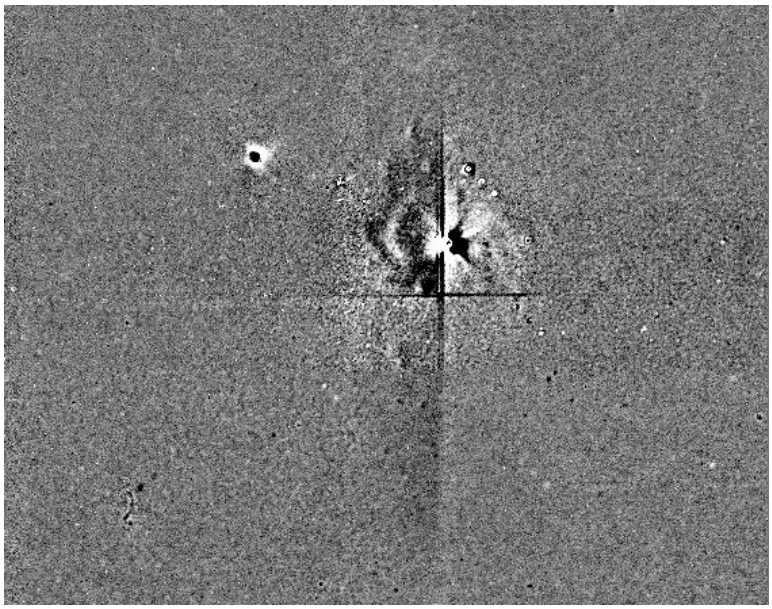

Figure 4.11: Example of bad subtraction due to the presence of numerous residuals in particular in the nuclear region (case of galaxy NGC7674).

obtaining the K-band maps for each galaxy, a "synthetic image" was created for every epoch by adding simulated supernovae to the search images using point-spread-functions drawn from each search image. The reference images were subtracted from the synthetic search images using exactly the same pipeline and reference image used for the supernova search. This technique allows us to measure detection efficiencies as a function of supernovae magnitude individually for every field.

K-band maps

The first step of the detection efficiency's pipeline is to obtain the K-band maps of the galaxies removing all stars in the image (the epoch with the best seeing). With `SExtractor` is built a catalogue of all the objects in the image. Then, removal occurs by replacing objects (their counts) with the mean value of the background computed in an annulus around each of them. Since the catalogue includes *all* the objects, then also the galaxies, there is the possibility to exclude interactively the galactic nuclei in order to prevent them from being removed. It also important to exclude any stars present near the galaxies, in order to prevent the removal of galactic counts (4.13).

Artificial Star Experiment

Obtained the K-band map, this image was then divided in different intensity bins,$\sim$ 10, a number variable depending on the galaxy analyzed (for very

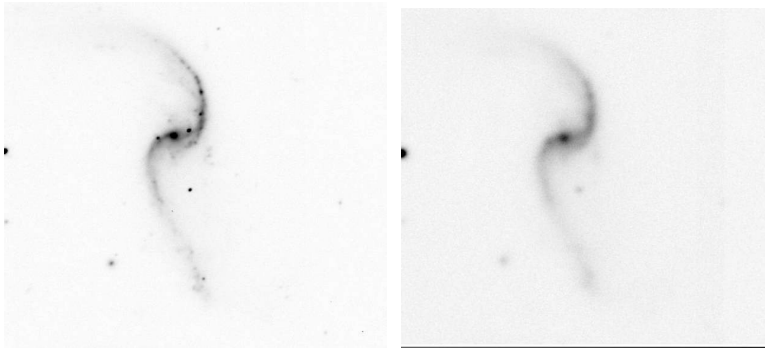

(a) (b)

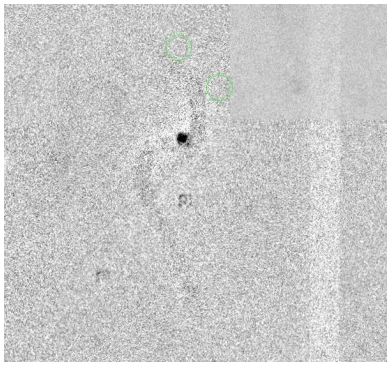

(c)

Figure 4.12: (a) HAWK-I image of the galaxy MCG-02-01-051 (Aug., 7 2010) with seeing of ~ 0.5. (b) HAWK-I image of the galaxy MCG-02-01-051 (Aug, 25 2009) with seeing of ~ 0.9. (c) Difference image in which is clearly visible a supernova, present in the image of August 2010. In this case the lack of residuals and the very good subtraction have made the detection of the events very easy.

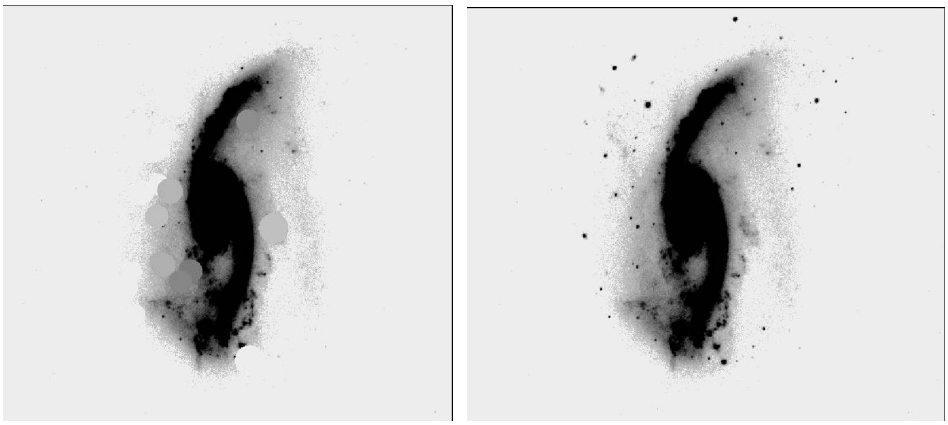

(a) (b)

Figure 4.13: (a)K-band map of the galaxy NGC6926 in wich are visible the "holes" of the oject removed inside the galactic flux. (b) The same of the figure (a), but without removng objects near the galactic nucleus.

small galaxies this number was smaller, for galaxy with an extended emission or for double galaxies could be larger). In figure 4.14 is shown an example of the intensity bins, with the relative contours, for the galaxy NGC6926. The choice to consider a few bin on the outskirts of the galaxy is due to the fact that the magnitude limit in these region does not change significantly, while bins are more crowded in the nuclear regions where is a higher stepness.
At this point, for each bin, was placed an artificial stars of different magni-

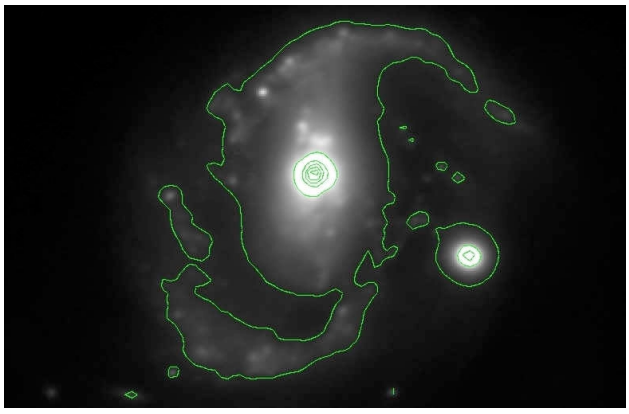

Figure 4.14: K-band map of NGC7130. Each green line refers to different intensity bins.

tude (from 12 to 20 mag, with lower values in the innermost regions where the detection is more difficult). 3 different experiments have been performed for each intensity bin. The search of the artificial stars is done on the differ-

ence images obtained with the same pipeline and reference image used for the SN search. In figure 4.15 is represented the output of the authomatic procedure. From this figure we can see that the magnitude limit is lower in the nuclear regions. This is true in particular in case of bad seeing or in presence of residual subtraction (more numerous in galaxies with very big and luminous nucleus). Another way to view this, is shown in figure 4.16

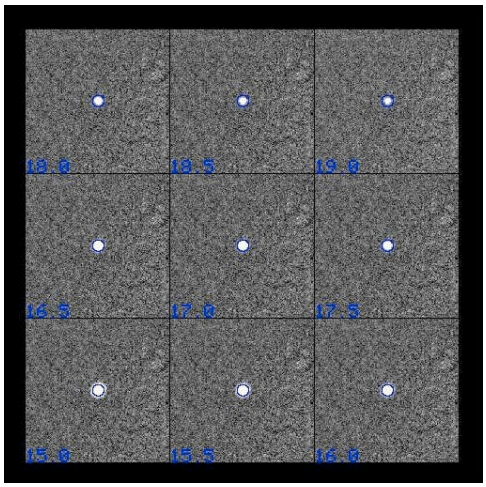

(a)

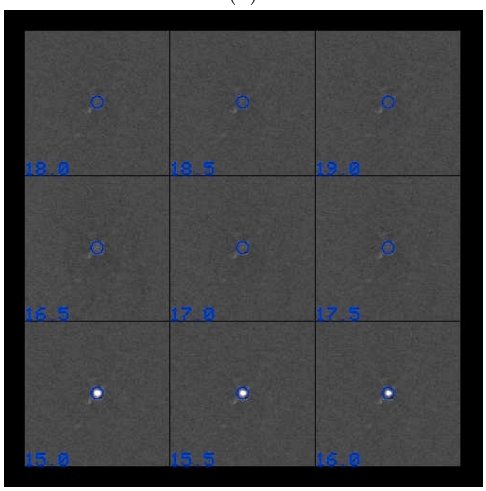

(b)

Figure 4.15: Artificial stars experiment in the outskirts (a) and in the nuclear regions (b). We can note that in the nuclear regions the detection is more difficult (magnitude limit of about 16.0), probably due to bad seeing of the reference image (1.93") combined with the luminous nucleus of the galaxy.

where is plotted the magnitude limit versus counts. Obviously, the nuclear region is in the direction of higher counts. So we can see that the magnitude limit is lower in particular in the nuclear region when the seeing is bad (in

general, $\gtrsim 1.2''$). For the outskirts there are no significant differences.

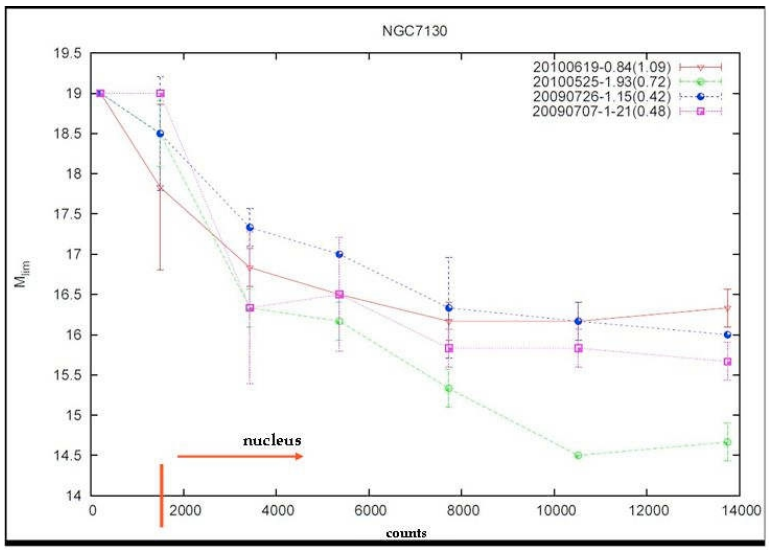

Figure 4.16: Plot of the magnitude limit vs. counts. The magnitude limit for epochs with worst seeing is lower in particular in the nuclear regions. Error bars represent the scatter due to 3 different experiments for each bin.

4.6 SN sample

The search had a slow start. During period 83 we have found 3 candidates but none of them turned out to be a SN. In one case we activated the ToO follow up, but the transient was shown not to be a SN, but a variable AGN. At the end however we collected 6 SN candidates (2 CC SNe, 1 type Ic SN and 1 type Ia SN). In two cases we have obtained the discovery images (SN 2010hp and SN 2011ee), and classification spectra with X-shooter. Finally in two cases it was impossible to obtain a spectroscopic classification of the SN candidate due to its faintness. The objects are listed in Tab. 4.4 where we report coordinates and offsets from the galaxy nucleus. From the latter and assuming a distance for the parent galaxy as derived from the recession velocity (Tab.4.1) and the adopted Hubble constant we computed the projected linear distance of the SN from the galaxy nucleus (col. 6). The last column list the available references. We remark the fact that two SNe were first discovered by others. This is not surprising given the relatively wide temporal sampling of our search. We stress that a) we had no influence on the scheduling of the observations for the given galaxies (which follows the rules of the automatic ESO service mode scheduler) and b) in both cases the objects were independently re-discovered by our SN search pipeline.

Table 4.4: List of detected SNe

SN	galaxy	R.A.	Dec.	offset	m-M	r[Kpc]	Refs
2010	IC4687/6	18:13:40.213	-57:43:28.00	2.6E 2.8N	34.21	6.5	
2010bt	NGC7130	12:21:41.46	40:51:19.2	9E 14S	34.08	5.3	IAUC 2250,2252
2010gp	NGC6240	16:52:57.39	2:23:16.4	22W 47S	35.07	25.9	IAUC 2388,2390
2010hp	MCG-02-01-52	0:18:50.01	-10:21:40.6	2.6W 2.7N	35.24	2.1	IAUC 2246,2249
2011ee	NGC7674	23:27:57.341	+08:46:38.10	9.3E 6.3S	35.39	8.9	CBET 2773
2011	IC1623A	01:07:46.229	-17:30:29.48	4E 7S	34.54	3.2	

All the candidates have been detected at least in two of our search images. The transient K-band magnitudes were measured by means of aperture photometry on the difference images and calibrated with respect to 2MASS catalog stars in the field (see the next paragraphs). Upper limits measured on pre-discovery images are also reported. In all cases, but for the candidate in IC4687, we obtained follow-up photometry with other telescopes in optical or infrared . These latter images were reduced using standard procedure in IRAF. Given that suitable templates image were not available for most filters, the SN magnitude was measured by mean of PSF fitting technique. Optical band magnitudes were then calibrated with reference to observations of Landolt standard stars.

Spectroscopic observations were obtained for four of the candidates (epoch, spectral and instruments are reported in Tab.4.5). Also in this case the data were reduced using standard procedure in IRAF. The extracted spectra, after wavelength and flux calibration, were compared with a library of template archive spectra using the automatic spectral comparison tool GELATO. The best fit spectral template and its SN type and phase are reported in Tab.4.5 but for SN in IC 4687 for which the spectrum was to noisy for a meaningful comparison. For completeness the table includes the result of the spectroscopic observations of SN 2010gp from Folatelli et al (2010). We then

Table 4.5: Log of spectroscopic observations

SN		range (nm)	res. (nm)	Instrument			
2010bt	2010 Apr 18	350-1000	1.4	EFOSC/NTT		IIn	max
2010hp	2010 Sep 17			EFOSC/NTT	??	II	??
2011ee	2011 Jul 17	340-1000	0.2	XSHOOTER/VLT	1997ei	Ic	+25d
2010 IC4687	2010 June 5			XSHOOTER/VLT			
2010gp	2010 Jul 23	Folatelli etal 2010			2002bo	Ia	just before max

analyzed the available photometry performing a simultaneous comparison of the absolute luminosity and color with that well observed SN templates with the aim to derive an estimate of the epoch and magnitude at maximum and a constraint on the extinction in the host galaxy. For the two SNe

Table 4.6: Characteristic of the detected SNe

SN	galaxy	type	template	JDmax(R)	mag(R)	mag(K)	AB_g	AB_h
2010	IC4687/6	II:	2005cs	55270 (20)		17.9 (0.2)	0.43	
2010bt	NGC7130	IIn	1999em	55240 (10)	16. (1.0)	16.1 (0.2)	0.44	?
2010gp	NGC6240	Ia	2006X	55405 (3)	16. (0.1)	16.9 (0.1)	0.33	0.5 (0.2)
2010hp	MCG-02-01-52	II	2007od	55399 (5)	17.6 (0.2)	17.2 (0.1)	0.16	$\sim$0.0
2011ee	NGC7674	Ic	2007gr	55645 (5)	18.5 (0.2)	17.8 (0.3)	0.25	0.5 (0.2)
2011	IC1623A	IIb:	1999em	55660 (10)	19.0 (0.2)	17.7 (0.2)	0.07	0.0 (0.2)

without useful spectroscopy we use the photometry to assign the SN classification. Results are reported in Tab 4.6. We stress that given that only sparse photometry is available the problem is degenerate and we can find different acceptable solutions.

We found that the infrared and optical photometry of the transient in IC 1623 are best fitted by the type IIP SN 1999em with negligible exctinction. More uncertain is the case of SN in IC4687 were only two K band measurements are available. These measures, and available upper limits, translated in absolute magnitudes which are best matched with the light curve of SN 2005cs (refs...) and therefore the SN is assumed of type II.

All together we found one type Ia and five core collapse SNe.

4.6.1 SN 2010gp in NGC 6240

SN 2010gp was discovered on 2010 July 14.10 UT by Maza et al. (Maza et al., 2010) in the spiral galaxy NGC 6240 with the 0.41-m 'PROMPT 1' telescope located at Cerro Tololo. Green et al. confirmed that SN 2010gp is a type-Ia supernova with high expansion velocity around maximum light (Green, 2010). The SN is located at $R.A. = 16h52m57s.39 \pm 0''.1, Decl. = +2°23'16''.4 \pm 0''.1$ (equinox 2000), which is about 22" west and 47" south of the center of the galaxy NGC 6240.
SN 2010gp was also discovered indipendently by our search, on 21 of July, and was observed in other 2 epochs (in August and September). In figure 4.17 are shown the 3 HAWK-I images in wihich the SN was detected. Nothing is visible on HAWK-I image taken on May 2010 (also shown in figure 4.17). In the table 4.7 are reported the photometric observations of the SN 2010gp, obtained with the HAWK-I@VLT and with the NTT telescope, with the corresponding estimated magnitudes.

In figure 4.18 are shown the near infrared and optical light curves of the SN 2010gp compared to the light curves of the type Ia SN 2006X. Relative to other SN 2006X has a broader light curve in the U band, a more prominent bump/shoulder feature in the V and R bands, a more pronounced secondary maximum in the I and NIR bands, and a remarkably smaller late-time decline rate in the B band. Is clear that our first observation of the SN 2010gp is just few days before the maximum. In figure 4.19 we can see that SN2010gp

SN	Telescope	Date	Fiter	mag
2010gp	HAWK-I	Jul,21 2010	K	17.4(0.1)
	HAWK-I	Aug,8 2010	K	16.85(0.1)
	HAWK-I	Sept,16 2010	K	17.9(0.1)
	SOFI	Sept,15 2010	JHK	17.75(K)(0.03)
	EFOSC2	Sept,15 2010	B	19.72(0.05)
			V	18.42(0.03)
			R	18.11(0.03)
			I	18.14(0.03)

Table 4.7: Optical and NIR photometry of the SN 2010gp obtained at the HAWK-I and NTT telescopes. In the last column there are the apparent magnitude.

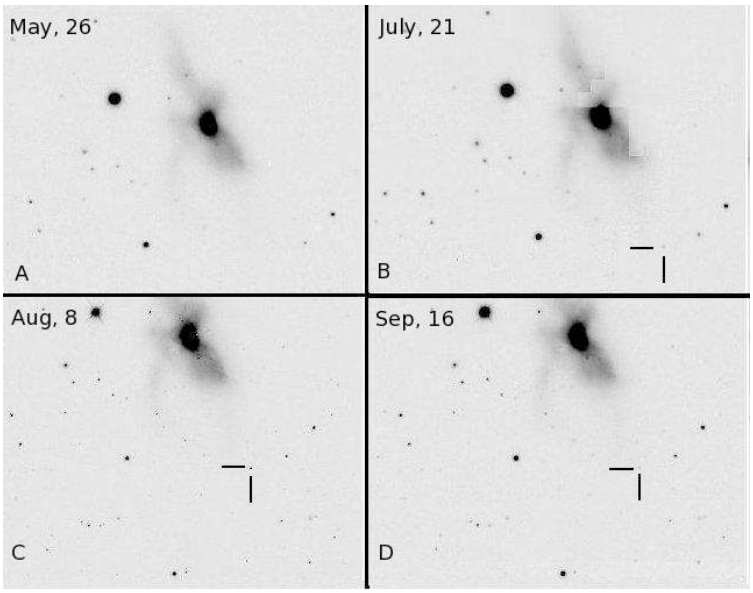

Figure 4.17: K-band HAWK-I images of the galaxy NGC 6240 with the SN 2010gp. The top left image (A) is the pre-explosion image taken on May 26 when the SN is not present, while the other 3 images (B,C,D) are taken in July, August and September.

suffers of a slight reddening: in fact, from the color curve, the value for the color B-V is about 1-1.2 mag.

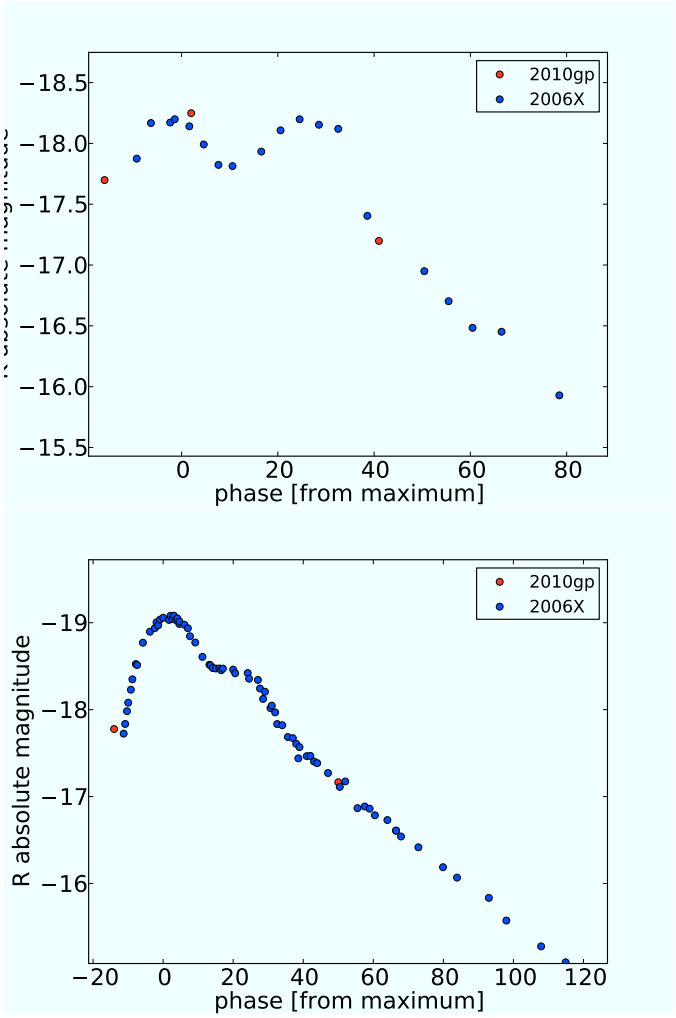

Figure 4.18: *Top:* Near Infrared light curve of the SN 2010gp from the HAWK-I data, superimposed on the curve of the SN 2006X, a type Ia SN. *Bottom:* The same in the optical (R-band). The point before the maximum come from Maza et al. 2010 (Maza et al., 2010). Is clear from the comparison that the SN 2010gp is a type Ia SN observed just a few days before the first maximum.

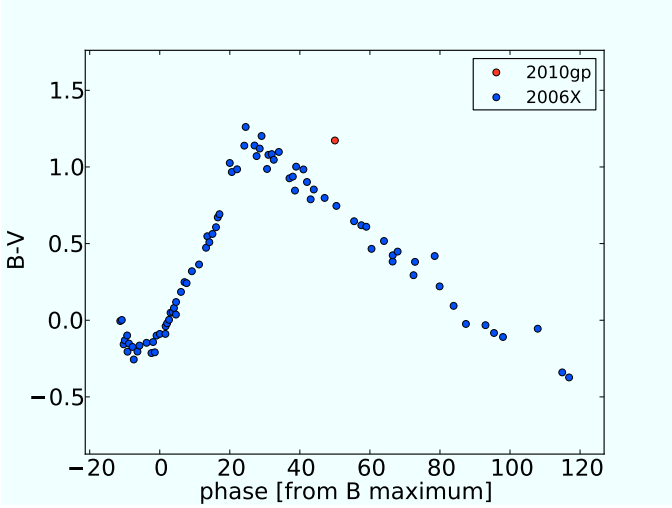

Figure 4.19: B-V color vs phase from the B maximum. Is clear that the SN 2010gp, from the comaprison with the SN 2006X,is slight reddened.

The host galaxy NGC 6240

SN 2010gp was not the only SN found in NGC 6240. In fact, Sato et al (2000, (Sato & Li, 2000)) report the discovery of a type IIn SN in NGC 6240, discovered 2000/04/1.5 on behalf of the Lick Observatory Supernova Search. Due to its proximity, NGC 6240 (fig. 4.20) ($z \sim 0.024, D \simeq 98 Mpc$) is one of the brightest objects in the IRAS All-Sky Survey and was one of the early identified LIRGs with a total infrared luminosity of about $10^{11.7} L_{\odot}$. Optical studies of NGC 6240 reveal a morphologically irregular galaxy with clear tidal extensions, two nuclei and prominent dust lanes, strongly suggesting a merging system. The two galactic nuclei found in the central region have a projected separation between 1".5 and 1".8 at X-ray and radio wavelengths. the fact that the observed distance between the nuclei depends on the wavelength at which they are observed, indicates large amounts of dust extinction in the center of the galaxy. The presence of the double nucleus is clear also in the near infrared images, instead at mid infrared wavelenght, figure 4.21, most of the contribution to the MIR luminosity comes from only one of the two nuclei (Egami et al. 2006 (Egami et al., 2006)). In particular, the southern nucleus provide $\sim 80\% - 90\%$ of the total flux at these wavelenghts $(8 - 25 \mu m)$ within a radius of $<$200 pc. Moreover, the southern nucleus has a mid-infrared spectrum and a mid/far-infrared spectral energy distribution consistent with starburst. Alternatively it's possible to attribute up to 60% of the bolometric luminosity to an AGN, consistent with X-ray observations, if the AGN is heavely obscured (up to $A_V < 1000$ mag) and emits mostly in the far-infrared.

Indeed, Hagiwara et al., 2011 (Hagiwara et al., 2011), through a radio

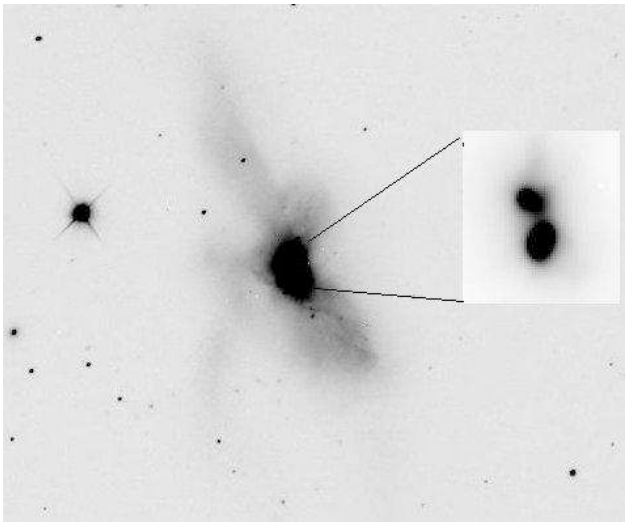

Figure 4.20: HAWK-I K-band image of NGC 6240, in which are cleraly visible the tidal extensions, and the two nuclei in the box zoom in the right.

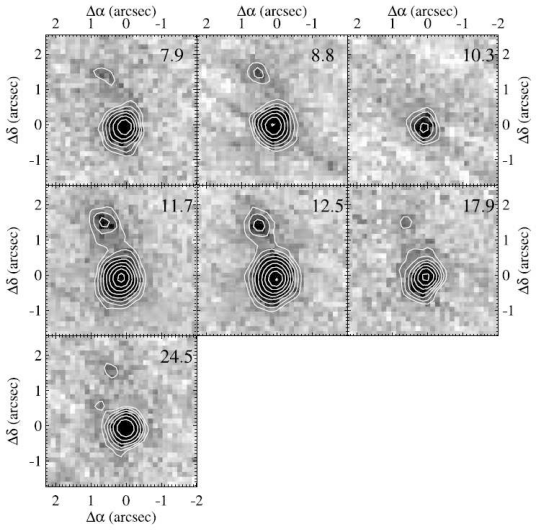

Figure 4.21: Mid-infrared images of NGC 6240 obtained with the MERLIN Camera on the Keck II 10 m telescope on Mauna Kea in Hawaii. North is up and east is left. The observed wavelength (in microns) is denoted in each panel. The contour maps were produced from Gaussian-smoothed images (Gaussian FWHM=2 pixels). The lowest contour corresponds to 2 σ above the sky level, which was calculated in the nonsmoothed image, and the successive contours correspond to factor of 1.4 increases in surface brightness (Egami et al. 2006 (Egami et al., 2006))

analysis of the two nuclei, suggest that the southern nucleus hosts an AGN and a circumnuclear starburst. They also found, very close to the southern nucleus, two other radio sources, that they identify as long-lived radio SNe that result from ongoing circumnuclear star formation.
SN 2000 bg was located, instead, away from the southern nucleus, at about 11" (fig. 4.22), and even more distant is SN 2010gp, at about 44", in the outskirts of the galaxy. From IRAC/ACS images of Bush et al.2008 (Bush et al., 2008) we can see that SN 2010gp lies just near the end of a tidal tail and a faint dust lane.

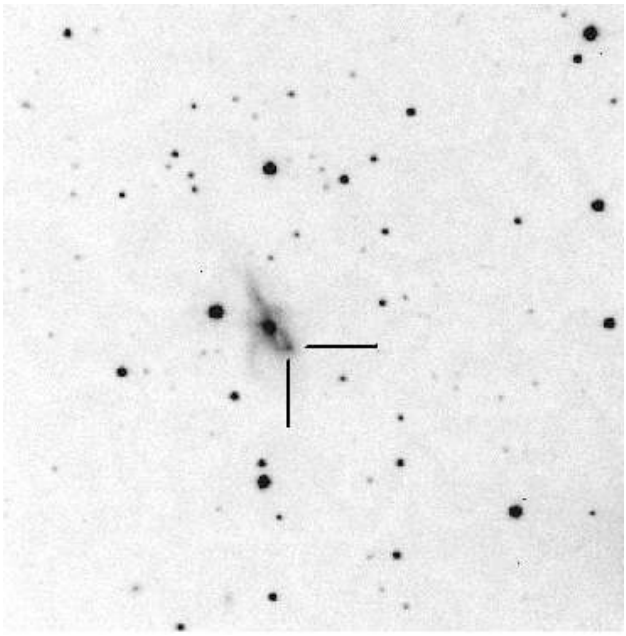

Figure 4.22: SN 2000bg discovered by Sato et. al with the KAIT telescope (Sato & Li, 2000)

4.6.2 SN 2010bt in NGC 7130

SN 2010bt was discovered on 2010 April 17.10 UT by Berto Monard (Monard, 2010) in the spiral galaxy NGC7130. The supernova is located at R.A. = 21h48m20s.22, Decl. = -34°57'16".5 (equinox 2000.0), which is 9" west and 14" south of the center of NGC7130. Turatto et al. (2010) obtained a spectrogram of 2010bt on April 18.39 UT. The comparison of this spectrum with GELATO shows strong resemblance to several type-IIn supernovae a few days after explosion. A broad H_{alpha} component is also present, from which an expansion velocity of about 4500 km/s, is derived.
SN 2010bt was also discovered indipendently by our search, on 25 of May,

and was observed in other 2 epochs (in June and July). In figure 4.23 are shown the 3 HAWK-I images in wihich the SN was detected. Nothing is visible on HAWK-I image taken on June 2009 (also shown in figure 4.23). In the table 4.8 are reported the photometric observations of the SN 2010bt, obtained with the HAWK-I@VLT, the NTT telescope and CTIO, with the corresponding estimated magnitudes.

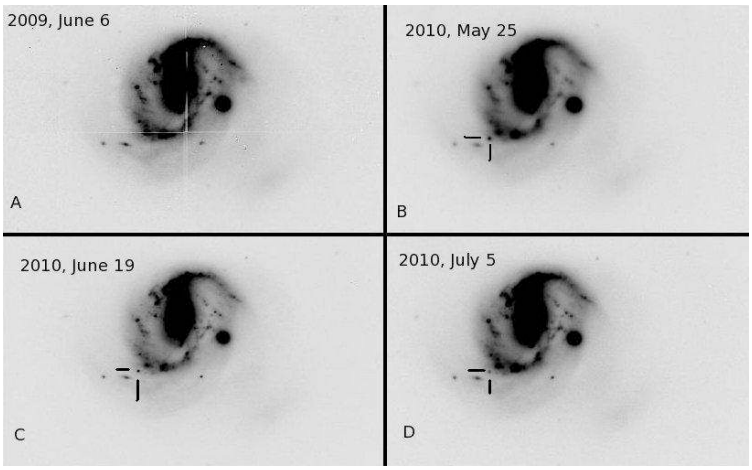

Figure 4.23: K-band HAWK-I images of the galaxy NGC 7130 with the SN 2010bt. The top left image (A) is the pre-explosion image taken on 2009, June 6 when the SN is not present, while the other 3 images (B,C,D) are taken in 2010, May, June and July.

In figure 4.24 are shown the near infrared and optical light curves of the SN 2010bt compared to the light curves of the type IIn SN 2008D. Is clear that our first observation of the SN 2010bt is about 50 days after the maximum. In figure 4.25 we can see that SN2010bt suffers of a slight reddening: in fact, from the color curve, the value for the color B-V is about 1-1.2 mag.

4.6.3 The host galaxy NGC7130

NGC 7130 (fig. 4.26), a nearby galaxy ($\sim 64 Mpc, z = 0.016$) with high infrared luminosity (about $10^{11.2} L_{\odot}$) is an example of a starburst/AGN composite galaxy, classified on the basis of optical emission line ratios as a normal Seyfert2 type.
The NGC 7130 K band shows an inner bar oriented at P.A.=0°not visible at optical wavelengths. In the digital sky survey it can be seen that NGC 7130 has two dwarf companion galaxies located to the northwest at 50" (15.5 kpc) and to the southwest at 30" (9 kpc). An H_{α} image shows two bright arms and circumnuclear extended emission, but the [O III] image only shows emission concentrated in the nucleus. There is an extremely luminous infrared

SN	Telescope	Date	Filter	mag
	CTIO	Apr,27 2010	B	17.89(0.18)
			V	17.16(0.16)
			R	16.73(0.09)
			I	16.39(0.14)
	CTIO	Apr,30 2010	B	18.11(0.15)
			V	17.36(0.13)
			R	16.89(0.10)
			I	16.66(0.09)
	CTIO	May,03 2010	B	18.24(0.14)
			V	17.52(0.12)
			R	16.99(0.09)
			I	16.70(0.11)
	CTIO	May,07 2010	B	18.56(0.06)
			V	17.79(0.05)
			R	17.30(0.04)
			I	16.96(0.06)
	CTIO	May,18 2010	B	19.58(0.11)
			V	18.59(0.09)
			R	17.98(0.06)
			I	17.69(0.07)
	CTIO	May,23 2010	B	19.84(0.14)
			V	18.84(0.12)
			R	18.19(0.08)
			I	17.91(0.12)
2010bt	HST	Oct,09 2010	V	22.50(0.05)
	NTT	Sept,15 2010	B	22.55(0.44)
			V	21.34(0.38)
			R	20.39(0.34)
			I	20.29(0.17)
	NTT	Oct,04 2010	B	23.25(0.32)
			V	22.11(0.29)
			R	21.45(0.29)
			I	20.56(0.24)
	NTT	Oct,28 2010	B	24.40(0.37)
			V	23.91(0.34)
			R	22.69(0.48)
			I	21.21(0.33)
	HAWK-I	May,25 2010	K	16.9(0.05)
	HAWK-I	June,19 2010	K	18.08(0.10)
	HAWK-I	july,05 2010	K	18.68(0.10)

Table 4.8: Optical and NIR photometry of the SN 2010bt obtained at the HAWK-I, CTIO and NTT telescopes. In the last column there are the apparent magnitude.

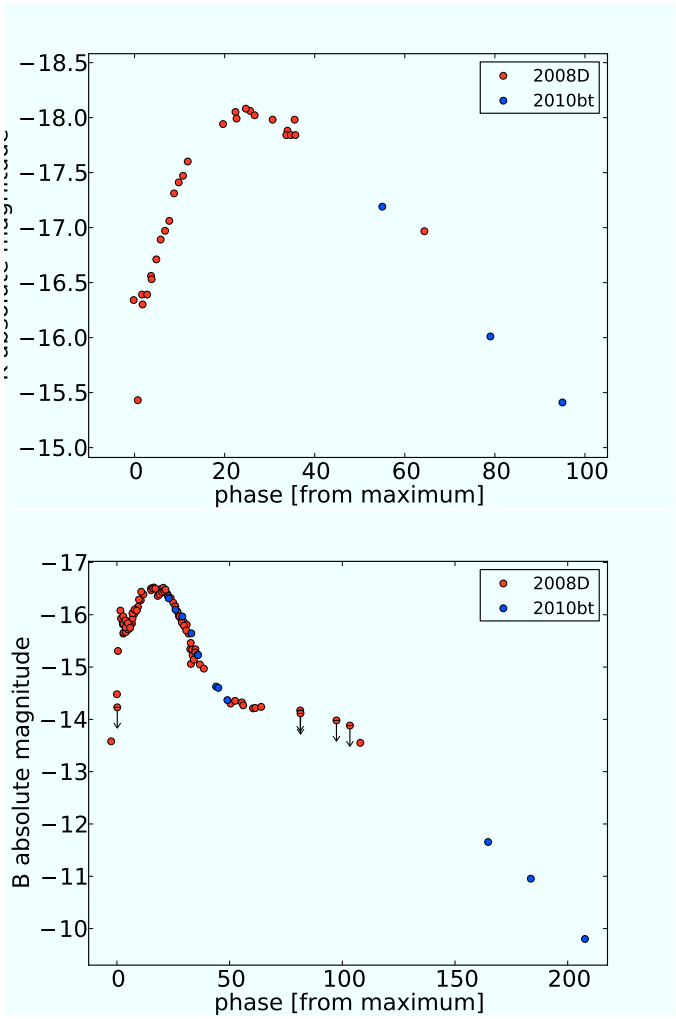

Figure 4.24: *Top:* Near Infrared light curve of the SN 2010b from the HAWK-I data, superimposed on the curve of the SN 2008D, a type IIn SN. *Bottom:* The same in the optical (B-band). In this case data come from CTIO and HST. Is clear from the comparison that the SN 2010bt is a type II SN observed about 50 days after the first maximum.

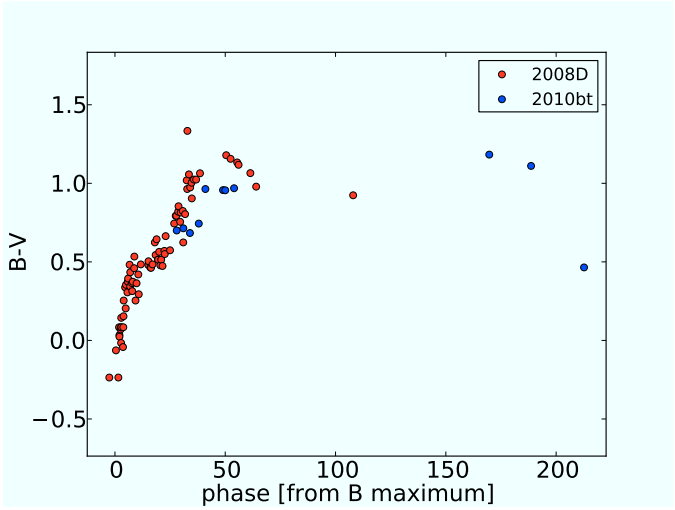

Figure 4.25: B-V color vs phase from the B maximum. Is clear that the SN 2010bt, from the comaprison with the SN 2008D,is slight reddened.

source, with a very compact radio source. NGC 7130 looks very asymmetric, with a spiral arm to the northwest being more distorted and less organized than the arm to the southeast. This is probably related to the presence of the dwarf companion galaxy located to the northwest of NGC 7130. There are also two spiral arm segments located in the outer part of two dust lanes that run in the northsouth direction toward the center. These lanes could be tracing the leading edge of the near-IR bar. The inner structure is boxy with the major axis aligned at P.A.=90°, perpendicular to the near-IR bar (González Delgado et al., 1998).

4.6.4 SN 2010hp in MCG-02-01-051/2

We discovered SN 2010hp on 2010 July 21.26 UT in the spiral galaxy MCG-02-01-051/2 (Miluzio & Cappellaro, 2010). The supernova is located at R.A. = 0h18m50s.01, Decl.= -10°21'40".6 (equinox 2000.0), which is 2".6 west and 2".7 north of the center of MCG -02-01-52. In figure 4.27 are shown the HAWK-I discovery image and the two other epochs in which the SN was detectable. Nothing is visible at this position on K-band images taken on 2009 Aug. 25.41 (top left in figure 4.27). In the table 4.9 are reported the photometric/spectroscopic observations of the SN 2010hp, obtained with the HAWK-I@VLT and with the NTT telescope, with the corresponding estimate of the magnitude.
Marion et al. obtained the spectroscopic confirmation that SN 2010hp is a type-II supernova more than 30 days past maximum light (Marion et al., 2010). We also obtained an independent spectroscopic classification of SN 2010hp with X-Shooter@VLT, in optical and NIR spectrum (UVB, VIS and

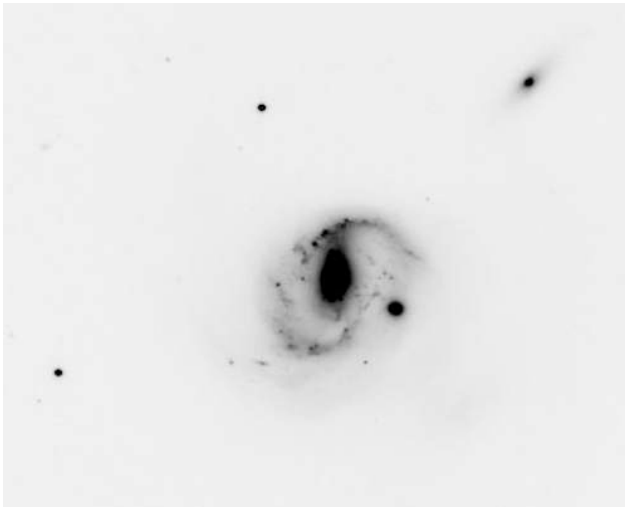

Figure 4.26: HAWK-I K-band image of NGC 7130, with a spiral arm to the northwest being more distorted and less organized than the arm to the southeast. Is also visible a companion located to the northwest of the galaxy.

NIR arms). Assuming a recession velocity for the host galaxy of 8070 km/s, with the Gelato code (Harutyunyan et al. 2008, (Harutyunyan et al., 2008) available at website URL https://gelato.tng.iac.es/login.cgi) we obtained a good match with the spectrum of the SN 1999em at about +60 days in the plateau phase, with reddening of about E(B-V)=0.4. The spectrum contains all the feature of a typical type II Supernova, in particular are clearly visible the lines of the Balmer series (Figure 4.28). Others visible lines are that of NaII, and the doublet of FeII and in the near infrared the CaII emission triplet.

In figure 4.29 are shown the near infrared and optical absolute light curves of the SN 2010hp compared to the absolute light curves of the type II SN 2007od. SN 2007od is a bright IIP, with a short plateau, a bright peak ($M_V = -18$ mag). Is clear that our first NIR observation of the SN 2010hp is very close to the maximum. There is no evicence for significant reddening from the color comparison.

SN	Telescope	Date	Fiter	mag
	HAWK-I	Jul,21 2010	K	17.25(0.05
	HAWK-I	Aug,7 2010	K	17.17(0.05)
	X-Shooter	Sept,8 2010	UVB,VIS,NIR	
	HAWK-I	Sept,10 2010	K	17.20(0.10)
	EFOSC2	Sept,14 2010	UBVRI,gm11+16	20.20(U)(0.03)
				19.61(B)(0.03)
				18.70(V)(0.03)
				18.28(R)(0.03)
				17.89(I)(0.03)
	SOFI	Sept,16 2010	JHK+BG	17.24(J)(0.1)
				16.93(H)(0.1)
				16.96(K)(0.1)
2010hp	SOFI	Oct,28 2010	J	18.48(0.1)
			H	18.51(0.1)
			K	17.99(0.15)
	EFOSC	Oct,29 2010	B	>19.13(0.03)
			V	19.61(0.03)
			R	18.83(0.03)
			I	18.83(0.03)
	EFOSC	Jan,01 2011	B	>20.83
			V	>20.02
			R	>18.46
			I	19.50(0.05))
	EFOSC	Jun,24 2011	R,gm16(not vis)	>21.4(R)

Table 4.9: Optical and NIR photometry/spectroscopy of the SN 2010gp obtained at the HAWK-I, X-Shooter and NTT telescopes. In the last column there are the apparent magnitude. In red the row referred to the discovery image.

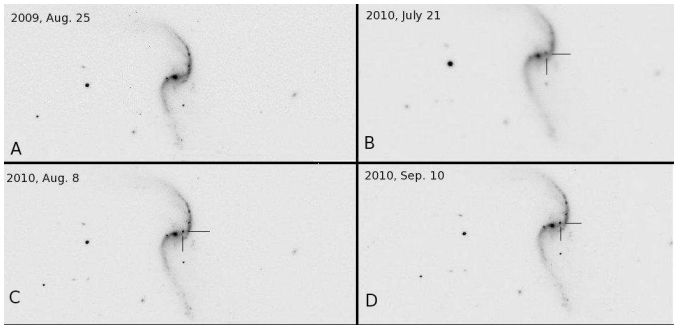

Figure 4.27: K-band HAWK-I images of the galaxy MCG-02-01-051 with the SN 2010hp. The top left image (A) is the "pre-explosion" image taken on 2009, Aug. 25 when the SN is not present, while the other 3 images (B,C,D) are taken in July, August and September. The image taken on 2010, July 27 is the discovery image (CBET2446).

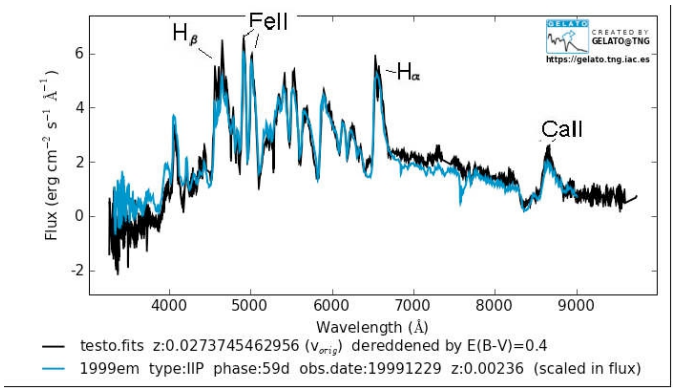

Figure 4.28: UVB+VIS spectrum of SN 2010hp matched with the spectrum of type II SN 1999em (with the GELATO code) about 60 days after the maximum, with the principal emission/absorption lines, including the lines of the Balmer series.

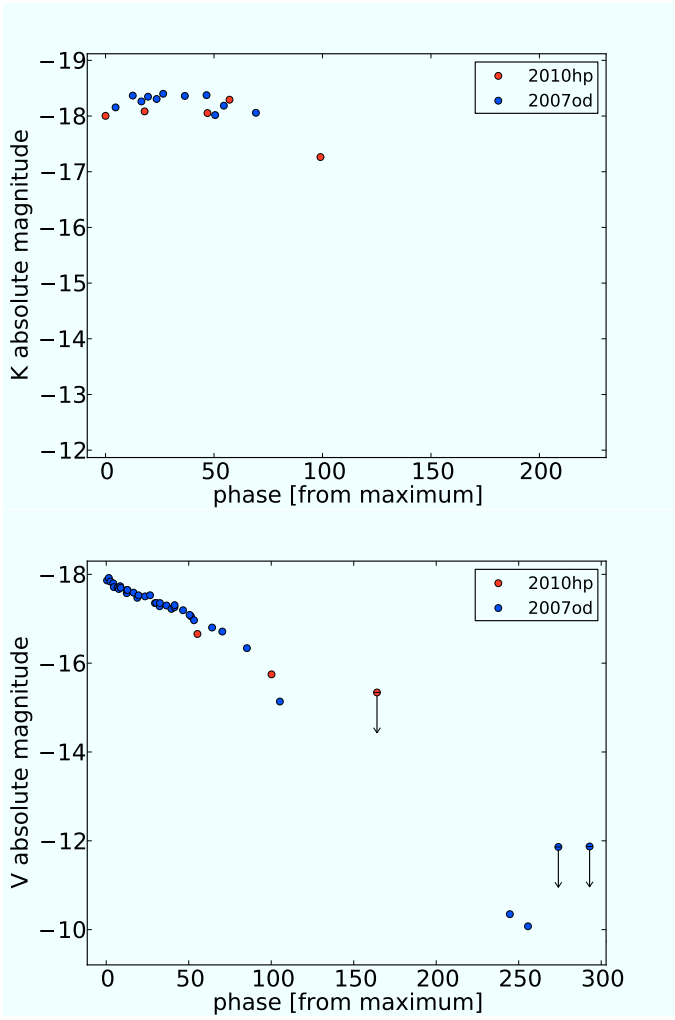

Figure 4.29: *Top:* Near Infrared light curve of the SN 2010hp from the HAWK-I data, superimposed on the curve of the SN 2007od, a type II SN. Is clear from the comparison that the SN 2010hp is a type II SN observed near to the maximum. *Bottom:* The same in the optical (R-band). Points with arrow are only an upper limit. In this case the first observations is several days after the maximum.

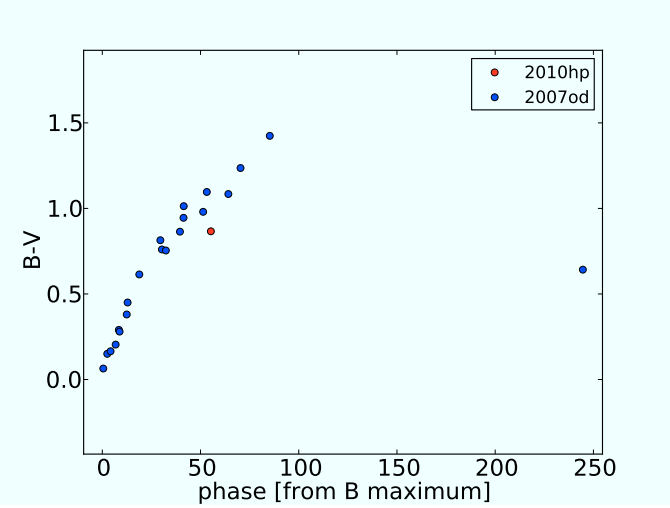

Figure 4.30: B-V color vs phase from the B maximum. Is clear that the SN 2010hp, from the comaprison with the SN 2007od, is in practice no reddened.

Parameter	Value
Redshift	0.027
$Log(L_{FIR}/L_{\odot})$	11.27
SFR ($M_{\odot}yr^{-1}$)	44.43
SN rate ($SNyr^{-1}$)	0.52

Table 4.10: Observing parameters of galaxy MCG-02-01-051/2.

The host galaxy MCG -02-01-051/2

MCG -02-01-051/2 or Arp 256 (figure 4.31 is composed of two galaxies separated by 54". Arp 256 N (north) is an SB(s)c galaxy, while Arp 256 S (south) is an SB(s)b galaxy. At redshift z = 0.027, their distance is 98.1 Mpc, with a projected nuclear separation of 29 kpc. The IR luminosity is $\sim 10^{11.2} L_{\odot}$, but neither galaxy is known to have active galactic nucleus (AGN) activity and both show HII region-like spectra. The relatively large separation between the galaxies in Arp 256 suggests that the system is in an early phase of merging (Chen et al., 2002). In table 4.10 are summarize the useful parameters of these galaxies.
It's interesting to investigate the different trigger of star formation in the two component of Arp 256. In figure 4.32, from Chen et al. 2002 (Chen et al., 2002), is shown the HI, CO and radio continuum maps over an optical image. The HI distribution show a spiral pattern, but the peak emission do not correspond to the optical emission peaks. In contrast to the HI distribution, the CO emission associated with Arp 256S appears well confined within the circumnuclear region of the galaxy.No CO emission is detected in the nuclear

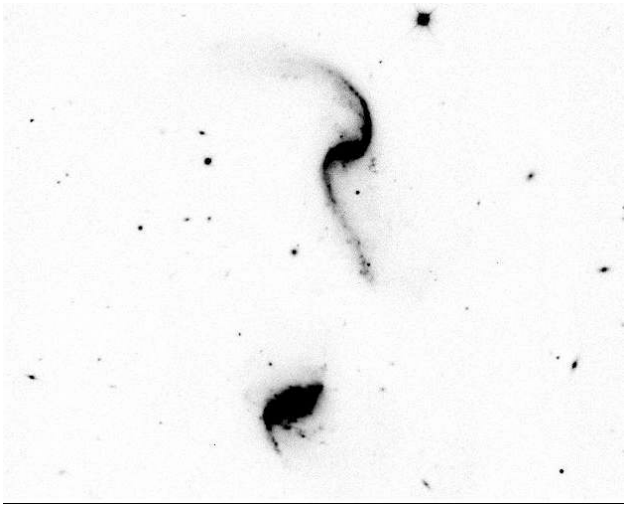

Figure 4.31: HAWK-I K-band image of the galaxy MCG -02-01-051/2, a double interacting galaxies in an early phase of merging.

regions of Arp 256N. A strong radio source also overlaps the bulge of Arp 256S. Weaker continuum emission is detected in the direction of Arp 256N, with the peak over the northern major spiral arm and a weaker peak over the southern major spiral arm. All these features corroborates the high level of activity in the southern source, implies the presence of a star -forming regions or AGN in Arp 256S. Actually, Veilleux et al. (1995) (Veilleux et al., 1995) find, via optical spectra, that both of the galaxies in Arp 256 are HII region-like, not powered by an AGN. From this discussion we can say that both the galaxies are starburst, with the major activity in Arp 256S. On the other hand, from the radio continuum map is clear that $\sim 75\%$ of the emission is from the southern source. Moreover, the lack of CO emission could imply that Arp 256N has little star formation activity. From other work, the H_α-band images of Arp 256N clearly show a peak of emission in the northern arm but not in its nucleus or in the southern arm. This is consistent with the location of SN 2010hp, with an offset of about 3" from the nucleus, at the beginning of the northern spiral arm of Arp 256N, within the main star forming region of Arp 256N.

4.6.5 SN 2011ee in NGC 7674

We discovered SN 2011ee on 2011 June 27.34 UT in the spiral galaxy NGC7674 (Miluzio et al., 2011). The supernova is located at R.A. = 23h27m57s.341, Decl. = +08d46'38".10 (equinox 2000.0) which is 9".3 east and 6".3 south of the center of NGC 7674. In figure 4.33 are shown the HAWK-I discovery image and the two other epochs in which the SN was detectable. Nothing is visible at this position on a K-band image taken on 2010 Sept. 7.14 (the

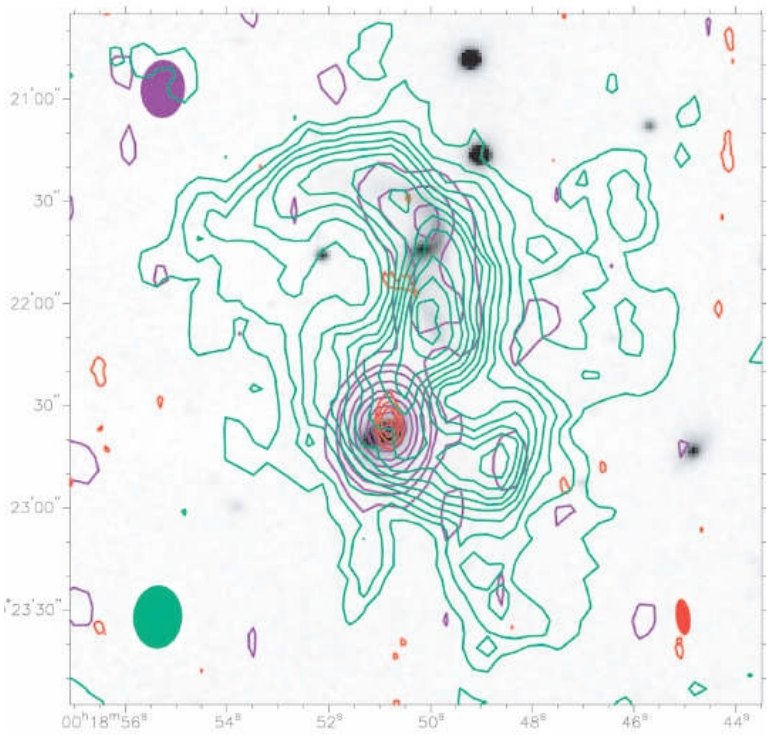

Figure 4.32: Zero-moment HI, CO, and radio continuum maps in contours over an optical image. The H i emission is marked by the green contours and beam size indicator. The blue contours mark the radio continuum image. The CO emission is given in red contours.

SN	Telescope	Date	Fiter	mag
2011ee	HAWK-I	Jun,27 2011	K	18.6(0.2)
	Liverpool	July,10 2011	R	18.5(0.1)
	X-Shooter	July,17 2011	UVB,VIS,NIR	
	HAWK-I	July,29 2011	K	18.4(0.1)
	HAWK-I	Aug,3 2011	K	18.5(0.1)
	HAWK-I	aug,23 2011	K	19.2(0.1)
	EFOSC	Sep,4 2011	B	21.11(0.05)
			V	20.54(0.03)
			R	19.99(0.03)
			I	19.75(0.03)

Table 4.11: Optical and NIR photometry/spectroscopy of the SN 2011ee obtained at the HAWK-I, X-Shooter, Liverpool and NTT telescopes. In the last column there are the apparent magnitude. In red the row referred to the discovery image.

image on the top left in figure 4.33). In the table 4.11 are reported the photometric/spectroscopic observations of the SN 2011ee, obtained with the HAWK-I@VLT, X-Shooter@VLT, the NTT telescope and with the Liverpool telescope, with the corresponding estimate of the magnitude.
An optical spectrum was obtained by Miluzio et al. with the Very Large Telescope (+ XShooter) at Paranal (ESO) on 2011 July 17.25 UT (range 340-1000 nm, resolution 0.02 nm) showing that the 2011ee is a type-Ic supernova. The GELATO code (Harutyunyan et al. 2008, (Harutyunyan et al., 2008) available at website URL https://gelato.tng.iac.es/login.cgi) gives a best match with typical type-Ic supernova at a mean phase of about 10 days after maximum (see figure 4.36).

In figure 4.34 are shown the near infrared and optical absolute light curves of the SN 2011ee compared to the absolute light curves of the type Ic SN 2007gr. SN 2007gr best is a broad-lined ("hypernova") type Ic SN 2002ap at early times, peaking with a B band magnitude of $M_B = -16.8$. The light curve comparison shows that our first NIR observation of the SN 2011ee is just few days before the maximum, while the first R-band observation is around maximum, fully consistent with the spectrum. In figure 4.35 we can see that SN2011ee is no reddened, compared to the color of the 2007gr.

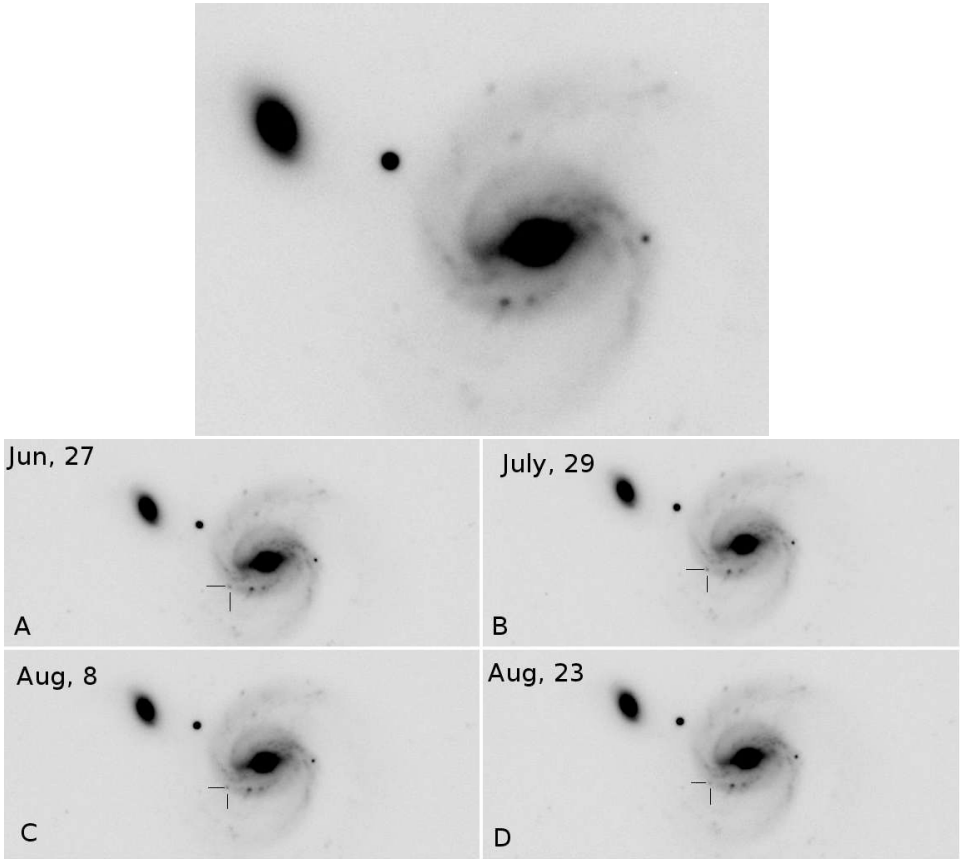

Figure 4.33: K-band HAWK-I images of the galaxy NGC7674 with the SN 2011ee. The top image is the "pre-explosion" image taken on 2010, Sept. 7 when the SN is not present, while the other 4 images (A,B,C,D) are taken in 2011, Jun, July, August and September. The image taken on 2011, Jun 27 is the discovery image (CBET2773).

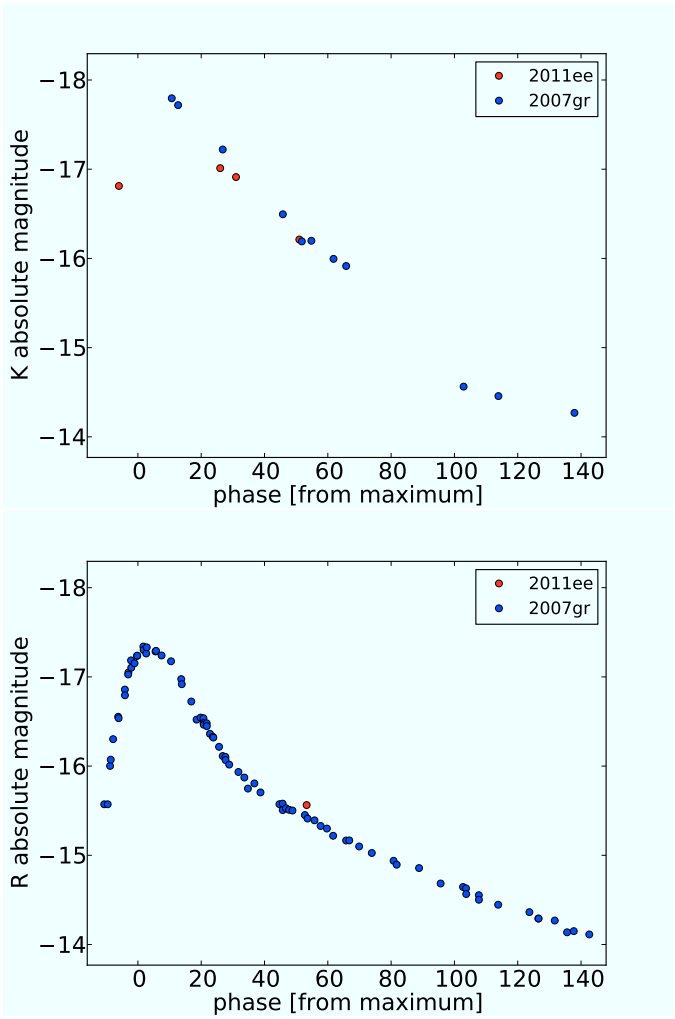

Figure 4.34: *Top:* Near Infrared light curve of the SN 2011ee from the HAWK-I data, superimposed on the curve of the SN 2007gr, a type Ic SN. Is clear from the comparison that the SN 2011ee is a type Ic SN observed few days before the maximum. *Bottom:* The same in the optical (R-band). In this case the first observations is around the maximum.

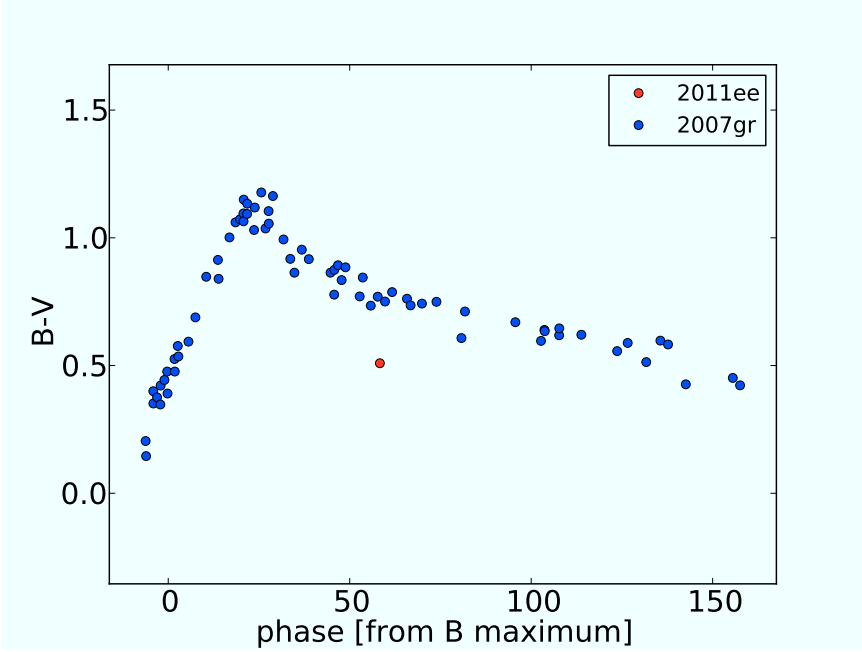

Figure 4.35: B-V color vs phase from the B maximum. Is clear that the SN 2011ee, from the comaprison with the SN 2007gr, is in practice no reddened.

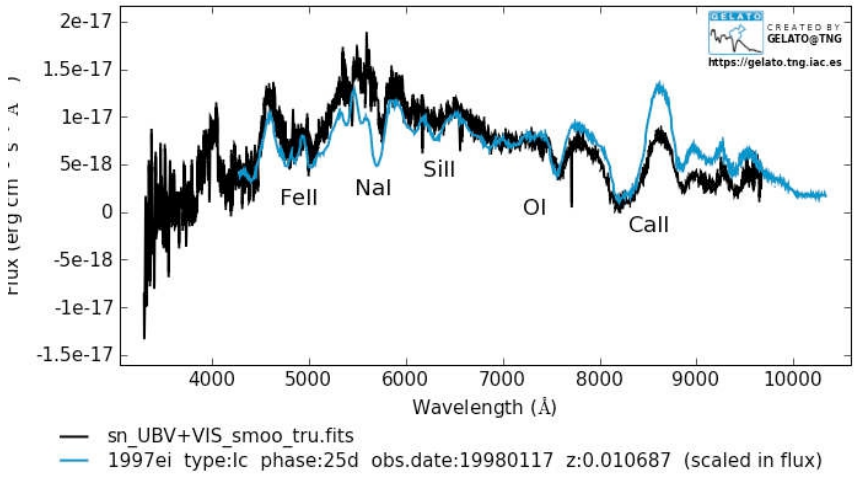

Figure 4.36: UVB+VIS spectrum of SN 2011ee matched with the spectrum of type Ic SN 1997ei (with the GELATO code) about 25 days after the maximum.

Parameter	Value
Redshift	0.029
$Log(L_{FIR}/L_{\odot})$	11.22
SFR ($M_{\odot}yr^{-1}$)	39.99
SN rate ($SNyr^{-1}$)	0.47

Table 4.12: Observing parameters of galaxy NGc 7674.

The host galaxy NGC7674

NGC 7674 (Fig. 4.37) is a type 2 Seyfert galaxy at a distance of about 115 Mpc which is classified as Sbc pec.
This galaxy has an infrared luminosity of $L_{IR} \sim 10^{11.22} L_{\odot}$ and it is the brightest member of the well-isolated Hickson 96 (H96) compact galaxy group, which consists of four interacting galaxies with a mean heliocentric velocity of 8760 kms^{-1} and a low velocity dispersion ($\sigma_V \sim 160 kms^{-1}$). The two largest members in this group, NGC 7674 (H96a) and NGC 7675 (H96b), are separated by a projected distance of 2'.2. The nuclear regions of NGC 7674 seems to be powered by an active galactic nucleus. The observed features in NGC 7674, as revealed in optical images, can be accounted for by tidal interactions with its companion galaxies in the group (Momjian et al., 2003). SN 2011ee is located in the eastern part of the galaxy, at the beginning of the spiral arm where is stronger the influence of the near companion H96c (H96b is further away with H96d).

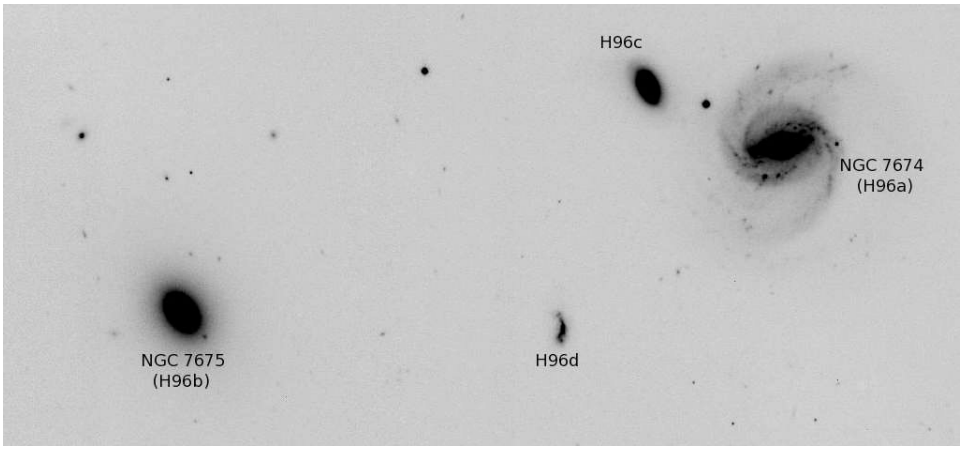

Figure 4.37: HAWK-I K-band image of Hickinson compact group 96. The brighest member of the group is the starburst galaxy NGC 7674 .

Parameter	Value
Redshift	0.017
$Log(L_{FIR}/L_{\odot})$	11.39
SFR ($M_{\odot}yr^{-1}$)	47.29
SN rate ($SNyr^{-1}$)	0.55

Table 4.13: Observing parameters of galaxy IC 4687.

SN	Telescope	Date	Fiter	mag
	HAWK-I	May,21 2010	K	17.95(0.1)
2010 in IC 4687	HAWK-I	Jun,16 2010	K	17.86(0.1)
	HAWK-I	June.28 2010	K	>17.7

Table 4.14: NIR photometry of the possible supernova in IC 4687/6 obtained with the HAWK-I telescope. In the last column there are the apparent magnitude. In red the row referred to the discovery image.

4.6.6 Possible Supernovae in IC 1623A/B and IC 4687/6

For these two possible supernova candidates it was impossible to obtain a spectroscopic classification due to their faintness. we have to rely on the light curve in order to confirm the candidate and assign a SN type.

PSN in NGC IC4687/6

Supernova in IC 4687/6 was discovered on 2010 May 21.34 UT in the galaxies pair IC4687/6. The transient is located at R.A. = 18h13m40s.213, Decl. = -57°43'28".0 (equinox 2000.0) which is 2".6 east and 2".8 north of the center of IC 4687. IC 4687 forms a triplet with two other galaxies: IC 4686, near IC 4687 (the galaxy at the top) and IC 4689, the galaxy at the bottom of the figure 4.38. IC 4687 has a chaotic body of stars, gas and dust and a large curly tail to the left. The two companions are partially obscured by dark bands of dust. The interacting triplet is 69.6 Mpc away from Earth, in the constellation of Pavo, the Peacock, at redshift of 0.017 and with $Log(L_{FIR}/L_{\odot} \sim 11.39$ (in the table 4.13 some observational data about IC 4687).
In figure 4.39 are shown the HAWK-I discovery image and the three other epochs in which the SN was detectable. Nothing is visible at this position on a K-band image taken on 2009 Aug. 8.14 (the image A on the top left in figure 4.39). In the table 4.14 are reported the estimated magnitudes.
An optical spectrum was obtained with the Very Large Telescope (ISAAC) at Paranal (ESO) at the end of May (2010) but it turned out to be useless to the low S/N.

The only way to classify this possible supernova is to compare the light

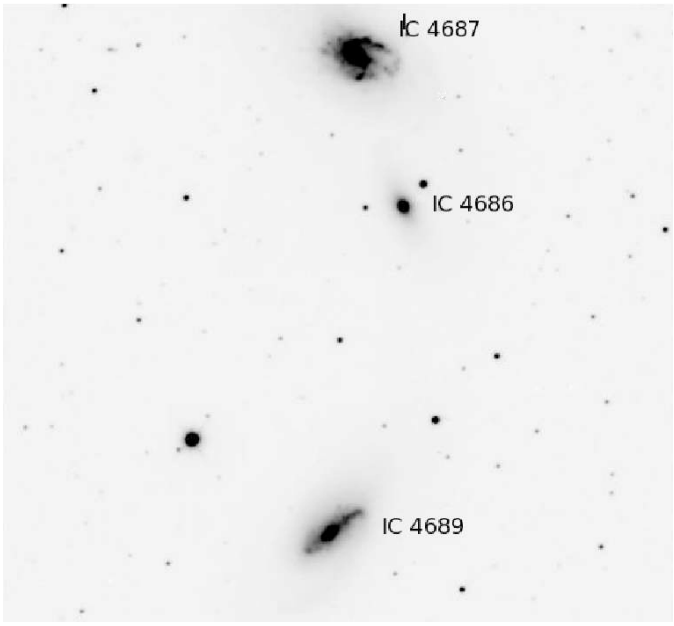

Figure 4.38: K-band HAWK-I images of the galaxies triplet with IC 4687 (top), Ic 4686 (in the middle) and Ic 4689 (bottom).

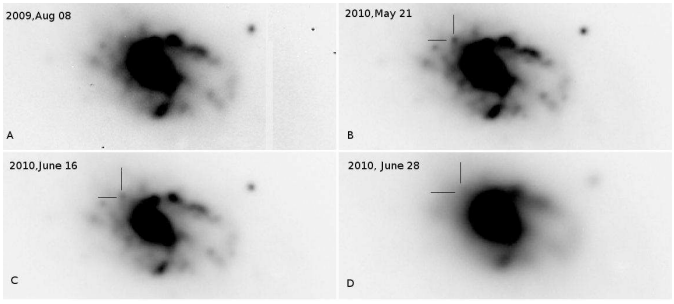

Figure 4.39: K-band HAWK-I images of the galaxy IC 4687 with the possible supernova. The top left image A is the "pre-explosion" image taken on 2009, Aug. 8 when the SN is not present, while the other 3 images (B,C,D) are taken in 2010, May and june.

curves with light curves of known supernovae. For this event we have only two K band measurements, so it's not so easy to constrain the absolute light curve. However, these measures, and available upper limits, translated in absolute magnitudes which are best matched with the light curve of SN 2005cs (e.g. Pastorello et al. 2009 (Pastorello et al., 2009)) and therefore the SN is assumed of type II (figure 4.40). SN 2005cs is an underluminous type IIP SN, more than a magnitude fainter than the mean IIP luminosity.
Unfortunately, it's no possible to give an estimate of the extinction of the host galaxy because no color curves are available for this object.

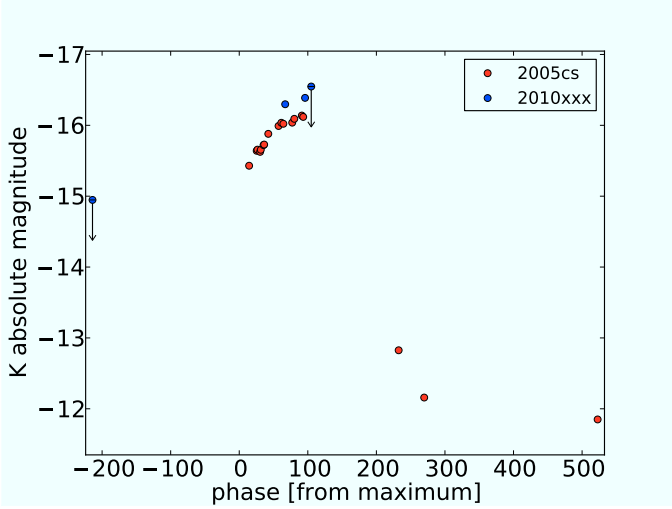

Figure 4.40: Near Infrared light curve of the possible supernova from the HAWK-I data, superimposed on the curve of the SN 2005cs, a type II SN. We have only two K band measurements available. These measures, and available upper limits, translated in absolute magnitudes which are best matched with the light curve of SN 2005cs and therefore the SN is assumed of type II.

PSN in IC 1623

The Supernova in IC 1623 (PSN J01074624-1730296) was discovered on 2011 07 21.36UT in the galaxy IC1623. The PSN is located at R.A. =01h07m46s.24 Decl. =-17d30'29".60 (equinox 2000.0) which is 3".6 east and 6".9 south of the center of IC 1623. .
In figure 4.41 are shown the HAWK-I discovery image and the two other epochs in wihich the SN was detectable. Nothing is visible at this position on a K-band image taken on 2010 Aug. 8 (the image A on the top left in figure 4.41). In the table 4.15 are reported the photometric observations of the PSN, obtained with HAWK-I@VLT, the NTT telescope and TNG, with the corresponding estimated magnitudes.

SN	Telescope	Date	Fiter	mag
PSN in IC1623	HAWK-I	July,21 2011	K	18.15(0.2)
	TNG	Aug,1 2011	V	>19.3
			R	19.5(0.2)
			I	19.0(0.2)
	HAWK-I	Aug,23 2011	K	18.72(0.2)
	NTT	Sep,4 2011	B	>21.3
			V	>20.0
			R	20.1(0.3)
			I	19.5(0.3)
	HAWK-I	Sep.8 2011	K	19.43(0.2)

Table 4.15: NIR/optical photometry of the possible supernova in IC 1623. In the last column there are the apparent magnitude. In red the row referred to the discovery image.

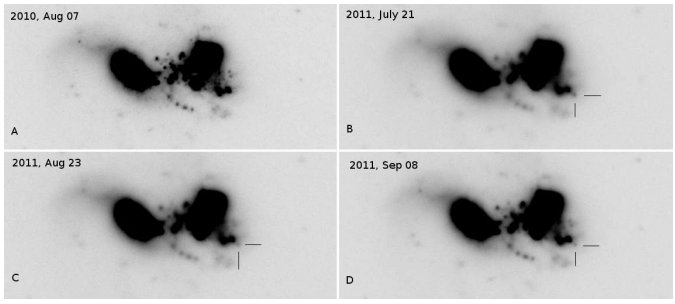

Figure 4.41: K-band HAWK-I images of the galaxy IC 1623 with the possible supernova. The top left image A is the "pre-explosion" image taken on 2010, Aug. 8 when the SN is not present, while the other 3 images (B,C,D) are taken in 2011, july. august and Septepmber.

To confirm and classify this transient we rely on the comparison of the light curves with light curves of known supernovae. In this case we have more measurements, so the photometric classification is easier. We found that the infrared and optical photometry of the transient in IC 1623 are best fit to the classical type IIP SN 1999em. The light curves of SN 1999em peak at a V band magnitude of $M_B = -15.76$, and the plateau phase lasts about 80 days, after which the light curve displays a steep decline ($\sim$2 mag in $\sim$40 d for the V-band), signalling the onset of the nebular phase and the start of the exponential decline (Elmhamdi et al., 2003),(Pooley et al., 2002).
From the comparison in figure 4.42, we can argued that the PSN is a type II SN discovered about 100 days after his maximum. The figure 4.43 shows

the color curve $(R-I)$, from which we can see that this PSN suffers little if any extinction in the host galaxy.

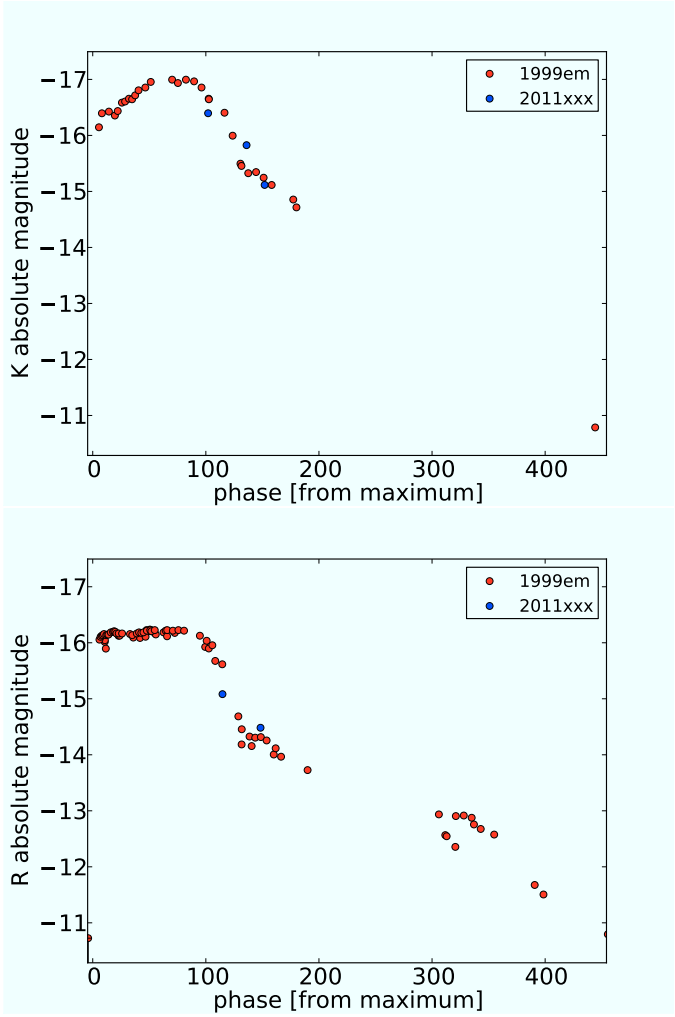

Figure 4.42: Near Infrared and optical light curves of the possible supernova in IC 1623, superimposed on the curve of the 1999em, a type II SN.

IC1623 (= VV114 = Arp 236), located at a distance of 80 Mpc, is an interacting systems undergoing vigorous starburst activity. Its infrared luminosity is $L_{IR} = 10^{11.5} L_{\odot}$ making it a LIRG and one of the brightest objects of the IRAS Bright Galaxy Sample. It appears to be an early-stage merger of two galaxies (see 4.16) that are aligned east-west with a projected nuclear separation of ∼6 kpc and referred in the literature as VV114E and VV114W. VV114 contains a large amount of dust ($M_{dust} = 1.2 \times 10^{8} M_{\odot}$) distributed across the galaxy with a dust temperature of 20-25 K. About half

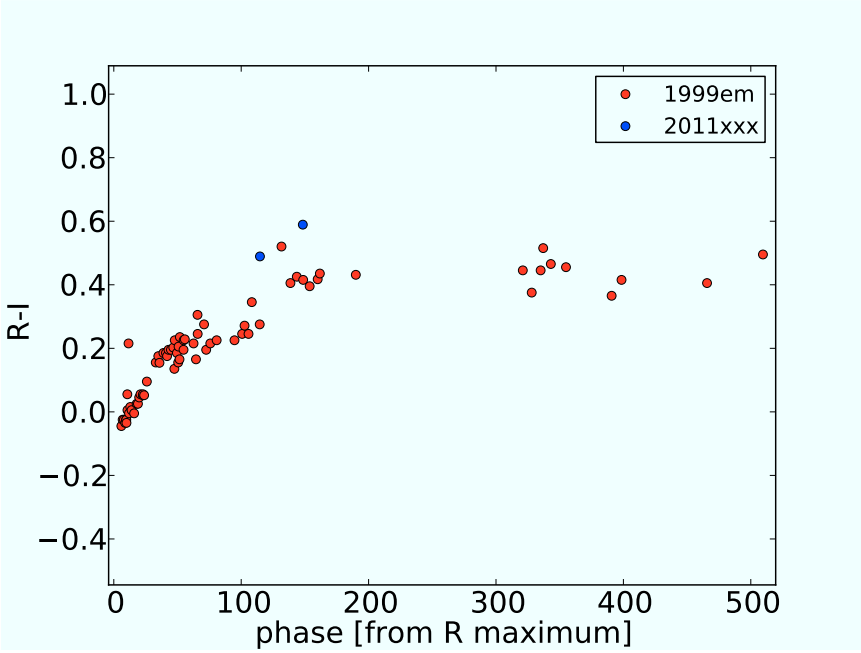

Figure 4.43: R-I color vs phase from the B maximum. Is clear that the PSN in IC 1623, from the comaprison with the SN 1999em, is in practice no reddened.

of the warmer dust traced in the mid- IR (MIR) is associated with VV 114E, where both compact (nuclear region) and extended emission are found ((Le Floc'h et al., 2002). The MIR spectrum also shows a sign of an AGN in VV 114E ((Le Floc'h et al., 2002)). Alonso-Herrero et al. (2002)((Alonso-Herrero et al., 2002)) detected abundant Hii regions in VV 114E and in the overlap region using the narrow band Paα images. Scoville et al. (2000) ((Scoville et al., 2000)) imaged the near-IR (NIR) emission using the Near- Infrared Camera and Multi-Object Spectrometer on board the Hubble Space Telescope and found that the highly optically obscured VV 114E is the brighter of the two in the NIR. Far-UV imaging using the Space Telescope Imaging Spectrograph found several hundred young star clusters in VV 114W, while no UV emission was found in VV 114E ((Goldader et al., 2002)), which suggests that most of the activity in VV 114E is obscured by dust and not visible in the UV emission.
Finally, nearly 65% of the MIR emission associated with the eastern component VV 114E, originate from the central 1kpc region. The MIR emission from the western component is more diffuse and does not peak in its nucleus. Rather, it displays a local maximum in a near HII region located in the overlap area of VV 114E and VV 114W. A large number of young star clusters and compact HII regions were also detected in the NIR throughout the same area, indicating a massive extranuclear star formation activity. This is interesting because the possible supernova was found very close to a probably HII region, confirming the extranuclear star formation activity around VV 114W.

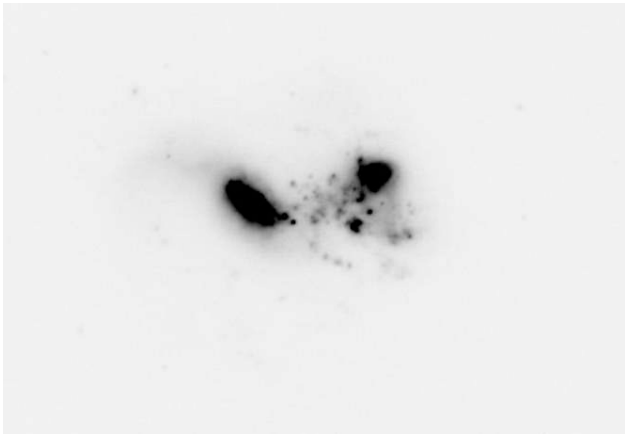

Figure 4.44: HAWK-I K-band image of the galaxy IC 1623 (VGV 114). Are clearly visible two nuclei with numerous other compact regions where the emission in the NIR is important.

Parameter	Value
Redshift	0.020
$Log(L_{FIR}/L_{\odot})$	11.50
SFR ($M_{\odot}yr^{-1}$)	72.68
SN rate ($SNyr^{-1}$)	0.86

Table 4.16: Observing parameters of galaxy IC 1623.

Chapter 5

Expected SN rate

Because of the small number of detected events it is not viable to derive direct statistical measurements of the rates of SNe in starburst galaxies. We use instead a MonteCarlo approach were we compute the number and properties of expected events based on adopted physical parameters and simulating the random chances of explosion and detection. By collecting a number of MonteCarlo experiments with the same input parameters we can test whether the observed events are within the expected distribution. If not we can vary the input parameters of the simulation and repeat the test until we found a satisfactory agreement.

It the following we first illustrate the simulation tool flow chart and the choice of the input parameters and in subsequent sections we analyze in detail the main input of the simulation.

5.1 Simulation tool

The MonteCarlo simulation tools was built in the Python environment. Inputs of the simulation are:

- the sample galaxy catalog including for each galaxy the following data: redshift, galactic extinction, infrared fluxes at 60 and 100 μ, B magnitude corrected for internal extinction, Hubble type [1].
- information describing the SN properties for each of the SN types considered here that are type Ia and, for core collapse, types IIP, IIL, IIn and Ib/c. The SN properties are described by light curves, luminosity functions, K-corrections and relative rates of the different core collapses subtypes.
- details of the search campaign, namely: log of observations, detection limit for each observation as a function of the position of the transient

[1] http://ned.ipac.caltech.edu/

inside the parent galaxy

- the adopted cosmological parameters: $\Omega_M = 0.3$ and $\Omega_\lambda = 0.7$

In addition there are a number of test parameters that are allowed to change for different simulation runs. These are:

- the number of SNe expected from a given star formation episode. For core collapse SNe this is determined only by the adopted mass range of the progenitors. In fact, for our purposes we ignore the very short time delay from star formation to explosion. For type Ia we need to consider the realization factor, that is the fraction of events in the proper mass range which occurs in suitable close binary systems.

- the adopted absorption depth and distribution inside the parent galaxies

- the adopted star formation distribution inside the parent galaxies

The simulation proceeds with the following operations for each individual galaxy:

- from IRAS 60 and 100 μ fluxes we derive the total infrared luminosity (TIR) and hereafter, adopting a proper conversion factor, the star formation rate (SFR).

- we then compute the expected number of SNe per year. Core collapse are sub-divided in different subtypes based on the observed distribution from optical SN searches (see next subsection)

- a time interval is chosen so that 100 SNe are expected to explode in the given galaxy and period. The time interval terminates with the last observations of the given galaxy and, given the expected SN rates is, for all galaxies much longer than the duration of our monitoring campaign. The reason to simulate 100 events is to avoid having to deal with fractional SN numbers for the different subtypes. Hereafter the epoch of explosion of each events is randomly chosen within the defined time interval.

- for each of the simulated SNe:

  we assigned a random absolute magnitude with the average value appropriate for the given subtype and adopted SN luminosity function.

  a random explosion site is chosen inside the parent galaxy. The random distribution is not uniform but follows the adopted star formation spatial distribution for the given galaxy.

an extinction value is assigned to the SN. This is extracted random from an adopted gaussian distribution with an average values that depends on the position of the simulated SN inside the parent galaxy and sigma equal to 1/3 of the average value.

5.2 From IRAS measurements to Star Formation Rate

The SFR in a starbursting region can be estimated on the basis of the FIR luminosity (defined as the flux between 42 and 122 μm, e.g Magnelli et al. (2010)), under the assumption that dust reradiates the overall bolometric luminosity and after calibration with stellar synthesis models. It is the most commonly quoted infrared flux, and quite often it is used as an indicator of the total level of activity in the interstellar medium.
Star formation rate is derived from L_{TIR}. Helou et al. (1988) provide a useful way of deriving the far-infrared flux from IRAS measurements:

$$FIR = 1.26 \times 10^{-14} \left[2.58\, f_\nu(60\mu m) + f_\nu(100\mu m)\right]$$

where FIR is in W m^{-2} ($= 10^3\ erg\, cm^{-2}\, s^{-1}$) and $f\nu$ are in Jansky.

Dale et al. (2001), with their SED model, derive infrared bolometric correction, for a given redshift as a function of the observed (redshifted) $f_\nu(60\mu m)/f_\nu(100\mu m)$ ratio, for the purpose of converting observed far-infrared fluxes to the total infrared luminosity. The total far infrared flux, TIR, results from:

$$\log \frac{TIR}{FIR} = a_0 + a_1 x + a_2 x^2 + a_3 x^3 + a_4 x^4$$

where $x = \log \frac{f_\nu(60\mu m)}{f_\nu(100\mu m)}$ and $[a(z=0)] \simeq [0.2378, -0.0282, 0.7281, 0.6208, 0.9118]$

Knowing the distance D, one can derive the luminosity:

$$L_{TIR} = 4\pi D^2\, TIR$$

Kennicutt et al. (1998) derive the relation of the SFR with the total L_{TIR}, adopting the mean luminosity for 10-100 Myr continuous bursts, solar abundances, and the Salpeter IMF and assuming that the dust reradiates all of the bolometric luminosity:

$$\frac{SFR}{1\, M_\odot\, yr^{-1}} = \frac{L_{TIR}}{2.2 \times 10^{43}\ \ [erg\, s^{-1}]} = \frac{L_{TIR}}{5.8 \times 10^{9}\ \ [L_\odot]}$$

5.3 SFR vs. SNR relation

To derive the SN rate is important to define two crucial parameters: the number of SNe per unit mass from one stellar generation, or SN productivity

(k_{SN}), and the distribution of the delay times (f_{SN}), the delay time (t_D) being the age of the progenitor star at explosion. These parameters control the rate at which SNe occur in a stellar population: at an epoch t since the beginning of star formation, the rate of SNe is obtained by summing the contribution of all past stellar generations, each weighted with the star formation rate (ψ) at the appropriate time:

$$\dot{n}_{SN}(t) = \int_0^t \psi(t - t_D) k_{SN} f_{SN}(t_D) dt_d. \tag{5.1}$$

for an instantaneous burst in which $\mathcal{M}$ solar masses of stars are formed. Eq. 5.1 becomes

$$\dot{n}_{SN}(t) = \mathcal{M} k_{SN} f_{SN}(t_D = t),$$

which shows that the SN rate following an instantaneous burst of star formation is proportional to the t_D through the product of the total mass of formed stars and the SN productivity.

5.3.1 Core Collapse SNe

For core collapse SNe the delay time from formation to explosion is short (from 2.5 My for star of 120 $M_\odot$ to 40 My for stars of 8 $M_\odot$).

Assuming that star formation have been constant for the last 40 My the expected CC SN rate $\dot{n}_{CC}$ is proportional to the ongoing SFR:

$$\dot{n}_{CC} = k_{CC} \times \psi \tag{5.2}$$

where $\psi = SFR$ and

$$k_{CC} = \frac{\int_{M_{CC,l}}^{M_{CC,u}} \phi(m) dm}{\int_{M_l}^{M_u} m \phi(m) dm}$$

where $M_{CC,u}$ and $M_{CC,l}$ are respectively the maximum and minimum stellar mass which give rise to a CC SN event and $\phi(m)$ is the initial mass function (IMF). This shows that the rate depends strongly on the IMF: flatter IMFs provide higher CC SN rate; for a salpeter-diet IMF, in a galaxy forming stars at a constant rate of $1 M_\odot/yr$, after the first $\sim$ 40 Myr from the beginning of SF one gets 1 CC event per century. For a universal IMF we thus expect that CC SN rate is basically proportional to the current SFR in all galaxies which have been forming stars since $\sim$ 40 Myr ago. For the *reference case* we assume a diet IMF, that is:

$$\begin{aligned} &\phi(m) \propto m^{-\alpha} \\ &\qquad \text{with} \quad \alpha = 1.3 \quad \text{for} \quad 0.1 < m < 0.5 M_\odot \\ &\qquad\qquad\ \ \alpha = 2.35 \quad \text{for} \quad 0.5 < m < 100 M_\odot \end{aligned}$$

The upper limit of CC SN progenitor is not well constrained. However, given the low number of massive stars k_{CC} is little influenced by the actual choice. We adopt $M_{CC,u} = 40 M_{\odot}$. More important is instead the lower limit of CC SN progenitor mass, the productivity decreasing by a factor of $\simeq 0.7$ if $M_{CC,l}$ goes from 8 to 10 $M_{\odot}$ for a Salpeter diet IMF. We adopt the value derived from direct detection and measurement of SN precursors: $M_{CC,u} = 8 M_{\odot}$ Smartt (2009).
With this assumption $k_{CC} = 0.0107\, M_{\odot}^{-1}$ (for a plain Salpeter IMF $k_{CC} = 0.00676$) *(cf. macro service.py)*

5.3.2 SN Ia

Because of the long delay time, the expected number of SN Ia strongly depends on the SFR history of the stellar population (and on the adopted SN progenitor scenarios). If the SN Ia productivity is constant in time we can write

$$\dot{n}_{Ia}(t) = k_{Ia} \mathcal{M}(t) \langle f_{Ia} \rangle_{\psi(t)},$$

where $)\langle f_{Ia} \rangle_{\psi(t)}$ is the average of the delay times weighted with the age distribution of the stellar population, or the SFH, and $\mathcal{M}$ is the total mass turned into stars upo to the epoch t. The total number of SNe from star formed in one stellar generation is $k_{Ia} = 2.5 \times 10^{-3}\, M_{\odot}^{-1}$ Greggio & Renzini (2011), that is, 2.5 SN Ia every 1000 $M_{\odot}$ of stars formed in one stellar generation. This means that from one stellar generation CC SNe outnumber SN Ia by a factor ~ 4.

In normal galaxies at any given time the $\dot{n}_{CC}/\dot{n}_{Ia}$ ratio is significantly lower and, depending on the star formation history, range from 0 for passive galaxies to $\sim$ 6 in average Scd galaxies ((SNII+SNIbc)/SNIa) (Li et al., 2011), as showed in the fig. 5.3.2. In fact, it is generally accepted that early-type galaxies (E/S0) are predominantly made of old stellar populations, while late-type galaxies (Sc/Scd) consist of mostly young stellar populations. The galaxies of our sample are all actively star forming and their current SFR is likely significantly higher than the average star forming galaxy. We take as reference a value of $\dot{n}_{CC}/\dot{n}_{Ia} = 10$.

5.4 Exctinction

Maximum extinction is taken as for the nucleus of Arp 220 from the work of Shioya et al. (2001). They construct a starburst model for the hidden starburst in Arp 220, assuming a model with continuus star formation and solar metallicity for the central regions of galaxies. They then compute the visual extinction necessary to hide the hidden starbursts. In Arp 220 there are two concentrations of thermal dust emission with which the hidden starbursts are associated. They find that A_V must be larger than 30 mag for

Figure 5.1: SN rates in average galaxies of different Hubble types (Li et al., 2011).

Hub.	SN	SNuB[b]	N_B^c	SNuK[b]	N_K^c	SNuM[b]	N_M^c
E	SN Ia	$0.243^{+0.048}_{-0.041}(0.038)$	35.0	$0.041^{+0.008}_{-0.007}(0.006)$	33.0	$0.051^{+0.010}_{-0.009}(0.008)$	33.0
S0	SN Ia	$0.253^{+0.038}_{-0.034}(0.057)$	56.0	$0.044^{+0.007}_{-0.006}(0.010)$	54.0	$0.056^{+0.009}_{-0.008}(0.013)$	54.0
Sab	SN Ia	$0.242^{+0.042}_{-0.036}(0.039)$	44.3	$0.059^{+0.010}_{-0.009}(0.010)$	43.3	$0.089^{+0.016}_{-0.013}(0.015)$	43.3
Sb	SN Ia	$0.184^{+0.030}_{-0.026}(0.036)$	50.2	$0.058^{+0.009}_{-0.008}(0.011)$	50.2	$0.095^{+0.016}_{-0.014}(0.018)$	49.2
Sbc	SN Ia	$0.166^{+0.032}_{-0.027}(0.029)$	36.6	$0.060^{+0.012}_{-0.010}(0.010)$	34.6	$0.112^{+0.023}_{-0.019}(0.018)$	34.6
Sc	SN Ia	$0.175^{+0.037}_{-0.031}(0.027)$	32.0	$0.073^{+0.015}_{-0.013}(0.012)$	32.0	$0.138^{+0.029}_{-0.024}(0.022)$	32.0
Scd	SN Ia	$0.161^{+0.041}_{-0.033}(0.043)$	23.0	$0.084^{+0.022}_{-0.018}(0.019)$	22.0	$0.174^{+0.045}_{-0.037}(0.038)$	22.0
Irr	SN Ia	$0.000^{+0.109}_{-0.000}(-)$	0.0	$0.000^{+0.048}_{-0.000}(-)$	0.0	$0.000^{+0.069}_{-0.000}(-)$	0.0
E	SN Ibc	$0.015^{+0.034}_{-0.012}(0.007)$	1.0	$0.003^{+0.006}_{-0.002}(0.001)$	1.0	$0.004^{+0.008}_{-0.003}(0.002)$	1.0
S0	SN Ibc	$0.036^{+0.028}_{-0.017}(0.010)$	4.0	$0.007^{+0.005}_{-0.003}(0.002)$	4.0	$0.009^{+0.007}_{-0.004}(0.003)$	4.0
Sab	SN Ibc	$0.224^{+0.065}_{-0.052}(0.072)$	18.5	$0.056^{+0.016}_{-0.013}(0.018)$	18.5	$0.086^{+0.025}_{-0.020}(0.028)$	18.5
Sb	SN Ibc	$0.206^{+0.056}_{-0.045}(0.065)$	20.5	$0.070^{+0.019}_{-0.015}(0.023)$	21.5	$0.113^{+0.031}_{-0.025}(0.037)$	20.5
Sbc	SN Ibc	$0.234^{+0.062}_{-0.050}(0.071)$	21.3	$0.092^{+0.025}_{-0.020}(0.029)$	21.3	$0.175^{+0.047}_{-0.038}(0.055)$	21.3
Sc	SN Ibc	$0.245^{+0.053}_{-0.045}(0.066)$	30.0	$0.106^{+0.023}_{-0.019}(0.028)$	30.0	$0.206^{+0.045}_{-0.037}(0.055)$	30.0
Scd	SN Ibc	$0.178^{+0.052}_{-0.041}(0.035)$	18.7	$0.097^{+0.029}_{-0.023}(0.021)$	17.7	$0.194^{+0.060}_{-0.047}(0.042)$	16.7
Irr	SN Ibc	$0.316^{+0.249}_{-0.151}(0.068)$	4.0	$0.073^{+0.095}_{-0.047}(0.034)$	2.0	$0.103^{+0.136}_{-0.067}(0.049)$	2.0
E	SN II	$0.000^{+0.014}_{-0.000}(-)$	0.0	$0.000^{+0.003}_{-0.000}(-)$	0.0	$0.000^{+0.003}_{-0.000}(-)$	0.0
S0	SN II	$0.020^{+0.015}_{-0.009}(0.006)$	4.0	$0.004^{+0.003}_{-0.002}(0.001)$	4.0	$0.005^{+0.004}_{-0.002}(0.001)$	4.0
Sab	SN II	$0.266^{+0.047}_{-0.041}(0.098)$	42.2	$0.066^{+0.012}_{-0.010}(0.024)$	42.2	$0.098^{+0.018}_{-0.015}(0.035)$	41.2
Sb	SN II	$0.282^{+0.043}_{-0.037}(0.106)$	56.3	$0.085^{+0.013}_{-0.012}(0.032)$	53.3	$0.144^{+0.023}_{-0.020}(0.055)$	53.3
Sbc	SN II	$0.466^{+0.058}_{-0.052}(0.134)$	80.1	$0.183^{+0.023}_{-0.020}(0.052)$	81.1	$0.335^{+0.042}_{-0.038}(0.098)$	79.1
Sc	SN II	$0.649^{+0.088}_{-0.078}(^{+0.364}_{-0.137})$	69.0	$0.280^{+0.038}_{-0.034}(^{+0.136}_{-0.058})$	68.0	$0.547^{+0.075}_{-0.066}(^{+0.245}_{-0.112})$	68.0
Scd	SN II	$0.695^{+0.097}_{-0.086}(^{+0.386}_{-0.135})$	65.3	$0.364^{+0.055}_{-0.048}(^{+0.176}_{-0.075})$	57.3	$0.767^{+0.116}_{-0.102}(^{+0.342}_{-0.154})$	56.3
Irr	SN II	$0.431^{+0.291}_{-0.186}(0.074)$	5.0	$0.162^{+0.128}_{-0.078}(0.039)$	4.0	$0.230^{+0.181}_{-0.110}(0.054)$	4.0

[a] Uncertainties are ordered as statistical and systematic (in parentheses).
[b] The rate for the average galaxy size.
[c] The number of SNe used in the rate calculation.

the western nucleus and 40 mag for the eastern nucleus Shioya et al. (2001). Other works (Scoville et al. (1998), Genzel et al. (1998)) found similar values for extinction, ranging from 15 to 45 mag. We take as reference value in our simulation $A_V = 30$ mag and we assumed that extinction is scaled with SFR, that is $A_V \propto SFR$. The extinction law in Starburst galaxies is described by the Calzetti law $R_V = 4.05 \pm 0.8$ Calzetti et al. (2000)

5.5 Star Formation distribution

A crucial ingredient to obtain an accurate estimate of the expected SN rate is the spatial distribution of the star fomation in starburst galaxies. This is a strongly debated issue.
From early observations of nearby starburst systems it has been clear that the bulk of the energy of these systems emerges in the thermal infrared. Because dust radiates through thermal emission to the radiation field in which it is embedded, thermal radiation by dust is the ideal way to trace the current location of the dominant luminosity sources, i.e., the most luminous stars, in starbursts. Analysis of the IRAS Bright Galaxy Sample showed that 30% of

the energy output in the local universe emerges in the mid- and far-infrared (5-200μm), and the bulk of this luminosity is due to star formation, as discussed by Kennicutt (1998), the efficacy of the IR luminosity as a tracer of the SFR depends on the contribution of the young stars to the heating of the dust, and requires that all the UV light from massive stars is absorbed by the dust.
The mid-IR luminosities are routinely used to estimate the SFRs of galaxies at cosmological distances (e.g., Elbaz et al. 2002; Le Floc'h et al. 2005). Observationally, the 12 μm luminosity is found to be a good indicator of the total IR luminosity of local galaxies. The advantage of using mid-IR luminosities compared to near-IR as indicators of the SFR is that they are not affected by the contribution from cold dust heated by old stars that may dominate the NIR-IR luminosities. Spitzer observations of nearby normal galaxies are now showing that there is a good correlation between the Paα or Hα luminosity (corrected for extinction) and the 24 μm luminosity of HII knots and HII regions (e.g., M51, Calzetti et al. 2005), indicating that the latter luminosity could also be a good potential SFR tracer.
Our survey is in the near-IR K-band which better traces the stellar mass of a galaxy and not directly the star formation. So, we can use the K-band luminosity as a proxy of the star distribution. But it's fundamental to know the map of the star formation, and we can do this only knowing the distribution of the mid/far infrared luminosity of the galaxies of our sample. In principle one may think to recover this information by analyzing Spitzer mid infrared images of the galaxies, all available in the Spitzer archive. Unfortunately although Spitzer provides highly sensitive imaging of LIRGs, it cannot resolve the sizes of the MIR emitting regions. For these relatively distant galaxies indeed it's very difficult to compare HAWK-I images and Spitzer images due to the large differences in resolution (HAWK-I pixel scale: 0.105 pixel/", Spitzer pixel scale: 1.2 pixel/").
This is illustrated in figure 5.2 where we can see the comparison between the luminosity profile in the HAWK-I images and Spitzer images (shown for 3 different channels of the latter instrument). The narrower profile of the HAWK-I K band luminosity is actually an instrument effect due to the better resolution of the K-band image compared to the resolution of the Spitzer images. In fact, as we will see later, the mid-infrared emission is in general more compact than the overall distribution of near-infrared light. We attempted to find the mid/far infrared relative distribution, the size of the star forming regions and then the star formation distribution in the literature, considering work that make use of other techniques or instrument (for example Gemini/T-reCS mid infrared imaging, Paα or Hα observations ...) but it turned out to be impossible to find detailed information for each galaxy. We then decided to rely on a statistical approach.

Hattori et al. (2004) performed Hα imaging observations of 22 luminous

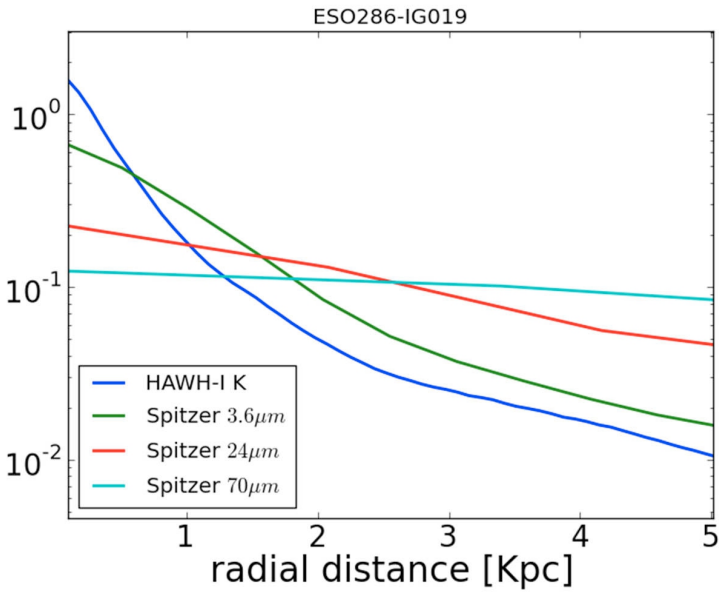

Figure 5.2: Comparison of the luminosity distribution for the different images of the galaxy ESO286-IG019 obtained with HAWK-I telescope and the different channel of the Spitzer telescope.

infrared galaxies to investigate how the distribution of star-forming regions in these galaxies is related to galaxy interactions. The half-light radius of Hα emission is a useful indicator of the size of the star-forming region. Therefore, Hα emission may be used to trace the spatial distribution of star-forming regions within individual galaxies. An advantage of Hα emission is its large range of spatial scales; i.e., it is sensitive to small- ($\sim$1") and large- ($\sim'$1') scale emission, and observations are insensitive to diffuse emission. Based on correlation diagrams between Hα flux and continuum emission for individual galaxies, a sequence for the distribution of star-forming regions was found as follows:*a)* very compact ($\sim$100 pc) nuclear starbursts with almost no star-forming activity in the outer regions (type 1), *b)* dominant nuclear starbursts $\leq$1 kpc in size with a negligible contribution from the outer regions (type 2), *c)* nuclear starbursts $\geq$1 kpc in size with a significant contribution from the outer regions (type 3), and *d* extended starbursts with relatively faint nuclei (type 4). These classes of star-forming regions were found to be correlate withglobal star-forming properties, such as star formation efficiency, far-infrared color, and dust extinction (see Fig. 5.3 and table 5.1). Indeed there is a clear tendency for the objects with more compact distributions of star-forming regions to show a higher star formation efficiency and an hotter far-infrared color. An appreciable fraction of the sample objects were

dominated by extended starbursts (type 4), which is unexpected in the standard scenario of interaction-induced starburst galaxies. Hattori et al (2004) also found that the distribution of star-forming regions was clearly related to galaxy morphology: disturbed objects tend to show a more concentrated distribution of star-forming regions. This suggests that the properties of galaxy interactions, such as dynamical phase and orbital parameters, play a more important role than the internal properties of progenitor galaxies, such as dynamical structure or gas mass fraction.

The conclusions of this work are confirmed by our analysis: we found the

Name	Morphological Class[a]	Type	log (f_{25}/f_{60})	log (f_{60}/f_{100})
NGC 23	S	3	−0.85	−0.23
III Zw 35	C	1	−1.07	−0.06
NGC 695	S	4	−0.97	−0.26
NGC 828	S	4	−1.06	−0.31
NGC 834	S	4	−0.89	−0.27
NGC 877	P	4	−0.92	−0.30
NGC 958	S	4	−0.79	−0.40
UGC 2238	S	3	−1.11	−0.27
NGC 1614	M	2	−0.63	−0.04
NGC 2623	M	1	−1.14	−0.03
Arp 55	C	3	−1.02	−0.19
NGC 3110	P	4	−1.03	−0.30
Arp 148	M	...	−1.27	−0.20
IC 2810	P	3	−0.98	−0.24
NGC 4194	M	2	−0.75	−0.01
UGC 8335	C	2	−0.79	−0.03
NGC 5653	S	4	−0.89	−0.33
Zw 049.057	S	1	−1.35	−0.15
NGC 6090	C	2	−0.71	−0.17
NGC 6621/22	C	3	−0.84	−0.25
NGC 7771	P	3	−0.97	−0.26
Mrk 331	P	2	−0.83	−0.08

[a] M = merger, C = close pair, P = pair, and S = single.
[b] $C_{60\mu} \equiv \alpha_{25\mu,60\mu} - \alpha_{60\mu,100\mu}$.

Figure 5.3: Galaxies sample of Hattori et al. 2004, with some properties of individual objects and some indicators of Hα distribution. For the complete table see Hattori et al. 2004 (Hattori et al., 2004)

same correlation between disturbed objects and concentration of the star for-

Type	$\log(f_{60}/f_{100})$	σ	$\log(f_{25}/f_{60})$	σ	Size of SB(D)
	Mean				(Kpc)
1	-0.081	0.052	-1.191	0.120	D<0.5-1
2	-0.067	0.059	-0.741	0.070	D<1
3	-0.244	0.026	-0.963	0.095	1<D<1.5
4	-0.314	0.043	-0.938	0.076	D>1.5-2 Kpc

Table 5.1: Mean and standard deviation of some of the star-forming properties for each type of object. The last column represent the estimated size of the starburst region.

mationa activity. An important test comes from two earlier works of Soifer et al. (2000, 2001) (Soifer et al., 2000) (Soifer et al., 2001). They reported observations for several infrared-luminous starburst galaxies in the mid-infrared from 8 to 18/25 μm using the Keck telescopes with spatial resolution approaching the diffraction limit. All the galaxies observed show evidence of strong interactions based on optical morphologies. With figure 5.4 (our reworking of the original figures) we can summarize their main conclusions. In the top we show the curves of growth of the 12.5 μm flux as a function of beam radius, compared with those at 2.2 μm and 1.1 (or 1.2) μm for the galaxies in the sample. Figure 5.4 (*top*) shows that for the galaxies where the 12.5 μm images account for the bulk of the total flux of the galaxy, the radius of the region producing 50% of the flux is between 100 pc and $\sim$300 pc, while the equivalent radius at 1.2 and 2.2 μm is between 1 and 2 kpc. Noticeable exceptions to this general trend are VV 114 and NGC 6090, where a substantial fraction ($\sim$60%) of the 12 μm light is not detected in the ground-based observation and is presumably extended, low surface brightness emission distributed all over the galaxies. For both VV 114E and NGC 6090 (the two curves at the top right of figure 5.4) the curves of growth at 2.2 and 12.5 μm are quite similar.
To summarize their conclusions:

- A substantial fraction, usually more than 50%, of the mid-infrared luminosity in these systems is generated in regions ranging in size from $\sim$100 pc to 1 kpc;
- Nuclear starbursts generally dominate the starburst activity in these galaxies;
- In some cases, most notably NGC 6090, substantial infrared luminosity is emitted from extranuclear regions and is more likely associated with the region of physical interaction between two galaxies;
- Mid-infrared emission is much more compact than is near-infrared emission in these galaxies.

This appears to confirm the results of Hattori et al. (2004) since the galaxies of Soifer et al. (2000,2001) are all strong interacting galaxies, some of that in common with the sample of Hattori. The fact that the majority of the galaxies of Soifer et al. have very compact starburst regions is consistent with the fact that severely disturbed objects had a more concentrated distribution of star-forming regions. So not surprising only two galaxies have diffuse mid-infrared emission. Following the paper of Hattori et al. 2004,

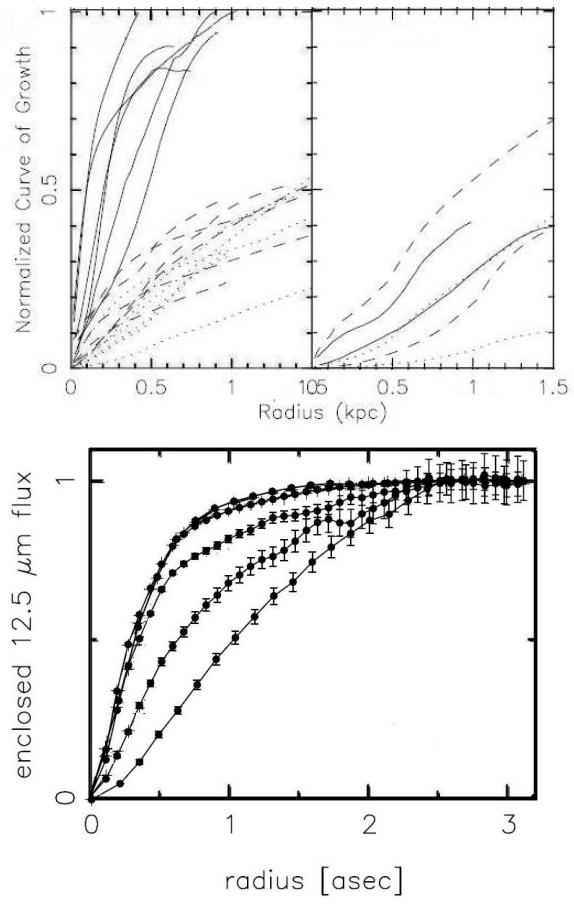

Figure 5.4: *Top*: Montage of the normalized curves of growth for the galaxies in the sample of Soifer et al. (2001) at 12.5 μm (solid line), 2.2 μm (dashed line), and 1.1 μm (or 1.2 km in the case of Mrk 331, dotted line). Curves in the left box represent the following galaxies: NGC1614, NGC2623, NGC3690AB, IC883, Mrk331; curves in the right box represent the galaxies VV114E and NGC6090. *Bottom*: Curves of growth for the following objects: IRAS 05189, IRAS 08572, UGC 5101, Mrk 231 and IRAS 17208.

we can try to estimate the size of the starburst region of the of galaxies of our sample based on the observed morphology and available infrared colors.

The first step is to classify morphologically the sample. Objects with strong tidal features and a single nucleus were classified as "mergers". Paired galaxies with overlapping disks or a connecting bridge were classified as "close pairs", where the projected separation ranges from ∼4 to 20 kpc. Galaxies that have nearby (<100 kpc) companion galaxies at the same redshift but no evident overlap between the primary galaxy and its companion were classified as "pairs". The remaining eight objects were classified as "single". Note that, although the "single" objects do not show strong tidal features, many of them show some distorted /asymmetric appearance. Thus, it is possible that some of the "single" objects are remnants of mergers or have experienced tidal interactions. In table 5.2 the M, C, P, and S represent merger, close pair, pair, and single, respectively. The important point is that this morphological classification appears to correlate with the infrared color, namely the $\log(f_{60}/f_{100})$-$\log(f_{25}/f_{60})$, so we can use these two parameters in order to have an indication of the starburst region size (f_{60}/f_{100} is related to the dust temperature). With this approach we obtained an estimate of the star forming region for all the galaxies of the sample. Since for several galaxies we can find in the literature estimates of the size of the star forming regions, we can immediately test the results obtained for our galaxies sample (last column). We can see that there is a good agreement between literature and our empirical estimates of the size of star forming regions confirming the fact that the size of the nuclear star-forming region increases from type 1 through type 2 and 3. In the type 3 objects there is a substantial contribution from the outer regions to the total Hα flux. The star-forming activity in the type 4 objects is dominated by extended starbursts. Figure 5.5 shows that galaxies with a strong concentration (type 1 and type 2) show the largest values of f60/f100, i.e., the highest dust temperature, whereas galaxies that are dominated by extended starbursts (type 4) show the smallest values, with type 3 lying between the two extremes. Except for type 1, the f25/f60 ratio shows a similar tendency as for f60/f100, although the difference between the types is less clear.

Investigating the relationship between star-forming properties and morphological class of the sample objects we can confirm that more disturbed objects tend to have a more compact distribution of the star-forming region. Although there are exceptions to this rule, this suggest that the degree of dynamical disturbance plays an important role in determining the distribution of star-forming regions. A possible explanation of this trend is that we are looking at an evolutionary sequence: as the merging process advances, star formation becomes more active and develops a more concentrated distribution. In other words, the interaction strength controls the distribution of star-forming regions: the stronger the dynamical disturbance, the more compact the region to which the star-forming activity is confined.

At an early stage of interaction, star formation occurs in both the nuclear and outer regions (type 3). As the process of interaction proceeds, the infall

Galaxy	Morphological Class	Type	$\log(f_{60}/f_{100})$	$\log(f_{25}/f_{60})$	SB size
CGCG011-076	S	3	-0.20	-0.89	
CGCG043-099	S	3	-0.19	-1.05	
ESO148-IG002	CP	2	0.01	-0.82	
ESO239-IG002	M	1	-0.04	-0.79	
ESO244-G012	CP	2	-0.10	-0.68	
ESO264-G036	S	4	-0.34	-0.96	
ESO286-IG019	M	1	0.07	-0.81	<1kpc Johansson 1991
ESO440-IG058	P	3	-0.23	-0.99	
ESO507-G070	S	2	-0.08	-1.21	
IC1623A/B	CP	2	-0.14	-0.80	<1kpc Soifer 2001
IC2545	M	1	0.005	-0.88	
IC2810	P	3	-0.22	-1.0	
IC4687/6	P	3	-0.13	-0.76	Diffuse emission Alonso-Herrero 2006
IRAS12224-0624	S	3	-0.14	-1.48	
IRAS14378-3651	S	2	-0.08	-1.0	
IRAS16399-0937	CP	3	-0.24	-0.87	
IRAS17207-0014	M	1	-0.05	-1.36	
IRAS18090+0130	P	4	-0.31	-0.98	
MCG-02-01-051/2	P	3	-0.14	-0.79	
MCG-03-04-014	S	3	-0.15	-0.91	
NGC0034	M	1	0.004	-0.85	
NGC0232	P	3	-0.23	-0.89	<500pc Iceto 1991
NGC3110	P	4	-0.30	-1.0	
NGC5010	S	4	-0.33	-0.85	
NGC5331	CP	4	-0.29	-1.0	
NGC6240	CP	2	-0.06	-0.81	<1kpc Egami 2006
NGC6926	S	4	-0.31	-0.83	
NGC7130	P	3	-0.19	-0.89	<1.5kpc Levenson 2005
NGC7592	CP	2	-0.12	-0.92	<1.5kpc Hattori 2002
NGC7674	P	3	-0.19	-0.45	

Table 5.2: Morpgological and type classification of the galaxies sample. We remember that: type 1 have compact SB (<500pc), type 2 have nuclear SB (<1kpc), type 3 have SB region >1kpc and type 4 have diffuse emission with extranuclear star formation.

of gas clouds activates nuclear star formation, making it the dominant energy source of the system (type 2). By the final phase, most of the gas clouds have fallen into the nuclear region, and the star-forming activity is confined to the nucleus (type 1). In this process the size of the nuclear star-forming region becomes gradually smaller.
The last information we need is the FIR flux in case of paired systems. In this way we can have all the information to have a good estimate of the size and the location of the star forming region in all the galaxies of our sample. In table 5.3 there are the pairs or close pairs galaxies with the information on the relative emission from each component (where available in literature).

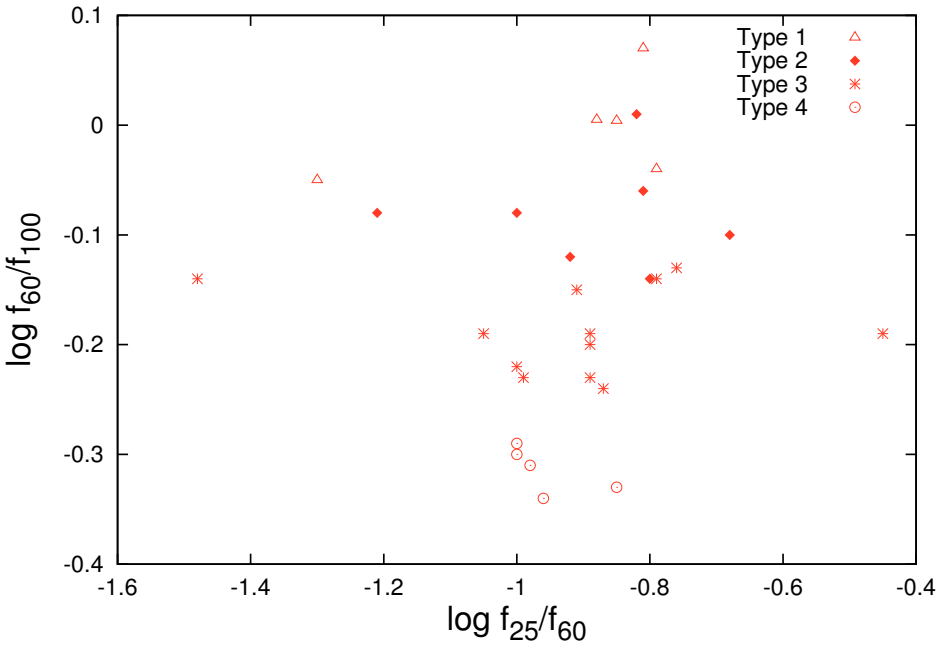

Figure 5.5: Galaxies with a strong concentration (type 1 and 2) show the largest values of f_{60}/f_{100}, i.e., the highest dust temperature, whereas galaxies that are dominated by extended starburst (type 4) show the smallest values, with type 3 lying between the two extremes. The small values of f_{25}/f_{60} in the type 1 objects are also expected to be caused by the compact distribution of nuclear star-forming regions. Therefore, the difference in the distribution of star-forming regions between the types can explain their segregation.

How is distributed the star formation?

As input of the simulation we need to adopt a simple prescription for the SF spatial distribution. We found that a good approximation is to assume

Galaxy	Main nucleus	% of FIR/MIR emission
ESO148-IG002	South	>80%
ESO244-G012	North	>50%
ESO440-IG058		
IC1623A/B	East	>80%
IC2810	Main	100%
IC4687/6		Diffuse
IRAS16399-0937	North	>90%
IRAS18090+0130		
MCG-02-01-051/2	South	>75%
NGC0232		
NGC3110	Main	100%
NGC5331		
NGC6240	South	80/90%
NGC7130	Main	70%
NGC7592	Main	–
NGC7674		

Table 5.3: Infrared luminosities distribution for paired galaxies. "Main nucleus" refers to the dominant galaxy in the pair.

that star formation is distributed as a power of L_K: $SFR \propto L_K^{\alpha}$, where tha value of α is choosen to fit the observed spatial distribution. The figure 5.6 is the same reworking of the figure of Soifer et al. (2001) that we introduced in the previous section. In this case we show that there is a clear difference between the distribution of the mid-infrared and near-infrared luminosity for the galaxies of the types 1-2 and 3-4 (in figure 5.6 we exclude from the plot galaxies that departed from the general trend for a given type). For each galaxies of Soifer et al. (2001) we extrapolate the surface mid/nir brightness as a function of the radius, then we plot on the same figure four different curves corresponding to different value of α: 1.25, 1.5, 1.75, 2.0. The value that best fits the distribution of the mid-infrared is take as reference for that galaxy. In figure 5.7 we show, as an example, these different curves for some galaxies of the different types of the sample of Soifer et al. (2001), with the corresponding value of α for the best fit. In Table 5.4 are shown the values for α for the different types of galaxies.

5.6 Estimate of the SN rate.

Through MonteCarlo simulations we estimated the expected SN rate, based on certain assumptions, in order to obtain a comparison with the observed rate. The main inputs have been discussed in the previous section. Here we compare the expected rate with the observed one for the *reference case*,

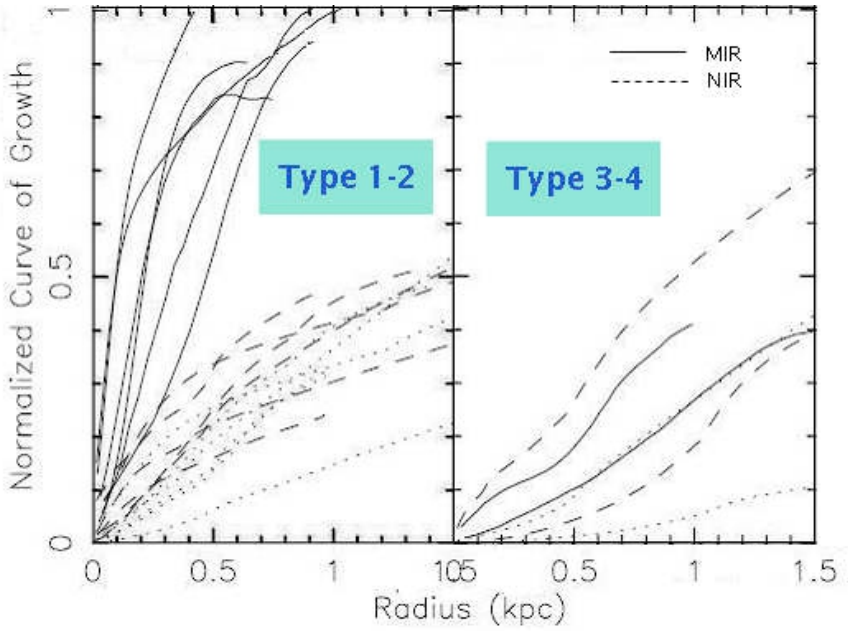

Figure 5.6: The same plot of the figure 5.4, *top*. In this case we show the clear difference of the mid/nir luminosity distribution for the different types of galaxies.

types	α
1	~ 2.0
2	~ 1.5
3	~ 1.25
4	~ 1.0

Table 5.4: Different values of α for the different types of galaxies.

where we used a series of reference values for the simulation. After that we investigate other cases, in which, for example, we consider a different IMF, luminosity function, a different range for the mass of the core-collpase progenitor, in order to analyse how the variation of these parameters influence the final results.
In table 5.5 are listed the values for the main parameters for the reference simulation. We use the L_{TIR}/SFR calibration from Kennicutt et al. (1998), and hence a Salpeter IMF. This imply that $k_{CC} = 0.00703$. As discussed above, we assume that the SFR is distributed as L_K^{α} where α has different values for the different types of galaxies and the extinction is scaled to SFR with a maximum values in the nucleus of about $A_V = 30$ mag (Shioya 2001). Finally, we assumed that the core-collapse progenitor masses ranges from 8

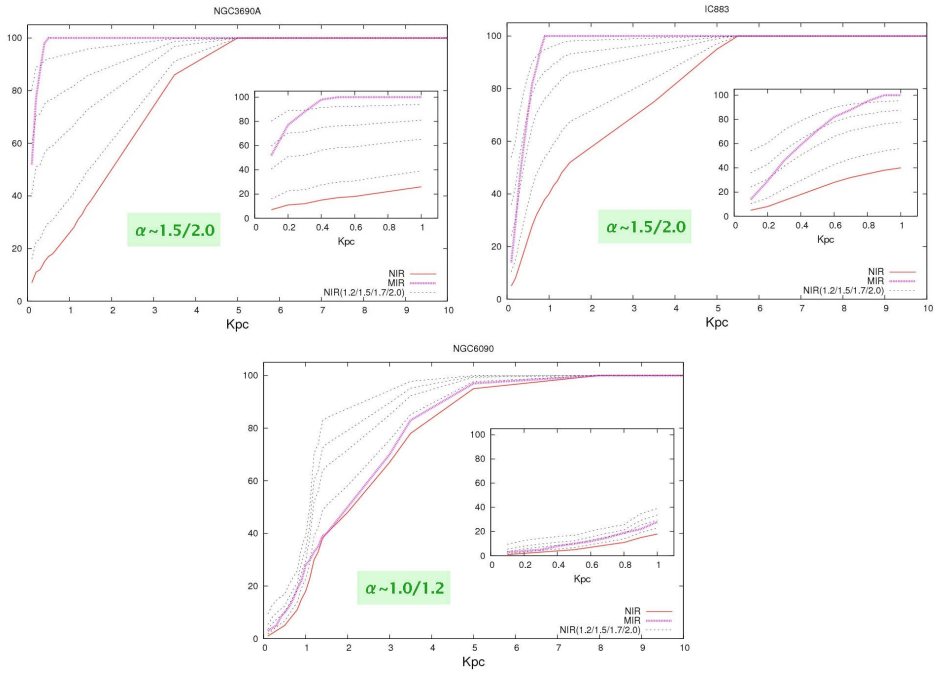

Figure 5.7: Curves of growth of 3 galaxies of the sample of Soifer et al. (2001). The red curves correspond to the NIR-luminosity, the purple curves to the MIR-luminosity. The dotted lines represent the K^{α} curves for different values of α:1.2, 1.5, 1.7 2.0.

to 50 $M_{\odot}$. We conducted 500 MonteCarlo simulation, and, with the adopted parameters and the measured search detection efficiency, we predict, on average, the discovery of 5.4±2.3 SNe in our search, of which 5.2±2.3 core collapse and 0.2±0.4 Ia. The expected number compares very well with the observed number. Indeed we found that the expected number of SNe is $\leq$ to 6 in 55% of the experiments. Even if we consider only the SNe with spectroscopic classification (4) their occurrence is significant (22%). Therefore The first fundamental conclusion is that the number of expected SNe is *consistent* with the observations, so *not* confirming the claim of previous infrared SN search that estimated a number of expected SNe higher than observed. In figure 5.8 is shown the histogram of the number of detected SNe out of 500 MonteCarlo experiments. In grey, we evidence the area of the histogram within $\pm 1\sigma$ from the average, showing that the number of observed SNe is consistent with the number of expected SNe.

Besides the plain number, from the simulation we can also derive the distribution of the expected properties of the SNe. In particular, in figure 5.9 we compare the expected and observed (tab 5.6) K magnitude distribution of SNe. In figure 5.10 we show the predicted extinction distribution. It turns

Reference simulation

L_{TIR}/SFR calibration	Kennicutt (1998)
IMF	Salpeter
SFR	$\propto K^{\alpha}$
α	merging: 2.0 close pair: 1.7 pair: 1.25 single: 1.0
A_V	30 mag (nucleus)
CC masse range	8-50$M_{\odot}$
LF	Gaussian
Light Curves	From LOSS search

Table 5.5: Main inputs parameters with their values for the reference simulation.

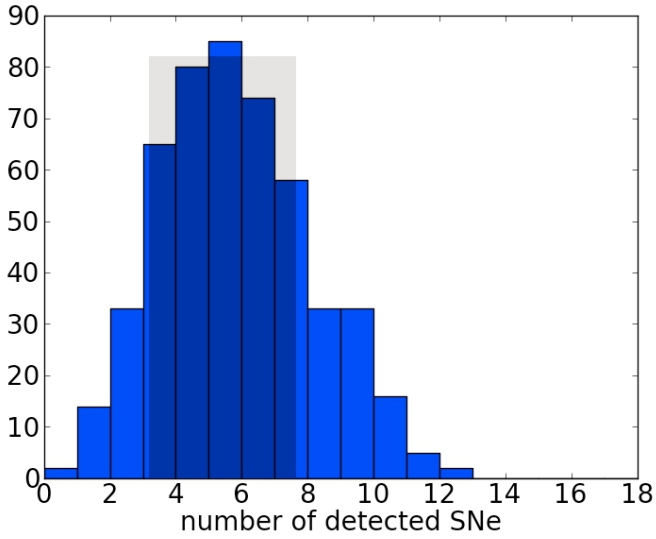

Figure 5.8: Histogram of the number of detected SNe out of 500 MonteCarlo experiments. The grey area represent the interval within 1σ.

out that events the adopted parameters we do expect that most SNe have low extinction. Also in this case we have consistency with observations: the supernovae that we have discovered are located mainly in the outskirts of the hosts galaxies, and suffers of little extinction. Finally, figure 5.11 is shows the radial distribution of the simulated SNe compared to the distribution of the observed SNe out of 500 MonteCarlo simulations. We can see that

Table 5.6: Magntude of the detected SNe.

SN	mag(K)
PSN 2010	17.9
2010bt	16.1
2010gp	16.9
2010hp	17.2
2011ee	17.8
PSN 2011	17.7

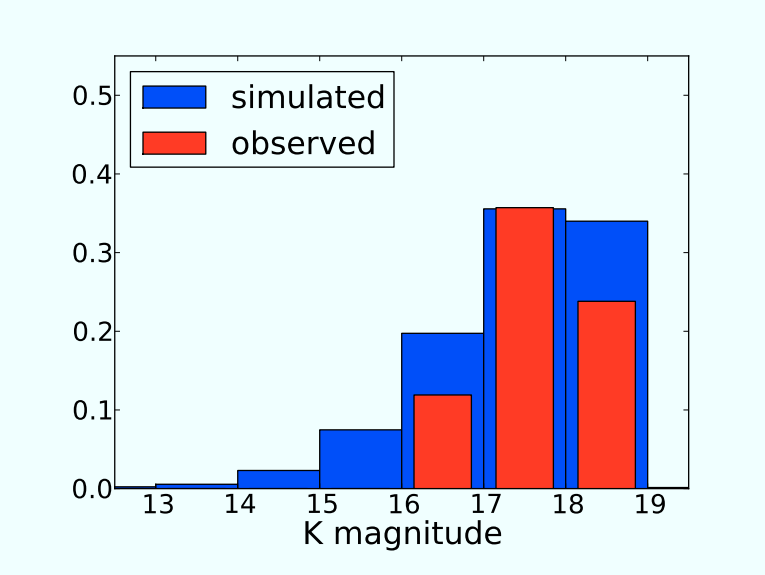

Figure 5.9: Expected K magnitude distribution of detectable SNe out of 500 MonteCarlo experiments.

toward the nuclear regions the number of expected (and observed) SNe decreases rapidly to zero. As we will discuss later this is due to a combination of higher extinction and lower detection efficiency in the nuclear regions.

5.6.1 Tests of simulation

To understand how a different choice of the tests parameters influence the expected rate, we can perform different MonteCarlo simulation varying, once at a time, each of the parameter. We can change, for example, the value of extinction, the core collapse mass range, the IMF or the magnitude limit. These are the main parameter but we can execute different tests also for the remaining inputs (e.g. the LF, the template light curves...).

Expected rate from L_B. Our galaxies are all actively star forming, then their SN rate is higher then in normal galaxies. To verify this, we compute the

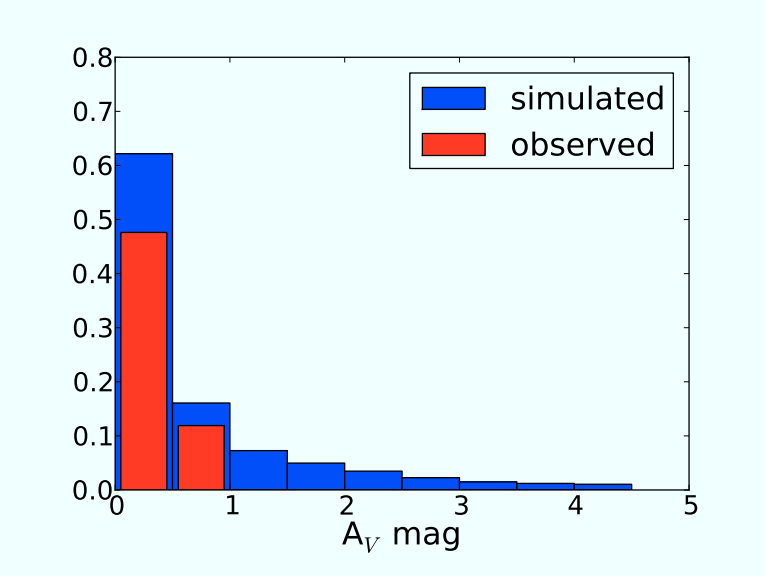

Figure 5.10: Expected A_V distribution of detectable SNe.

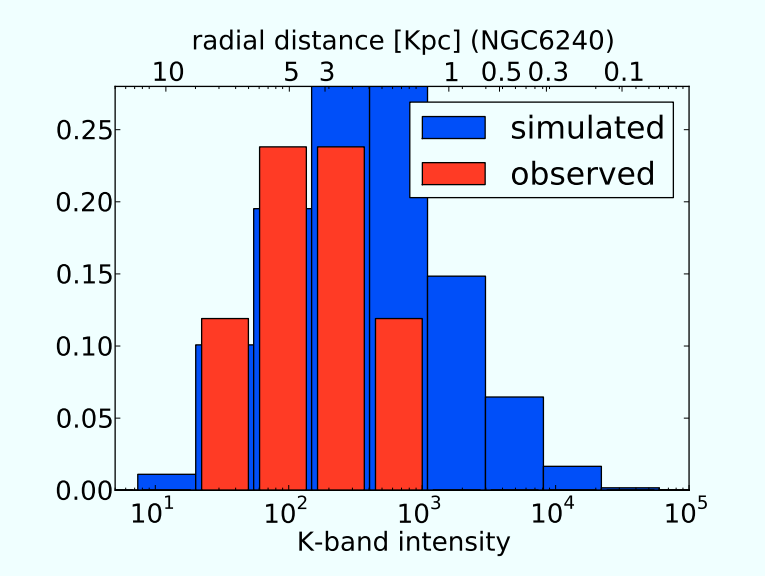

Figure 5.11: Comparison between the radial distirbution of simulated and detected SNe out of 500 MonteCarlo simulation.

expected rate from the B luminosity instead of the FIR luminosity. In this case the expected rate is $0.5\pm^{0.7}_{0.5}$ of which $0.5\pm^{0.7}_{0.5}$ core collapse and $0.1\pm^{0.2}_{0.1}$ Ia. Compared to the 6 SNe observed, this confirm that we are detecting more SNe than expected from the B luminosity. We know that galaxies of

our sample have far infrared emission that is about 10 times the average emisson. In this way we verified that also the rate is about 10 times the average rate of the normal galaxies. The hypothesis that the detected number of SNe is still compatible with expectations can be rejected at more than the 90% confidence level.

Effect of different A_V and M_{lim}. One point that we need to stress is that the SNe are not all the expected SNe that explode in a galaxy of our sample in the search period, but just those that we expect to be detected given our instrument capabilities and search strategy. To make the point we compute the expected number of SNe assuming no extinction and adopting a magnitude limit for detection in the nuclear regions that is the same as the outskirsts (19.0). In this way we can have an estimate of the number of SNe lost in our search due to the combined effect of high extinction and low magnitude limit in the innermost regions of starburst galaxies. The expected rate with A_V=0 and magnitude limit =19.0 throughout the galaxy is 13.4±3.7 of which 12.8±3.6 core collapse and 0.6±0.7 Ia. If we compare this value with that obtained in the reference case we can conclude that 60% of the events remain hidden in the nuclear regions due to a combination of high extinction and reduced detection efficiency.
As we see in the following by changing separately the values of extinction and magnitude limit, we deduce that the magnitude limit has a greater influence than the extinction on the value of the expected rate.
If the value of extinction is A_V=0 (the magnitude limit is lower in the nuclear regions if compared to the outskirsts, as in the reference case) the expected rate is slightly higher: 6.3±2.4. Viceversa, if we consider the same magnitude limit of the outskirst at all galactocentric positions, with the reference value (30) for the extinction, we obtain the following rate: 9.1±3.0. If we compare these value with the rate of the reference simulation we can say that about less than 40% of the number of missed SNe are lost due to extinction (∼0.9 SNe) and about more than 60% are missed due to low magnitude limit (∼3.7 SNe) in the nuclear region. This implies that also for little variation of the magnitude limit the rate can change significantly, while the changes are minor, even for substantial changes in the value of the extinction. To confirm this, we can assume an extreme value for the maximum extinction, namely A_V =200. In this case the number of expected events is 4.0±2.0, about 40% then for the reference simulation. We can also test for variation of the extinction distribution inside the galaxy; for instance if we assume that extinction is scaled with radial distance instead that SFR the rate is very similar to the reference case: 5.2±2.2 with a variation of only ∼2%. Moreover, instead of a random gaussian distribution of the extinction around a mean value, we consider a fixed extinction for the given position we obtain 5.5±2.4. We conclude that varying the extinction distribution inside the galaxy the expected rate changes only of a few percent, while to obtain a significantly variation (40%)

the extinction should takes extremely high values (>200 mag). However, we underline that *only* the combined effect of higher extinction and lower magnitude limit in the nuclear regions give the correct number of hidden SNe, because these two effect, when considered individually, are not sufficient to justify missing supernovae. Given that it is clear that even small error in the estimate of the M_{lim} have large effects in the expected numbers is crucial to obtain an accurate estimate of the detection efficiency in particular in the nuclear region where the magnitude limit is brighter. This is why we spent a major effort in this direction.

Expected rate from different IMF and CC SN progenitor mass range. An important assumption of the simulation is the IMFs. However, how we will show below, because of the IMF enters, both in the estimate of the number of SN progenitors and in the calibration of the luminosity vs. SFR relations, it turn out that the actual choice has little effect on the expected SN numbers.
In the reference simulation we use a Salpeter IMF:

$$\phi(m) \propto m^{-\alpha}$$
$$\text{with} \quad \alpha = 2.35 \quad \text{for} \quad 0.1 < m < 100 M_{\odot}$$

with core collapse mass range of 8-50 $M_{\odot}$. In this case $k_{CC} = 0.070$. If we adopt a different IMF as that of Kroupa, we must change k_{CC} in the SNR-SFR relation ($k_{CC} = 0.0105$), but change also the calibration of the relation between SFR and L_{TIR}. If we use a Kroupa IMf, the scaling constant between the new (Kroupa IMF) SFRs and those from Kennicutt 1998 (Salpeter IMF) is 0.86 (see Kennicutt et al. 2012). The number of expected events is 7.0±2.8. This imply that the IMF shape has little effect on the expected SNR (cf. Horiuchi et al. (2011) and Melinder et al. (2012)).
For an adopted IMF, there is still the choice of the adopted mass range of SN progenitors that take to different values of k_{CC} in Eq. 5.3. We consider for this discussion only the reference case of a Salpeter IMF. Changing the lower limit of the core collapse progenitor mass range from 8 to 10 $M_{\odot}$ (10-50 $M_{\odot}$), the expected SN number is 3.9±2.1 (∼30% lower than the expected rate obtained in the reference case). On the other hand, if we adopt a different upper limit, for example 100 $M_{\odot}$ instead of the standard value of 50 $M_{\odot}$ the expected number: 5.7±2.4, is only ∼5% higher then the reference simulation (5.4±2.3, table 5.7). That is, the rate is quite insensitive to the upper mass limit for M≥ 50 $M_{\odot}$. Most important is instead the dependence on the lower mass limit, with the productivity decreasing by a factor of $\simeq 0.7$ if $M_{CC,l}$ goes from 8 to 10 $M_{\odot}$ for a Salpeter IMF (cf. Greggio et al. (2001)).

Expected rate from different Luminosity Function. In the reference

simulation we use a gaussian SN absolute magnitude distribution for the luminosity function (LF), with average value and dispersion taken from Li et al 2011. To test the influence of our assumption we performed a simulation adopting the SN luminosity functioned the local Universe SN sample collected by the LF from Botticella et al. (2011, the so called HUGS-LF. With this choice the expected rate is lower: 3.3±1.8. HUGS is a local survey, within 11 Mpc and include about 20 objects (while the LOSS sample consist of 101 SNe). Horiuchi et al. (2011) (Horiuchi et al., 2011) says that faint CC SNe, that occupy the faintest end of the CC SNe LF, are very numerous enough in the very local (∼10 Mpc) volume that their volumetric rates are as large as the bright cosmic SNR measured by LOSS at larger distances. In particular, the very local 10 Mpc volume shows the faint fraction could be as high as ∼50%. In fact we found that in this case the expected number is lower (3.3 events) because a higher fraction of faint events fall below the detection limit.

Expected rate from different search reference. Finally, we tested the effect of using different search reference for light curves or core collapse subdivision. For the reference experiments we use data from LOSS search [14]. If we use data from the search of Cappelaro, Evans and Turatto (1999) [8] the rate is 6.1±2.5, only a few percent higher than the reference value. In tables 5.8 and 5.9 we listed the different data (SN absolute magnitude and dispersion and the core collapse subdivision) for the two search.

	Ia	σ	**IIL**	σ	**IIP**	σ	**Ibc**	σ	**IIn**	σ
CET99	-18.95	0.47	-17.05	0.53	-16.53	1.0	-17.11	0.95	-18.00	1.00
LOSS	-18.49	0.76	-17.44	0.64	-15.66	1.23	-16.09	1.24	-16.86	1.61

Table 5.7: SN absolute magnitude for the different reference search.

	ksn[IIP]	**ksn[IIL]**	**ksn[Ibc]**	**ksn[IIn]**
CET99	A*0.80/2	A*0.80/2	A*.17	A*0.80*0.03
LOSS	A*0.635*0.698	A*0.635*(0.097+0.119)	A*0.365	A*0.635*0.086

Table 5.8: Core collapse subdivision for the different reference search (A=ksn[CC]).

In table 5.10 are summarized the different value of the expected SN rate for the different cases analyzed in this chapter.

	Input parameter	Value	Expected SN rate
L_{TIR}	IMF	**8-50 $M_\odot$**	**5.4±2.3**
		Salpeter 10-50 $M_\odot$	3.9±2.1
		8-100 $M_\odot$	5.7±2.4
		Kroupa	8.1±2.9
	A_V	**30**	**5.4±2.3**
		0	6.3±2.4
		200	4.0±2.0
		radial	5.2±2.2
		fixed	5.5±2.4
	Magnitude limit	**radial**	**5.4±2.3**
		19.0	9.1±3.0
		fixed 25.0	45.5±6.5
		12.0	0.0
	A_V + Magnitude limit	0 + 19.0	13.4±3.7
	Reference search	**LOSS**	**5.4±2.3**
		CET99	6.1±2.5
	Luminosity Function	**Gaussian**	**5.4±2.3**
		LOSS	5.9±2.4
		HUGS	3.3±1.8
LB			0.5±0.7

Table 5.9: Summary of the different value of the expected SN rate out of 500 MonteCarlo simulations for different values of input parameters. In bold are shown values used in the reference simulation.

Chapter 6

Summary and Conclusions

Aims of the work

The rate of Supernovae is a crucial quantity in astrophysics. SNe dominate the chemical evolution of the universe and the dynamical properties of the ISM, providing at least part of the feedback needed to explain galaxy evolution. In particular, for an adopted SFR, measurements of the CC SN rates give information on the range of initial masses of their progenitors, as well as on the slope of the IMF at the high mass end. The SN Ia rate in galaxies undergoing strong SF can instead help to asses the relative importance of the prompt component. one of the main problems for measuring SN rate is related to the presence of dust that introduce a bias due to extinction. This is true in particular in star forming systems, as SB galaxies, where dust obscuration is usually larger than in normal galaxies. At the same time, the role of SNe rate is especially important in SB, where high FIR luminosity is a direct measure of their high SFR, that implies high SN rate. In particular, a large fraction of the massive star formation took place in LIRGs and ULIRGs: this implies that most SNe in starburst galaxies are expected to be core collapse events, with an expected rate at least one or two orders of magnitude larger than in normal galaxies. This seems in contradiction with the fact that very few SN have been discovered in SB galaxies. Most of the past and current SN searches are performed at optical wavelengths, where extinction is relatively high, so that we expect a detection bias. The missing SNe, while heavily obscured in the optical, are expected to show up at longer wavelength. Some attempts of SN searches in the IR were made, yielding the discovery of a few very obscured SNe. Although this is a step in the right direction, the number of detected events remaines short of a factor 3-10 with respect to expectations (Mannucci et al. (2003) [29], Mattila et al. (2004) Mattila et al. (2004)]). The proposed explanation is that most of the SNe are so embedded into the dust that their luminosity is vastly reduced even at near-IR wavelengths (likely $A_V > 30$mag, as found in Mattila et al. (2007)[31]). In this case, a NIR search detect only a fraction of the actual SN

explosions, and a survey at longer wavelenght should also be planned (e.g. radio searches). Another possibility is that if most of the FIR flux comes from the central arcsec, then the majority of the SNe are in the nuclear regions, where the presence of the residuals after subtraction, the problem of the spatial resolution of the instruments and the higher extinction in these regions make the discovery of the Sne very difficult. A few groups have attempted to address this issue using the most advanced imaging systems, HST (Cresci et al. 2007 Cresci et al. (2007)) and telescopes with adaptive optics and Laser Guide Stars (eg. Mattila et al. 2007 Mattila et al. (2007), Kankare et al. 2008 Kankare et al. (2008)). However, these are very expensive programs in term of telescope time which, while certainly valuable, they cannot be performed systematically.
Another possibility is the presence of AGNs dominating the FIR flux of most of the galaxies: in this case the FIR flux would not be related to the SN rate (at the beginning of this chapter was remembered as LIRGs and expecially ULIRGs can be characterized by the presence of central AGN).
The possibility that the relation between SFR and FIR (and than the relation between SFR-SNR) is incorrect could have fundamental implication on the study of the galaxy evolution. However, this is not a likely possibility as there is a robust concordance among several different methods and this relation has been stable through the years (e.g. Rieke et al. 1980).

At the present day, unfortunately, the statistics is still very low allow for definite conclusions. For this reason, we planned an alternative, complementary approach, which makes use of an excellent instrument as HAWK-I at the ESO Very Large Telescope, but of less valuable observing time, e.g. non-optimal weather conditions. This project started in 2008 and monitored 30 starburst galaxies in K band for 3 years. First aim of the work is to verify whether the observed SN rates in SB galaxies is consistent with their SFR, the latter as deduced from the FIR luminosity.

Survey strategy, galaxy sample and observations

We perform a snapshot IR search in a sample of 30 nearby starburst galaxies using HAWK-I@VLT. The search is performed in K band, where the extinction is strongly reduced compared to optical band ($A_B = 10$ mag corresponds to $A_K = 0.8$ mag only), in a sample of 30 nearby starburst galaxies.
Given that the CC SN infrared light curves evolve relatively slowly (they remains within 1 mag from maximum for 1-2 months) there is no need for frequent visits: for each target, visits are separeted by > 15 days. So, assuming at least 3 visits per galaxy per semester we planned 100 visits per observing period.
Our search is well suited as a filler for the gaps in the scheduling of service observing for non-optimal sky conditions, poor seeing or non-photometric

conditions.
Spectroscopic confirmation of SN candidates has been obtained with ISAAC@VLT (P83) and X-Shooter@VLT (P85/87) in ToO/GTO mode.
From the IRAS Revised Bright Galaxy Sample [? ? ?] we selected a sample of 30 SB galaxies with $z < 0.07$, FIR luminosity $\log(L_{FIR)}) < 10.8$ and visible at ESO from April to October (see Table 4.1). The galaxies of the sample are largely (90%)Luminous Infrared Galaxy (LIRGs, with $\log(L_{FIR} \geq 10^{11} L_{\odot})$, while the 3% (the most distant galaxies) belongs to ULIRGs (with $\log(L_{FIR} \geq 10^{12} L_{\odot})$.
Most of the galaxies of the sample are single galaxies (about 60-70%), and the remaining are double/interacting galaxies or contain double nucleus, sign of a recent merger. In figure 4.8 are shown the images of some galaxies of the sample analyzed in this work.
The program has been allocated in three periods, 83, 85 and 87(between April 2008 and October 2011) with completness execution respectively of 100% (P83) and 70% (P85 and 87) (Table 4.2). The figure 4.9 represent the seeing distribution of all the observations. Despite the lack of observing constraints, $\sim$87% of visits have seeing < 1.0", with an average value of about 0.6".

Data reduction and SN sample

Data reduction of HAWK-I images is a very complex process due to the fact that the detector is a mosaic. A crucial point is, in fact, building the image from the four chips.
After downloading images from the HAWK-I archive, data analysis is performed integrating Gasgano and EsoRex(the ESO Recipe Execution Tool) with custom programs, consisting of:

- Pre-reduction;
- Building mosaic images and refine astrometry;
- Register images using WCS
- Take difference of images with PSF match (ISIS[3, 2]);
- Artificial star experiment to test the limiting magnitude for SN detection.

In particular, to measure the SN rate it is crucial to obtain an accurate estimate of the detection efficiency of the search, through artificial star experiments. We searched the artificial stars on the difference images obtained with the same pipeline and reference image used for the search. The detection efficiency is strongly dependent on seeing, in particular in the nuclear region, where the magnitude limit is lower.

At the end we collected 6 SN candidates (2 CC SNe, 1 type Ic SN and 1 type Ia SN). In two cases we have obtained the discovery images (SN 2010hp and SN 2011ee), and classification spectra with X-shooter whilw in two cases it was impossible to obtain a spectroscopic classification of the SN candidate due to its faintness. We remark the fact that two SNe were first discovered by others. This is not surprising given the relatively wide temporal sampling of our search. Spectroscopic observations were obtained for four of the candidates (epoch, spectral and instruments are reported in Tab.4.5). We analyzed the available photometry performing a simultaneous comparison of the absolute luminosity and color with that well observed SN templates with the aim to derive an estimate of the epoch and magnitude at maximum and a constraint on the extinction in the host galaxy. For the two SNe without useful spectroscopy we used the photometry to assign the SN classification. Results are reported in Tab 4.6. All together we found one type Ia and five core collapse SNe.

The expected SN rate from MonteCarlo simulation

Because of the small number of detected events it is not viable to derive direct statistical measurements of the rates of SNe in starburst galaxies. We use instead a MonteCarlo approach were we compute the number and properties of expected events based on adopted physical parameters and simulating the random chances of explosion and detection. By collecting of a number of MonteCarlo experiments with the same input parameters we can test whether the observed events are within the expected distribution. If not we can vary the input parameters of the simulation and repeat the test until we found a satisfactory agreement.
The MonteCarlo simulation tools was built using Python. Inputs of the simulation are:

- the sample galaxy catalog
- data describing the SN properties for each of the considered SN types
- details of the monitoring campaign, in particular the detection limit for each observation as a function of the position of the transient inside the parent galaxy
- the adopted cosmological parameters: $H_0 = 72$, $\Omega_M = 0.3$ and $\Omega_\lambda = 0.7$

In addition there are a number of test parameters that are allowed to change for different simulation runs. These are:

- the number of SNe expected from a given star formation episode.
- the adopted absorption depth and distribution inside the parent galaxies

- the adopted star formation distribution inside the parent galaxies

For each step of the simulation see the first section of this chapter. Through MonteCarlo simulations we estimated the expected SN rate, based on above assumptions, in order to obtain a comparison with the observed rate. We compare the expected rate with the observed one in particular for the reference case, where we used a series of reference values for the simulation, then we investigate other cases, in which, for example, we consider a different IMF or luminosity function, a different range for the mass of the core-collpase progenitor, in order to analyse how the variation of these parameters influence the final results. In table 5.5 are listed the values for the main inputs for the reference simulation. We use the L_{TIR}/SFR calibration from Kennicutt et al. (1998), and a Salpeter IMF. This imply that $k_{CC} = 0.00703$. The SFR is distributed as L_K^{α} where α has different values for the different types of galaxies. We assumed that the extinction is scaled to SFR with a maximum values in the nucleus of about $A_V = 30$ mag (Shioya 2001). Finally, we assumed that the core-collapse progenitor masses ranges from 8 to 50 $M_{\odot}$. We conducted 500 MonteCarlo simulation, and, based on the search details and above assumptions, we should have expect the discovery of 5.4±2.3 SNe in our search, of which 5.2±2.3 core collapse and 0.2±0.4 Ia. We found that the expected number of SNe is $\leq$ to 6 in 55% of the experiments. Even if we consider only the SNe with spectroscopic classification (4) their occurrence is significant (22%).

Scientific Results and Conclusions

The *main* result is that the number of expected SNe is *consistent* with the observations, *not* confirming results of previous infrared SN search that obtained a number of expected SNe higher than observed. The comparison of predicted and observed K magnitude extinction distribution shows that even in a K-band search we expected to find mainly low extinction events. The emphasis of our approach is an *accurate estimate of the detection efficiency* as a function of the SN position in the host galaxy and the determination of the *size* and *distribution* of the *star formation* for each galaxy of our sample. We show that the detection efficiency is strongly dependent on the seeing in particular in the nuclear regions where the magnitude limit is lower. This implies that is important to obtain also an accurate estimate of the star formation spatial distribution in order to have an estimate of the number of SNe lost in the nuclear regions.
To understand how a different choice of the tests parameters can influence the expected rate, we varied each of them and compute the rate repeating the MonteCarlo simulation.
If we compute the expected rate from the B luminosity instead of far-infrared, we obtain $0.5\pm^{0.7}_{0.5}$. This confirm that galaxies of our sample have about 10 times the SFR than normal galaxies.

To understand the influence of A_V and detection effciency on the expected number of events, we consider the case of no extinction and same M_{lim} of the outskirsts (19.0) at all galactocentric position. We conclude that 60% of the events remain hidden in the nuclear regions due to a combination of high extinction and reduced detection efficiency, the latter having greater influence on the value of the expected rate. This imply that also for little variation of the magnitude limit the rate can change significantly, while the changes are minor even for substantial changes in the value of the extinction. This confirms that it is crucial to obtain the best possible estimate of the magnitude limit in particular in the nuclear region where the magnitude limit is lower.
Another important aspect is the choice of the IMF and the core collapse progenitor mass range. The IMF shape has *little* effect on the predicted SNR. Varying the upper or the lower limit of the range we confirmed that the rate is *quite insensitive to the upper mass limit* for M$\geq$ 50 $M_\odot$ while most important is instead the *great dependence on the lower cut off mass*, the productivity decreasing by a factor of simeq 0.7 if MCC,l goes from 8 to 10 $M_\odot$ for a Salpeter IMF.
The choice of an appropriate SN luminosity function is important, but less crucial the other parameters. Finally, we tested the effect of using different search reference for light curves or core collapse subdivision (for example from LOSS or CET99) but the differences in the expected rate are less than 5%.

State of art of SN searches in Starburst Galaxies

A conclusion of the previous chapter is that 60% of the events remain hidden in the nuclear regions due to a combination of high extinction and reduced detection efficiency. This imply that, to obtain a complete rate for the starburst galaxies, it is crucial to find the very nuclear supernovae. A possibility is to search missing supernovae at longer wavelenght where extinction is strongly reduced, as Radio. The existence of hidden supernova factory in the nuclei of LIRGs and ULIRGs has already been demontrated by high resolution radio observations. For example, VLBI observations of the nearby ULIRG Arp 220 have revealed luminous radio SNe within the innermost $\sim$150 pc nuclear regions at a rate indicating a SFR high enough to power its entire IR luminosity (Lonsdale et al. 2006). However, not all CCSNe are likely to become luminous at radio wavelenghts, and therefore radio searches for SNe can only provide a lower limit for the real SN rates.
Another possibility is the use of high spatial resolution for the detection of the innermost nuclear supernovae. This can be achieved with space-based imaging (e.g., Cresci et al. 2007, colina et al. 2007), imaging from Antarvtica

(Burton et al. 2005), or ground-based adaptive optics (AO) imaging providing resolutions 5 times better than under typical natural seeing conditions. The potential of current 8 m class telescopes equipped with AO was firstly demonstrated by the discovery of SN2004ip in the LIRG nuclear regions using the NACO AO system with a natural guide star on the Very Large telescope (Mattila et al. 2007). In this case the supernova is a core collapse event suffering from a host galaxy extinction of up to about 40 mag in the V band. Kankare et al. (2008) confirmed the discovery of a supernova (SN2008cs) using the ALTAIR/NIRI adaptive optics system on the Gemini-North Telescope. SN2008cs is the first SN discovered using laser guide star adaptive optics and is a core-collapse event suffering from a very high host galaxy extinction of about 15.7 mag in the V-band. With the same instrument Kankare et al. (2010) reported the discovery of two other supernovae in the very nuclear regions of the galaxy IC 883: SN2010cu, located at only 180 pc, and SN2011hi, located at 380 pc from the nucleus. At the present day the statistics is still very low, due to the fact that these programs are expensive in term of telescope time, and that, however, the advanced technique of LGS is available only at VLT. Then it is crucial to increase the results using the very high resolution of AO to detect very nuclear supernovae, also in case of very high extinction.

The future of IR searches

The next generation of large ground-based/space telescopes, JWST, TMT, E-ELT, and GMT will allow spectroscopy of SNe up to redshift 3, and extend studies to even higher redshifts also for core collapse SNe for which the results at redshift $z \gtrsim 0.5$ are practically nonexistent. These studies may at last elucidate the progenitors of SNe Ia, enable studies of SN Ia evolution over vast stretches of cosmic time and allow us to trace the whole star formation history of the Universe.
Ground-based surveys in the coming decade will detect thousands of Type Ia supernovae at redshift <1. However, a space observatory is the only feasible route to obtaining $\sim$1000 high-precision light curves in the NIR that is rest-frame V band, for z$>$0.8. At lower z the space-based calibration and NIR data will enable lower systematic errors than can be achieved from the ground. Improved dark-energy constraints from the SNIa Hubble diagram require substantial reduction in systematic errors of SNIa distance moduli, that is 0.01 mag or less. They also benefit from an extension to z$>$0.8 where we currently have only a relative handful of events from HST.
The Hubble space telescope imaged the 320 square arcmin in two GOODS fields. The SN rate of discovery was about 1 supernova at z$>$1 per epoch imaged, equivalent to 10 SNe per square degree per epoch. With the ACS

instrument it is possible to reach AB magnitude of about 25. A similar depth would be reached in about 30s of exposure with JWST NIRCam. The supernova follow-up would include measuring the light curve and obtaining a spectroscopic confirmation for the redshift. Given the importance of systematics, reaching to higher redshift and observing the rest-frame near infrared are likely to be the major contributions of JWST to the characterization of SNIa as distance indicators. With new generation of space telescope we will able to combine depth and wide field of view. For exaplme, the space telescope Euclid project will conduct a wide-area photometric survey of 20,000 square degrees reaching galaxies out to z$\sim$2, with slitless spectroscopy to obtain redshifts. There will also be a deeper survey of 40 square degrees. The telescope is 1.2m and there are a total of 680 mega-pixels of detectors. While with the current combination of 8-metre-class ground-based telescopes and the Hubble Space Telescope, supernova searches can reach around half the age of the Universe, infrared spectroscopy with the E-ELT combined with imaging from the upcoming James Webb Space Telescope will allow us to extend the search for supernovae to redshifts beyond 4, a look-back time of nearly 90% of the age of the Universe. The E-ELT is an excellent instrument, that will be able to study supernova explosions in extraordinary detail. The use of Adaptive Optics will reduce the field of view, making the use more suitable for the follow up on single object.
Another excellent ground-based telescope is the Large Synoptic Survey Telescope (LSST), with the aims to survey the entire visible sky every few days. It would be excellent at discovering SNIa. The main survey will obtain light curves in 6 bands and photometric redshifts of about million Type Ia supernovae per year, and the rapid sampling 'mini-survey' of selected areas will yield well sampled light curves of tens of thousands of supernovae to a limiting redshift beyond one (leading to an independent test of dark energy dynamics; Riess et al 2007).
Concerning the IR, an excellent ground-based IR facility is the VISTA telescope, with a wide ($\sim 1^{\circ}$) field of view it can be used to searches supernovae at intermediate redshift, not only in actively star forming galaxies, but also in normal galaxies. We remember, in fact, that SN with very high reddening have been found also in normal galaxies. In this case, since SNe are not concentrated in the nuclear regions as starburst galaxies, the wide field of view of VISTA is very useful also to study the influence of different galaxy inclination (and then different extinction) on the SN rate.

Bibliography

Agüero, E. L., Paolantonio, S., & Günthardt, G. 2000, AJ, 119, 94

Alard, C. 2000, AAPS, 144, 363

Alard, C. & Lupton, R. H. 1998, ApJ, 503, 325

Alonso-Herrero, A., Rieke, G. H., Rieke, M. J., & Scoville, N. Z. 2002, AJ, 124, 166

Barris, B. J. & Tonry, J. L. 2006, ApJ, 637, 427

Blanc, G. & Greggio, L. 2008, NewA, 13, 606

Botticella, M. T., Riello, M., Cappellaro, E., Benetti, S., Altavilla, G., Pastorello, A., Turatto, M., Greggio, L., Patat, F., Valenti, S., Zampieri, L., Harutyunyan, A., Pignata, G., & Taubenberger, S. 2008, AAP, 479, 49

Botticella, M. T., Smartt, S. J., Kennicutt, R. C., Cappellaro, E., Sereno, M., & Lee, J. C. 2012, AAP, 537, A132

Bush, S. J., Wang, Z., Karovska, M., & Fazio, G. G. 2008, ApJ, 688, 875

Bushouse, H. A., Borne, K. D., Colina, L., Lucas, R. A., Rowan-Robinson, M., Baker, A. C., Clements, D. L., Lawrence, A., & Oliver, S. 2002, ApJS, 138, 1

Calzetti, D., Armus, L., Bohlin, R. C., Kinney, A. L., Koornneef, J., & Storchi-Bergmann, T. 2000, ApJ, 533, 682

Cappellaro, E., Evans, R., & Turatto, M. 1999, AAP, 351, 459

Cappellaro, E., Riello, M., Altavilla, G., Botticella, M. T., Benetti, S., Clocchiatti, A., Danziger, J. I., Mazzali, P., Pastorello, A., Patat, F., Salvo, M., Turatto, M., & Valenti, S. 2005, AAP, 430, 83

Chen, J., Lo, K. Y., Gruendl, R. A., Peng, M.-L., & Gao, Y. 2002, AJ, 123, 720

Cole, S., Aragon-Salamanca, A., Frenk, C. S., Navarro, J. F., & Zepf, S. E. 1994, MNRAS, 271, 781

Cresci, G., Mannucci, F., Della Valle, M., & Maiolino, R. 2007, AAP, 462, 927

Dahlen, T., Strolger, L.-G., & Riess, A. G. 2008, ApJ, 681, 462

Dahlen, T., Strolger, L.-G., Riess, A. G., Mobasher, B., Chary, R.-R., Conselice, C. J., Ferguson, H. C., Fruchter, A. S., Giavalisco, M., Livio, M., Madau, P., Panagia, N., & Tonry, J. L. 2004, ApJ, 613, 189

Dopita, M. A., Pereira, M., Kewley, L. J., & Capaccioli, M. 2002, ApJS, 143, 47

Egami, E., Neugebauer, G., Soifer, B. T., Matthews, K., Becklin, E. E., & Ressler, M. E. 2006, AJ, 131, 1253

Eggen, O. J., Lynden-Bell, D., & Sandage, A. R. 1962, ApJ, 136, 748

Elmhamdi, A., Danziger, I. J., Chugai, N., Pastorello, A., Turatto, M., Cappellaro, E., Altavilla, G., Benetti, S., Patat, F., & Salvo, M. 2003, MNRAS, 338, 939

Goldader, J. D., Meurer, G., Heckman, T. M., Seibert, M., Sanders, D. B., Calzetti, D., & Steidel, C. C. 2002, ApJ, 568, 651

González Delgado, R. M., Heckman, T., Leitherer, C., Meurer, G., Krolik, J., Wilson, A. S., Kinney, A., & Koratkar, A. 1998, ApJ, 505, 174

Green, D. W. E. 2010, Central Bureau Electronic Telegrams, 2390, 3

Greggio, L. 2005, AAP, 441, 1055

Greggio, L. & Renzini, A. 2011, Stellar Populations. A User Guide from Low to High Redshift

Greusard, D., Friedli, D., Wozniak, H., Martinet, L., & Martin, P. 2000, AAPS, 145, 425

Haan, S., Surace, J. A., Armus, L., Evans, A. S., Howell, J. H., Mazzarella, J. M., Kim, D. C., Vavilkin, T., Inami, H., Sanders, D. B., Petric, A., Bridge, C. R., Melbourne, J. L., Charmandaris, V., Diaz-Santos, T., Murphy, E. J., U, V., Stierwalt, S., & Marshall, J. A. 2011, AJ, 141, 100

Hagiwara, Y., Baan, W. A., & Klöckner, H.-R. 2011, AJ, 142, 17

Harutyunyan, A. H., Pfahler, P., Pastorello, A., Taubenberger, S., Turatto, M., Cappellaro, E., Benetti, S., Elias-Rosa, N., Navasardyan, H., Valenti, S., Stanishev, V., Patat, F., Riello, M., Pignata, G., & Hillebrandt, W. 2008, AAP, 488, 383

Hattori, T., Yoshida, M., Ohtani, H., Ishigaki, T., Sugai, H., Hayashi, T., Ozaki, S., & Ishii, M. 2002, PASJ, 54, 393

Hattori, T., Yoshida, M., Ohtani, H., Sugai, H., Ishigaki, T., Sasaki, M., Hayashi, T., Ozaki, S., Ishii, M., & Kawai, A. 2004, AJ, 127, 736

Hill, T. L., Heisler, C. A., Norris, R. P., Reynolds, J. E., & Hunstead, R. W. 2001, AJ, 121, 128

Horiuchi, S., Beacom, J. F., Kochanek, C. S., Prieto, J. L., Stanek, K. Z., & Thompson, T. A. 2011, ApJ, 738, 154

Johansson, L. 1991, AAP, 241, 389

Johansson, L. & Bergvall, N. 1988, AAP, 192, 81

Kankare, E., Mattila, S., Ryder, S., Alonso-Herrero, A., Diaz Santos, T., Colina Instituto, L., Kotilainen, J., Perez-Torres, M.-A., Vaisanen, P., Alberdi, A., Efstathiou, A., Romero, C., & Colina, L. 2008, Central Bureau Electronic Telegrams, 1391, 1

Kennicutt, Jr., R. C. 1984, ApJ, 277, 361

—. 1998, ApJ, 498, 541

Kim, D.-C. & Sanders, D. B. 1998, ApJS, 119, 41

Knop, R. A., Soifer, B. T., Graham, J. R., Matthews, K., Sanders, D. B., & Scoville, N. Z. 1994, AJ, 107, 920

Kuznetsova, N., Barbary, K., Connolly, B., Kim, A. G., Pain, R., Roe, N. A., Aldering, G., Amanullah, R., Dawson, K., Doi, M., Fadeyev, V., Fruchter, A. S., Gibbons, R., Goldhaber, G., Goobar, A., Gude, A., Knop, R. A., Kowalski, M., Lidman, C., Morokuma, T., Meyers, J., Perlmutter, S., Rubin, D., Schlegel, D. J., Spadafora, A. L., Stanishev, V., Strovink, M., Suzuki, N., Wang, L., Yasuda, N., & Supernova Cosmology Project. 2008, ApJ, 673, 981

Le Floc'h, E., Charmandaris, V., Laurent, O., Mirabel, I. F., Gallais, P., Sauvage, M., Vigroux, L., & Cesarsky, C. 2002, AAP, 391, 417

Li, W., Chornock, R., Leaman, J., Filippenko, A. V., Poznanski, D., Wang, X., Ganeshalingam, M., & Mannucci, F. 2011, MNRAS, 412, 1473

Li, W., Filippenko, A. V., & Riess, A. G. 2001, ApJ, 546, 719

Madau, P., Pozzetti, L., & Dickinson, M. 1998, ApJ, 498, 106

Magnelli, B., Lutz, D., Berta, S., Altieri, B., Andreani, P., Aussel, H., Castañeda, H., Cava, A., Cepa, J., Cimatti, A., Daddi, E., Dannerbauer, H., Dominguez, H., Elbaz, D., Förster Schreiber, N., Genzel, R., Grazian, A., Gruppioni, C., Magdis, G., Maiolino, R., Nordon, R., Pérez Fournon,

I., Pérez García, I., Poglitsch, A., Popesso, P., Pozzi, F., Riguccini, L., Rodighiero, G., Saintonge, A., Santini, P., Sanchez-Portal, M., Shao, L., Sturm, E., Tacconi, L., Valtchanov, I., Wieprecht, E., & Wiezorrek, E. 2010, AAP, 518, L28

Mannucci, F., Della Valle, M., Panagia, N., Cappellaro, E., Cresci, G., Maiolino, R., Petrosian, A., & Turatto, M. 2005, AAP, 433, 807

Mannucci, F., Maiolino, R., Cresci, G., Della Valle, M., Vanzi, L., Ghinassi, F., Ivanov, V. D., Nagar, N. M., & Alonso-Herrero, A. 2003, AAP, 401, 519

Marion, G. H., Challis, P., & Berlind, P. 2010, Central Bureau Electronic Telegrams, 2449, 1

Matteucci, F. & Recchi, S. 2001, ApJ, 558, 351

Mattila, S., Meikle, W. P. S., & Greimel, R. 2004, AAP, 48, 595

Mattila, S., Väisänen, P., Farrah, D., Efstathiou, A., Meikle, W. P. S., Dahlen, T., Fransson, C., Lira, P., Lundqvist, P., Östlin, G., Ryder, S., & Sollerman, J. 2007, ApJ, 659, L9

Maza, J., Hamuy, M., Antezana, R., Gonzalez, L., Silva, S., Folatelli, G., Cartier, R., Forster, F., Marchi, S., Pignata, G., Cifuentes, M., Conuel, B., Reichart, D., Ivarsen, K., Haislip, J., Crain, A., Foster, D., Nysewander, M., & Lacluyze, A. 2010, Central Bureau Electronic Telegrams, 2388, 1

Miluzio, M., Benetti, S., Botticella, M. T., Cappellaro, E., Ochner, P., & Valenti, S. 2011, Central Bureau Electronic Telegrams, 2773, 1

Miluzio, M. & Cappellaro, E. 2010, Central Bureau Electronic Telegrams, 2446, 1

Momjian, E., Romney, J. D., Carilli, C. L., & Troland, T. H. 2003, ApJ, 597, 809

Monard, L. A. G. 2010, Central Bureau Electronic Telegrams, 2250, 1

Neill, J. D., Sullivan, M., Balam, D., Pritchet, C. J., Howell, D. A., Perrett, K., Astier, P., Aubourg, E., Basa, S., Carlberg, R. G., Conley, A., Fabbro, S., Fouchez, D., Guy, J., Hook, I., Pain, R., Palanque-Delabrouille, N., Regnault, N., Rich, J., Taillet, R., Aldering, G., Antilogus, P., Arsenijevic, V., Balland, C., Baumont, S., Bronder, J., Ellis, R. S., Filiol, M., Gonçalves, A. C., Hardin, D., Kowalski, M., Lidman, C., Lusset, V., Mouchet, M., Mourao, A., Perlmutter, S., Ripoche, P., Schlegel, D., & Tao, C. 2006, AJ, 132, 1126

Pain, R., Hook, I. M., Deustua, S., Gabi, S., Goldhaber, G., Groom, D., Kim, A. G., Kim, M. Y., Lee, J. C., Pennypacker, C. R., Perlmutter, S., Small, I. A., Goobar, A., Ellis, R. S., McMahon, R. G., Glazebrook, K., Boyle, B. J., Bunclark, P. S., Carter, D., & Irwin, M. J. 1996, ApJ, 473, 356

Pastorello, A., Valenti, S., Zampieri, L., Navasardyan, H., Taubenberger, S., Smartt, S. J., Arkharov, A. A., Bärnbantner, O., Barwig, H., Benetti, S., Birtwhistle, P., Botticella, M. T., Cappellaro, E., Del Principe, M., di Mille, F., di Rico, G., Dolci, M., Elias-Rosa, N., Efimova, N. V., Fiedler, M., Harutyunyan, A., Höflich, P. A., Kloehr, W., Larionov, V. M., Lorenzi, V., Maund, J. R., Napoleone, N., Ragni, M., Richmond, M., Ries, C., Spiro, S., Temporin, S., Turatto, M., & Wheeler, J. C. 2009, MNRAS, 394, 2266

Pooley, D., Lewin, W. H. G., Fox, D. W., Miller, J. M., Lacey, C. K., Van Dyk, S. D., Weiler, K. W., Sramek, R. A., Filippenko, A. V., Leonard, D. C., Immler, S., Chevalier, R. A., Fabian, A. C., Fransson, C., & Nomoto, K. 2002, ApJ, 572, 932

Poznanski, D., Maoz, D., Yasuda, N., Foley, R. J., Doi, M., Filippenko, A. V., Fukugita, M., Gal-Yam, A., Jannuzi, B. T., Morokuma, T., Oda, T., Schweiker, H., Sharon, K., Silverman, J. M., & Totani, T. 2007, MNRAS, 382, 1169

Rafanelli, P. & Marziani, P. 1992, AJ, 103, 743

Richmond, M. W., Filippenko, A. V., & Galisky, J. 1998, PASP, 110, 553

Salpeter, E. E. 1955, ApJ, 121, 161

Sanders, D. B., Egami, E., Lipari, S., Mirabel, I. F., & Soifer, B. T. 1995, AJ, 110, 1993

Sato, Y. & Li, W. D. 2000, iaucirc, 7392, 1

Scoville, N. Z., Evans, A. S., Thompson, R., Rieke, M., Hines, D. C., Low, F. J., Dinshaw, N., Surace, J. A., & Armus, L. 2000, AJ, 119, 991

Shioya, Y., Trentham, N., & Taniguchi, Y. 2001, ApJ, 548, L29

Smartt, S. J. 2009, ARAA, 47, 63

Soifer, B. T., Neugebauer, G., Matthews, K., Egami, E., Becklin, E. E., Weinberger, A. J., Ressler, M., Werner, M. W., Evans, A. S., Scoville, N. Z., Surace, J. A., & Condon, J. J. 2000, AJ, 119, 509

Soifer, B. T., Neugebauer, G., Matthews, K., Egami, E., Weinberger, A. J., Ressler, M., Scoville, N. Z., Stolovy, S. R., Condon, J. J., & Becklin, E. E. 2001, AJ, 122, 1213

Soifer, B. T., Sanders, D. B., Madore, B. F., Neugebauer, G., Danielson, G. E., Elias, J. H., Lonsdale, C. J., & Rice, W. L. 1987, ApJ, 320, 238

Steidel, C. C., Adelberger, K. L., Giavalisco, M., Dickinson, M., & Pettini, M. 1999, ApJ, 519, 1

Steidel, C. C., Giavalisco, M., Dickinson, M., & Adelberger, K. L. 1996, AJ, 112, 352

Turatto, M., Benetti, S., Cappellaro, E., & Bufano, F. 2010, Central Bureau Electronic Telegrams, 2252, 1

Veilleux, S., Kim, D.-C., Sanders, D. B., Mazzarella, J. M., & Soifer, B. T. 1995, ApJS, 98, 171

Zink, E. C., Lester, D. F., Doppmann, G., & Harvey, P. M. 2000, ApJS, 131, 413

Appendix A

The galaxy sample

CGCG011-076

This is an intermediate galaxy with bars (SAB(s)b), located at about 102.4 Mpc (z=0.02). Belonging to the luminosity class of LIRGs, is a IR object with $\log L_{FIR}/L_{\odot} = 11.27$. On this galaxy there are no works devoted in the literature and are not supernovae exploded in the past. In figure A.1 we show the HAWK-I K-band image of this galaxy.

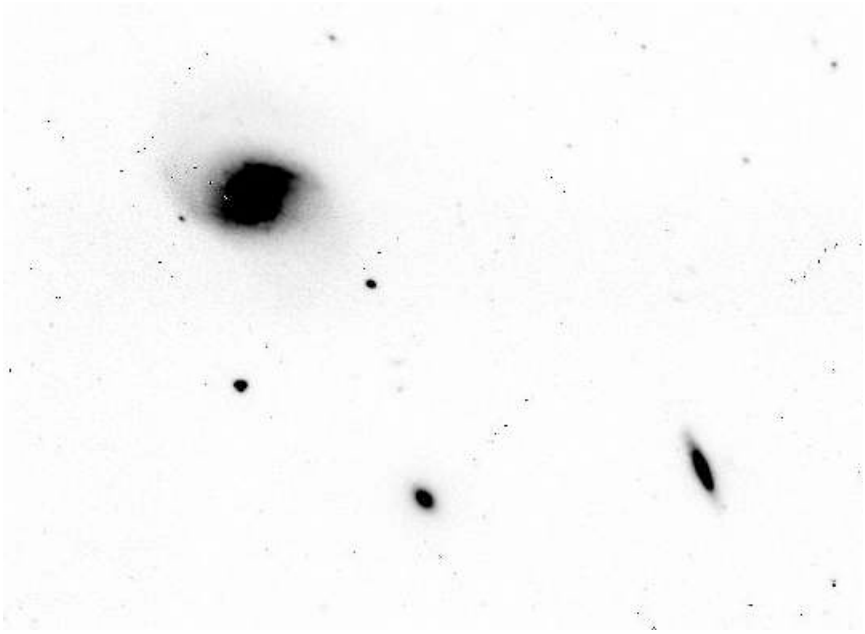

Figure A.1: HAWK-I K-band image of the galaxy CGCG011-076.

CGCG043-099

CGCG043-099 or VV 283 is a spiral galaxy located at about 155 Mpc ($z \simeq 0.04$) that belong to the luminosity class of LIRGs. Like many merging systems, VV 283 is a very luminous infrared system, radiating $\log L_{FIR}/L_{\odot} = 11.58$. From figure A.2 VV 283 looks like a single peculiar galaxy, but is in fact a pair of merging galaxies. A tidal tail swirls out from a messy central region and splits into two branches. The upward twisting branch is brightened by luminous blue star knots.

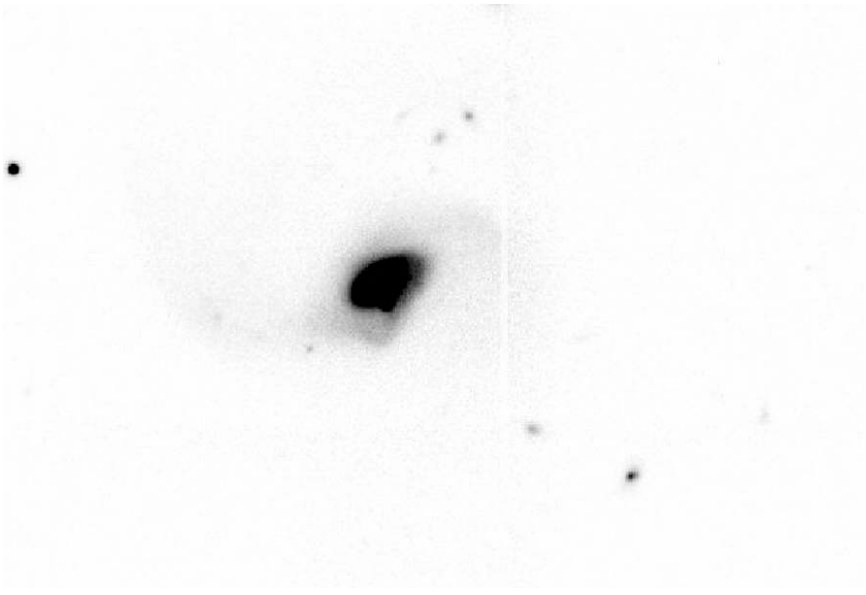

Figure A.2: HAWK-I K-band image of the galaxy CGCG043-099.

ESO148-IG002

ESO 148-IG002 (A.3)is one of the most luminous infrared galaxies known ($L_{IR} \simeq 2.3 \times 10^{12} L_{\odot}$). The bulk of this radiation originates from a warm dust component heated by a burst of star formation. This galaxy consist of two former disc galaxies in close interaction. Two nuclei, separeted by 5 kpc in projection, dominate the central region, from which two arms emanate to a distance of 40 kpc. Centered on the nucleus of one of galaxies, a flattened system of ionized gas of relatively high ionization is found. The emission-lines originating in this region exhibit broad wings, extending towards the blue. The extension of these wings corresponds to a velocity difference of at least $1500 kms^{-1}$. the spectrum of the central region is of moderate excitation and the lines are broad, having widths typical of Seyfert 2 galaxies. The radial velocity of the ionized gas is about $300 km\, s^{-1}$ lower than that of the stars.

spectral features characteristic of Wolf-Rayet stars (predominantly of type WN) are present over the whole central region (Johansson & Bergvall, 1988).

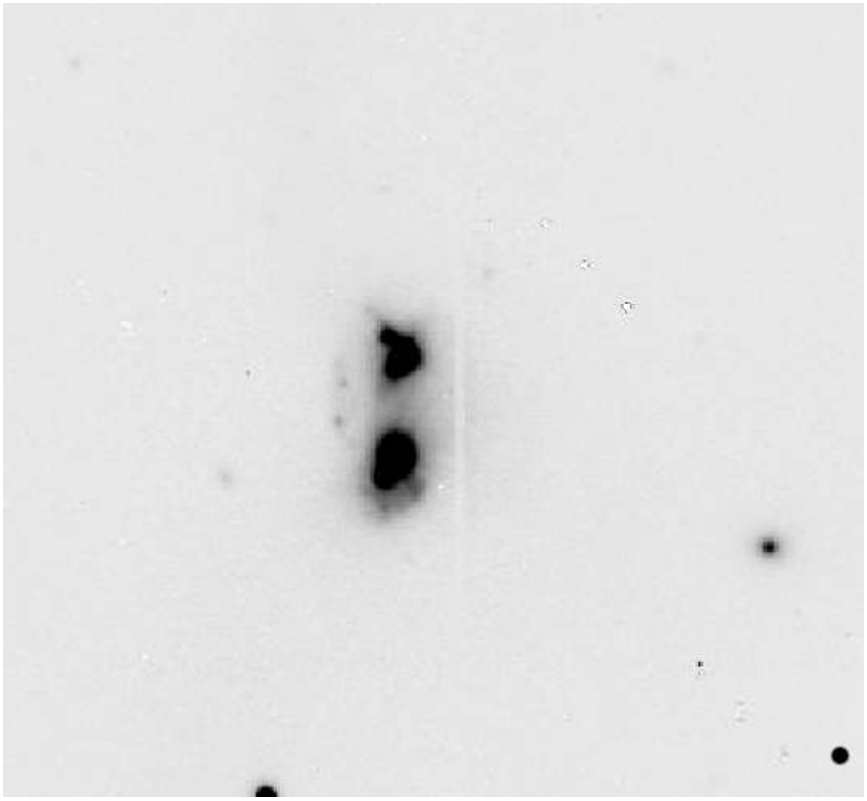

Figure A.3: HAWK-I K-band image of the galaxy ESO 148-IG002. Is clearly visibile the structure with two nuclei.

ESO239-IG002

ESO 239-IG002 is a LIRGs with $\log L_{FIR}/L_{\odot} = 11.75$ located at about 174 Mpc ($z \simeq 0.043$). this galaxy is most likely the result of a cosmic collision or a lengthy merger process that will eventually result in an elliptical galaxy. The messy intermediate stage is a galaxy with long, tangled tidal tails that envelope the galaxy's core (fig. A.4).

ES244-G012

ESO 244-G012 (A.5) is a luminous IR object ($L_{FIR} > 10^{11} L_{\odot}$)that presents the general appearance of a peculiar distorted galaxy. The most prominent

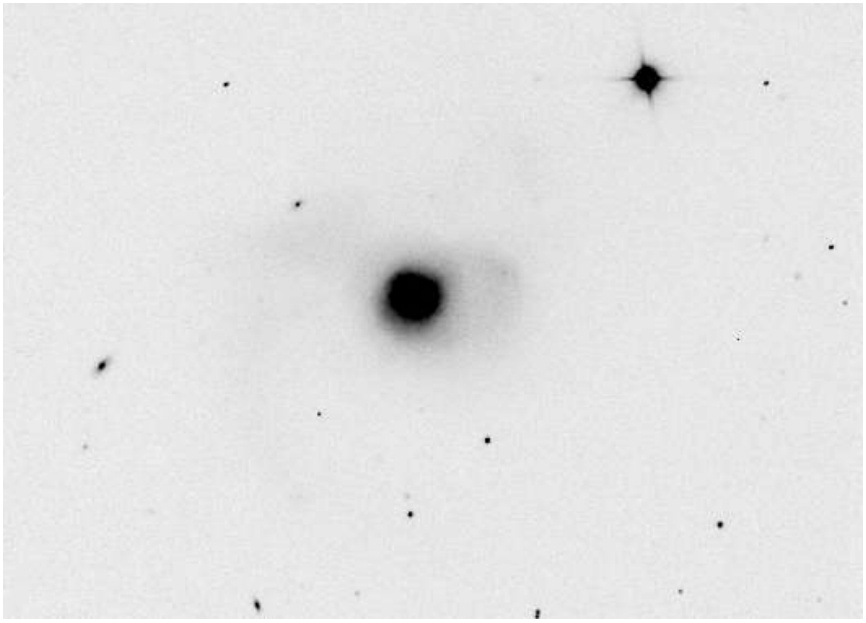

Figure A.4: HAWK-I K-band image of the galaxy ESO 239-IG002

features of its central body are two distinct nuclei separated by about 18". The northern one shows tails/jets ; a long asymmetric tail or arm is clearly visible up to about 40 kpc from the center of the main body. These characteristics are indicative of strong interactions between galaxies or of colliding or merger systems.
Its far infrared colors clearly indicate this object as a starburst. IR flux comes from dust heated as a consequence of an intense star formation activity. This activity is originated from molecular gas that generally is largely observed to be concentrated toward the centers. Consequently, although we primarily assume that the IR flux is mainly produced in the two nuclei, the highest concentration of molecular gas found around the northern one indicates that the starburst characteristics deduced from IR data are in reference to this nucleus. Among several possibilities this could indicate that the southern component is relatively young or has retarded star formation, whereas the northern one is older with a considerable amount of gas available. Moreover, the starburst nature of the northern nucleus, observed in the optical range, is in agreement with the properties of ESO 244-G012 detected in the far infrared, and with the CO and radio observations (Agüero et al., 2000).

ESO264-G036

ESO264-G036 is a single-barred object, located at about 84 Mpc ($z \simeq 0.02$). Is a luminous infrared galaxy with $\log L_{FIR}/L_{\odot} = 11.24$. Its starburst com-

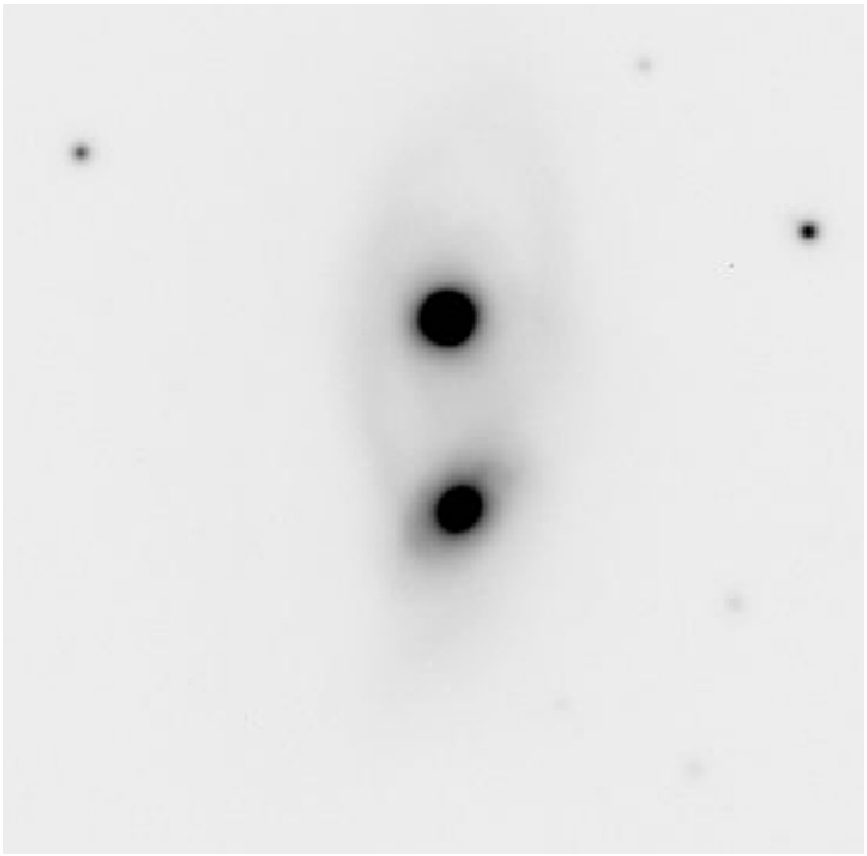

Figure A.5: HAWK-I K-band image of the galaxy ESO 244-G012. Is clearly visibile the structure with two nuclei.

ponent defined in Rowan-Robinson & Crawford (1989) suggests a transition case between starburst and non-starburst galaxies. The well-defined primary bar ends at $\simeq$18" where a slight twist is observed due to the start of the spiral arms. In the inner region (within the innermost 2.5"), there is probably a star-forming region, close to the bar ends (Greusard et al., 2000).

ESO286-IG019

ESO286-IG019 (A.7) is an exceptionally luminous source of infrared radiation ($L_{IR} \sim 10^{12} L_{\odot}$), originating in warm dust heated by young stars. This galaxy is the result of the merging of two disk galaxies. The galaxy has undergone an intense burst of star formation that ended about 8 Myr ago. The total mass of the old stars in the galaxy is about $3^{11} M_{\odot}$, and the mass of young stars formed in the recent starburst is about $8 \times 10^9 M_{\odot}$, or $\sim 2\%$ of the total stellar mass. In addition to the stars, the galaxy also contains

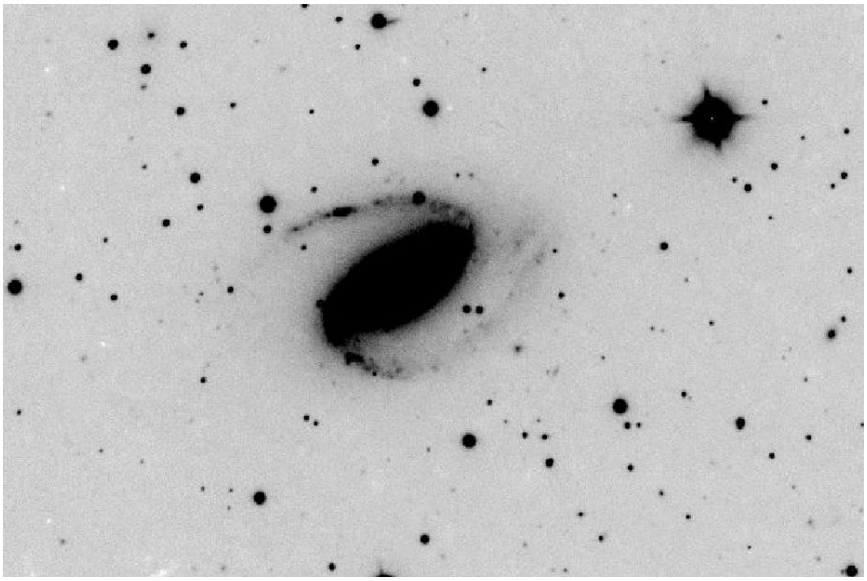

Figure A.6: HAWK-I K-band image of the galaxy ESO 264-G036

a large amount of molecular hydrogen. The main source of ionization for the interstellar medium are photoionization from the young stars, in combination with interstellar shock originating from the star-forming region (e.g. supernova winds, Wolf-Rayet winds, etc.).
ESO286-IG019 shows only one nucleus. Emanating form the central component are two tidal tails, one very prominent, extending to the south, and another, much shorter, extending to the northwest (Johansson, 1991).

ESO440-IG058

ESO440-IG58 or VV 835 is a pair of luminous galaxies ($\log L_{FIR}/L_{\odot} = 11.33$) located at 6.6 Mpc ($z \sim 0.02$). In figure A.8 we can see that the southern galaxy is the dominant member of the pairs. Using ATCA, Hill et al. (2001) found that southern galaxy contains an extended radio emission that probably traces the star formation in the disk of the galaxy.

ESO507-G070

ESO507-G070 is an irregular nearby galaxy, located at 94 Mpc ($z \sim 0.2$) belongig to the luminosity class of LIRGs ($\log L_{FIR}/L_{\odot} = 11.44$). ESO 507-70 is an odd-looking galaxy that is probably the remnant of an earlier merger process. It is a chaotic swirl of gas, dust and stars with no sign of the conjectured original spiral or elliptical structure, now lost and distorted beyond recognition in a gravitational encounter with another galaxy (Fig. A.9).

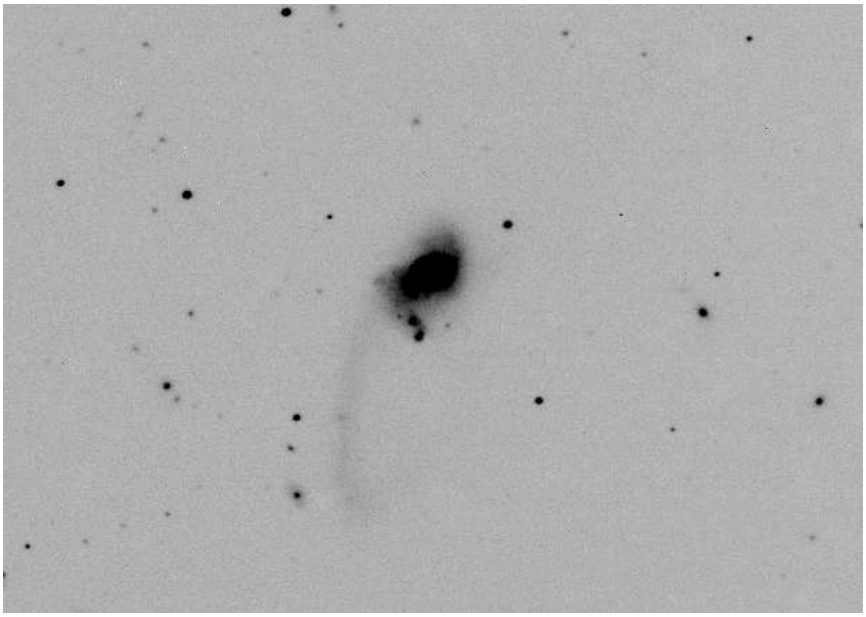

Figure A.7: HAWK-I K-band image of the galaxy ESO 286-IG019. This galaxy have one central nucleus, with two tidals tail emanating from this central component: one is very prominent, extending to the south.

IC1623

IC1623 (= VV114 = Arp 236), located at a distance of 80 Mpc, is an interacting systems undergoing vigorous starburst activity. Its infrared luminosity is $L_{IR} = 10^{11.5} L_{\odot}$ making it a LIRG and one of the brightest objects of the IRAS Bright Galaxy Sample. It appears to be an early-stage merger of two galaxies (see A.10) that are aligned east-west with a projected nuclear separation of ∼6 kpc and therefore referred in the literature as VV114E and VV114W. At optical wavelengths, VV114 shows a highly disturbed morphology with very faint tidal tails extending over 25 kpc from the center (Arp 1966). The western component, VV114W, is more extended than the eastern one, and dominates the emission in the visible. ((Knop et al., 1994)). VV114 contains a large amount of dust ($M_{dust} = 1.2 \times 10^8 M_{\odot}$) distributed across the galaxy with a dust temperature , of 20-25 K. About half of the warmer dust traced in the mid- IR (MIR) is associated with VV 114E, where both compact (nuclear region) and extended emission are found ((Le Floc'h et al., 2002). The MIR spectrum also shows a sign of an AGN in VV 114E ((Le Floc'h et al., 2002)). Alonso-Herrero et al. (2002)((Alonso-Herrero et al., 2002)) detected abundant Hii regions in VV 114E and in the overlap region using the narrowband Paa images. Scoville et al. (2000) ((Scoville et al., 2000)) imaged the near-IR (NIR) emission using the Near- Infrared Camera

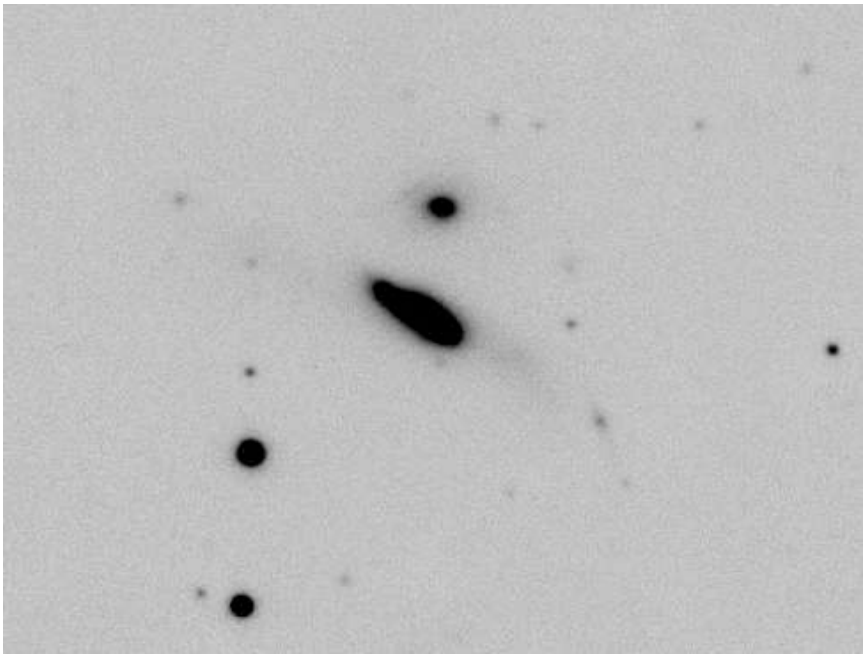

Figure A.8: HAWK-I K-band image of the galaxy ESO 440-IG058. Are visible the two component of this pair, in which the southern member is the dominant one.

and Multi-Object Spectrometer on board the Hubble Space Telescope and found that the highly optically obscured VV 114E is the brighter of the two in the NIR. Far-UV imaging using the Space Telescope Imaging Spectrograph found several hundred young star clusters in VV 114W, while no UV emission was found in VV 114E ((Goldader et al., 2002)), which suggests that most of the activity in VV 114E is obscured by dust and not visible in the UV emission.

IC2545

IC2545 seems to be a single S-shaped object (Fig. A.11) but is actually a pair of merging galaxies located at about 137 Mpc ($z \sim 0.03$) and very luminous in the infrared ($\log(L_{FIR}/L_{\odot}) \sim 11.66$). The two cores of the parent galaxies in the central region are not visible in our HAWK-I images. Other telltale markers for the collision include two pronounced tidal arms of gas and stars flung out from the central region. The tidal arm curving upwards and clockwise in the image contains a number of blue star clusters. IC 2545 glows strongly in the infrared part of the spectrum, another sign that it is a pair of merging galaxies.

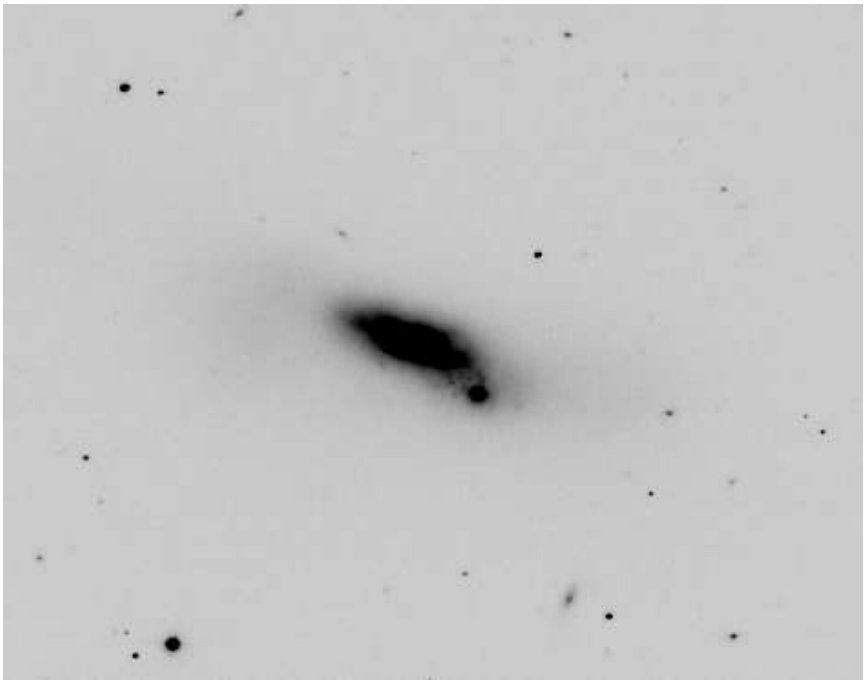

Figure A.9: HAWK-I K-band image of the galaxy ESO 507-G070.

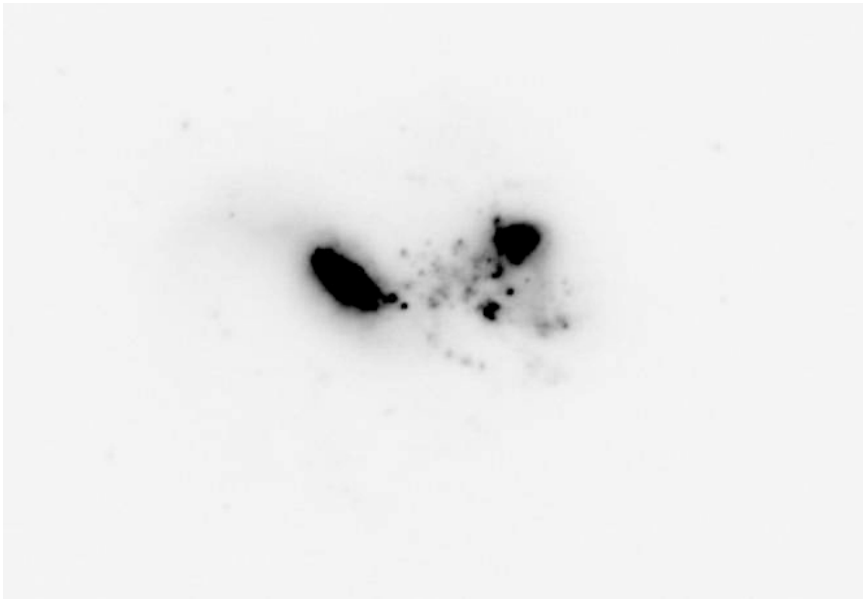

Figure A.10: HAWK-I K-band image of the galaxy IC 1623 (VGV 114). Are clearly visible two nuclei with numerous other compact regions where the emission in the NIR is important.

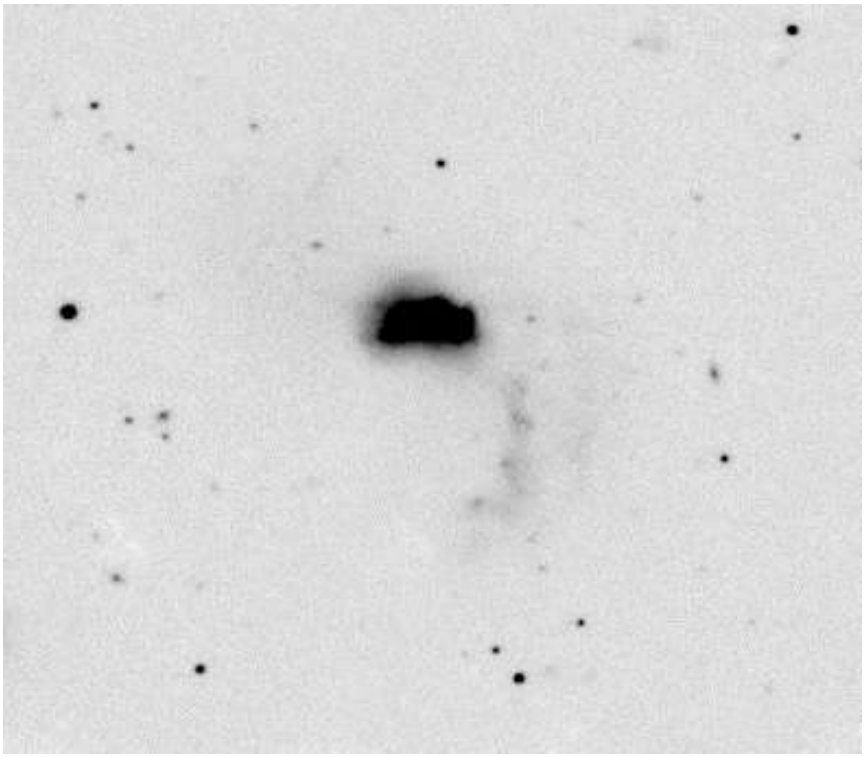

Figure A.11: HAWK-I K-band image of the galaxy IC 2545, with the two visible tidal arms of stars and gas flunging out from the central region.

IC2810

IC 2810 is a disk galaxy viewed nearly edge-on. Is classified as LIRG with a $Log(L_{FIR}/L_{\odot}) \sim 11.60$ and is located at about 141 Mpc ($z \sim 0.034$). In the NIR HAWK-I image (fig. A.12) the most prominent features are bars that extend for about 8-8.5 kpc to the northwest and southeast. The continuum image shows a bright nucleus and a linearly extended disk; in contrast, the H_{α} image reveals a warped structure that is more distinct on the south side of the nucleus. The brightest H_{α} emission in the nucleus is extended by $\sim 3''$ ($\sim$2 kpc) toward the north (Hattori et al., 2004). There is a small companion galaxy (IC 2810b), which is also edge-on $\sim$70" ($\sim$48 kpc) to the southeast. Compact H_{α} emission is detected from the nucleus (Hattori et al., 2004).

IC4687/6

IC 4687 forms a triplet with two other galaxies: IC 4686, near IC 4687 (the galaxy at the top) and IC 4689, the galaxy at the bottom of the figure A.13. IC 4687 has a chaotic body of stars, gas and dust and a large curly tail to

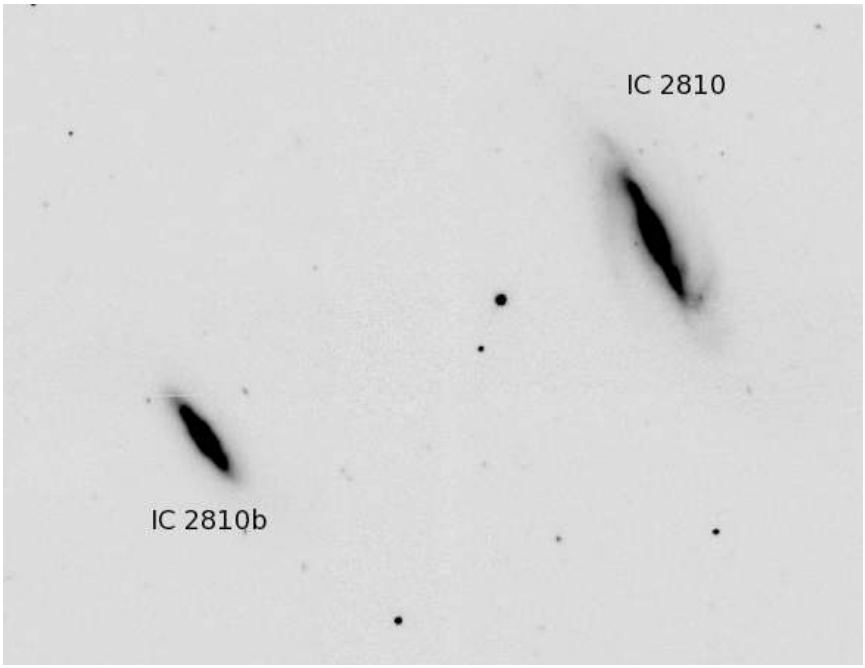

Figure A.12: HAWK-I K-band image of the galaxy IC 2810. At about 48 kpc to the southeast there is a small companion, IC 2810b.

the left. The two companions are partially obscured by dark bands of dust. The interacting triplet is 69.6 Mpc away from Earth, in the constellation of Pavo, the Peacock, at redshift of 0.017 and with $\log(L_{FIR}/L_{\odot} \sim 11.39)$

IRAS 12224-0624

IRAS 12224-0624 is a single, nearby ($\sim$108 Mpc, $z \sim 0.02$) and luminous infrared galaxy ($\log(L_{FIR}/L_{\odot} \sim 11.30)$). In figure A.14 we can see the isolation of the object, for the which are not present particular work in the literature.

IRAS 14378-3651

Our HAWK-I image (Fig. A.15) show a group of isolated objects, located at about 276 Mpc ($z \sim 0.068$, is the most distant object of our sample), and exceptionally luminous in the infrared ($\log(L_{FIR}/L_{\odot} \sim 12.08)$) with a central elliptical-like galaxy that has no remarkable features (see also Bushouse et al. (2002)). The HST images reveal that the main galaxy has multiple shells and an inner spiral pattern, along with a faint companion to the south. The center of the main galaxy appears to have a single nucleus in both the optical

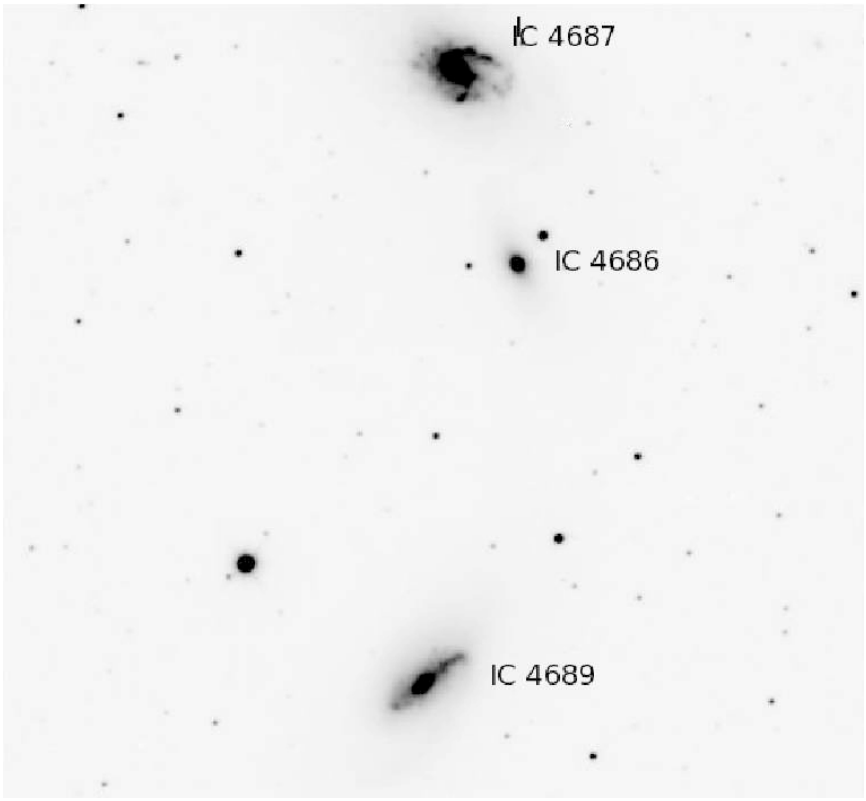

Figure A.13: K-band HAWK-I images of the galaxies triplet with IC 4687 (top), Ic 4686 (in the middle) and Ic 4689 (bottom).

and near-IR HST images. The nucleus in the H-band image is point-like, showing the instrumental diffraction spikes. The shells and inner arms are faintly visible in the H-band image, as are two bright spots that appear in the outer envelope.

IRAS 16399-0937

IRAS 16399-0937 consists of a close pairs of galaxy (Fig. A.16) with a separation of only 3 kpc, located at about 112.6 Mpc ($z \sim 0.03$) with IR luminosity $\log(L_{FIR}/L_{\odot} \sim 11.55)$. As in other close pairs, in contrast to near IR luminosity distribution, all or the main part of the mid-Ir emission is emitted from one nucleus in this double nuclei system. In this case the two nuclei are of roughly the same size and luminosity in near-IR band, albeit most of the mid-IR emission (>90%) originates only from one of the nuclei in this case the northern nucleus, (Haan et al., 2011)).

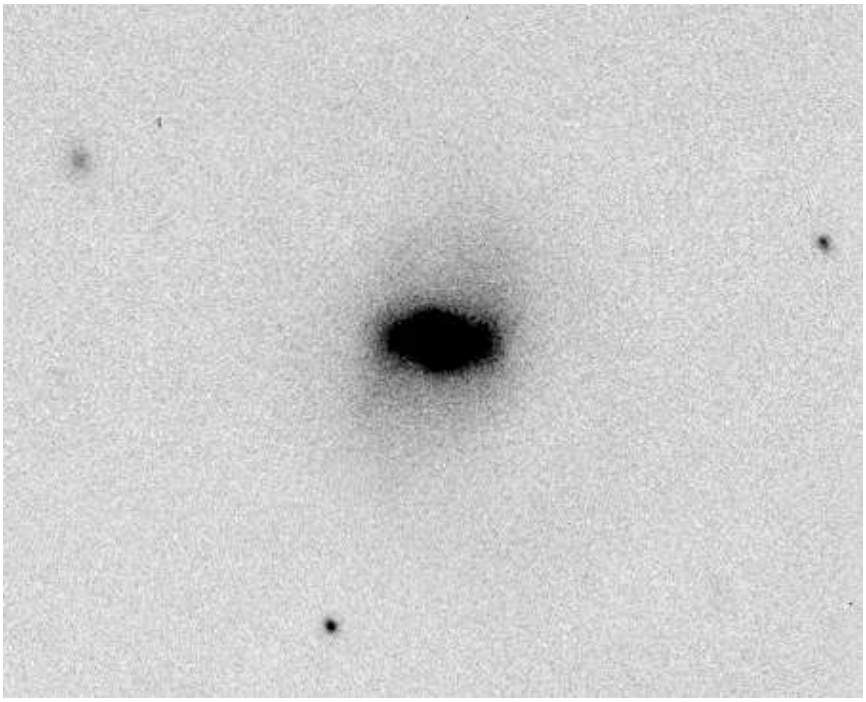

Figure A.14: K-band HAWK-I images of the galaxy IRAS12224-0624

IRAS 17207-0014

IRAS 17207-0014 is the most luminous infrared object of our sample with infrared luminosity $\log(L_{FIR}/L_{\odot} \sim 12.42)$, located at about 178 Mpc ($z \sim 0.04$). From fig. A.17 it seems a single object but his very high IR luminosity and the presence of several tidal features suggests that this galaxy is likely a remnant of a complete merger.

IRAS 18090+0130

IRAS 18090+0130 consist of two interacting spiral galaxies (fig. A.18) located at 121 Mpc ($z \sim 0.03$) with high infrared luminosity ($\log(L_{FIR}/L_{\odot} \sim 12.42)$). The galaxy to the right displays a dim plume of luminosity that extends to the left in the direction of the second spiral. Both galaxies are partly obscured by dust lanes.

MCG -02-01-051/2

MCG -02-01-051/2 or Arp 256 (figure A.19 is composed of two galaxies separated by 54". Arp 256 N (north) is an SB(s)c galaxy, while Arp 256 S (south) is an SB(s)b galaxy. At redshift z = 0.027, their distance has been

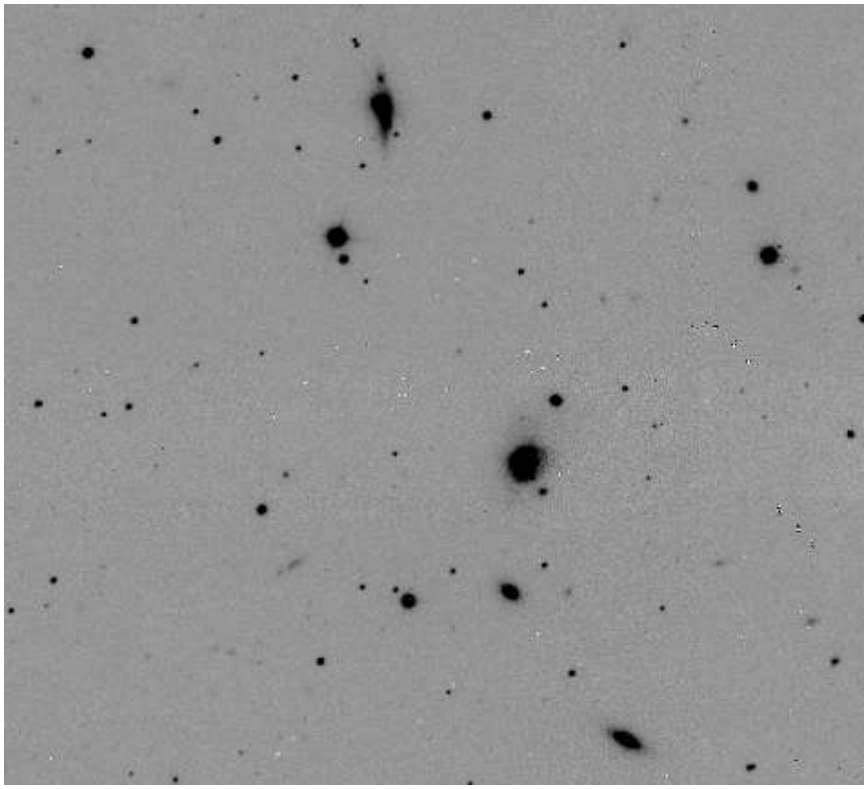

Figure A.15: K-band HAWK-I images of the galaxy IRAS 14378-3651.

calculated at 98.1 Mpc, with a projected nuclear separation of 29 kpc. The IR luminosity is $\sim 10^{11.2} L_{\odot}$, but neither galaxy is known to have active galactic nucleus (AGN) activity and both show HII region-like spectra. The relatively large separation between the galaxies in Arp 256 suggests that the system is in an early phase of merging and thus is of interest as an observational example of a LIRG in the early stages of the formation process (Chen et al., 2002).

MCG-03-04-014

MCG-03-04-014 is a single spiral galaxy located at about 142 Mpc ($z \sim 0.035$) with high infrared luminosity $\log(L_{IR}/L_{\odot}) \sim 11.59$. Despite in fig. A.20 seems to be a single object without strong tidal features, it is possible, as suggests the high infrared luminosity, that is a remnant of merger or have experienced tidal interactions in the past.

NGC 34

NGC 34 is a luminous infrared galaxy (LIRG) located at 85.2 Mpc, with an infrared luminosity of $\log(L_{IR}/L_{\odot}) \sim 11.3$, suggesting that both the

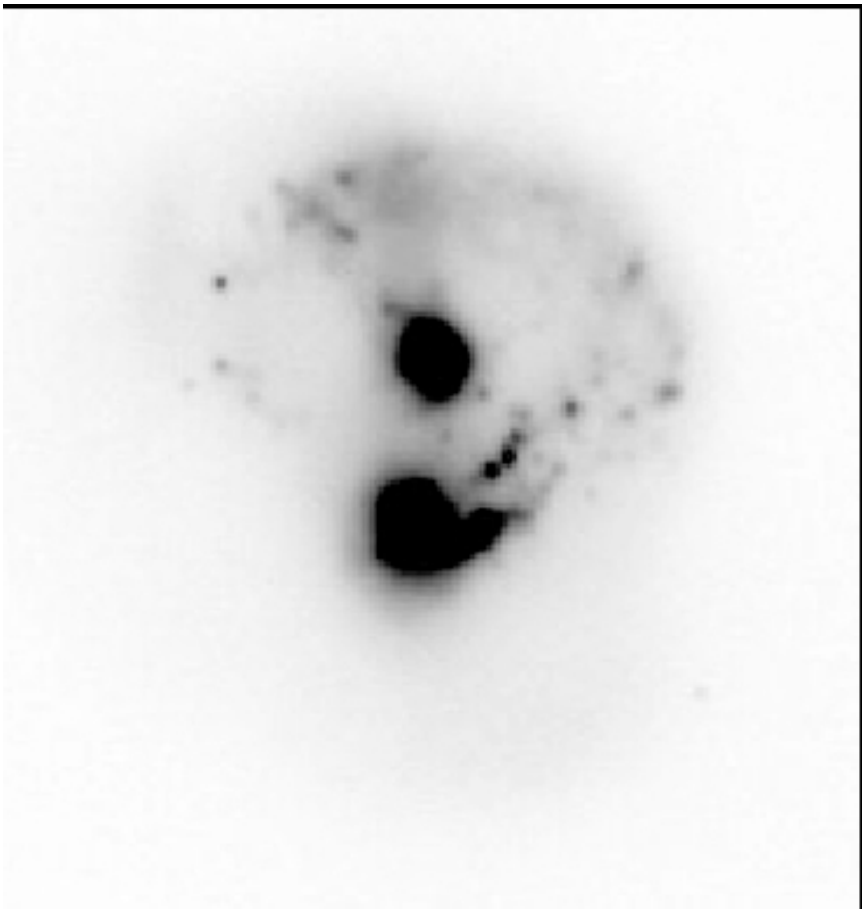

Figure A.16: K-band HAWK-I images of the galaxy IRAS 16399-0937, in which are visible the two near nuclei.

starburst and the AGN contribute significantly to it. The optical nuclear spectrum of NGC 34 also shows signs of the presence of an AGN and starburst. It appears composite and exhibits a weak [OIII] emission line relative to H_β or H_α, placing NGC 34 in a transition category of objects with nuclear spectra between starburst and Seyfert 2. The galaxy features a single, very red nucleus, a main spheroid containing a prominent blue central disk and much outer fine structure, and two linear tidal tails to the northeast and south of the main body reveal this to be a remnant of two merged disk galaxies. In addition to these tails, there are other optical features typical of a merger remnant: a single nucleus and an envelope that contains dust lanes, ripples, fans, and jets of luminous matter. Also, there is a cloud of luminous debris to the northwest of the nucleus (NW cloud), whose origin could be either remnant material from one of the progenitors or a companion (A.21).

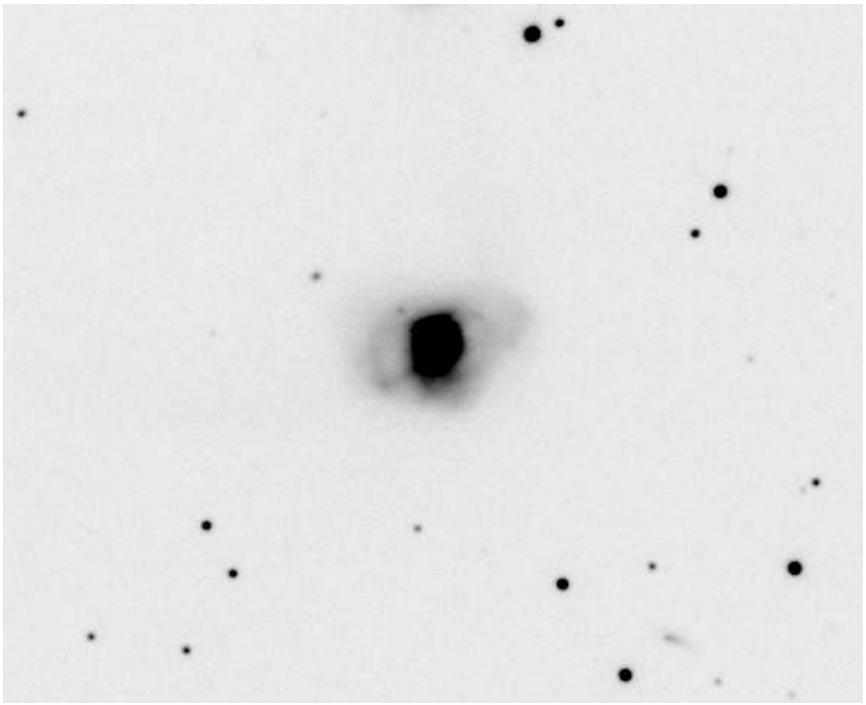

Figure A.17: K-band HAWK-I images of the galaxy IRAS 17207-0014

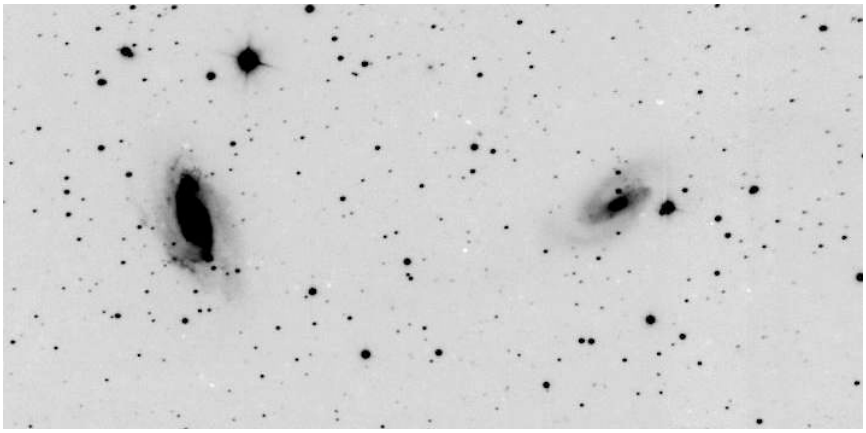

Figure A.18: K-band HAWK-I images of the galaxy IRAS 18090+0130.

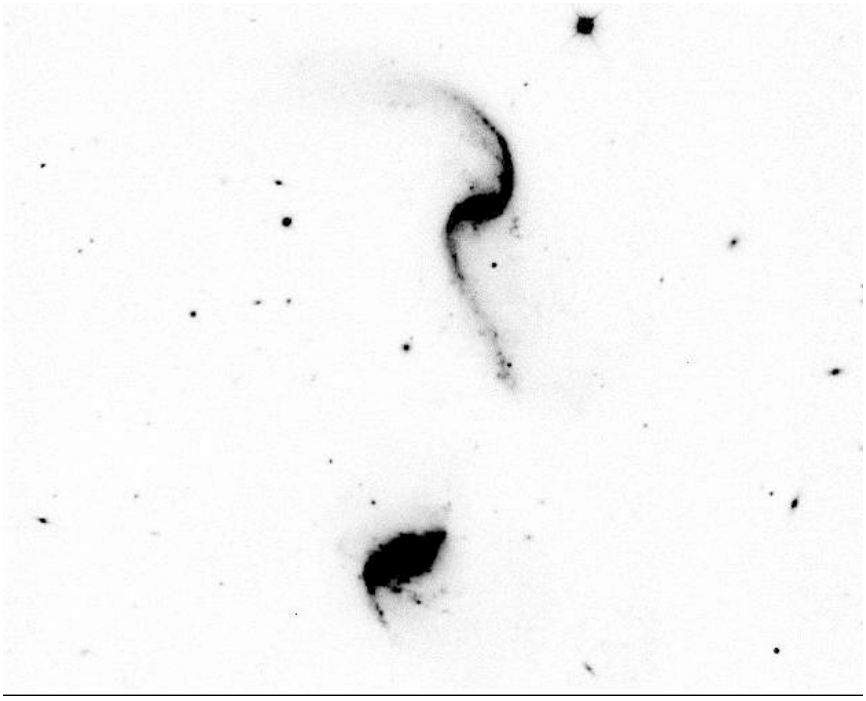

Figure A.19: HAWK-I K-band image of the galaxy MCG -02-01-051/2, a double interacting galaxies in an early phase of merging.

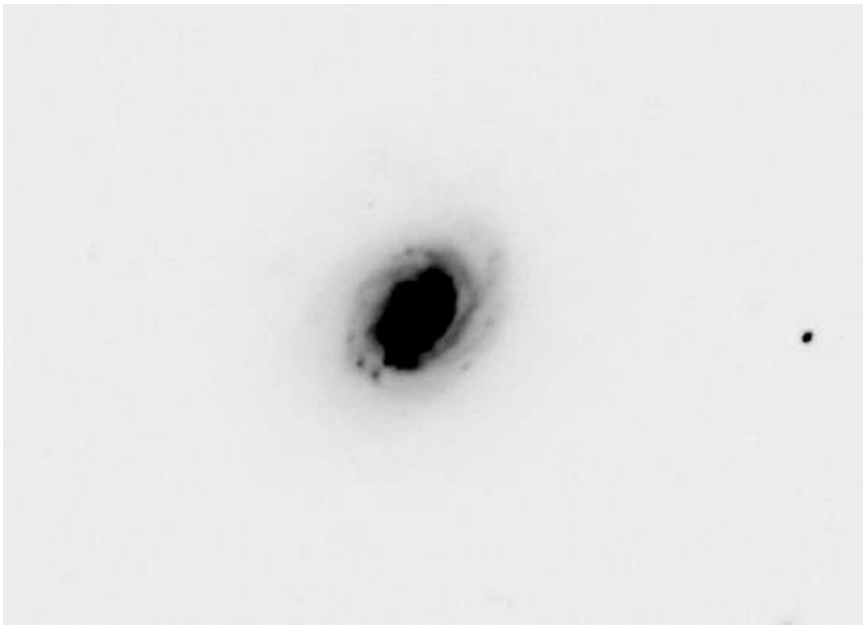

Figure A.20: HAWK-I K-band image of the galaxy MCG-03-04-014.

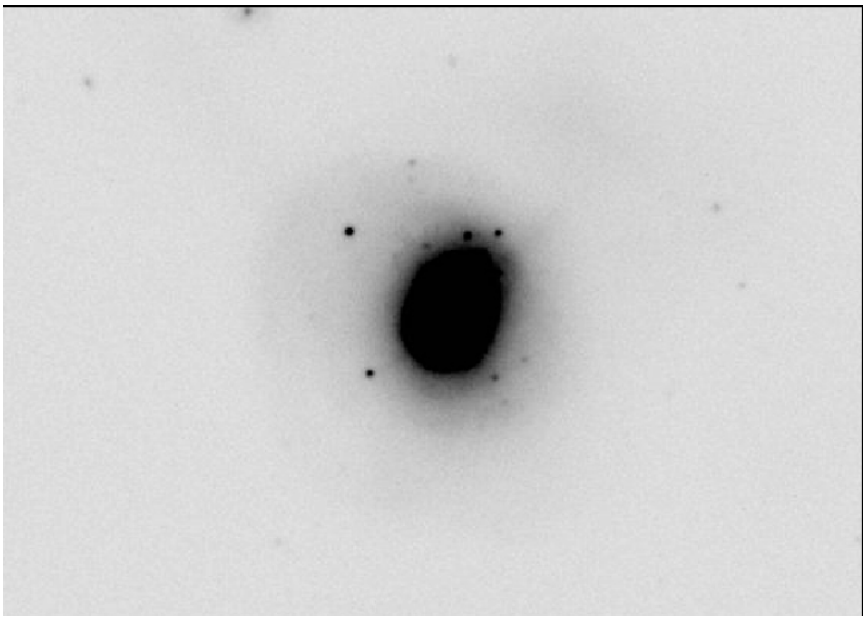

Figure A.21: HAWK-I K-band image of the galaxy NGC 0034, characterized by a single nucleus and twolinear tidal tails.

NGC 232

Located at about 91 Mpc ($z \sim 0.02$), NGC 232 is a luminous infrared barred spiral galaxy ($\log(L_{FIR}/L_{\odot} \sim 11.51)$) with two companion (NGC 235 and PGC 2570, see fig. A.22) at about 30 kpc. In the northern spiral arm of this galaxy exploded the type Ia SN 2006et, as indicated in the same figure (obviously, the supernova is not visible but is only indicated the position where this object exploded). H_{α} image shows an H_{α} knot in between the two galaxies and is likely to be a result of the interaction. The knot can not be seen in R-band continuum images, indicating that it is either a region of current star formation, or else (more probably) indicates the position of shock-excited gas in the merging system (Dopita et al., 2002).

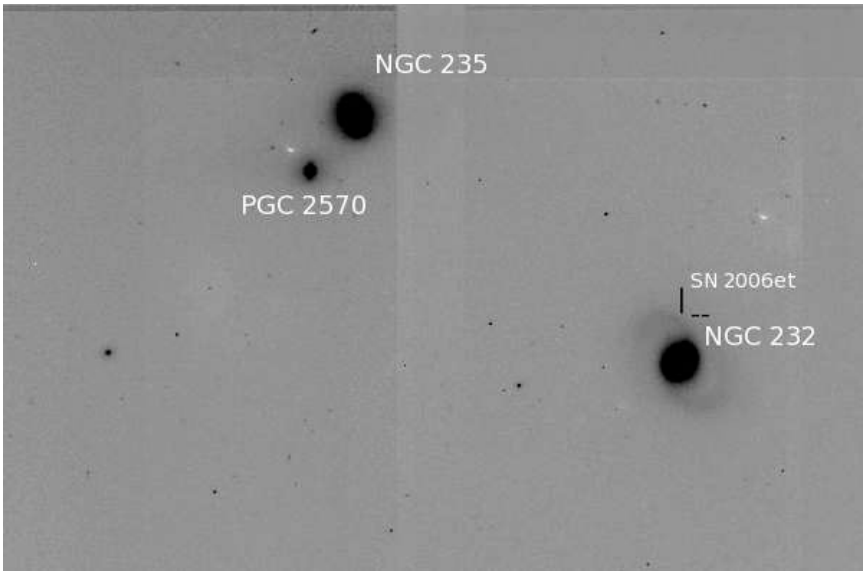

Figure A.22: HAWK-I K-band image of NGC 232, with two far companion: NGC 235 and PGC 2570. Is also indicated the position where the SN2006et exploded in September of 2006.

NGC 3110

This galaxy is paired with MCG -01-26-013 (fig. A.23, located at about 69 Mpc ($z \sim 0.016$), at a separation of 1.9'. Both the R-band continuum and H_{α} images exhibit strong knots in the spiral arms of NGC 3110. The H_{α} emission in MCG -01-26-013, however, is concentrated toward its nucleus (Dopita et al., 2002). The IRAS source has been associated with NGC 3110 rather than its companion (Zink et al., 2000), with $\log(L_{FIR}/L_{\odot} \sim 11.29)$.

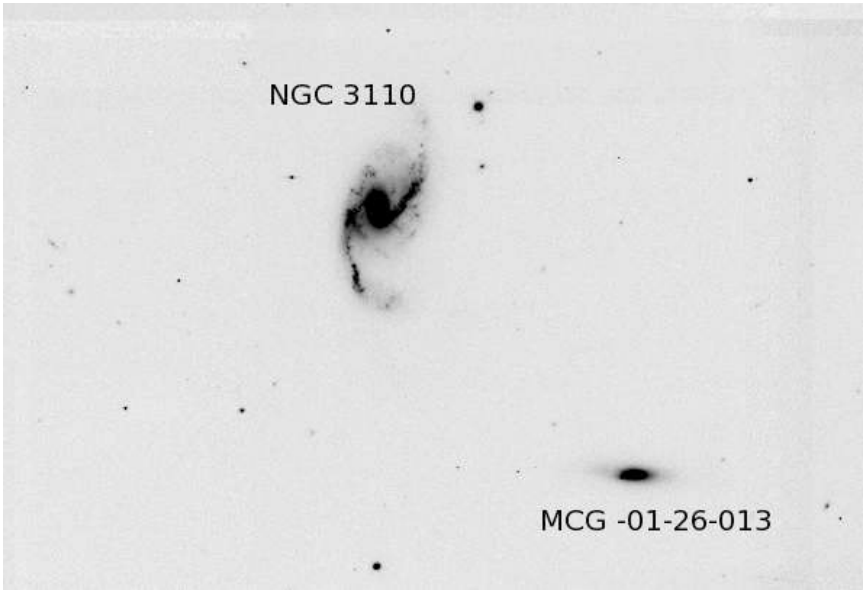

Figure A.23: HAWK-I K-band image of NGC 3110 with MCG -01-26-013.

NGC 5010

NGC 5010 is an intermediate (S0) galaxy (fig. A.24) and is the nearest galaxy of our sample. Is in fact located at only 41 Mpc ($z \sim 0.09$) and, at the same time, the least luminous with $\log(L_{FIR}/L_{\odot} \sim 10.84$. This implies that this galaxy has the lowest SFR among our smple of galaxies, with only 11.79 $M_{\odot}yr^{-1}$.

NGC 5331

NGC 5331 (A.25) is a pair of interacting galaxies with their spiral arms beginning to touch. There is a blue trail flowing to the right of the system. NGC 5331 is very bright in the infrared, with about a hundred thousand million times the luminosity of the Sun ($\log(L_{FIR}/L_{\odot} \sim 11.5)$), placing this galaxy among the LIRGs. It is located in the constellation Virgo, the Maiden, at about 137 Mpc.

NGC 6240

Due to its proximity, NGC 6240 (A.26) ($z \sim 0.024, D \simeq 98Mpc$) is one of the brightest objects in the IRAS All-Sky Survey and was one of the early identified LIRGs with a total infrared luminosity of about $10^{11.7}L_{\odot}$. Optical studies of NGC 6240 reveal a morphologically irregular galaxy with clear tidal extensions, two nuclei and large dust lanes, strongly suggesting a

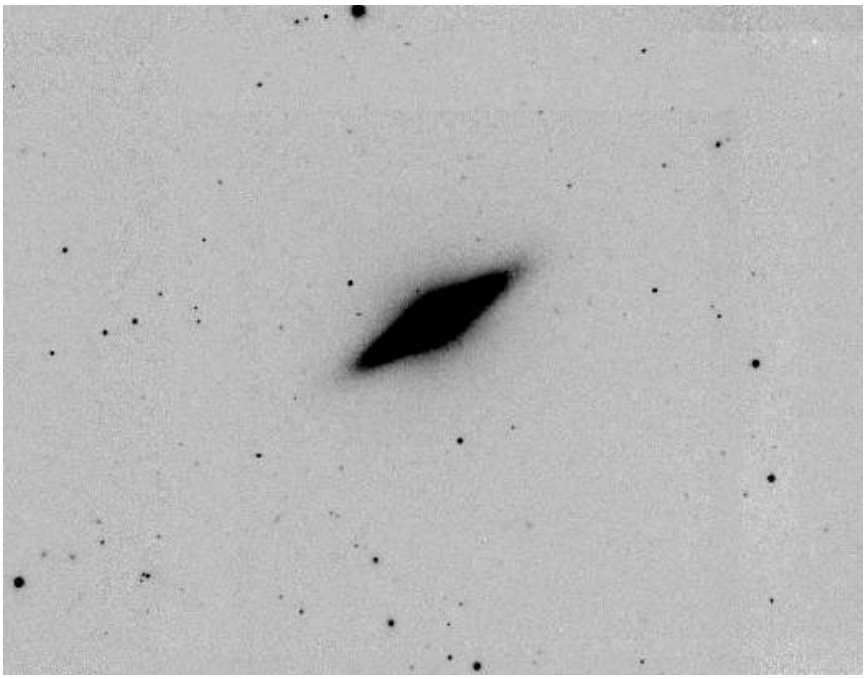

Figure A.24: HAWK-I K-band image of NGC 5010

merging system. The two galactic nuclei found in the central region have a projected separation between 1".5 and 1".8 at X-ray and radio wavelengths, but the observed distance between the nuclei depends on the wavelength at which they are observed, indicating large amounts of dust extinction in the center of the galaxy.

NGC 6926

NGC 6926 is a spiral galaxy (fig. A.27), which makes a pair with a dwarf elliptical NGC 6929 located 4' east (not visible in figure A.27, and is disturbed by the companion. This galaxy radiates luminous infrared emission of $L_{FIR} \sim 1.4^{11.1} L_{\odot}$, placing this galaxy in the LIRGs class. The distance to the galaxy has been estimated to be 80 Mpc ($z = 0.02$). The galaxy has been classified into Seyfert 2 from optical spectroscopy.

NGC 7130

NGC 7130 (A.28), a nearby galaxy ($\sim 64 Mpc, z = 0.016$) with high infrared luminosity (about $10^{11.2} L_{\odot}$) is an example of a starburst/AGN composite galaxy, classified on the basis of optical emission line ratios as a normal Seyfert2 type.

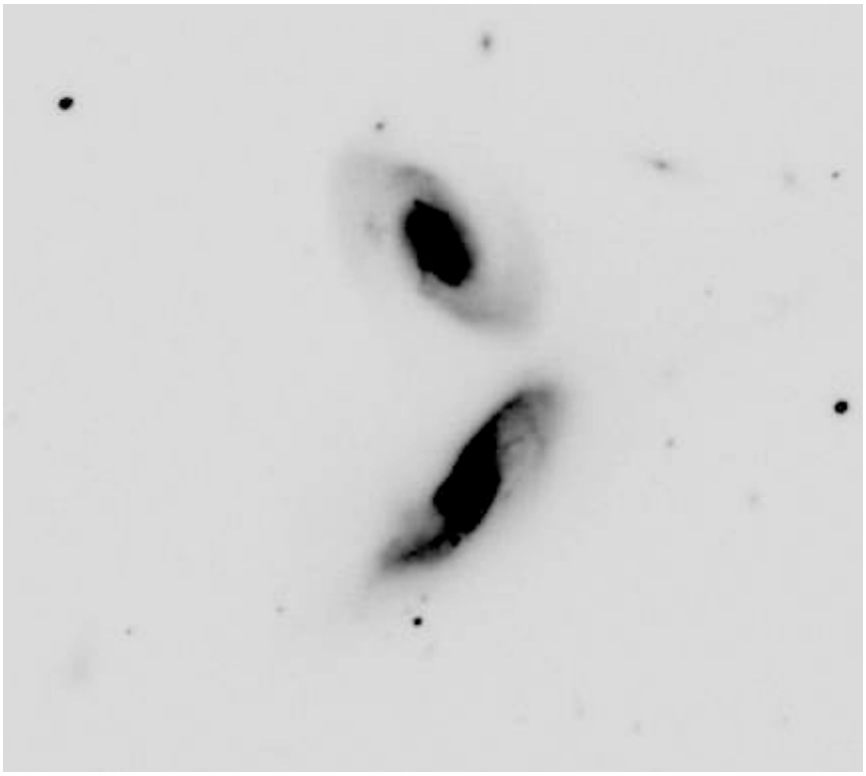

Figure A.25: HAWK-I K-band image of NGC 5331, a pair of interacting spiral galaxies.

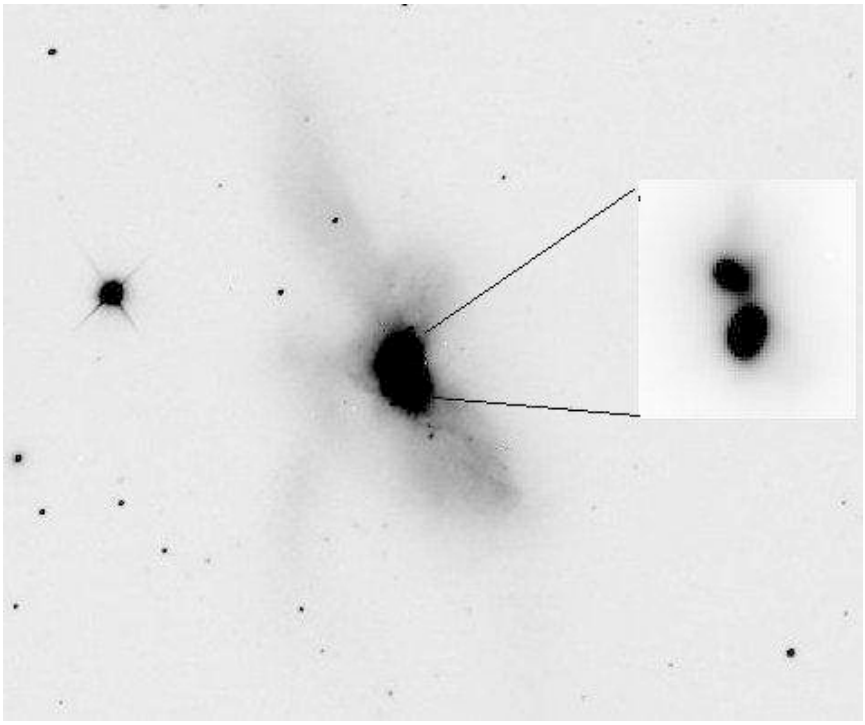

Figure A.26: HAWK-I K-band image of NGC 6240, in which are cleraly visible the tidal extensions, and the two nuclei in the box zoom in the right.

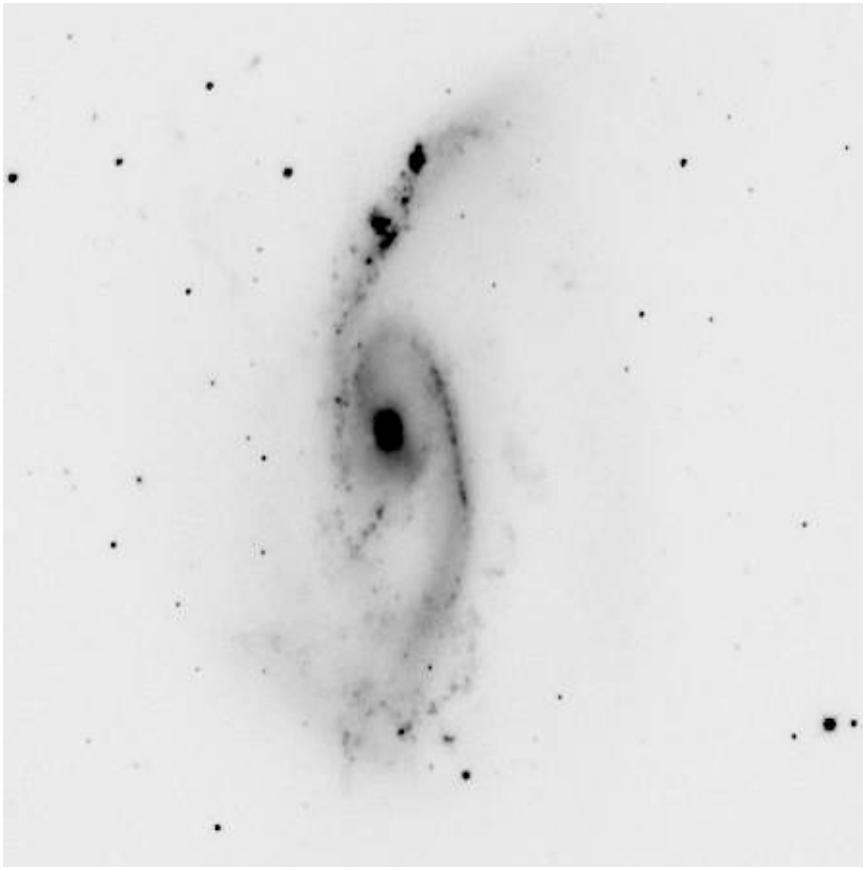

Figure A.27: HAWK-I K-band image of NGC 6926, a spiral galaxies with evident arms in the north and south direction.

The NGC 7130 K band shows an inner bar oriented at P.A.=0°not visible at optical wavelengths. In the digital sky survey it can be seen that NGC 7130 has two dwarf companion galaxies located to the northwest at 50" (15.5 kpc) and to the southwest at 30A" (9 kpc). An H_α image shows two bright arms and circumnuclear extended emission, but the [O III] image only shows emission concentrated in the nucleus. There is an extremely luminous infrared source, with a very compact radio source. NGC 7130 looks very asymmetric, with a spiral arm to the northwest being more distorted and less organized than the arm to the southeast. This is probably related to the presence of the dwarf companion galaxy located to the northwest of NGC 7130. There are also two spiral arm segments located in the outer part of two dust lanes that run in the northsouth direction toward the center. These lanes could be tracing the leading edge of the near-IR bar. The inner structure is boxy with the major axis aligned at P.A.=90°, perpendicular to the near-IR bar (González Delgado et al., 1998).

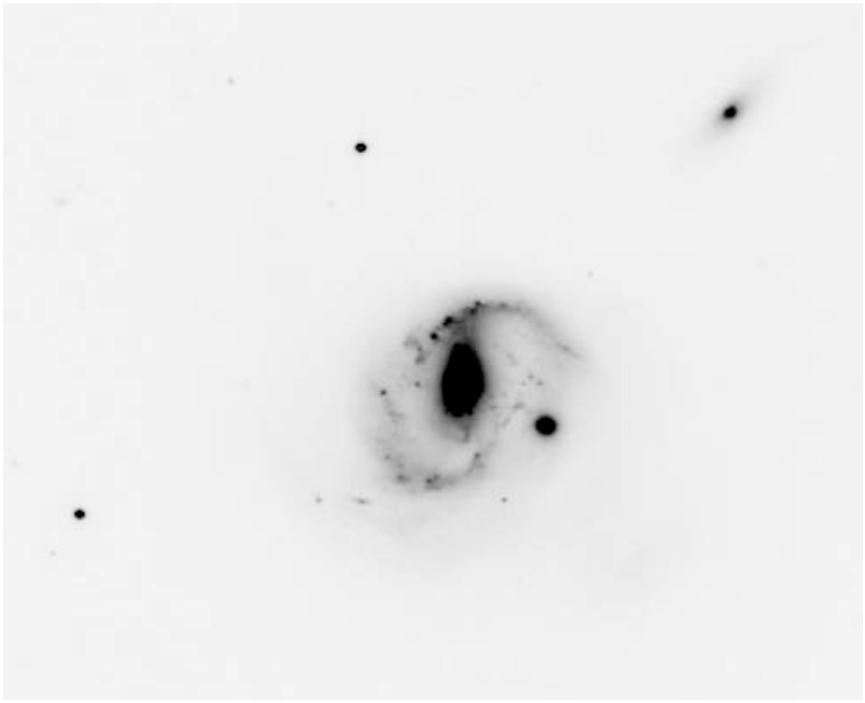

Figure A.28: HAWK-I K-band image of NGC 7130, with a spiral arm to the northwest being more distorted and less organized than the arm to the southeast. Is also visible a companion located to the northwest of the galaxy.

NGC 7592

NGc 7592, located at about $\sim 100 Mpc, z \sim 0.024$, is an infrared-luminous ($L_{IR} \sim 10^{11.2} L_{\odot}$) merger hosting a Seyfert 2 nucleus and two HII nuclei (Rafanelli & Marziani, 1992). In optical broad-band images, the three bright nuclei are arranged in a regular triangle with a length of the sides of $\sim 10''$. For convenience, we use the following terms: NGC 7592 W, E, and S for the western, eastern, and southern parts of the system and NGC 7592 A, B, and C, respectively, for each nucleus (fig. A.29). In these definitions, NGC 7592 B is located at 10."9 east and 1."6 south of NGC 7592 A, and NGC 7592 C at 5." 0 east and 11."2 south. NGC 7592 W is classified as a Seyfert 2 galaxy and the nuclei of NGC 7592 E and S are known to show HII region-like spectra. There are also several long tails around the main body; a northern tail extends from the north-west part of NGC 7592 W to the east, while a second tail sweeps from NGC 7592 S to the west and a third tail extends to the east from NGC 7592 E, and then curves downward (Hattori et al., 2002).

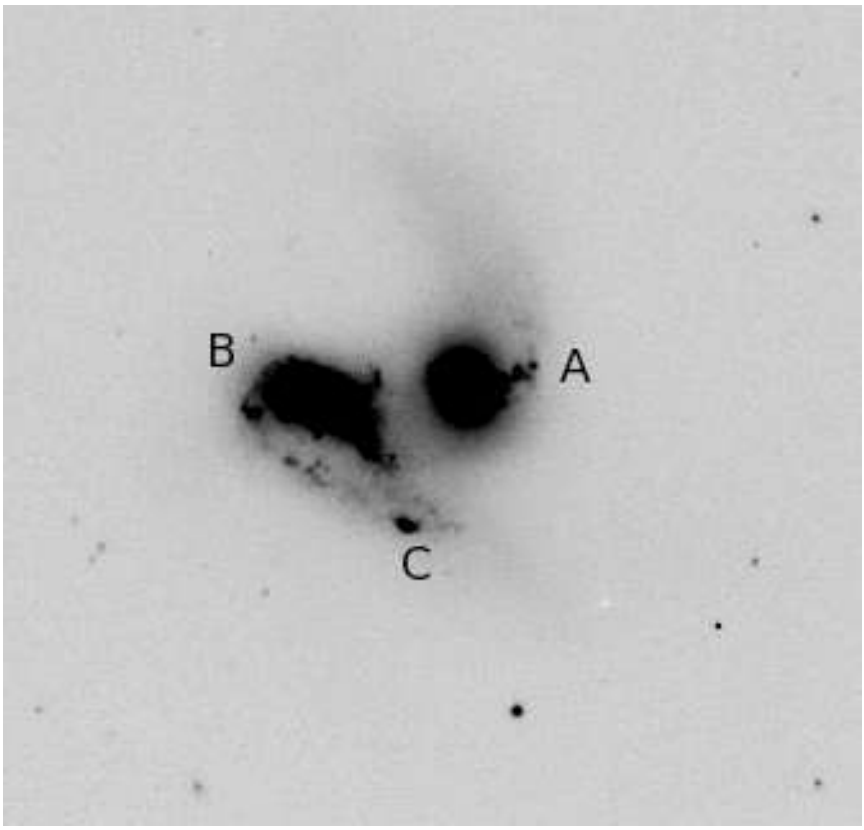

Figure A.29: HAWK-I K-band image of NGC 7592. The three nuclei are clearly visible. For the name of the nuclei see the text.

NGC 7674

NGC 7674 (Fig. A.30) is a type 2 Seyfert galaxy at a distance of about 115 Mpc which is classified as Sbc pec.
This galaxy has an infrared luminosity of $L_{IR} \sim 10^{11.22} L_{\odot}$.It is the brightest member of the well-isolated Hickson 96 (H96) compact galaxy group, which consists of four interacting galaxies with a mean heliocentric velocity of 8760 kms^{-1} and a low velocity dispersion ($\sigma_V \sim 160 kms^{-1}$). The two largest members in this group, NGC 7674 (H96a) and NGC 7675 (H96b), are separated by a projected distance of 2'.2. The observed features in NGC 7674, as revealed in optical images, can be accounted for by tidal interactions with its companion galaxies in the group (Momjian et al., 2003).

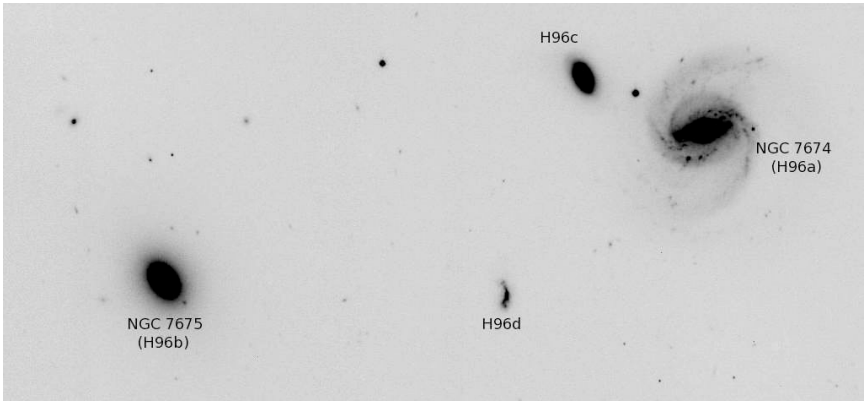

Figure A.30: HAWK-I K-band image of Hickinson compact group 96. The brighest member of the group is the starburst galaxy NGC 7674 .